



Spence, Ronald Richard. (2014) *The oxidehydrogenation of C-4 alkenes over zinc ferrite*. PhD thesis.

<http://theses.gla.ac.uk/5662/>

Copyright and moral rights for this work are retained by the author

A copy can be downloaded for personal non-commercial research or study, without prior permission or charge

This work cannot be reproduced or quoted extensively from without first obtaining permission in writing from the author

The content must not be changed in any way or sold commercially in any format or medium without the formal permission of the author

When referring to this work, full bibliographic details including the author, title, awarding institution and date of the thesis must be given

Enlighten:Theses  
<http://theses.gla.ac.uk/>  
theses@gla.ac.uk



# **The Oxidation of C-4 Alkenes over Zinc Ferrite.**

**Ronald Richard Spence**

**MRSC CChem**

Submitted in fulfilment of the requirements for the degree  
of MSc

**University of Glasgow  
School of Chemistry**

**July 2014**

©Ronald Spence 2014

## Abstract

In 1863 1,3-butadiene was isolated from the pyrolysis of amyl alcohol as an unknown hydrocarbon, but it was not until 1886 that Henry Edward Armstrong identified the hydrocarbon as butadiene. Around 95 % of 1,3-butadiene produced comes from the steam cracking of crude oil, however the outstanding 5 % is produced by on demand dehydrogenation and oxidative dehydrogenation processes.

The activity and selectivity of various catalysts for the conversion of C4 alkenes to 1,3-butadiene by oxidative dehydrogenation has been studied. Catalysts examined were bulk zinc ferrite and iron oxide catalysts produced by different precipitation methods and supported zinc ferrite and vanadia on  $\theta$ -alumina catalysts, which were produced with differing loadings. The majority of the study related to 1-butene, but cis-2-butene and trans-2-butene were also examined.

The catalysts were characterised pre and post reaction using BET Surface Area, Thermogravimetric Analysis-Differential Scanning Calorimetry, X-Ray Diffraction, Raman Spectroscopy, Acid Site Analysis, SQUID (Superconducting Quantum Interference Device) and EPR (Electron Paramagnetic Resonance) techniques.

The catalysts were tested under the flowing conditions at a reaction temperature of 693 K and a molar gas ratio 0.75:1:15 oxygen:alkene:steam.

$\theta$ -alumina supported zinc ferrite, iron doped zinc ferrite and vanadia catalysts were found to be poor 1-butene ODH catalysts compared to the bulk zinc ferrite catalysts since they only gave moderate 1-butene conversion. Also all of the supported catalysts with the exception of the highest zinc ferrite loading catalyst suffered from deactivation and increasing cis-2-butene and trans-2-butene selectivity with time on stream.

Iron enriched zinc ferrite and iron oxide bulk catalysts were also found to be poor 1-butene ODH catalysts since they only gave moderate to very low 1-butene conversion and with one exception deactivated with time on stream.

Bulk zinc ferrite catalysts were prepared from 0.6 M and 3 M sodium hydroxide with the catalysts prepared from 3 M sodium hydroxide to be the most effective at butene ODH (typical yield of ~37 %), whereas the 0.6 M catalysts required in excess of 60 hours on stream to fully activate.

The bulk zinc ferrite catalysts produced from 3 M sodium hydroxide were used to study the temperature stability of the catalyst, determine a bed profile, investigate space velocity changes, study different feed isomers and the inclusion of an isomerisation catalyst before the bulk zinc ferrite.

The catalyst was found have good temperature stability and a broad operating window. The bed profiling and space velocity studies revealed that the space velocity could be increased by a factor of 6 with no major loss to conversion or selectivity.

The introduction of an isomerisation catalyst before the zinc ferrite catalyst gave an increase in 1-butene conversion but this increase was attributed to an increase in isomerisation products. Nevertheless the use of an alumina pre-bed did result in higher butadiene yields with the best result being obtained with a 1:1 mixed alumina:zinc ferrite bed (54 %). Comparison between the pure butene isomers showed that trans-2-butene gave the highest 1,3-butadiene selectivity, butene conversion and lowest rate of isomerisation with an overall butadiene yield of ~75 %.

Comparison of the bulk zinc ferrite catalyst pre and post reaction revealed that the surface area was reduced by at least 50 % after reaction. This was, in most part, due to the steam. Characterisation of the surface acid sites on a fresh zinc ferrite compared to that after use revealed that there was a decrease in the number of acid sites with no strong acid sites remaining.

## Acknowledgements

I dedicate this MSc thesis to the memory of my late father Alexander Spence without whose encouragement and dedication to my education in my early formative years I would not have become the person I am today.

Firstly I would like to thank David Jackson not only for his assistance as my supervisor in this project but his friendship over more years than either of us care to remember.

I would next like thank Andy Monaghan for carrying out the TGA Analysis on the catalyst samples and for training me in the use of BET and XRD equipment, also his friendship as a fellow technician over the previous 15 years.

Next I wish to thank Jim Gallagher for his assistance in the use of the SEM equipment and interpretation of SEM results.

Grateful thanks to Michael Beglan and Stephy Wilson respectively for AA and Acid Site analyses.

Additional thanks go to Dr. Stephen Sproules and Dr. Vicki Millway for carrying out respectively EPR paramagnetic and SQUID magnetic measurements on catalysts and their assistance in the interpretation of the results.

Lastly many thanks to Invista Textiles (UK) Limited for funding the MSc project and to Dr. Keith Whiston for his help and advice throughout the project.

## Declaration

The work contained in this thesis, submitted for the degree of Doctor of philosophy, is my own work, except where due reference is made to other authors. No material within has been previously submitted for a degree at this or any other university.

Ron Spence

## Contents

1	Introduction	30
2	Aims of Project	45
3	Experimental	46
3.1	Material	46
3.2	Catalysts	47
3.3	Supported Catalyst Preparation	47
3.3.1	Stock Solutions	47
3.3.2	Spray Impregnation	48
3.3.3	High Temperature and Pressure Impregnation	48
3.4	Bulk Catalyst Preparation	49
3.5	Catalyst Characterisation	51
3.5.1	Surface Area Determination	51
3.5.2	Thermo-gravimetric Analysis Differential Scanning Calorimetry	52
3.5.3	X-Ray Diffraction	53
3.5.4	Raman Spectroscopy	54
3.5.6	Atomic Adsorption Analysis	56
3.6	Fixed Bed Reactor	56
3.6.1	Catalyst Pre-treatment	58
3.6.2	Experimental Method	58
3.6.3	Catalyst Testing	58
3.7	Analysis	60
3.7.1	Scanning Electron Microscope/Electron-dispersive X-Ray Spectroscopy	60
3.7.2	Gas Chromatography	60
3.7.3	Gas Chromatography Calibration	61
3.7.4	Gas Chromatography Result Calculations	67
3.7.5	Acid Site Analysis	68
3.7.6	Magnetic Analysis	71
3.7.6.1	SQUID	71
3.7.6.2	EPR	71

4	Experimental	72
4.1	$\theta$ -Alumina Support	72
4.1.1	Pre-Reaction Characterisation $\theta$ -Alumina	72
4.1.1.1	Pre-Reaction X-Ray Diffraction Analysis $\theta$ -Alumina	72
4.1.1.2	Pre-Reaction Raman Spectroscopy Analysis $\theta$ -Alumina	73
4.1.1.3	Pre-Reaction Surface Area Analysis $\theta$ -Alumina	75
4.1.1.4	Pre-Reaction Thermo-gravimetric Analysis- Differential Scanning Calorimetry Analysis $\theta$ -Alumina	75
4.1.2	Catalyst Testing $\theta$ -Alumina	76
4.1.3	Post Reaction Characterisation $\theta$ -Alumina	79
4.1.3.1	Post Reaction X-Ray Diffraction Analysis $\theta$ -Alumina	79
4.1.3.2	Post Reaction Raman Spectroscopy Analysis $\theta$ -Alumina	79
4.1.3.3	Post Reaction Surface Area Analysis $\theta$ -Alumina	80
4.1.3.4	Post Reaction Thermo-gravimetric Analysis- Differential Scanning Calorimetry Analysis $\theta$ -Alumina	80
4.2	Zinc Ferrite Supported on $\theta$ -Alumina	81
4.2.1	Pre-Reaction Characterisation Zinc Ferrite on $\theta$ -Alumina	81
4.2.1.1	Pre-Reaction AA Analysis Zinc Ferrite $\theta$ -Alumina	81
4.2.1.2	Pre-Reaction X-Ray Diffraction Analysis Zinc Ferrite $\theta$ -Alumina	82
4.2.1.3	Pre-Reaction Raman Spectroscopy Analysis Zinc Ferrite on $\theta$ -Alumina	84
4.2.1.4	Pre-Reaction Surface Area Measurements Zinc Ferrite on $\theta$ -Alumina	88
4.2.1.5	Pre-Reaction Thermo-gravimetric Analysis- Differential Scanning Calorimetry Analysis Zinc Ferrite on $\theta$ -Alumina	88
4.2.1.6	Pre-Reaction Scanning Electron Microscopy Analysis Zinc Ferrite on $\theta$ -Alumina	93
4.2.2	Catalyst Testing Supported Zinc Ferrite on $\theta$ -Alumina	95
4.2.3	Post Reaction Characterisation Zinc Ferrite on $\theta$ -Alumina	98
4.2.3.1	Post Reaction X-Ray Diffraction Analysis Zinc Ferrite on $\theta$ -Alumina	98

	4.2.3.2	Post Reaction Raman Spectroscopy Analysis Zinc Ferrite on $\theta$ -Alumina	100
	4.2.3.3	Post Reaction Surface Area Measurements Zinc Ferrite on $\theta$ -Alumina	104
	4.2.3.4	Post Reaction Thermo-gravimetric Analysis-Differential Scanning Calorimetry Analysis Zinc Ferrite on $\theta$ -Alumina	104
4.3		Vanadia Supported on $\theta$ -Alumina	107
	4.3.1	Pre-Reaction Characterisation Vanadia on $\theta$ -Alumina	107
	4.3.1.1	Pre-Reaction AA Analysis Vanadia on $\theta$ -Alumina	107
	4.3.1.2	Pre-Reaction X-Ray Diffraction Analysis Vanadia on $\theta$ -Alumina	108
	4.3.1.3	Pre-Reaction Raman Spectroscopy Analysis Vanadia on $\theta$ -Alumina	109
	4.3.1.4	Pre-Reaction Surface Area Measurements Vanadia on $\theta$ -Alumina	112
	4.3.1.5	Pre-Reaction Thermo-gravimetric Analysis-Differential Scanning Calorimetry Analysis Vanadia on $\theta$ -Alumina	112
	4.3.2	Catalyst Testing Supported Vanadia on $\theta$ -Alumina	115
	4.3.3	Post Reaction Characterisation Vanadia on $\theta$ -Alumina	117
	4.3.3.1	Post Reaction X-Ray Diffraction Analysis of Vanadia $\theta$ -Alumina	117
	4.3.3.2	Post Reaction Raman Spectroscopy Analysis Vanadia on $\theta$ -Alumina	119
	4.3.3.3	Post Reaction Surface Area Measurements Vanadia on $\theta$ -Alumina	119
	4.3.3.4	Post Reaction Thermo-gravimetric Analysis-Differential Scanning Calorimetry Analysis Vanadia on $\theta$ -Alumina	120
4.4		Zinc Ferrite ZF0.6MBP Bulk Catalyst	122
	4.4.1	Pre-Reaction Characterisation of Zinc Ferrite ZF0.6MBP	122
	4.4.1.1	Pre-Reaction AA Analysis of Zinc Ferrite ZF0.6MBP	122
	4.4.1.2	Pre-Reaction X-Ray Diffraction Analysis of Zinc Ferrite ZF0.6MBP	122
	4.4.1.3	Pre-Reaction Raman Spectroscopy Analysis of Zinc Ferrite ZF0.6MBP	124

4.4.1.4	Pre-Reaction Surface Area Measurements of Zinc Ferrite ZF0.6MBP	125
4.4.1.5	Pre-Reaction Thermo-gravimetric Analysis-Differential Scanning Calorimetry Analysis of Zinc Ferrite ZF0.6MBP	126
4.4.1.6	Acid Site Analysis of Zinc Ferrite ZF0.6MBP	128
4.4.1.7	Pre-Reaction Electron Paramagnetic Resonance Measurements of Zinc Ferrite ZF0.6MBP	129
4.4.1.8	Pre-Reaction Scanning Electron Microscopy Analysis of Zinc Ferrite ZF0.6MBP	130
4.4.2	Catalyst Testing Zinc Ferrite ZF0.6MBP	131
4.4.3	Post Reaction Characterisation of Zinc Ferrite ZF0.6MBP	133
4.4.3.1	Post Reaction X-Ray Diffraction Analysis of Zinc Ferrite ZF0.6MBP	133
4.4.3.2	Post Reaction Ambient Temperature Raman Spectroscopy Analysis of Zinc Ferrite ZF0.6MBP	135
4.4.3.3	Post Reaction Surface Area Measurements of Zinc Ferrite ZF0.6MBP	137
4.4.3.4	Post Reaction Thermo-gravimetric Analysis-Differential Scanning Calorimetry Analysis of Zinc Ferrite 0.6MBP	138
4.4.3.5	Post Reaction Acid Site Analysis of Zinc Ferrite ZF0.6MBP	139
4.4.3.6	Post Reaction Electron Paramagnetic Resonance Measurements of Zinc Ferrite ZF0.6MBP	140
4.4.3.7	Post Reaction Scanning Electron Microscopy Analysis of Zinc Ferrite ZF0.6MBP	141
4.5	Zinc Ferrite ZF3MBPC Bulk Catalyst	142
4.5.1	Pre-Reaction Characterisation of Zinc Ferrite ZF3MBPC	142
4.5.1.1	Pre-Reaction AA Analysis of Zinc Ferrite ZF3MBPC	142
4.5.1.2	Pre-Reaction X-Ray Diffraction Analysis of ZF3MBPC	142
4.5.1.3	Pre-Reaction Raman Spectroscopy Analysis of Zinc Ferrite ZF3MBPC	143
4.5.1.4	Pre-Reaction Surface Area Measurements of Zinc Ferrite ZF3MBPC	144

4.5.1.5	Pre-Reaction Thermo-gravimetric Analysis- Differential Scanning Calorimetry Analysis of Zinc Ferrite ZF3MBPC	145
4.5.1.6	Pre-Reaction Acid Site Analysis of Zinc Ferrite ZF3MBPC	146
4.5.1.7	Pre-Reaction Magnetic and Electron Paramagnetic Resonance Measurements of Zinc Ferrite ZF3MBPC	147
4.5.2	Catalyst Testing Zinc Ferrite ZF3MBPC	149
4.5.3	Post Reaction Characterisation of Zinc Ferrite ZF3MBPC	167
4.5.3.1	Post Reaction X-Ray Diffraction Analysis of ZF3MBPC	167
4.5.3.2	Post Reaction Raman Spectroscopy Analysis of Zinc Ferrite ZF3MBPC	168
4.5.3.3	Post Reaction Surface Area Measurements of Zinc Ferrite ZF3MBPC	169
4.5.3.4	Post Reaction Thermo-gravimetric Analysis- Differential Scanning Calorimetry Analysis of Zinc Ferrite ZF3MBPC	170
4.5.3.5	Post Reaction Acid Site Analysis of Zinc Ferrite ZF3MBPC	172
4.5.3.6	Post Reaction Magnetic and Electron Paramagnetic Resonance Measurements of Zinc Ferrite ZF3MBPC	172
4.6	Zinc Ferrite ZF3MBPD Bulk Catalyst	174
4.6.1	Pre-Reaction Characterisation of Zinc Ferrite ZF3MBPD	174
4.6.1.1	Pre-Reaction AA Analysis of Zinc Ferrite ZF3MBPD	174
4.6.1.2	Pre-Reaction X-Ray Diffraction Analysis of ZF3MBPD	174
4.6.1.3	Pre-Reaction Raman Spectroscopy Analysis of Zinc Ferrite ZF3MBPD	175
4.6.1.4	Pre-Reaction Surface Area Measurements of Zinc Ferrite ZF3MBPD	176
4.6.1.5	Pre-Reaction Thermo-gravimetric Analysis- Differential Scanning Calorimetry Analysis of Zinc Ferrite ZF3MBPD	177
4.6.1.6	Pre-Reaction Acid Site Analysis of Zinc Ferrite ZF3MBPD	177
4.6.2	Catalyst Testing Zinc Ferrite ZF3MBPD	178

4.6.3	Post Reaction Characterisation of Zinc Ferrite ZF3MBPD	183
4.6.3.1	Post Reaction X-Ray Diffraction Analysis of ZF3MBPD	183
4.6.3.2	Post Reaction Raman Spectroscopy Analysis of Zinc Ferrite ZF3MBPD	184
4.6.3.3	Post Reaction Surface Area Measurements of Zinc Ferrite ZF3MBPD	187
4.6.3.4	Post Reaction Thermo-gravimetric Analysis-Differential Scanning Calorimetry Analysis of Zinc Ferrite ZF3MBPD	187
4.6.3.5	Post Reaction Acid Site Analysis of Zinc Ferrite ZF3MBPD	189
4.7	Iron Enriched Zinc Ferrites Bulk Catalysts ZFFeNH3P, ZFFeNH3P and ZFFeNaOHP	189
4.7.1	Pre-Reaction Characterisation of Iron Enriched Zinc Ferrites	189
4.7.1.1	Pre-Reaction AA Analysis of Iron Enriched Zinc Ferrites	189
4.7.1.2	Pre-Reaction X-Ray Diffraction Analysis of Iron Enriched Zinc Ferrites	190
4.7.1.3	Pre-Reaction Raman Spectroscopy Analysis of Iron Enriched Zinc Ferrites	192
4.7.1.4	Pre-Reaction Surface Area Measurements of Iron Enriched Zinc Ferrites	196
4.7.1.5	Pre-Reaction Thermo-gravimetric Analysis-Differential Scanning Calorimetry Analysis of Iron Enriched Zinc Ferrites	196
4.7.2	Catalyst Testing Iron Enriched Zinc Ferrites	201
4.7.3	Post Reaction Characterisation of Iron Enriched Zinc Ferrites	204
4.7.3.1	Post Reaction X-Ray Diffraction Analysis of Iron Enriched Zinc Ferrites	204
4.7.3.2	Post Reaction Raman Spectroscopy Analysis of Iron Enriched Zinc Ferrites	208
4.7.3.3	Post Reaction Surface Area Measurements of Iron Enriched Zinc Ferrites	211
4.7.3.4	Post Reaction Thermo-gravimetric Analysis-Differential Scanning Calorimetry Analysis of Iron Enriched Zinc Ferrites	212

4.8	Iron Oxide Catalysts Bulk Catalysts Fe <sub>2</sub> O <sub>3</sub> NH <sub>3</sub> P and Fe <sub>2</sub> O <sub>3</sub> NaOHP	212
4.8.1	Pre-Reaction Characterisation of Iron Oxide Catalysts	212
4.8.1.1	Pre-Reaction X-Ray Diffraction Analysis of Iron Oxide Catalysts	212
4.8.1.2	Pre-Reaction Raman Spectroscopy Analysis of Iron Oxide Catalysts	214
4.8.1.3	Pre-Reaction Surface Area Measurements of Iron Oxide Catalysts	216
4.8.1.4	Pre-Reaction Thermo-gravimetric Analysis-Differential Scanning Calorimetry Analysis of Iron Oxide Catalysts	216
4.8.2	Catalyst Testing Iron Oxide Catalysts	219
4.8.3	Post Reaction Characterisation of Iron Oxide Catalysts	222
4.8.3.1	Post Reaction X-Ray Diffraction Analysis of Iron Oxide Catalysts	222
4.8.3.2	Post Reaction Raman Spectroscopy Analysis of Iron Oxide Catalysts	224
4.8.3.3	Post Reaction Surface Area Measurements of Iron Oxide Catalysts	225
4.8.3.4	Post Reaction Thermo-gravimetric Analysis-Differential Scanning Calorimetry Analysis of Iron Oxide Catalysts	226
4.9	Zinc Ferrite Citrate Precursor	226
4.9.1	Characterisation of Zinc Ferrite Citrate Precursor	226
4.9.1.1	X-Ray Diffraction Analysis of Zinc Ferrite Citrate Precursor	226
4.9.1.2	Raman Spectroscopy Analysis of Zinc Ferrite Citrate Precursor	227
4.9.1.3	Surface Area Measurements of Zinc Ferrite Citrate Precursor	229
4.9.1.4	Thermo-gravimetric Analysis-Differential Scanning Calorimetry Analysis of Zinc Ferrite Citrate Precursor	229
5	Discussion	234
5.1	Alumina Support	234
5.2	θ-Alumina Supported Zinc Ferrite Catalysts	235

5.3	$\theta$ -Alumina Supported Vanadia Catalysts	238
5.4	Bulk Zinc Ferrite ZF0.6MBP Catalysts	239
5.5	Bulk Zinc Ferrite ZF3MBPC Catalyst	242
5.6	Bulk Zinc Ferrite ZF3MBPD Catalyst	250
5.7	Iron Enriched Zinc Ferrite Catalysts	251
5.8	Iron Oxide Catalysts	254
6	Conclusion	256
7	References	259

## List of Figures

Figure 1.1	Crude Oil Refining Schematic	31
Figure 1.2	Internal View of Steam Cracking Furnace	32
Figure 1.3	Steam Cracking Unit	34
Figure 1.4	2011 Butadiene World Consumption	35
Figure 1.5	2009 Global Usage of 1,3-Butadiene	36
Figure 1.6	Extraction Process Schematic	37
Figure 1.7	Dehydrogenation Plant Schematic	39
Figure 1.8	Oxidative Dehydrogenation Plant Schematic	41
Figure 3.1	The BET Equation	52
Figure 3.2	Schematic of hot-stage XRD chamber	53
Figure 3.3	Scherrer Equation	54
Figure 3.4	Linkam CCR100 Environmental Cell	55
Figure 3.5	Linkam CCR 100 Environmental Cell Schematic	55
Figure 3.6	Fixed Bed Reactor	57
Figure 3.7	Methane Calibration	62
Figure 3.8	Ethane Calibration	62
Figure 3.9	Ethene Calibration	63
Figure 3.10	Propane Calibration	63
Figure 3.11	Butane Calibration	64
Figure 3.12	Iso-Butane Calibration	64
Figure 3.13	Carbon Dioxide Calibration	65
Figure 3.14	1-Butene Calibration	65
Figure 3.15	Cis-2-Butene Calibration	66
Figure 3.16	Trans-2-Butene Calibration	66
Figure 3.17	1,3-Butadiene Calibration	67
Figure 3.18	Typical Conversion Profile	68
Figure 3.19	Acid Site Analysis Rig	70
Figure 4.1	Pre-Reaction XRD Spectra of $\theta$ -Alumina at 303 K, 573 K and 873 K	72
Figure 4.2	Pre-Reaction Raman Spectra of $\theta$ -Alumina at 303 K, 673 K and 873 K	73
Figure 4.3	Pre-Reaction $\theta$ -Alumina TGA and Derivative Weight	76

Figure 4.4	Selectivity/Conversion Major Components $\theta$ -Alumina Bed Volume 3 cm <sup>3</sup>	77
Figure 4.5	Selectivity Minor Components $\theta$ -Alumina Bed Volume 3 cm <sup>3</sup>	77
Figure 4.6	Selectivity/Conversion Major Components $\theta$ -Alumina Bed Volume 1 cm <sup>3</sup>	78
Figure 4.7	Selectivity Minor Components $\theta$ -Alumina Bed Volume 1 cm <sup>3</sup>	78
Figure 4.8	Post Reaction Ambient Temperature XRD Spectra of $\theta$ -Alumina	79
Figure 4.9	Post Reaction $\theta$ -Alumina TGA and Derivative Weight	81
Figure 4.10	Pre-Reaction XRD Spectra of 3.45 % Zinc Ferrite on $\theta$ -Alumina at 303 K, 573 K and 873 K	82
Figure 4.11	Pre-Reaction XRD Spectra of 3.2 % Fe/0.39 % Zn on $\theta$ -Alumina at 303 K, 573 K and 873 K	83
Figure 4.12	Pre-Reaction Room Temperature XRD Spectra of 8.81 % ZnFe <sub>2</sub> O <sub>4</sub> /0.49 % Fe on $\theta$ -Alumina	84
Figure 4.13	Pre-Reaction Raman Spectra of 3.45 % Zinc Ferrite on $\theta$ -Alumina at 303 K, 573 K and 773 K	85
Figure 4.14	Pre-Reaction Raman Spectra of 3.2 % Fe/0.39 % Zn on $\theta$ -Alumina at 303 K, 573 K and 873K	85
Figure 4.15	Pre-Reaction Ambient Temperature Raman Spectra of 8.81 % ZnFe <sub>2</sub> O <sub>4</sub> /0.49 % Fe on $\theta$ -Alumina	86
Figure 4.16	Pre-Reaction 3.45 % Zinc Ferrite on $\theta$ -Alumina TGA and Derivative Weight	89
Figure 4.17	Pre-Reaction TGA/DSC Mass Spectrometer Profile from 3.45 % Zinc Ferrite on $\theta$ -Alumina m/e 30	89
Figure 4.18	Pre-Reaction TGA/DSC Mass Spectrometer Profile from 3.45 % Zinc Ferrite on $\theta$ -Alumina m/e 44	90
Figure 4.19	Pre-Reaction TGA/DSC Mass Spectrometer Profile from 3.45 % Zinc Ferrite on $\theta$ -Alumina m/e 46	90
Figure 4.20	Pre-Reaction 3.2 % Fe/0.39 % Zn on $\theta$ -Alumina TGA and Derivative Weight	91
Figure 4.21	Pre-Reaction TGA/DSC Mass Spectrometer Profile from 3.2 % Fe/0.39% Zn on $\theta$ -Alumina m/e 30	91
Figure 4.22	Pre-Reaction TGA/DSC Mass Spectrometer Profile from 3.2 % Fe/0.39 % Zn on $\theta$ -Alumina m/e 44	92
Figure 4.23	Pre-Reaction 8.81 % ZnFe <sub>2</sub> O <sub>4</sub> /0.49 % Fe on $\theta$ -Alumina TGA and Derivative Weight	92

Figure 4.24	Pre-Reaction TGA/DSC Mass Spectrometer Profile from 8.81 % ZnFe <sub>2</sub> O <sub>4</sub> /0.49 % Fe on $\theta$ -Alumina m/e 30	93
Figure 4.25	Pre-Reaction 3.45 % Zinc Ferrite on $\theta$ -Alumina SEM Micrograph	93
Figure 4.26	Pre-Reaction 3.2 % Fe <sub>2</sub> O <sub>3</sub> /0.39 % on $\theta$ -Alumina SEM Micrograph	94
Figure 4.27	Pre-Reaction 8.81 % ZnFe <sub>2</sub> O <sub>4</sub> /0.49 % Fe on $\theta$ -Alumina SEM Micrograph	94
Figure 4.28	Selectivity/Conversion Major Components 3.45 % Zinc Ferrite on $\theta$ -Alumina	95
Figure 4.29	Selectivity Minor Components 3.45 % Zinc Ferrite on $\theta$ -Alumina	96
Figure 4.30	Selectivity/Conversion Major Components 3.2 % Fe/0.39 % Zn on $\theta$ -Alumina	96
Figure 4.31	Selectivity Minor Components 3.2 % Fe/0.39 % Zn on $\theta$ -Alumina	97
Figure 4.32	Selectivity/Conversion Major Components 8.81 % ZnFe <sub>2</sub> O <sub>4</sub> /0.49 % Fe on $\theta$ -Alumina	97
Figure 4.33	Selectivity Minor Components 8.81 % ZnFe <sub>2</sub> O <sub>4</sub> /0.49 % Fe on $\theta$ -Alumina	98
Figure 4.34	Post Reaction Ambient Temperature XRD Spectra of 3.45 % Zinc Ferrite on $\theta$ -Alumina	99
Figure 4.35	Post Reaction Ambient Temperature XRD Spectra of 3.2 % Fe/0.39 % Zn on $\theta$ -Alumina	99
Figure 4.36	Post Reaction Ambient Temperature XRD Spectra of 8.81 % ZnFe <sub>2</sub> O <sub>4</sub> /0.49 % Fe on $\theta$ -Alumina	100
Figure 4.37	Post Reaction Ambient Temperature Raman Spectra of 3.45 % Zinc Ferrite on $\theta$ -Alumina	101
Table 4.38	Post Reaction Ambient Temperature Raman Spectra of 3.2 % Fe/0.39 % Zn on $\theta$ -Alumina	101
Figure 4.39	Post Reaction Ambient Temperature Raman Spectra of 8.81 % Zinc Ferrite/0.49 % Fe on $\theta$ -Alumina	102
Figure 4.40	Post Reaction 3.45 % Zinc Ferrite on $\theta$ -Alumina TGA and Derivative Weight	105
Figure 4.41	Post Reaction TGA/DSC Mass Spectrometer Profile from 3.45 % Zinc Ferrite on $\theta$ -Alumina m/e 44	105
Figure 4.42	Post Reaction 3.2 % Fe/0.39% Zn on $\theta$ -Alumina TGA and Derivative Weight	106
Figure 4.43	Post Reaction TGA/DSC Mass Spectrometer Profile from 3.2 % Fe/0.39 % Zn on $\theta$ -Alumina m/e 30	106

Figure 4.44	Post Reaction 8.81 % ZnFe <sub>2</sub> O <sub>4</sub> /0.49 % Fe on $\theta$ -Alumina TGA and Derivative Weight	107
Figure 4.45	Pre-Reaction Temperature Programmed XRD Spectra of 0.5 % Vanadia on $\theta$ -Alumina at 303 K, 573 K and 873 K	108
Figure 4.46	Pre-Reaction Ambient Temperature XRD Spectra of 3.3 % Vanadia on $\theta$ -Alumina	109
Figure 4.47	Pre-Reaction Temperature Programmed Raman Spectra of 0.5 % Vanadia on $\theta$ -Alumina at 303 K, 373K and 873 K	110
Figure 4.48	Pre-Reaction Ambient Temperature Raman Spectra of 3.3 % Vanadia on $\theta$ -Alumina	110
Figure 4.49	Pre-Reaction 0.5 % Vanadia on $\theta$ -Alumina TGA and Derivative Weight	113
Figure 4.50	Pre-Reaction GA/DSC Mass Spectrometer Profile from 0.5 % Vanadia on $\theta$ -Alumina m/e 44	113
Figure 4.51	Pre-Reaction GA/DSC Mass Spectrometer Profile from 0.5 % Vanadia on $\theta$ -Alumina m/e 30	114
Figure 4.52	Pre-Reaction 3.3 % Vanadia on $\theta$ -Alumina TGA and Derivative Weight	114
Figure 4.53	Pre-Reaction GA/DSC Mass Spectrometer Profile from 3.3 % Vanadia on $\theta$ -Alumina m/e 44	115
Figure 4.54	Selectivity/Conversion Major Components 0.5 % Vanadia on $\theta$ -Alumina	116
Figure 4.55	Selectivity Minor Components 0.5 % Vanadia on $\theta$ -Alumina	116
Figure 4.56	Selectivity/Conversion Major Components 3.3 % Vanadia on $\theta$ -Alumina	117
Figure 4.57	Selectivity Minor Components 3.3 % Vanadia on $\theta$ -Alumina	117
Figure 4.58	Post Reaction Ambient Temperature XRD Spectra of 0.5 % Vanadia on $\theta$ -Alumina	118
Figure 4.59	Post Reaction Ambient Temperature XRD Spectra of 3.3 % Vanadia on $\theta$ -Alumina	119
Figure 4.60	Post Reaction 0.5 % Vanadia on $\theta$ -Alumina TGA and Derivative Weight	121
Figure 4.61	Post Reaction 3.3 % Vanadia on $\theta$ -Alumina TGA and Derivative Weight	121
Figure 4.62	Pre-Reaction Ambient Temperature XRD Spectra of Zinc Ferrite ZFO.6MBP	123

Figure 4.63	Pre-Reaction Ambient Temperature XRD Spectra of Zinc Ferrite ZF0.6MBP 24HSPT	123
Figure 4.64	Pre-Reaction Ambient Temperature Raman Spectra of Zinc Ferrite ZF0.6MBP	124
Figure 4.65	Pre-Reaction Ambient Temperature Raman Spectra of Zinc Ferrite ZF0.6MBP 24HSPT	125
Figure 4.66	Pre-Reaction Zinc Ferrite ZF0.6MBP TGA and Derivative Weight	126
Figure 4.67	Pre-Reaction Zinc Ferrite ZF0.6MBP TGA/DSC DSC	127
Figure 4.68	Pre-Reaction TGA/DSC Mass Spectrometer Profile from ZF0.6MBP TGA/DSC m/e 44	127
Figure 4.69	Pre-Reaction Zinc Ferrite ZF0.6MBP 24HSPT TGA and Derivative Weight.	128
Figure 4.70	Pre-Reaction Zinc Ferrite ZF0.6MBP Acid Site Analysis	129
Figure 4.71	EPR Profile of Pre-Reaction Zinc Ferrite ZF0.6MBP EPR	129
Figure 4.72	EPR Profile of Steamed Pre-Reaction Zinc Ferrite ZF0.6MBP EPR 24HSPT	130
Figure 4.73	Pre-Reaction Zinc Ferrite ZF0.6MBP SEM Micrograph	130
Figure 4.74	Selectivity/Conversion Major Components Zinc Ferrite ZF0.6MBP	132
Figure 4.75	Selectivity Minor Components Zinc Ferrite ZF0.6MBP	132
Figure 4.76	Selectivity/Conversion Major Components Zinc Ferrite ZF0.6MBP 24HSPT	133
Figure 4.77	Selectivity Minor Components Zinc Ferrite ZF0.6MBP 24HSPT	133
Figure 4.78	Post Reaction Ambient Temperature XRD Spectra of Zinc Ferrite ZF0.6MBP	134
Figure 4.79	Post Reaction Ambient Temperature XRD Spectra of Zinc Ferrite ZF0.6MBP 24HSPT	135
Figure 4.80	Post Reaction Ambient Temperature Raman Spectra of Zinc Ferrite ZF0.6MBP	136
Figure 4.81	Post Reaction Ambient Temperature Raman Spectra of Zinc Ferrite ZF0.6MBP 24HSPT	136
Figure 4.82	Post Reaction Zinc Ferrite ZF0.6MBP TGA and Derivative Weight	139
Figure 4.83	Post Reaction Zinc Ferrite ZF0.6MBP Acid Site Analysis	140
Figure 4.84	EPR Profiles of Post-Reaction Zinc Ferrite ZF0.6MBP	140
Figure 4.85	EPR Profile of Post Reaction Zinc Ferrite ZF0.6MBP 24HSPT	141
Figure 4.86	Post Reaction Zinc Ferrite 0.6MBP SEM Micrograph 67 Hours	142

Figure 4.87	Pre-Reaction Ambient Temperature XRD Spectra of Zinc Ferrite ZF3MBPC	143
Figure 4.88	Pre-Reaction Ambient Temperature Raman Spectra of Zinc Ferrite ZF3MBPC	144
Figure 4.89	Pre-Reaction Zinc Ferrite ZF3MBPC TGA and Derivative Weight	145
Figure 4.90	Pre-Reaction Zinc Ferrite ZF3MBPC TGA/DSC DSC	146
Figure 4.91	Pre-Reaction TGA/DSC Mass Spectrometer Profile from Zinc Ferrite ZF3MBPC m/e 44	146
Figure 4.92	Pre-Reaction Zinc Ferrite ZF3MBPC Acid Site Analysis	147
Figure 4.93	Pre-Reaction Zinc Ferrite ZF3MBPC SQUID Magnetic Measurement	148
Figure 4.94	Pre-Reaction Zinc Ferrite ZF3MBPC EPR Magnetic Measurement	148
Figure 4.95	Selectivity/Conversion Major Components Zinc Ferrite ZF3MBPC Bed Volume 3 cm <sup>3</sup>	150
Figure 4.96	Selectivity Minor Components Zinc Ferrite ZF3MBPC Bed Volume 3 cm <sup>3</sup>	150
Figure 4.97	Selectivity/Conversion Major Components Zinc Ferrite ZF3MBPC Bed Volume 2 cm <sup>3</sup>	151
Figure 4.98	Selectivity Minor Components Zinc Ferrite ZF3MBPC Bed Volume 2 cm <sup>3</sup>	151
Figure 4.99	Selectivity/Conversion Major Components Zinc Ferrite ZF3MBPC Bed Volume 1 cm <sup>3</sup>	152
Figure 4.100	Selectivity Minor Components Zinc Ferrite ZF3MBPC Bed Volume 1 cm <sup>3</sup>	152
Figure 4.101	Selectivity/Conversion Major Components Zinc Ferrite ZF3MBPC Bed Volume 0.5 cm <sup>3</sup>	153
Figure 4.102	Selectivity Minor Components Zinc Ferrite ZF3MBPC Bed Volume 0.5 cm <sup>3</sup>	153
Figure 4.103	Bed Volume Comparison of Selectivities and Conversion at 50 Hours on Stream Zinc Ferrite ZF3MBPC	154
Figure 4.104	Selectivity/Conversion Major Components Zinc Ferrite ZF3MBPC Temperature Variation 693 K - 653 K - 693 K	155
Figure 4.105	Selectivity Minor Components Zinc Ferrite ZF3MBPC Temperature Variation 693 K - 653 K - 693 K	155
Figure 4.106	Selectivity/Conversion Major Components Zinc Ferrite ZF3MBPC Temperature Variation 693 K - 713 K - 693 K	156

Figure 4.107	Selectivity Minor Components Zinc Ferrite ZF3MBPC Temperature Variation 693 K - 713 K - 693 K	156
Figure 4.108	Selectivity/Conversion Major Components Zinc Ferrite ZF3MBPC Temperature Variation 693 K - 633 K - 693 K	157
Figure 4.109	Selectivity Minor Components Zinc Ferrite ZF3MBPC Temperature Variation 693 K - 633 K - 693 K	157
Figure 4.110	Selectivity/Conversion Major Components Zinc Ferrite ZF3MBPC Temperature Variation 693 K - 613 K	158
Figure 4.111	Selectivity Minor Components Zinc Ferrite ZF3MBPC Temperature Variation 693 K - 613 K	158
Figure 4.112	Selectivity/Conversion Major Components Zinc Ferrite ZF3MBPC Double Flow Bed Volume 3 cm <sup>3</sup>	159
Figure 4.113	Selectivity Minor Components Zinc Ferrite ZF3MBPC Double Flow Bed Volume 3 cm <sup>3</sup>	160
Figure 4.114	Selectivity/Conversion Major Components Zinc Ferrite ZF3MBPC Double Flow Bed Volume 1 cm <sup>3</sup>	160
Figure 4.115	Selectivity Minor Components Zinc Ferrite ZF3MBPC Double Flow Bed Volume 1 cm <sup>3</sup>	161
Figure 4.116	Selectivity/Conversion Major Components Zinc Ferrite ZF3MBPC Normal Flow Bed + Argon Bed Volume 1 cm <sup>3</sup>	161
Figure 4.117	Selectivity Minor Components Zinc Ferrite ZF3MBPC Normal Flow Bed + Argon Bed Volume 1 cm <sup>3</sup>	162
Figure 4.118	Flow Comparison of Selectivities and Conversion at 50 Hours on Stream Zinc Ferrite ZF3MBPC Bed Volume 3 cm <sup>3</sup>	162
Figure 4.119	Flow Comparison of Selectivities and Conversion at 50 Hours on Stream Zinc Ferrite ZF3MBPC Bed Volume 1 cm <sup>3</sup>	163
Figure 4.120	Selectivity/Conversion Major Components Dual Bed $\theta$ -Alumina/Zinc Ferrite ZF3MBPC 3:1	164
Figure 4.121	Selectivity/Minor Components Dual Bed $\theta$ -Alumina/Zinc Ferrite ZF3MBPC 3:1	164
Figure 4.122	Selectivity/Conversion Major Components Dual Bed $\theta$ -Alumina/Zinc Ferrite ZF3MBPC 1:1	165
Figure 4.123	Selectivity/Minor Components Dual Bed $\theta$ -Alumina/Zinc Ferrite ZF3MBPC 1:1	165
Figure 4.124	Selectivity/Conversion Major Components Dual Bed $\theta$ -Alumina/Zinc Ferrite ZF3MBPC1:1 Mixed	166

Figure 4.125	Selectivity Minor Components Dual Bed $\theta$ -Alumina/Zinc Ferrite ZF3MBPC 1:1 Mixed	166
Figure 4.126	Dual Bed Comparison of Selectivities and Conversion at 50 Hours on Stream $\theta$ -Alumina:Zinc Ferrite ZF3MBPC	167
Figure 4.127	Post Reaction Ambient Temperature XRD Spectra of Zinc Ferrite ZF3MBPC	168
Figure 4.128	Post Reaction Ambient Temperature Raman Spectra of Zinc Ferrite ZF3MBPC	169
Figure 4.129	Post Reaction Zinc Ferrite ZF3MBPC TGA and Derivative Weight	171
Figure 4.130	Post Reaction TGA/DSC Mass Spectrometer Profile from Zinc Ferrite ZF3MBPC m/e 44	171
Figure 4.131	Post Reaction Zinc Ferrite ZF3MBPC Acid Site Analysis	172
Figure 4.132	Post Reaction Zinc Ferrite ZF3MBPC SQUID Magnetic Measurement	173
Figure 4.133	EPR Profile of Post Reaction Zinc Ferrite ZF3MBPC	173
Figure 4.134	Pre-Reaction Ambient Temperature XRD Spectra of Zinc Ferrite ZF3MBPD	175
Figure 4.135	Pre-Reaction Ambient Temperature Raman Spectroscopy of Zinc Ferrite ZF3MBPD	176
Figure 4.136	Pre-Reaction Zinc Ferrite ZF3MBPD TGA and Derivative Weight	177
Figure 4.137	Pre-Reaction Zinc Ferrite ZF3MBPD Acid Site Analysis	178
Figure 4.138	Selectivity/Conversion Major Components Zinc Ferrite ZF3MBPD Bed Volume 3 cm <sup>3</sup>	179
Figure 4.139	Selectivity Minor Components Zinc Ferrite ZF3MBPD Bed Volume 3 cm <sup>3</sup>	179
Figure 4.140	Selectivity/Conversion Major Components Zinc Ferrite ZF3MBPD Alkene 1-Butene Bed Volume 1 cm <sup>3</sup>	180
Figure 4.141	Selectivity Minor Components Zinc Ferrite ZF3MBPD Alkene 1-Butene Bed Volume 1 cm <sup>3</sup>	180
Figure 4.142	Selectivity/Conversion Major Components Zinc Ferrite ZF3MBPD Alkene Cis-2-Butene Bed Volume 1 cm <sup>3</sup>	181
Figure 4.143	Selectivity Minor Components Zinc Ferrite ZF3MBPD Alkene Cis-2-Butene Bed Volume 1 cm <sup>3</sup>	181
Figure 4.144	Selectivity/Conversion Major Components Zinc Ferrite ZF3MBPD Alkene Trans-2-Butene Bed Volume 1 cm <sup>3</sup>	182
Figure 4.145	Selectivity Minor Components Zinc Ferrite ZF3MBPD Alkene Trans-2-Butene Bed Volume 1 cm <sup>3</sup>	182

Figure 4.146	Isomer Effect on Selectivities and Conversion at 10 Hours on Stream Zinc Ferrite ZF3MBPD Bed Volume 1 cm <sup>3</sup>	183
Figure 4.147	Post Reaction Ambient Temperature XRD Spectra of Zinc Ferrite ZF3MBPD	184
Figure 4.148	Post Reaction Ambient Temperature Raman Spectroscopy of Zinc Ferrite ZF3MBPD	185
Figure 4.149	Post Reaction Zinc Ferrite ZF3MBPD TGA and Derivative Weight	188
Figure 4.150	Post Reaction TGA/DSC Mass Spectrometer Profile from Zinc Ferrite ZF3MBPD m/e 44	188
Figure 4.151	Post Reaction Zinc Ferrite ZF3MBPD Acid Site Analysis	189
Figure 4.152	Pre-Reaction Ambient Temperature XRD Spectra of Iron Enriched Zinc Ferrite ZFFeNH3P	190
Figure 4.153	Pre-Reaction Ambient Temperature XRD Spectra of Iron Enriched Zinc Ferrite ZFFeNH3PD	191
Figure 4.154	Pre-Reaction Ambient Temperature XRD Spectra of Iron Enriched Zinc Ferrite ZFFeNaOHP	192
Figure 4.155	Pre-Reaction Ambient Temperature Raman Spectra of Iron Enriched Zinc Ferrite ZFFeNH3P	193
Figure 4.156	Pre-Reaction Ambient Temperature Raman Spectra of Iron Enriched Zinc Ferrite ZFFeNH3PD	193
Figure 4.157	Pre-Reaction Ambient Temperature Raman Spectra of Iron Enriched Zinc Ferrite ZFFeNaOHP	194
Figure 4.158	Pre-Reaction Iron Enriched Zinc Ferrite ZFFeNH3P TGA and Derivative Weight	197
Figure 4.159	Pre-Reaction Iron Enriched Zinc Ferrite ZFFeNH3P TGA/DSC DSC	197
Figure 4.160	Pre-Reaction Iron Enriched Zinc Ferrite ZFFeNH3PD TGA and Derivative Weight	198
Figure 4.161	Pre-Reaction Iron Enriched Zinc Ferrite ZFFeNH3PD TGA/DSC DSC	198
Figure 4.162	Pre-Reaction TGA/DSC Mass Spectrometer Profile from ZFFeNH3PD m/e 28	199
Figure 4.163	Pre-Reaction TGA/DSC Mass Spectrometer Profile from ZFFeNH3PD m/e 30	199
Figure 4.164	Pre-Reaction Iron Enriched Zinc Ferrite ZFFeNaOHP TGA and Derivative Weight	200
Figure 4.165	Pre-Reaction Iron Enriched Zinc Ferrite ZFFeNaOHP TGA/DSC DSC	200

Figure 4.166	Selectivity/Conversion Major Components Iron Enriched Zinc Ferrite ZFFeNH3P Bed Volume 3 cm <sup>3</sup>	201
Figure 4.167	Selectivity Minor Components Iron Enriched Zinc Ferrite ZFFeNH3P Bed Volume 3 cm <sup>3</sup>	202
Figure 4.168	Selectivity/Conversion Major Components Iron Enriched Zinc Ferrite ZFFeNH3PD Bed Volume 3 cm <sup>3</sup>	202
Figure 4.169	Selectivity Minor Components Iron Enriched Zinc Ferrite ZFFeNH3PD Bed Volume 3 cm <sup>3</sup>	203
Figure 4.170	Selectivity/Conversion Major Components Iron Enriched Zinc Ferrite ZFFeNaOHP Bed Volume 1 cm <sup>3</sup>	203
Figure 4.171	Selectivity Minor Components Iron Enriched Zinc Ferrite ZFFeNaOHP Bed Volume 1 cm <sup>3</sup>	204
Figure 4.172	Post Reaction Ambient Temperature XRD Spectra of Iron Enriched Zinc Ferrite ZFFeNH3P	205
Figure 4.173	Post Reaction Ambient Temperature XRD Spectra of Iron Enriched Zinc Ferrite ZFFeNH3PD	206
Figure 4.174	Post Reaction Ambient Temperature XRD Spectra of Iron Enriched Zinc Ferrite ZFFeNaOHP	207
Figure 4.175	Post Reaction Ambient Temperature Raman Spectra of Iron Enriched Zinc Ferrite ZFFeNH3P	208
Figure 4.176	Post Reaction Ambient Temperature Raman Spectra of Iron Enriched Zinc Ferrite ZFFeNH3PD	209
Figure 4.177	Post Reaction Ambient Temperature Raman Spectra of Iron Enriched Zinc Ferrite ZFFeNaOHP	209
Figure 4.178	Pre-Reaction Ambient Temperature XRD Spectra of Iron Oxide Catalyst Fe2O3NaOHP	213
Figure 4.179	Pre-Reaction Ambient Temperature XRD Spectra of Iron Oxide Catalyst Fe2O3NH3P	214
Figure 4.180	Pre-Reaction Ambient Temperature Raman Spectra of Iron Oxide Catalyst Fe2O3NaOHP	215
Figure 4.181	Pre-Reaction Ambient Temperature Raman Spectra of Iron Oxide Catalyst Fe2O3NH3P	215
Figure 4.182	Pre-Reaction Iron Oxide Catalysts Fe2O3NaOHP TGA and Derivative Weight	217
Figure 4.183	Pre-Reaction Iron Oxide Catalysts Fe2O3NaOHP TGA/DSC DSC	217
Figure 4.184	Pre-Reaction TGA/DSC Mass Spectrometer Profile from Iron Oxide Catalyst Fe2O2NaOHP m/e 18	218

Figure 4.185	Pre-Reaction Iron Oxide Catalysts Fe <sub>2</sub> O <sub>3</sub> NH <sub>3</sub> P TGA and Derivative Weight	218
Figure 4.186	Pre-Reaction Iron Oxide Catalysts Fe <sub>2</sub> O <sub>3</sub> NH <sub>3</sub> P TGA/DSC DSC	219
Figure 4.187	Selectivity/Conversion Major Components Iron Oxide Catalyst Fe <sub>2</sub> O <sub>3</sub> NaOHP Bed Volume 1 cm <sup>3</sup>	220
Figure 4.188	Selectivity Minor Components Iron Oxide Catalyst Fe <sub>2</sub> O <sub>3</sub> NaOHP Bed Volume 1 cm <sup>3</sup>	220
Figure 4.189	Selectivity/Conversion Major Components Iron Oxide Catalyst Fe <sub>2</sub> O <sub>3</sub> NH <sub>3</sub> P Bed Volume 1 cm <sup>3</sup>	221
Figure 4.190	Selectivity Minor Components Iron Oxide Catalyst Fe <sub>2</sub> O <sub>3</sub> NH <sub>3</sub> P Bed Volume 1 cm <sup>3</sup>	221
Figure 4.191	Post Reaction Ambient Temperature XRD Spectra of Iron Oxide Catalyst Fe <sub>2</sub> O <sub>3</sub> NaOHP	222
Figure 4.192	Post Reaction Ambient Temperature XRD Spectra of Iron Oxide Catalyst Fe <sub>2</sub> O <sub>3</sub> NH <sub>3</sub> P	223
Figure 4.193	Post Reaction Ambient Temperature Raman Spectra of Iron Oxide Catalyst Fe <sub>2</sub> O <sub>3</sub> NaOHP	224
Figure 4.194	Post Reaction Ambient Temperature Raman Spectra of Iron Oxide Catalyst Fe <sub>2</sub> O <sub>3</sub> NH <sub>3</sub> P	225
Figure 4.195	Ambient Temperature XRD Spectra of Zinc Ferrite Citrate Precursor	227
Figure 4.196	Ambient Temperature Raman Spectra of Zinc Ferrite Citrate Precursor	227
Figure 4.197	Zinc Ferrite Citrate Precursor TGA and Derivative Weight	230
Figure 4.198	Zinc Ferrite Citrate Precursor TGA/DSC DSC	230
Figure 4.199	TGA/DSC Mass Spectrometer Profile Zinc Ferrite Citrate Precursor m/e 18	231
Figure 4.200	TGA/DSC Mass Spectrometer Profile Zinc Ferrite Citrate Precursor m/e 28	231
Figure 4.201	TGA/DSC Mass Spectrometer Profile Zinc Ferrite Citrate Precursor m/e 30	232
Figure 4.202	Zinc Ferrite TGA/DSC Mass Spectrometer Profile Citrate Precursor m/e 44	232
Figure 4.203	TGA/DSC Mass Spectrometer Profile Zinc Ferrite Citrate Precursor m/e 46	233
Figure 4.204	TGA/DSC Mass Spectrometer Profile Zinc Ferrite Citrate Precursor m/e 32	233

Figure 5.1	Reaction Schematic	234
Figure 5.2	Comparison of Pre and Post Reaction Zinc Ferrite ZF0.6MBP EPR Magnetic Measurement	240
Figure 5.3	Comparison of Pre and Post Reaction Pre-Steamed Zinc Ferrite ZF0.6MBP 24HSPT EPR Magnetic Measurement	242
Figure 5.4	Comparison of Pre and Post Reaction Zinc Ferrite ZF03MBPC SQUID Magnetic Measurement	243
Figure 5.5	Comparison of Pre and Post Reaction Zinc Ferrite ZF3MBPC EPR Paramagnetic Measurement	244
Figure 5.6	Bed Length Comparison of Selectivities and Conversion at 50 Hours on Stream Zinc Ferrite ZF3MBPC	245
Figure 5.7	Comparison of Average Gas Composition Post 3cm <sup>3</sup> Alumina Bed and Gas Composition Post Reaction Alumina:Zinc Ferrite (ZF3MBPC) 3:1 at 50 h TOS.	248
Figure 5.8	Comparison of Average Gas Composition Post 1cm <sup>3</sup> Alumina Bed and Gas Composition Post Reaction Alumina:Zinc Ferrite (ZF3MBPC) 1:1 at 50 h TOS.	249
Figure 5.9	Comparison of Gas Composition Post Reaction Alumina:Zinc Ferrite (ZF3MBPC) 3:1, 1:1 and 1:1 Mixed at 50 h TOS.	250

## List of Tables

Table 1.1	Crude Oil Composition Variation	30
Table 1.2	Steam Cracker Product Composition	33
Table 3.1	Materials	46
Table 3.2	Supported Catalysts 1	48
Table 3.3	Supported Catalysts 2	49
Table 3.4	Bulk Catalysts (Preparation Method 1)	49
Table 3.5	Bulk Catalysts (Preparation Method 2)	50
Table 3.6	Bulk Catalysts (Calcination Conditions)	51
Table 3.7	Catalyst Testing List	59
Table 4.1	Comparison of Pre-Reaction Raman Shift Bands $\theta$ -Alumina to Literature	74
Table 4.2	Pre-Reaction Surface Area Results $\theta$ -Alumina	75
Table 4.3	Catalyst Testing List $\theta$ -Alumina	76
Table 4.4	Post Reaction Surface Area Results $\theta$ -Alumina	80
Table 4.5	Pre- Reaction Atomic Adsorption Results Zinc Ferrite $\theta$ -Alumina	81
Table 4.6	Comparison of Pre-Reaction Raman Shift Bands Zinc Ferrites on $\theta$ -Alumina to Literature	87
Table 4.7	Pre-Reaction Surface Area Results Zinc Ferrite on $\theta$ -Alumina	88
Table 4.8	Catalyst Testing List Supported Zinc Ferrite Catalyst	95
Table 4.9	Comparison of Post Reaction Raman Shift Bands Zinc Ferrites on $\theta$ -Alumina to Literature	103
Table 4.10	Post Reaction Surface Area Measurements Zinc Ferrite on $\theta$ -Alumina	104
Table 4.11	Pre-Reaction Atomic Adsorption Results Vanadia on $\theta$ -Alumina	107
Table 4.12	Comparison of Pre-Reaction Raman Shift Bands Vanadia on $\theta$ -Alumina to Literature	111
Table 4.13	Pre-Reaction Surface Area Results Vanadia on $\theta$ -Alumina	112
Table 4.14	Catalyst Testing List Supported Vanadia Catalyst on $\theta$ -Alumina	115
Table 4.15	Post Reaction Surface Area Measurements Vanadia on $\theta$ -Alumina	120
Table 4.16	Pre-reaction AA Analysis of Zinc Ferrite ZF0.6MBP	122
Table 4.17	Comparison of Pre-Reaction Raman Shift Bands Zinc Ferrite ZF0.6MBP and ZF0.6MBP 24HSPT to Literature	125

Table 4.18	Pre-Reaction Surface Area Measurements of Zinc Ferrite ZF0.6MBP	126
Table 4.19	Catalyst Testing List Zinc Ferrite ZF0.6MBP	131
Table 4.20	Comparison of Post Reaction Raman Shift Bands Zinc Ferrite ZF0.6MBP and ZF0.6MBP 24HSPT to Literature	137
Table 4.21	Post Reaction Surface Area Measurements of Zinc Ferrite ZF0.6MBP	138
Table 4.22	Pre-Reaction AA Analysis of Zinc Ferrite ZF3MBPC	142
Table 4.23	Comparison of Pre-Reaction Raman Shift Bands Zinc Ferrite ZF3MBPC to Literature	144
Table 4.24	Pre-Reaction Surface Area Analysis of Zinc Ferrite ZF3MBPC	145
Table 4.25	Catalyst Testing List Zinc Ferrite ZF3MBPC	149
Table 4.26	Bed Volume Comparison of Selectivities and Conversion at 50 Hours on Stream Zinc Ferrite ZF3MBPC	154
Table 4.27	Average 1-Butene Conversion and Selectivities of Major Products	159
Table 4.28	Flow Comparison of Selectivities and Conversion at 50 Hours on Stream Zinc Ferrite ZF3MBPC Bed Volume 3 cm <sup>3</sup>	163
Table 4.29	Flow Comparison of Selectivities and Conversion at 50 Hours on Stream Zinc Ferrite ZF3MBPC Bed Volume 1 cm <sup>3</sup>	163
Table 4.30	Dual Bed Comparison of Selectivities and Conversion at 50 Hours on Stream $\theta$ -Alumina:Zinc Ferrite ZF3MBPC	167
Table 4.31	Comparison of Post Reaction Raman Shift Bands Zinc Ferrite ZF3MBPC to Literature	169
Table 4.32	Post Reaction Surface Area Measurements of Zinc Ferrite ZF3MBPC	170
Table 4.33	Pre-Reaction AA Analysis of Zinc Ferrite ZF3MBPD	174
Table 4.34	Comparison of Pre-Reaction Raman Shift Bands Zinc Ferrite ZF3MBPD to Literature	176
Table 4.35	Pre-Reaction Surface Area Measurements of Zinc Ferrite ZF3MBPD	177
Table 4.36	Catalyst Testing List Zinc Ferrite ZF3MBPD	178
Table 4.37	Isomer Effect on Selectivities and Conversion at 10 Hours on Stream Zinc Ferrite ZF3MBPD Bed Volume 1 cm <sup>3</sup>	183
Table 4.38	Comparison of Post Reaction Raman Shift Bands Zinc Ferrite ZF3MBPD to Literature	186
Table 4.39	Post Reaction Surface Area Measurements of Zinc Ferrite ZF3MBPD	187

Table 4.40	Pre-Reaction AA Analysis of Iron Enriched Zinc Ferrites	190
Table 4.41	Pre-Reaction Iron Enriched Zinc Ferrite ZFFeNH3P Particle Size Measurement	191
Table 4.42	Pre-Reaction Iron Enriched Zinc Ferrite ZFFeNH3PD Particle Size Measurement	191
Table 4.43	Pre-Reaction Iron Enriched Zinc Ferrite ZFFeNaOHP Particle Size Measurement	192
Table 4.44	Comparison of Pre-Reaction Raman Shift Bands Iron Enriched Zinc Ferrite to Literature	195
Table 4.45	Pre-Reaction Surface Area Measurements of Iron Enriched Zinc Ferrites	196
Table 4.46	Catalyst Testing List Iron Enriched Zinc Ferrites	201
Table 4.47	Post Reaction Iron Enriched Zinc Ferrite ZFFeNH3P Particle Size Measurement	205
Table 4.48	Post Reaction Iron Enriched Zinc Ferrite ZFFeNH3PD Particle Size Measurement	206
Table 4.49	Post Reaction Iron Enriched Zinc Ferrite ZFFeNaOHP Particle Size Measurement	207
Table 4.50	Comparison of Post Reaction Raman Shift Bands Iron Enriched Zinc Ferrite to Literature	210
Table 4.51	Post Reaction Surface Area Measurements of Iron Enriched Zinc Ferrites	212
Table 4.52	Pre-Reaction Iron Oxide Catalyst Fe2O3NaOHP Particle Size Measurement	213
Table 4.53	Pre-Reaction Iron Oxide Catalyst Fe2O3NH3P Particle Size Measurement	214
Table 4.54	Comparison of Pre-Reaction Raman Shift Bands Iron Oxide to Literature	216
Table 4.55	Pre-Reaction Surface Area Measurements of Iron Oxide Catalysts	216
Table 4.56	Catalyst Testing List Iron Oxide Catalysts	219
Table 4.57	Post Reaction Iron Oxide Catalyst Fe2O3NaOHP Particle Size Measurement	222
Table 4.58	Post Reaction Iron Oxide Catalyst Fe2O3NH3P Particle Size Measurement	223
Table 4.59	Comparison of Post Reaction Raman Shift Bands Iron Oxide to Literature	225
Table 4.60	Post Reaction Surface Area Measurements of Iron Oxide Catalysts	226

Table 4.61	Comparison of Raman Shift Bands Zinc Ferrite Citrate Precursor to Literature	228
Table 4.62	Surface Area Measurements of Zinc Ferrite Citrate Precursor	229
Table 5.1	Zinc Ferrite ZF3MBPC Temperature Stability Test Regime	245
Table 5.2	Zinc Ferrite ZF3MBPC Gas and Weight Hour Space Velocities	246
Table 5.3	Comparison of Average Gas Composition Post 3 cm <sup>3</sup> Alumina Bed and Gas Composition Post Reaction Alumina:Zinc Ferrite (ZF3MBPC) 3:1 at 50 h TOS	248
Table 5.4	Comparison of Average Gas Composition Post 1 cm <sup>3</sup> Alumina Bed and Gas Composition Post Reaction Alumina:Zinc Ferrite (ZF3MBPC) 3:1 at 50 h TOS	249
Table 5.5	Comparison of Rig Off Gas Composition Post Reaction Alumina:Zinc Ferrite (ZF3MBPC) 3:1, 1:1 and 1:1 Mixed at 50 h TOS	250

## 1. Introduction.

Crude oil was first discovered ca. 4000 BC as oil seepage on the banks of the Euphrates River in what is now modern day Iraq. In the 4<sup>th</sup> century AD, oil wells to a depth of 240 metres were being drilled in China using bamboo poles fitted with bits. By the late 16<sup>th</sup> century hand dug wells to a depth of 35 metres could be found in Baku, Azerbaijan. In 1848 the first modern oil well was drilled northeast of Baku, Azerbaijan on the Asperon peninsula.[1] Today crude oil is found in more than 25 locations throughout the world and is the main energy source for the developed and developing world.

Crude oil contains a highly complex mixture of hydrocarbons: paraffins, naphthenes, aromatics and asphaltics. This mixture varies from oil to oil which determines the oil's properties. Table 1.1 below shows the composition variation of oil.

**Table 1.1 Crude Oil Composition Variation[2]**

Hydrocarbon	Average (%)	Range (%)
Paraffins	30	15 to 60
Naphthenes	49	40 to 60
Aromatics	15	3 to 30
Asphaltics	6	remainder

Crude oil therefore has to undergo a number of purification or refining steps to produce usable products. The various purification steps are outlined below in the schematic in figure 1.1.

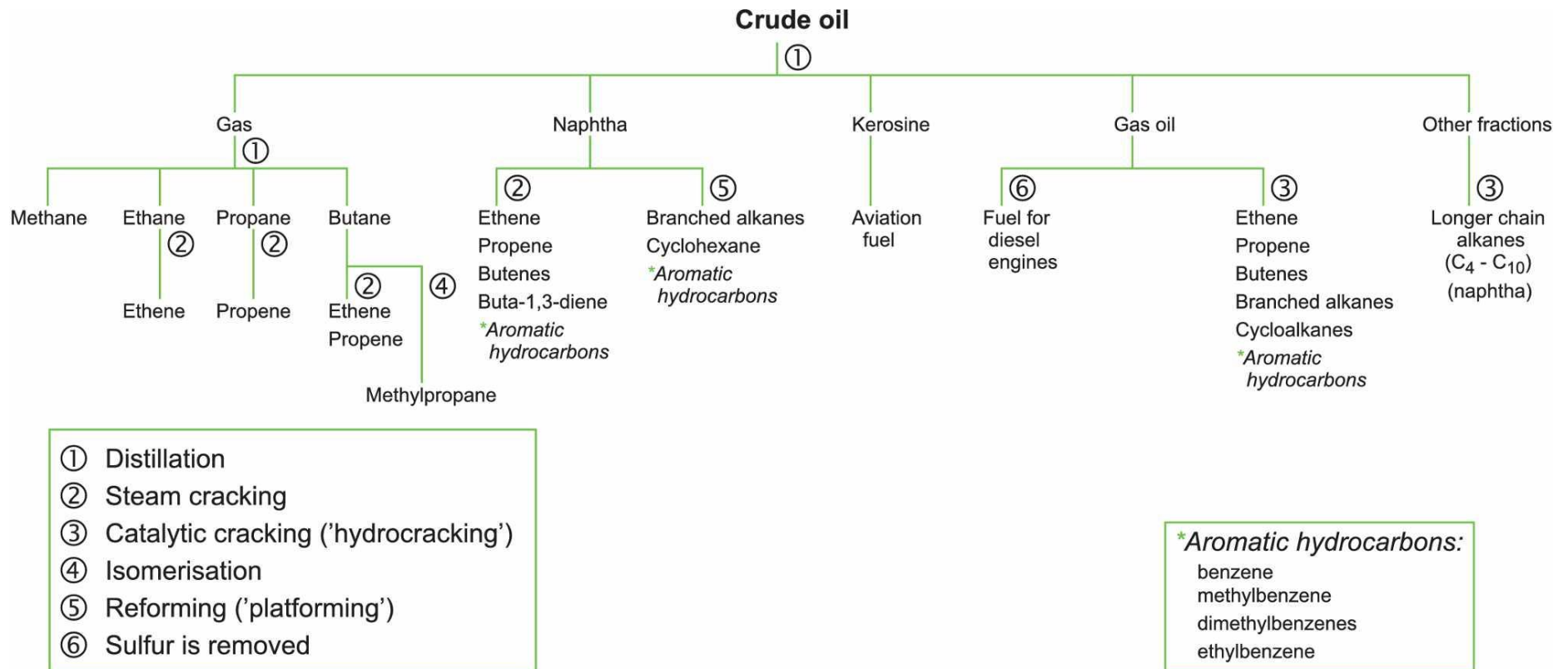


Figure 1.1 Crude Oil Refining Schematic.[3]

As can be seen from figure 1.1 both steam cracking and catalytic cracking can produce C<sub>2</sub>, C<sub>3</sub> and C<sub>4</sub> alkenes and C<sub>4</sub> dienes, but only catalytic cracking produces branched and cyclic alkanes. The ethene and propene produced by crackers are used to produce polymers such as polyethylene and polypropylene. The 1,3-butadiene produced is used in the manufacture of synthetic rubber or elastomers such as styrene-butadiene rubber (SBR), polybutadiene rubber (PBR), polychloroprene (Neoprene), acrylonitrile butadiene styrene (ABS) and acrylonitrile butadiene (NBR).

Figure 1.2 below shows the inside of a tubular reactor being used for steam cracking naphtha. The temperature is in the region of 1150 K.



**Figure 1.2 Internal View of Steam Cracking Furnace[3]**

1. Naphtha vapour flows through the inside of the tubes in the furnace
2. Rows of furnace guns which burn methane to generate heat inside the furnace
3. A peephole

The yields of the various products can be controlled to a certain degree by varying a number of process conditions such as cracker temperature and gas flow rates as shown in table 1.2.

**Table 1.2 Steam Cracker Product Composition[3]**

Product	Low Severity (1000 K residence time 0.5 s)	High Severity (1150 K residence time 0.1 s)
Hydrogen	1	1
Methane	15	18
Ethene	19	32
Propene	16	13
C4 hydrocarbons	10	9
RPG*	36	18
Others	3	9

\*RPG raw pyrolysis gas

The cracker effluent is passed through a number of distillation columns to separate the various hydrocarbons produced in the cracker.

Figure 1.3 shows the steam cracking unit at Wilton in the north east of England with its associated distillation columns.



**Figure 1.3 Steam Cracking Unit[3]**

1. Debutaniser which separates the C4 hydrocarbons from the C1 - C3 hydrocarbons
2. Depropaniser which separates out the C3 hydrocarbons
3. Deethaniser which separates out the C2 hydrocarbons
4. Demethaniser which separates out the methane
5. C3 splitter which separates propene from propane
6. C2 splitter which separates ethene from ethane

Due to crackers being unable to meet the demand for certain alkenes and dienes (propene, butenes and butadiene) there is a requirement to produce the alkenes and dienes from the respective C3/C4 alkanes.

1,3-butadiene was first isolated as an unknown hydrocarbon in 1863 from the pyrolysis of amyl alcohol[4] and in 1886 Henry Edward Armstrong identified it as butadiene[5]. Sergei Lebedev was the first to polymerise 1,3 butadiene into polybutadiene[6], which unfortunately was too soft to be a substitute for natural rubber.

Steam cracking produces 95 % of the world production capacity of 1,3-butadiene; the remaining 5 % is produced by various dehydrogenation and oxidative dehydrogenation methods.

In 2011 the estimated global market for 1,3-butadiene was 22 billion US dollars and it is expected to reach 32 billion US dollars by 2018[7]. Although the vast majority of this is supplied directly from the crackers a small but significant amount needs to be prepared by either dehydrogenation or oxidative dehydrogenation. Indeed the conversion of butene to butadiene is a major industrial process.

Figure 1.4 below shows the 2011 butadiene world consumption by region.

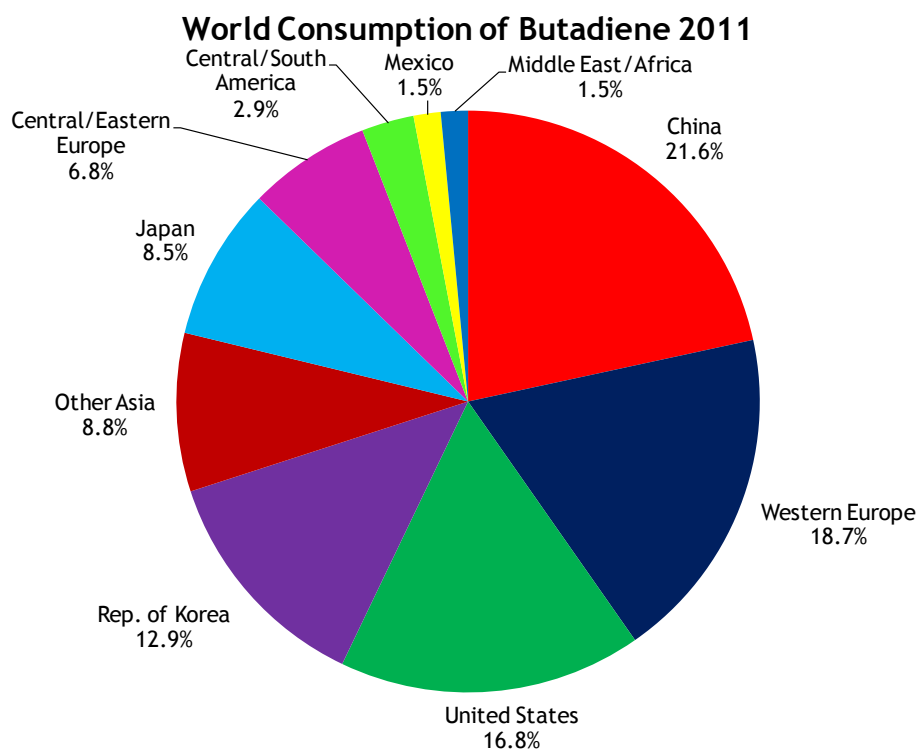
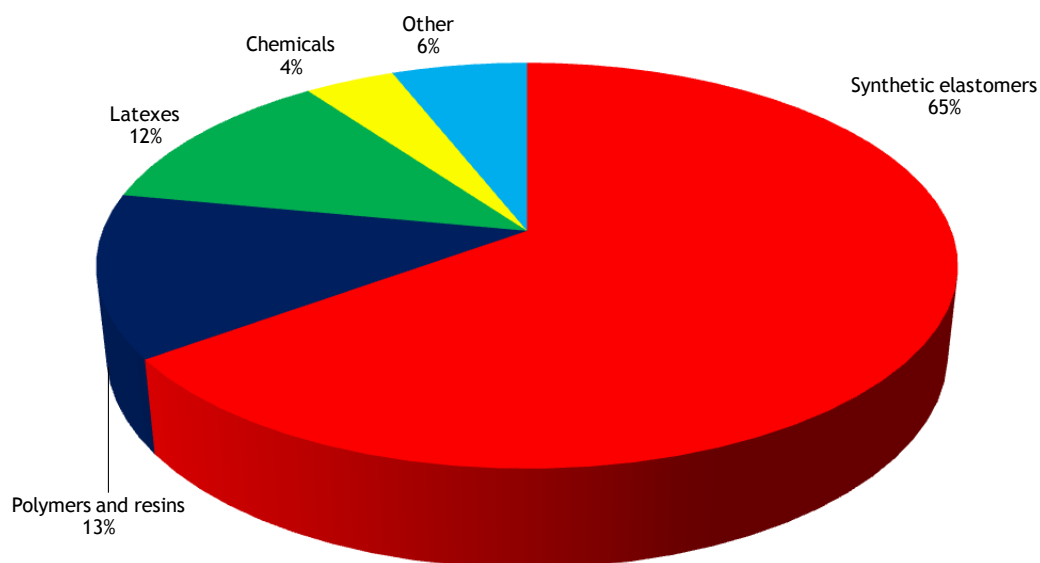


Figure 1.4 2011 Butadiene World Consumption[8]

Figure 1.5 below shows the 2009 butadiene global usage by end product.



**Figure 1.5 2009 Global Usage of 1,3-Butadiene[9]**

There are three different commercial processes for extracting butadiene from the C4 fraction exiting the ethylene steam cracker:-

BASF Process

Nippon-Zeon Process

Shell Process

BASF and Nippon-Zeon use dimethylformamide (DMF) and Shell use acrylonitrile (ACN). The schematic in figure 1.6 below shows the BASF extraction process.

Standard Configuration

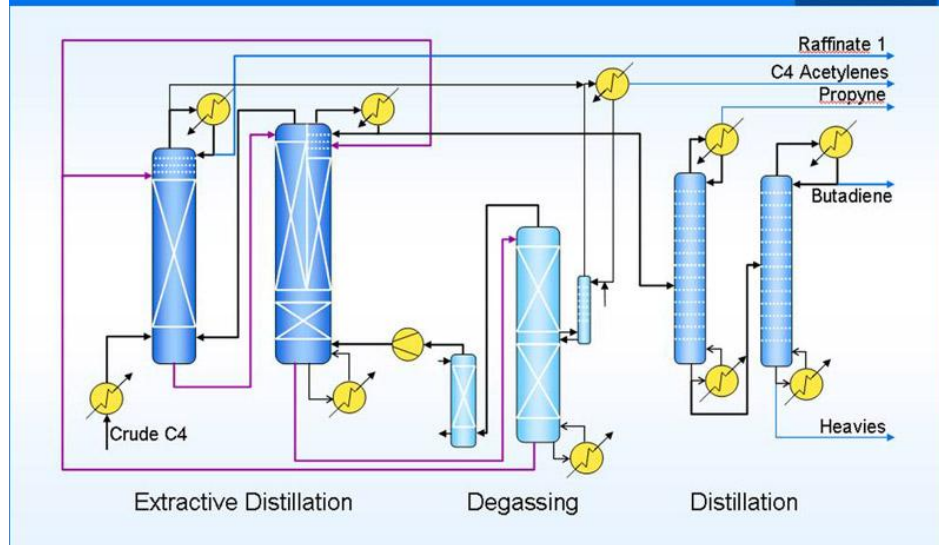
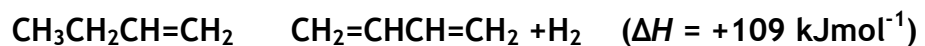


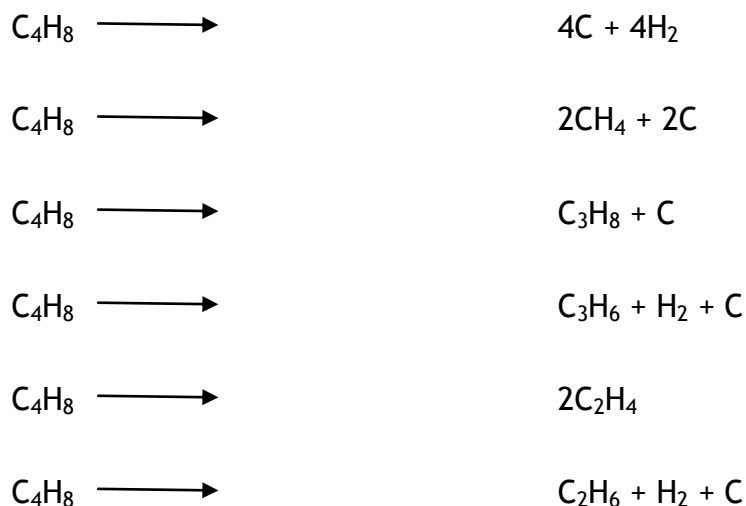
Figure 1.6 Extraction Process Schematic[10]

The 5 % of the world's production of 1,3-butadiene that is not produced directly from a cracker is generated from butenes by oxidative dehydrogenation.

The dehydrogenation of n-butenes is endothermic and requires constant heat input:



In order to achieve economic conversion temperatures in the region of 600-700 K are required. The equilibrium for n-butane dehydrogenation to butene is more favourable than that of butene to butadiene and so can be run at a lower temperature. Cracking and secondary reactions including carbon deposition can occur at these temperatures, hence catalyst selection and reducing residence times becomes highly important. The possible cracking products are shown below.



Other potential reactions are ethane to acetylene or ethene, and propane to propene, in each case the equilibrium favours the reactants therefore very small amounts of these products will be produced at these temperatures.

Dehydrogenation involves an increase in the number of moles of gas, therefore a reduction in partial pressure favours the forward reaction. In some processes steam is added to lower the partial pressure of the hydrocarbons, which can decrease coke deposition, isomerisation and polymerization. If the catalysts are unstable in the presence of steam, then the dehydrogenation process can be operated under reduced pressure. This will shift the equilibrium of dehydrogenation towards butadiene.

There are a number of existing methods for the dehydrogenation of butane/butene to butadiene, e.g. Houdry and Dow operate dehydrogenation processes but there are also a number of oxidative dehydrogenation methods e.g. Phillips O-X-D, Petro-Tex.

The Houdry process is one of the oldest and commercially important processes. A water sensitive chromia/alumina catalyst is heated to 600-620 K at pressure of 0.2-0.4 bar. The catalyst rapidly deactivates by carbon deposition so catalyst regeneration is undertaken by introducing air to burn off the coke after a few minutes, while the reaction mixture is removed from the catalyst by evacuation between the dehydrogenation and regeneration periods. It is the oxidation of coke that supplies the energy required for the dehydrogenation reaction. In this way a 30-40 % conversion of butane with a yield of 63 % butadiene can be achieved. Figure 1.7 below is a schematic of the Catadiene (Houdry) Process.

## Butadiene: Dehydrogenation of n-Butane

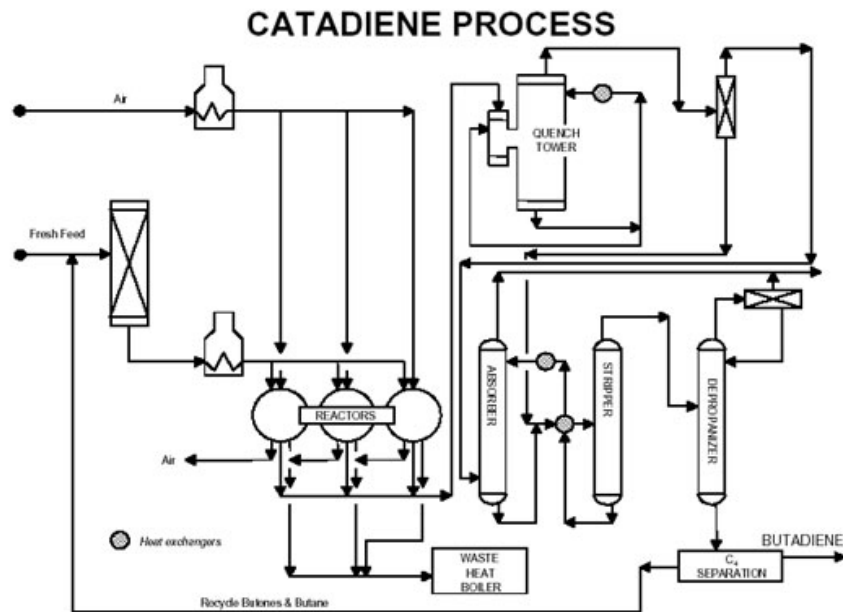


**Figure 1.7 Dehydrogenation Plant Schematic[11]**

The Dow process utilises butene in place of butane in the presence of steam. A  $\text{Cr}_2\text{O}_3$  stabilised Ca-Ni-phosphate catalyst is used at a temperature of 600-675 K and 1 bar pressure. The addition of superheated steam in the ratio of 20:1 water:butene provides the heat required for dehydrogenation. A butene conversion of 50 % and a butadiene selectivity of 90 % can be achieved. The catalyst requires to be regenerated for 11 minutes every 15 minutes; continuous production is normally achieved by the use of parallel reactors. Shell and Phillips Petroleum have developed similar methods using Fe-Cr-oxide and Fe-oxide-bauxite catalysts respectively.

Although commercial dehydrogenation catalysts are based on chromium oxide or supported platinum, a search of the literature reveals considerable research into finding alternatives for the present catalysts. Much of this work relates to the conversion of butane to butenes with much less regard to 1,3-butadiene.

Harlin *et. al*[12] examined the effect of magnesium or zirconium doping of alumina supported vanadia catalysts on butane dehydrogenation. Three different pretreatment methods were compared: calcination, hydrogen reduction and carbon monoxide reduction. The calcined catalysts gave the highest 1,3-butadiene yields. While Ajayi *et. al*[13] investigated the activity of

chromium, vanadium, chromium/vanadium MCM-41 supported catalysts for the dehydrogenation of n-butane. In that study the catalysts were prepared by incipient wetness using chromium nitrate and ammonium metavanadate. Catalyst activity was determined by passing 4 % n-butane in nitrogen over the catalysts at 873 K, 1.2 % Cr:2.8 % V on MCM-41 gave the highest yield at 17.8 %

Stobbe *et. al*[14] examined the dehydrogenation of 1-butene using iron oxide supported on magnesium oxide. Catalysts were prepared by incipient wetness using two different metal precursors, ammonium iron (III) citrate and ammonium iron(III) EDTA. A 1-butene, steam and nitrogen gas mix was passed over the catalysts at 873 K to evaluate their activity. Iron oxide on magnesium oxide catalyst prepared from ammonium iron(III) citrate gave the highest yield at 17 %.

In the oxidative dehydrogenation of butene to butadiene, the inclusion of oxygen into the reaction at temperatures up to 600 K removes hydrogen and coke due to combustion, thereby displacing the equilibrium and regenerating the catalyst during the reaction. Industrially, air is introduced in sufficient quantities so that the endothermic dehydrogenation reaction is balanced by exothermic water production. This causes catalyst lifetime, butadiene selectivity and butane conversion to be enhanced. Figure 1.8 below shows a schematic of the Nippon-Zeon dehydrogenation of n-butenes Oxo-D process.

## OXO-D PROCESS

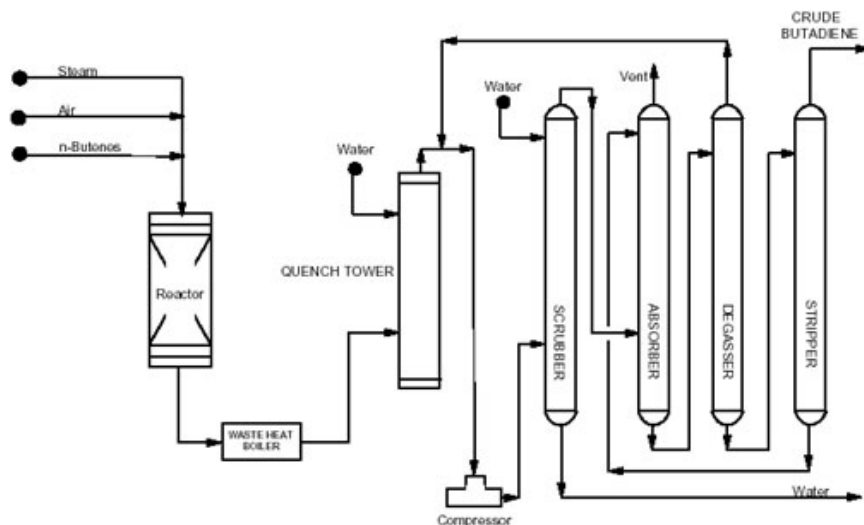


**Figure 1.8 Oxidative Dehydrogenation Plant Schematic[11]**

In 1965 Petro-Tex developed a process to dehydrogenate n-butenes to 1,3-butadiene using a heterogeneous metal ferrite catalyst at temperatures between 550-600 K. Butadiene with selectivities up to 93 % could be achieved by steam addition at a conversion of 65 %. Texas Petrochemicals is planning to build a butadiene plant based on its butane dehydrogenation process, which will be on-stream in Houston, Texas, by 2016.

Commercial ODH catalysts are normally mono metal oxides such as  $\text{Fe}_2\text{O}_3$  or ferrites such as  $\text{ZnFe}_2\text{O}_4$ . A search of the literature reveals extensive research into improving existing catalysts and finding new and novel substitutes.

Lee *et. al*[15] examined sulphated zinc ferrite. Calcined zinc ferrite was added to a solution of ammonium sulphate filtered, dried and calcined. The activity of zinc ferrite and sulphated zinc ferrite was compared by passing an n-butene/air/steam gas mix over the catalysts. Sulphated zinc ferrite showed the highest 1,3-butadiene yield.

Zhang *et. al*[16] studied temperature and oxygen:butene ratio effects over  $\alpha$ -iron oxide, zinc ferrite and biphasic (zinc ferrite/ $\alpha$ -iron oxide) catalysts. Catalyst activity was determined by passing an n-butene/steam/air mix over the catalysts. Biphasic material (zinc ferrite:iron oxide 1:0.35) gave the highest

1,3-butadiene yield with an oxygen:n-butene ratio of 0.95 at a temperature of 633 K.

Toledo *et. al*[17] compared the activity of iron oxide supported on zinc aluminate and zinc aluminium ferrite towards the oxidative dehydrogenation of 1-butene to 1,3-butadiene. Activity was determined by passing over the catalyst a 1-butene, oxygen and helium gas mixture at 693 K. The 8 % FeO<sub>x</sub> on zinc aluminate gave the highest 1,3-butadiene yield.

Jung *et. al* studied the oxidative dehydrogenation of C4 raffinate using an n-butene:air:steam gas mix over two different phases of bismuth molybdate ( $\alpha$ -Bi<sub>2</sub>Mo<sub>3</sub>O<sub>12</sub> and  $\gamma$ -Bi<sub>2</sub>MoO<sub>6</sub>).  $\gamma$ -Bismuth molybdate proved to give the highest 1,3-butadiene yield[18] The activity of a multi-component bismuth molybdate (Co<sub>9</sub>Fe<sub>3</sub>Bi<sub>1</sub>Mo<sub>12</sub>O<sub>51</sub>) was investigated using an air:steam:butene gas mix; where butene was either n-butene, 1-butene, or 2-butene. The best 1,3-butadiene yield was achieved using 1-butene.[19] The effect of varying the reaction conditions (temperature, steam:butene ratio and GHSV) on the activity of the multi-component bismuth molybdate catalyst was investigated. The optimum conditions to generate the highest 1,3-butadiene yield from n-butene was steam:butene 15:1, temperature 693 K and GHSV 675 h<sup>-1</sup>. [20]

Park *et. al.* investigated the activity of doped bismuth molybdate catalysts using 1-butene:air:steam gas mix. Bismuth molybdate was doped with iron (Fe=0.00-1.00) and a BiMoFe<sub>0.65</sub> oxide catalyst gave the highest 1,3-butadiene yield.[21] The BiMoFe<sub>0.65</sub> oxide was then doped with nickel (Ni=0.00-0.20) and a BiMoFe<sub>0.65</sub>Ni<sub>0.05</sub> oxide catalyst gave the highest yield to 1,3-butadiene.[22] Finally a BiMoFe<sub>0.65</sub> oxide was doped with phosphorus (P=0.00-0.60) and a BiMoFe<sub>0.65</sub>P<sub>0.10</sub> oxide catalyst gave the highest yield to 1,3-butadiene.[23] The best performing doped bismuth molybdate catalyst is BiMoFe<sub>0.65</sub>P<sub>0.1</sub> giving a 1,3-butadiene yield and selectivity of 66 % and 91 % respectively with a 1-butene conversion of 74 %.

Soares *et. al*[24] studied the oxidative dehydrogenation of 1-butene over  $\beta$ ,  $\gamma$  and mixed  $\beta\gamma$  bismuth molybdates. Reactions were carried out at three temperatures 593,643 and 693 K with a 3.1 % (v/v) 1-butene in air gas flow.

Butene conversion and selectivity to 1,3-butadiene increased with both increasing temperature and increasing  $\gamma$ -bismuth molybdate content of catalyst.

Liu *et. al*[25] examined the oxidative dehydrogenation of 1-butene over carbon nanotubes and activated charcoals (AC-1 and AC-2), an  $\alpha$ -iron oxide was also run for comparison. 1-butene, oxygen gas mix with mole ratios of 1:1 and 1:2 were passed over the catalysts at 673 K. Carbon nanotubes with a 1:2 mole ratio of 1-butene and oxygen gave the highest 1,3-butadiene yield.

According to the literature cited above the best performing ferrite catalyst was obtained by Lee *et. al* using a sulphated  $\text{ZnFe}_2\text{O}_4$  (0.5) giving 1,3-butadiene yield and selectivity of 78 % and 98 % respectively and n-butene conversion of 80 %. Conditions used were n-butene:oxygen:steam ratio of 1:0.75:15 at 693 K at a gas hour space velocity (GHSV) of  $475 \text{ h}^{-1}$ . The best performing bismuth molybdate catalyst was obtained by Jung *et. al* using  $\text{Co}_9\text{Fe}_3\text{BiMo}_{12}\text{O}_{51}$  giving 1,3-butadiene yield and selectivity of 85 % and 87 % respectively and 1-butene conversion of 97 %. The conditions used were 1-butene:oxygen:steam ratio of 1:0.75:15 at 693 K at a gas hour space velocity (GHSV) of  $475 \text{ h}^{-1}$ .

A patent search revealed patents outlining modifications to existing ferrite and molybdate catalysts.

Christmann cited the manufacture and use of phosphorus[26] or silicon[27] doped zinc, magnesium, cobalt or nickel ferrite catalysts. The doping increased the robustness and extended the production life of the ferrite catalyst but had no effect on the 1,3-butadiene yield.

Croce *et. al*[28] reported doping magnesium or barium ferrite with lanthanides, phosphorus or silicon. This doping in conjunction with the addition of chlorine in the reaction gas stream improved the catalyst activity at lower reaction temperatures.

Woskow[29] cited the use of rhenium or platinum group metal modified supported metal ferrite catalysts for the oxidative dehydrogenation of 2-butene to 1,3-butadiene. The 2-butene conversion rose from 31 % to 49 % and the

1,3-butadiene yield increased from 29 % to 45 % with the addition of 0.2 % palladium.

Shin *et. al*[30] reported the preparation of iron bismuth molybdates for use in the oxidative dehydrogenation of 1-butene to 1,3-butadiene. The best results were achieved with a Bi:Mo:Fe mole ratio of 1:1:0.65 compared to a Bi:Mo mole ratio of 1:1 . The conversion increased from 37 % to 73 % and yield increased from 36 % to 69 %.

Finally in a recent patent Mamedov *et. al*[31] cited modifying zinc ferrite catalysts with elements from group 2A, 3A and 6A. Introduction of these modifiers resulted in increased catalyst stability and 1,3-butadiene yield dependent on modifier and preparation conditions used.

As can be seen from above there has been extensive research carried out over the last 50 years to understand and improve the ‘on demand’ dehydrogenation and oxidative dehydrogenation of n-butane and n-butenes to 1,3-butadiene. Numerous patents have been filed to highlight improvements in catalysts design. In this work we will attempt to better understand use of zinc ferrite for the oxidative dehydrogenation of n-butenes to 1,3-butadiene. The aims of this project are outlined in section 2 below.

## **2. Aims of Project.**

The aim of this study was to investigate the activity and selectivity of a number of catalysts for the oxidative dehydrogenation of C4 alkenes to 1,3-butadiene. The catalysts prepared were supported zinc ferrite and vanadia on  $\theta$ -alumina, bulk iron oxide and zinc ferrites produced using a number of precipitation methods.

The C4 alkenes used were 1-butene, cis-2-butene and trans-2-butene.

### 3. Experimental

#### 3.1 Materials

The support chosen was  $\theta$ -alumina trilobe extrudate supplied by Johnson Matthey, with a surface area of  $95 \text{ m}^2\text{g}^{-1}$  and a pore volume of  $0.52 \text{ cm}^3\text{g}^{-1}$ . It was predried in an oven overnight at 353 K.

**Table 3.1 Materials**

<b>Material</b>	<b>Supplier</b>	<b>Purity</b>
Zinc Chloride	Alfa Aesar	98+ %
Zinc Nitrate Hexahydrate	Sigma Aldrich	98 %
Ferric Chloride Hexahydrate	Alfa Aesar	97 %
Ferric Nitrate Nonahydrate	Alfa Aesar	98+ %
Ammonium Metavanadate	Sigma Aldrich	99 %
Citric Acid	Fisher Scientific	100 %
Oxalic Acid Dihydrate	Fisher Scientific	100 %
Sodium Hydroxide	Sigma Aldrich	98-100 %
Ammonia Solution	Fluka	25 %
20% Oxygen balance Argon	BOC	
Argon	BOC	99.995 %
1-Butene	BOC	99.5 %
Cis-2-Butene	BOC	99.4 %
Trans-2-Butene	BOC	99 %
Quadruple component calibration gas	Scientific & Technical Gases Limited	1 % 1-Butene, 1% cis-2-Butene, 1 % trans-2-Butene, 1 % 1,3-Butadiene balance Nitrogen

**Table 3.1 Materials (Continued)**

<b>Material</b>	<b>Supplier</b>	<b>Purity</b>
Multi-component calibration gas	Scientific & Technical Gases Limited	3 % Ethane, 3 % Ethene, 1 % Propane, 0.5 % N-Butane, 0.5 % Iso-Butane, 0.25 % N-Pentane, 0.25 % N-Hexane, 3 % Hydrogen, 3 % Nitrogen, 3 % Carbon Monoxide, 3 % Carbon Dioxide, balance Methane

### **3.2 Catalysts**

A total of fifteen catalysts were prepared, five as supported catalysts and ten as bulk catalysts. Two different methods were used to produce the supported catalysts; spray impregnation and high-temperature, high-pressure impregnation. All the bulk catalysts were prepared by co-precipitation using different metal precursors and precipitation agents.

### **3.3 Supported Catalyst Preparation**

#### **3.3.1 Stock Solutions**

Four stocks solutions were prepared for use in spray impregnation, and high-pressure, high-temperature impregnation as follows:-

1. Zinc nitrate hexahydrate (10.14 g) and ferric nitrate nonahydrate (30.06 g) were dissolved in 100 cm<sup>3</sup> deionised water.
2. Zinc nitrate hexahydrate (16.48 g) and ferric nitrate nonahydrate (48.85 g) were dissolved in 100 cm<sup>3</sup> deionised water.
3. Ammonium metavanadate (2.34 g) and oxalic acid dihydrate (4.99 g) were dissolved in 100 cm<sup>3</sup> deionised water.

4. Ammonium metavanadate (16.38 g) and oxalic acid dihydrate (34.93 g) were dissolved in 100 cm<sup>3</sup> deionised water.

### 3.3.2 Spray Impregnation[32]

A known weight of  $\theta$ -alumina was placed in a Pascall Lab Mixer. The appropriate volume of a stock solution (table 3.2, prep number 3-5) to fill the pores was transferred into a Degussa SG-1 sprayer, which was sprayed into the Pascall Lab Mixer whilst it was rotating. The  $\theta$ -alumina was then left mixing for one hour. The resultant supported catalyst was removed from the mixer and dried in an oven at 353 K overnight before being crushed and sieved to a particle size of (250-425 microns). This was subsequently calcined at 873 K for 3 hours (table 3.3).

### 3.3.3 High Temperature and Pressure Impregnation[33]

A known weight of  $\theta$ -alumina was placed in a Parr reactor along with a known volume of the appropriate stock solution to achieve the required loading (table 3.2, prep number 1). The reactor was sealed, heated to 393 K, left for 5 hours and allowed to cool overnight. Excess liquid was filtered off using a buchi funnel. The resultant supported catalyst was dried in an oven at 353 K overnight then crushed and sieved (250 - 425 microns) which was then calcined at 873 K for 3 hours (table 3.3).

**Table 3.2 Supported Catalysts 1**

Prep Number	Catalyst	Weight $\theta$ -Alumina (g)	Stock Solution	Volume Sprayed
1	15 % ZnFe <sub>2</sub> O <sub>4</sub> on alumina	47.5	1	60
2	8 % ZnFe <sub>2</sub> O <sub>4</sub> on alumina	47.5	1	28
3	25 % ZnFe <sub>2</sub> O <sub>4</sub> on alumina	37.5	2	5 x 20
4	3.5 % VO <sub>x</sub> on alumina	48.25	3	28
5	3.5 % VO <sub>x</sub> on alumina	48.25	4	25

Table 3.2 above outlines the support, stock solution and volume used in preparing the supported catalysts.

**Table 3.3 Supported Catalysts 2**

Catalyst	Drying Conditions		Calcination Conditions	
	Temp (K)	Time (Hours)	Temp (K)	Time (Hours)
15 % ZnFe <sub>2</sub> O <sub>4</sub> on alumina	353	16	873	3
8 % ZnFe <sub>2</sub> O <sub>4</sub> on alumina	353	16	873	3
25 % ZnFe <sub>2</sub> O <sub>4</sub> on alumina	353	16	873	3
3.5 % VO <sub>x</sub> on alumina	353	16	873	3
3.5 % VO <sub>x</sub> on alumina	353	16	873	3

Table 3.3 above outlines the drying and calcinations conditions used on the supported catalysts.

All supported catalysts were crushed and sieved (250 - 450 microns) prior to calcination.

### 3.4 Bulk Catalyst Preparation

Two different generic catalyst preparation methods were used. In the first method the metal precursors were added to the precipitating agent[34],[35] (table 3.4) and in the second the precipitating agent was added to the metal precursor(s)[36],[37] (table 3.5). Only in the case of ZFNH3D was the precipitating agent added dropwise.

**Table 3.4 Bulk Catalysts (Preparation Method 1)**

Catalyst	Metal Precursor				Precipitation Agent(NaOH)		Temp (K)
	ZnCl <sub>2</sub> (g)	Vol (cm <sup>3</sup> )	FeCl <sub>3</sub> 6H <sub>2</sub> O (g)	Vol (cm <sup>3</sup> )	Molarity	Vol (cm <sup>3</sup> )	
ZF0.6MP	1.42	100	5.61	100	0.6	1000	343
ZF0.6MBP	4.26	100	16.83	100	0.6	3000	343
ZF3MBPD	84.9	500	336	500	3.0	3000	278
ZF3MBPC	84.9	500	336	500	3.0	3000	278

Table 3.4 above outlines the weights of precipitating agent, metal precursors, and volume of deionised water, preparation temperature and precipitating agent molarity used in the first method of preparation.

Table 3.5 outlines the weights of precipitating agent, metal precursors, volume of deionised water, preparation temperature and precipitating agent molarity used in the second method of preparation.

**Table 3.5 Bulk Catalysts (Preparation Method 2)**

Catalyst	Metal Precursor			Precipitation Agent			Temp (K)
	ZnNO <sub>3</sub> 6H <sub>2</sub> O (g)	Fe <sub>2</sub> NO <sub>3</sub> 9H <sub>2</sub> O (g)	Vol (cm <sup>3</sup> )	Agent	Molarity	Vol (cm <sup>3</sup> )	
ZFC	10.14	30.06	100	Citric Acid	3.2	100	358
ZFFeNH <sub>3</sub> P	25	100	500	NH <sub>3</sub>	14.8	90	278
ZFFeNH <sub>3</sub> PD	25	100	500	NH <sub>3</sub>	14.8	90	278
ZFFeNH <sub>3</sub> P	50	200	1000	NH <sub>3</sub>	14.8	180	278
ZFFeNaOHP	50	200	1000	NaOH	14.8	180	278
Fe <sub>2</sub> O <sub>3</sub> NH <sub>3</sub> P		200	1000	NH <sub>3</sub>	14.8	180	278
Fe <sub>2</sub> O <sub>3</sub> NaOHP		200	1000	NaOH	14.8	180	278

ZF0.6MP and ZF0.6MBP were stirred at 343 K for 1 hour and then allowed to cool overnight (table 3.6, rows 2 and 3). ZFC was stirred vigorously at 358 K for 8 hours (table 3.6, row 1).

All of the catalysts were prepared using a basic precipitation agent, with the exception of ZFC, and were filtered by allowing the precipitate to settle, decanting the excess liquor and adding fresh deionised water. This process was continued until a neutral pH was obtained. In the case of ZF3MBPC a centrifuge was used to speed up the washing process. ZFC was placed in an oven at 353 K for 16 hours, the temperature was the raised to 373 K and left for 96 hours to dry. Two different methods were employed for adding ammonia to the metal nitrates; addition as a single aliquot ZFFeNH<sub>3</sub>P and dropwise over 15 minutes ZFF3NH<sub>3</sub>PD. The anticipated Fe:Zn ration for the iron enriched zinc ferrite catalysts is 3:1.

**Table 3.6 Bulk Catalysts (Calcination Conditions)**

Catalyst	Conditions					
	Aging		Drying		Calcination	
	Temp (K)	Time (Hours)	Temp (K)	Time (Hours)	Temp (K)	Time (Hours)
ZFC	353	8	373	96	748	4
ZFO.6MP			448	16	748	4
ZFO.6MBP			448	16	748	4
ZF3MBPD			443	16	748	4
ZF3MBPC			443	16	748	4
ZFFeNH <sub>3</sub> P	333	16	448	8	973	10
ZFFeNH <sub>3</sub> PD	333	16	448	8	973	10
ZFFeNaOH <sup>I</sup>	333	16	448	8	973	10
Fe <sub>2</sub> O <sub>3</sub> NH <sub>3</sub>	333	16	448	8	973	10
Fe <sub>2</sub> O <sub>3</sub> NaOH	333	16	448	8	973	10

All bulk catalysts with the exception of ZFC were crushed and sieved (250 - 450 microns) prior to calcination.

### 3.5 Catalyst Characterisation

Catalyst characterisation of the prepared catalysts involved BET surface area measurements, thermo-gravimetric analysis, room temperature and hot stage X-ray diffraction measurements, room temperature and hot stage Raman spectroscopy measurements, atomic absorption analysis and acid site determinations.

#### 3.5.1 Surface Area Determination

The surface area and pore size for each catalyst was determined using a Micromeritics Gemini II 2375 Surface Area Analyser. Approximately 0.03 - 0.08 g of catalyst was weighed into a glass sample tube and degassed in a flow of N<sub>2</sub> overnight at 383 K before the measurement was carried out. Determining the number of molecules needed to form a monolayer is the underlying principle in

surface area measurements. In practice however, the molecules may absorb to form multi-layers. The surface area was calculated using the BET (Brunauer-Emmett-Teller) equation shown in figure 3.1 below.

$$\frac{P}{V(P_0-P)} = \frac{1}{V_m C} + \frac{(C-1)P}{V_m C P_0}$$

**Figure 3.1: The BET equation**

Where

V =	volume of gas absorbed at equilibrium pressure P
V <sub>m</sub> =	volume necessary to form a monolayer
P <sub>0</sub> =	saturated vapour pressure of the adsorbent gas at the temperature of measurement
C =	constant

For the supported catalysts, the BET method yields the total surface area of the support and active phase (zinc ferrite, vanadia).

### 3.5.2 Thermogravimetric Analysis-Differential Scanning Calorimetry

Thermogravimetric analysis-differential scanning calorimetry of the catalysts was performed using a SDT Q600 series combined TGA/DSC instrument with an online ESS Evolution Mass Spectrometer. Approximately 0.005 g of catalyst was heated from ambient to 748 K (bulk catalysts) and to 873 K (supported catalysts) under a 2 % oxygen balance argon mixture with a flow rate of 100 cm<sup>3</sup>min<sup>-1</sup> and a heating rate of 10 Kmin<sup>-1</sup>. Species monitored had m/es equal to 18, 28, 30, 32, 44 and 46 which corresponded to H<sub>2</sub>O, CO, NO, O<sub>2</sub>, CO<sub>2</sub>, N<sub>2</sub>O and NO<sub>2</sub> respectively.

### 3.5.3 X-Ray Diffraction

Hot-stage XRD spectra of the catalysts was performed on a Siemens D5000 fitted with an Anton Parr XRK900 environmental cell, a water-cooled, vacuum tight, stainless steel chamber with a beryllium window.

The temperature was increased from ambient at a rate of  $12 \text{ Kmin}^{-1}$  to a maximum of 748 K (bulk catalysts) and 873 K (supported catalysts). Spectra were taken at 100 K intervals using a hold time of 1 hour. The step size was 0.02 with a scan time of 2 seconds per step from  $5-85 2\theta$ . A flow of 2 % oxygen balance argon was passed over the sample at  $20 \text{ cm}^3\text{min}^{-1}$ .

XRD spectra analysis was carried out using Bruker Advanced X-Ray Solutions DIFFRAC<sup>plus</sup> Release 2004 EVA Version 10.0 rev.0 software.

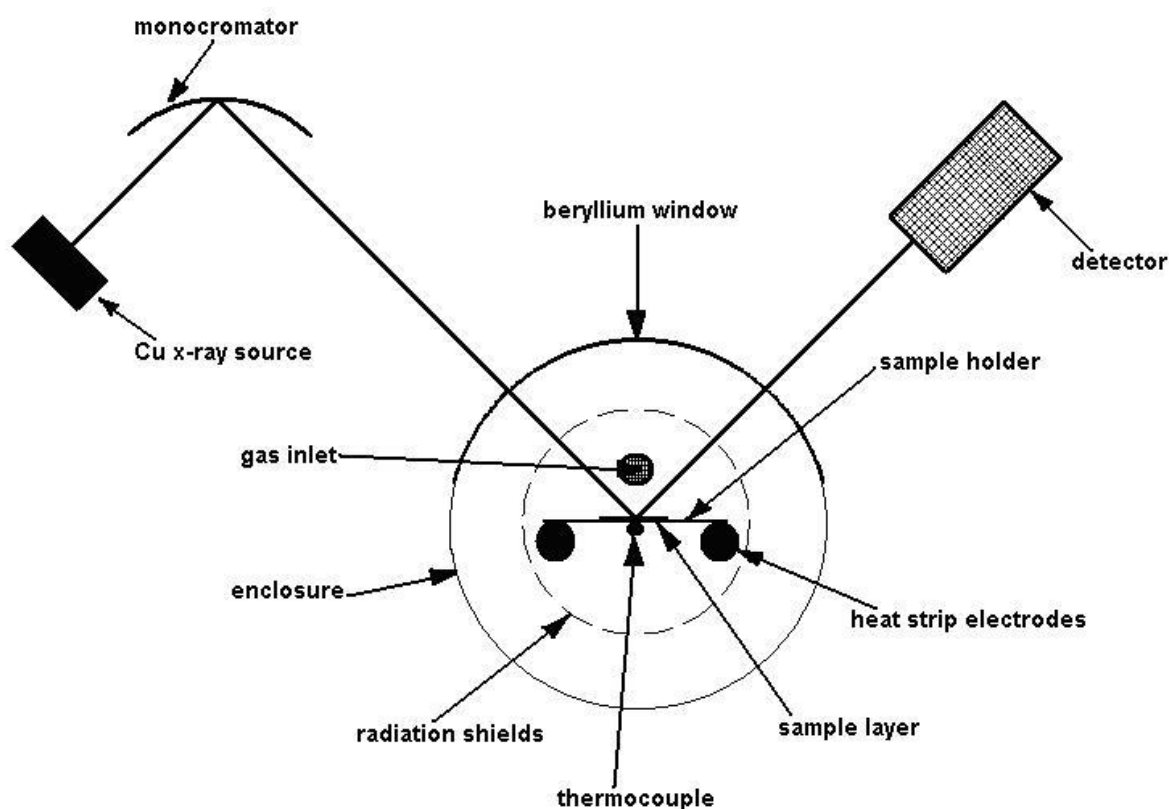


Figure 3.2 Schematic of hot-stage XRD chamber[38]

Standard flat plate ambient temperature XRD spectra of calcined catalyst samples were run on a Siemens D5000 on a spinning flat plate with a step size of

0.02 and a scan rate of 1 second per step from 5-85 2 $\theta$ . Catalyst particle size was calculated from the XRD spectra using the Scherrer Equation.

$$d = \frac{K\lambda}{B\cos\theta}$$

**Figure 3.3:** Scherrer Equation

Where

d = particle size

K= shape factor (Scherrer's constant)

$\lambda$  = wavelength of x-ray source

B = full width half maximum

$\theta$  = diffraction angle

#### **3.5.4 Raman Spectroscopy**

Temperature programmed Raman spectra were taken on a Horiba LabRAM HR fitted with a water cooled Linkam CCR100 environmental cell. The temperature was increased from ambient at a rate of 10 Kmin<sup>-1</sup> to a maximum of 748 K (bulk catalysts) and 873 K (supported catalysts). A gas mixture of 2 % oxygen balance argon was passed over the sample at 20 cm<sup>3</sup>min<sup>-1</sup> with a temperature ramp rate of 10 Kmin<sup>-1</sup>. The spectra were taken with a 150 mW 562 nm green laser from 100 to 1750 cm<sup>-1</sup>.

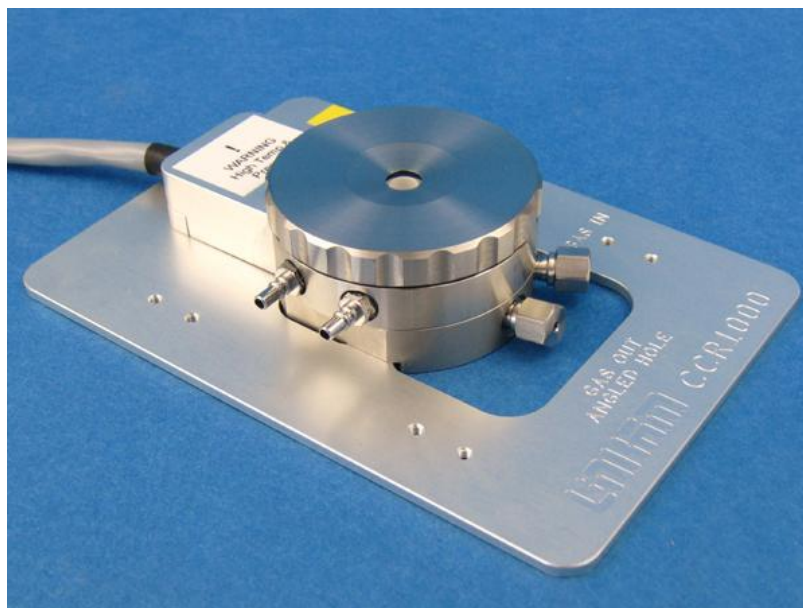


**Figure 3.4: Linkam CCR100 Environmental Cell[39]**

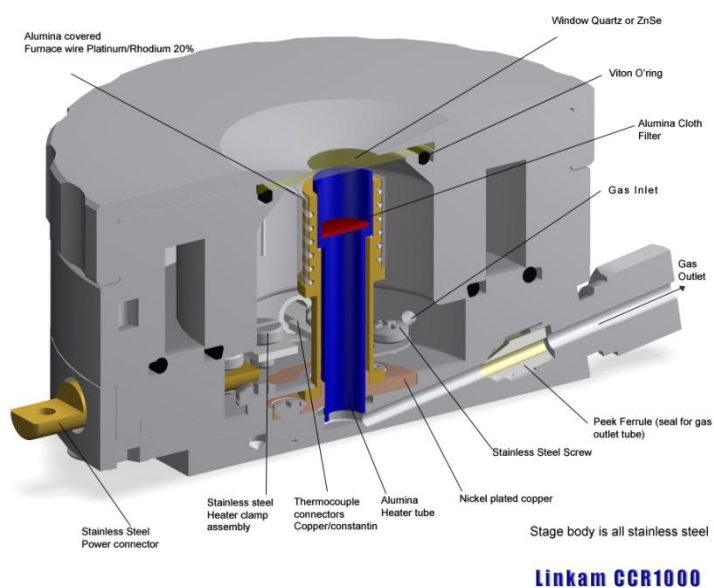


**Figure 3.5 Linkam CCR100 Environmental Cell Schematic[39]**

Ambient temperature Raman were taken on a Horiba LabRAM HR by mounting the catalyst sample on a glass microscope slide.

### **3.5.5 Atomic Absorption Analysis**

Elemental analysis was carried out using a Perkin Elmer Analyst 400 Atomic Absorption Spectrophotometer with Winlab32.

### **3.6 Fixed Bed Reactor**

Reactions were carried out in a 60 cm long glass lined stainless steel reactor. Reactor and trace heating were controlled by a DMG Controls control system. Gas flows were controlled by glass variable area flowmeters. Figure 3.6 shows a schematic of the fixed bed reactor.

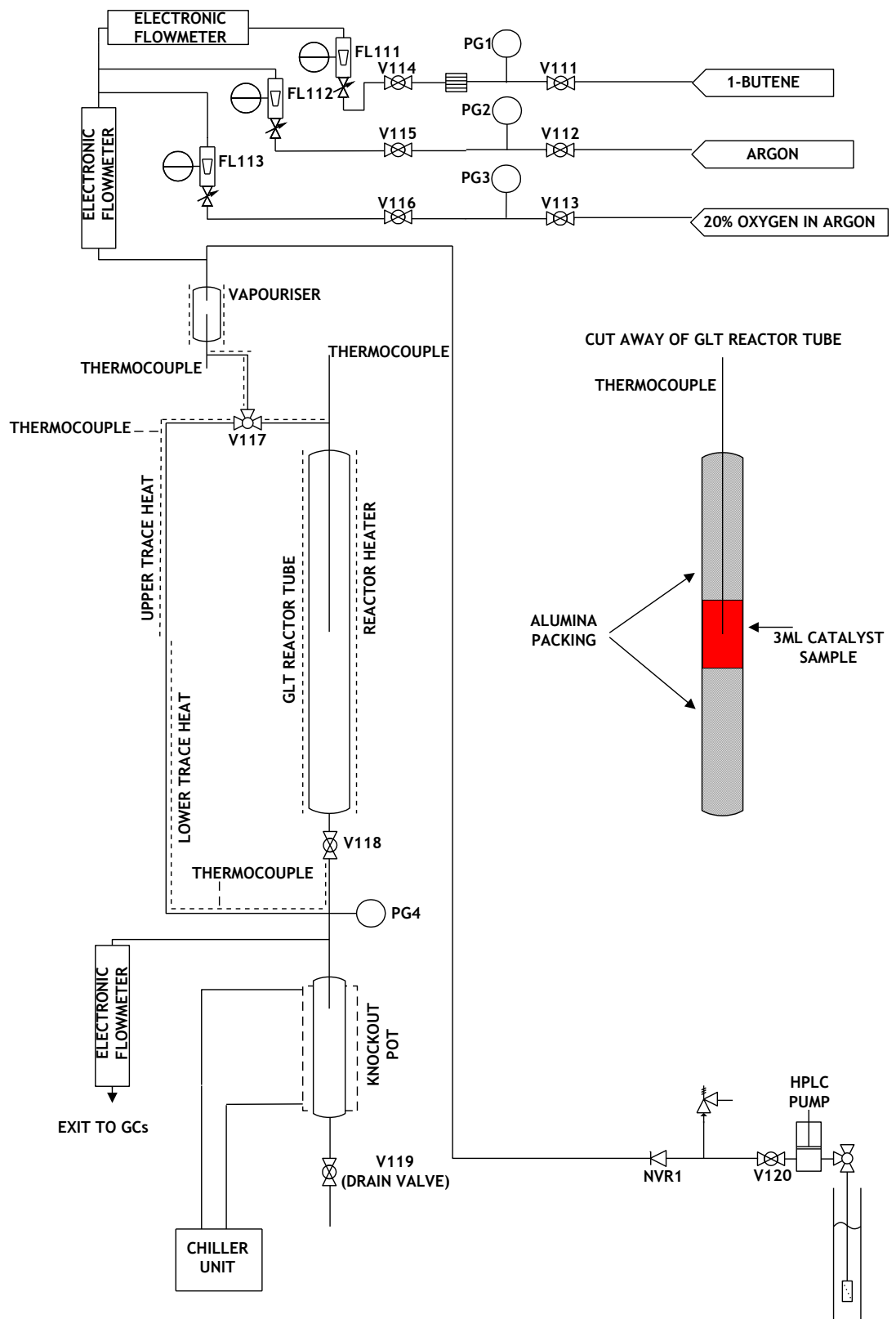


Figure 3.6: Fixed Bed Reactor

### 3.6.1 Catalyst Pre-treatment

All catalysts were crushed and sieved to give a particle size range of 250 - 425 micron. Bulk catalysts were calcined under air at  $10 \text{ K min}^{-1}$  from ambient to 748 K and held at this temperature for four hours. Supported catalysts were calcined under air at  $10 \text{ K min}^{-1}$  from ambient to 873 K and held at this temperature for four hours.

### 3.6.2 Experimental Method

All reactions were carried out under the following conditions. The 20 % oxygen balance argon gas mixture flow was set at  $37.5 \text{ cm}^3 \text{ min}^{-1}$ , vapouriser and upper trace temperature set at 473 K, bottom trace temperature set at 373 K. The reactor was heated to 743 K at  $5 \text{ K min}^{-1}$ , held for one hour then cooled to 693 K. The gas flow was diverted through the bypass line and the HPLC pump set at  $0.120 \text{ cm}^3 \text{ min}^{-1}$ . Once the steam had been running for 1 hour, n-butene (where n-butene = 1-butane, cis-2-butene, or trans-2-butene) was introduced at a flow of  $10 \text{ cm}^3 \text{ min}^{-1}$ . The molar ratio of the gas to the reactor was 0.75:1:15 oxygen:1-butene:steam. The flows were allowed to stabilise for one hour and then three baseline samples were taken. The gas flow was then diverted back through the reactor and samples taken approximately every 30 minutes during the working day and every 60 minutes during the night. The reaction was closed down in the following sequence: the n-butene flow was stopped, 30 minutes later the steam flow was terminated, the 20 %  $\text{O}_2/\text{Ar}$  gas mixture was left flowing for 3 hours before all of the heaters were switched off and finally the gas flow was stopped once the reactor reached ambient temperature.

### 3.6.3 Catalyst Testing

The prepared catalysts were loaded into the reactor as depicted in figure 2.3, the upper section of the reactor was packed with  $\alpha$ -alumina, then  $X \text{ cm}^3$  of catalyst was loaded (where  $X = 0.5, 1.0, 2.0, 3.0 \text{ cm}^3$ ) and finally the lower section packed with more  $\alpha$ -alumina.

Prior to full catalyst testing two steam-only reactions were carried out on the ZF0.6MP catalyst for 67 and 196 hours respectively to ascertain the effects of high temperature steam on the catalyst. A portion of ZF0.6MBP was pre-treated with steam for 24 hours to ascertain if this had any effect ZF0.6MBP 24HSPT. The catalyst test reactions were carried out as outlined in table 3.7 below.

**Table 3.7: Catalyst Testing List**

Reaction No	Catalyst Code	Bed Vol (cm <sup>3</sup> )	Weight (g)
3	3.2 %Fe/0.39 % Zn/Al <sub>2</sub> O <sub>3</sub>	3	1.9981
4	3.45 % ZF/Al <sub>2</sub> O <sub>3</sub>	3	2.2867
5	ZF0.6MBP	3	3.8695
6	8.81 %ZF/0.49 % Zn/Al <sub>2</sub> O <sub>3</sub>	3	2.2698
7	ZF3MBPD R	3	2.7175
8	ZF3MBPC R	3	3.7896
9	0.5 % VO <sub>x</sub> /Al <sub>2</sub> O <sub>3</sub>	3	1.9218
11	ZF0.6MBP 24HSPT	3	4.0215
12	ZF3MBPC	2	2.5316
13	ZF3MBPC	1	1.2942
14	3.3 % VO <sub>x</sub> /Al <sub>2</sub> O <sub>3</sub>	3	2.0732
16	ZF3MBPC	3	3.8750
17	ZF3MBPC	1	1.2277
18	ZFFeNH <sub>3</sub> P	3	5.8493
19	Alumina R	3	1.9703
20	ZFFeNH <sub>3</sub> PD	3	7.5162
22	ZF3MBPC	1	1.1478
23	ZF3MBPC	1	1.1632
24	Al <sub>2</sub> O <sub>3</sub> /ZF3MBPC	3:1	1.8529: 1.1170
25	ZFFeNaOHP	1	2.4339
28	Fe <sub>2</sub> O <sub>3</sub> NaOHP	1	0.9612
29	Fe <sub>2</sub> O <sub>3</sub> NH <sub>3</sub> P	1	2.1434
30	Alumina	1	0.6914

**Table 3.7: Catalyst Testing List (Continued)**

Reaction No	Catalyst Code	Bed Vol (cm <sup>3</sup> )	Weight (g)
31	Al <sub>2</sub> O <sub>3</sub> /ZF3MBPC	1:1	1.0920:0.6820
33	Al <sub>2</sub> O <sub>3</sub> /ZF3MBPC	1:1 (Mixed)	0.6490/1.1718
34	ZF3MBPC	0.5	0.6927
35	ZF3MBPD	1 (1-butene)	0.7148
36	ZF3MBPD	1 ( cis-2-butene)	0.7080
37	ZF3MBPD	1 (trans-2-butene)	0.6825

### 3.7 Analysis

#### 3.7.1 Scanning Electron Microscope/Electron-dispersive X-Ray Spectroscopy

Surface morphology and element mapping were determined using a Philips XL30 environmental SEM/EDX. Imaging was obtained using a tungsten filament operating at 25 KV using secondary electron imaging. Analysis was carried out with an Oxford Instruments X-ACT 10mm liquid nitrogen free detector with INCA Energy 250 software. Samples were mounted on an alumina pin stub fitted with a carbon tab.

#### 3.7.2 Gas Chromatography

Online samples were analysed using two gas chromatographs. Hydrocarbon analysis was carried out on a Thermo Scientific Focus gas chromatograph fitted with a flame ionization detector and an automatic gas sampling valve with a 50 µL sample loop. The column used was a Chrompack sodium sulphate on alumina 50 metre, 0.53 mm ID, 1 µm film thickness with helium as the carrier gas. Carbon dioxide analysis was carried out on a Thermo Scientific Trace gas chromatograph fitted with a thermal conductivity detector and an automatic gas sampling valve with a 2.5 cm<sup>3</sup> sample loop. The column used was a Hewlett Packard PoraPLOT Q 30 metre, 0.53 mm ID, 4 µm film thickness with helium as the carrier gas. Data handling and analysis was carried out using Chrom-Card version 2.5.0 software.

#### Thermo Scientific Focus Conditions

Oven	373 K held 8 min, ramped to 393 K at 10 Kmin <sup>-1</sup> , ramped to 468 K at 20 Kmin <sup>-1</sup> , held 10.75/41 min
Inlet	473 K, split flow 38 cm <sup>3</sup> min <sup>-1</sup> , split ratio 25
Carrier	1.5 cm <sup>3</sup> min <sup>-1</sup>
Detector	523 K, hydrogen flow 30 cm <sup>3</sup> min <sup>-1</sup> , air flow 300 cm <sup>3</sup> min <sup>-1</sup>

#### Thermo Scientific Trace Conditions

Oven	313 K held 5 min, sample time delay 24.5 min.
Inlet	473 K, split flow 120 cm <sup>3</sup> min <sup>-1</sup>
Carrier	4.0 cm <sup>3</sup> min <sup>-1</sup>
Detector	473 K block temperature

### 3.7.3 Gas Chromatography Calibration

The multi-component calibration gas was injected onto the columns using the following sample loops:-

2000 µL, 500 µL, 250 µL, 100 µL and 50 µL to calibrate for methane, ethane, ethene, propane, butane, and iso-butane. While the 2000 µL, 500 µL and 250 µL sample loops were used for carbon dioxide calibration.

The quadruple calibration gas was injected onto the columns using the following sample loops:-

500 µL, 250 µL, 100 µL and 50 µL to calibrate for 1-butene, cis-2-butene, trans-2-butene and 1,3-butadiene.

The relationship between the ethane and ethene calibration factors was used to calculate the isobutene calibration factors.

The calibration graphs are shown below in figures 3.7 to 3.17.

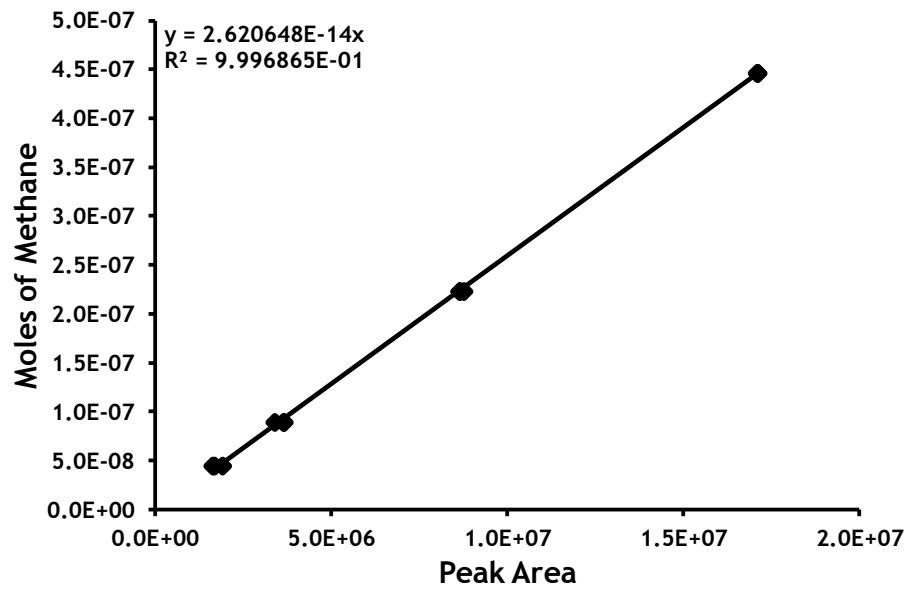


Figure 3.7: Methane Calibration

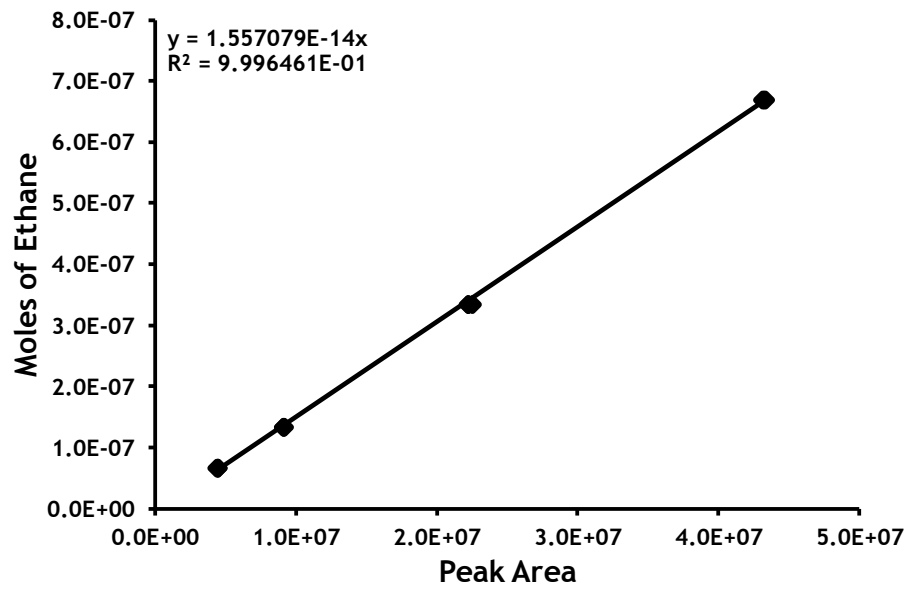


Figure 3.8: Ethane Calibration

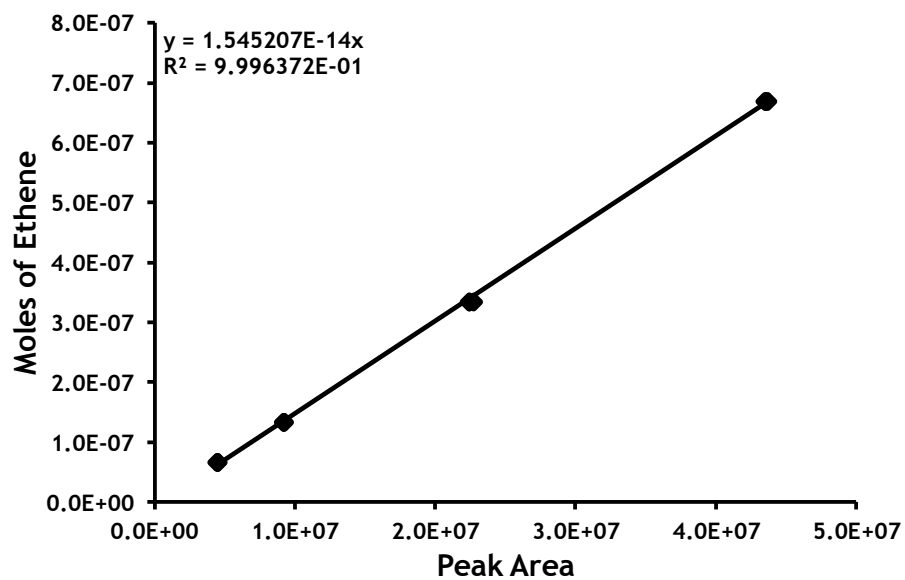


Figure 3.9: Ethene Calibration

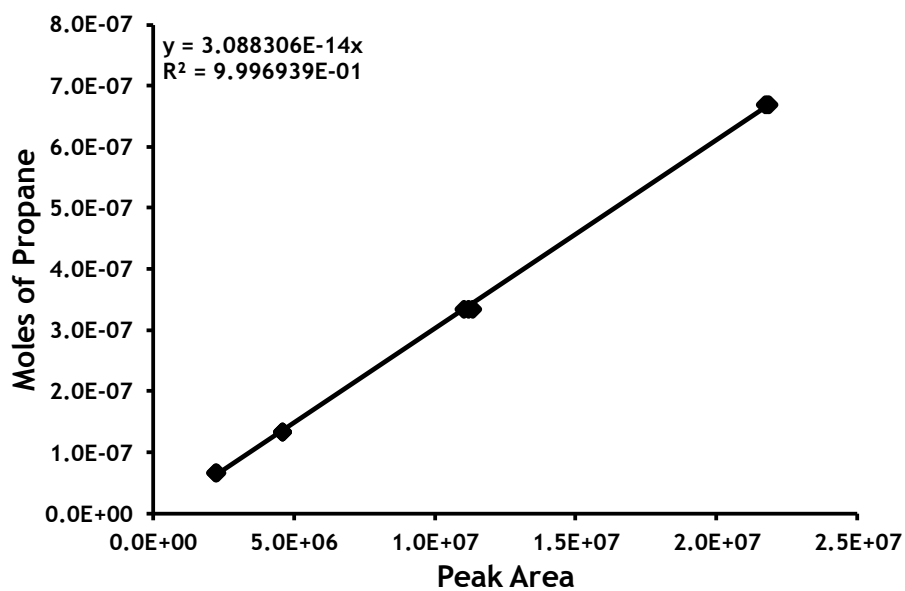


Figure 3.10: Propane Calibration

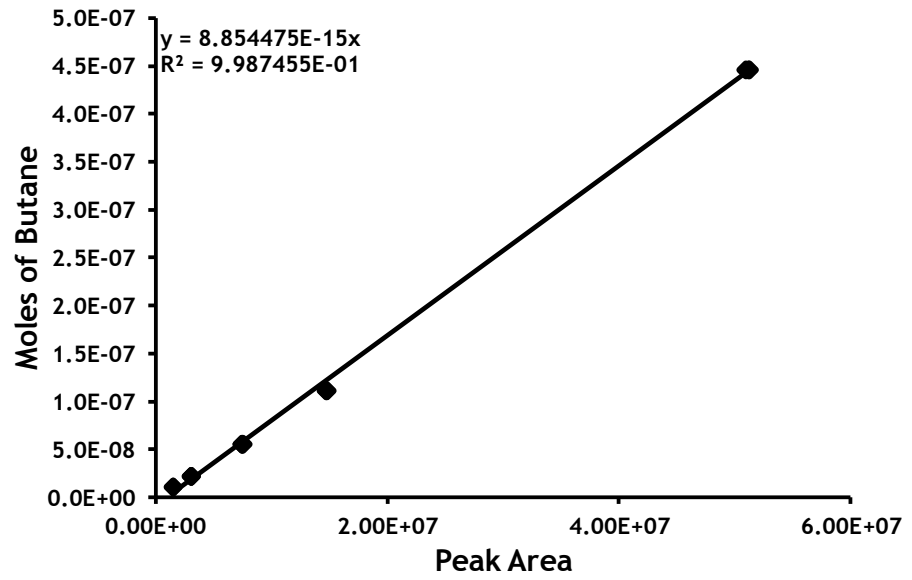


Figure 3.11: Butane Calibration

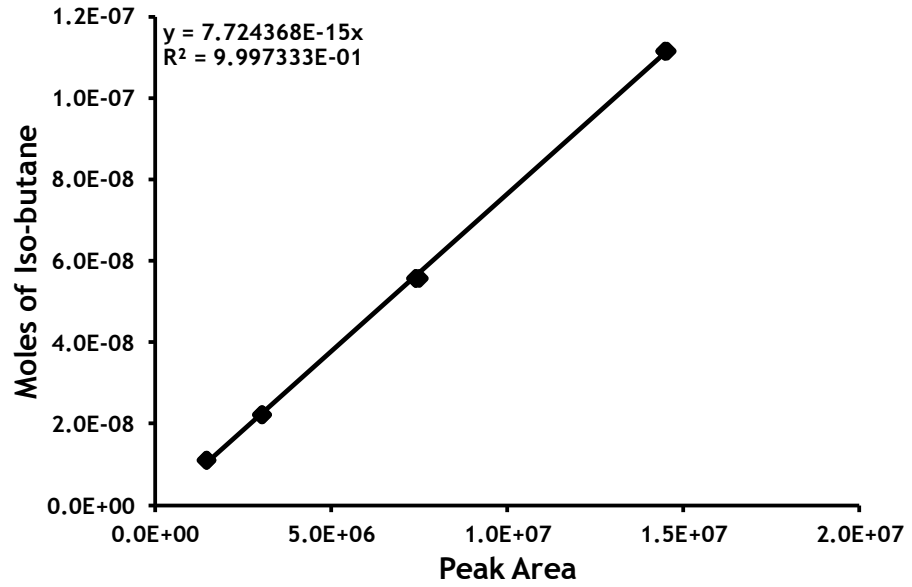


Figure 3.12: Iso-Butane Calibration

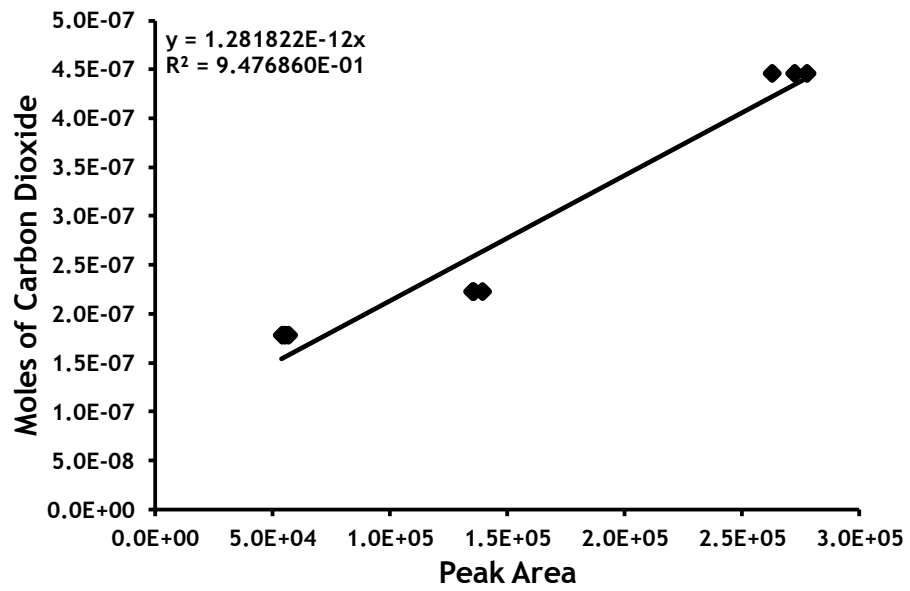


Figure 3.13: Carbon Dioxide Calibration

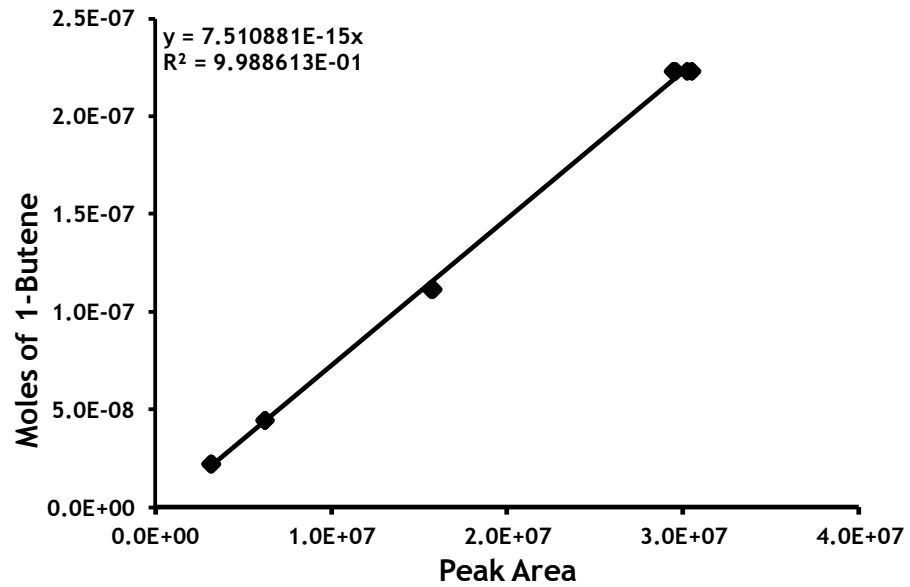


Figure 3.14: 1-Butene Calibration

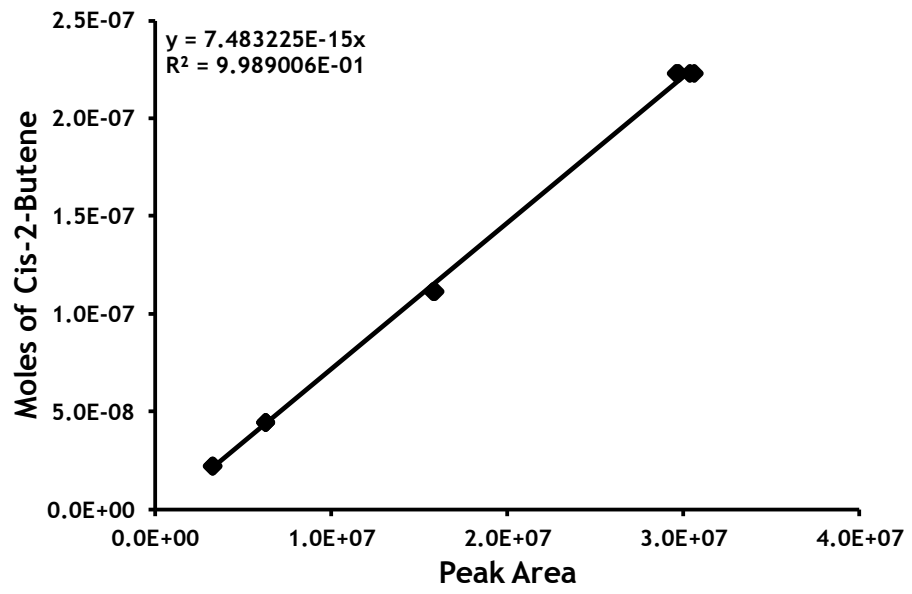


Figure 3.15: Cis-2-Butene Calibration

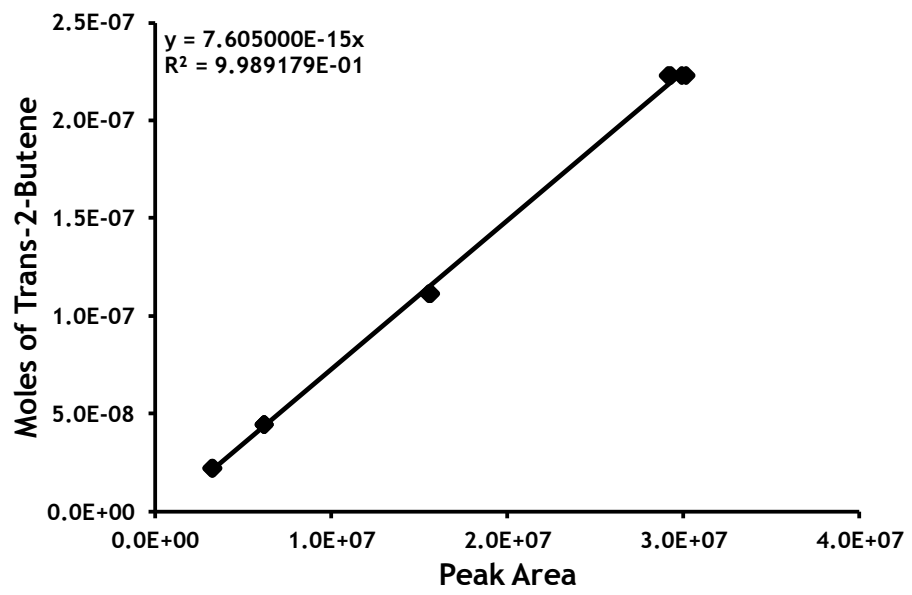


Figure 3.16: Trans-2-Butene Calibration

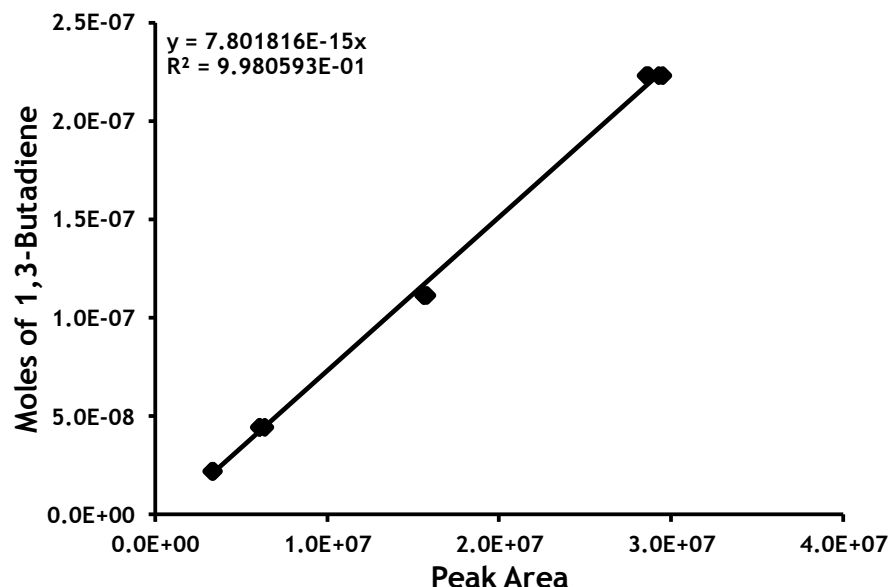


Figure 3.17 1,3-Butadiene Calibration

### 3.7.4 Gas Chromatography Result Calculations.

Yield, selectivity and conversion were calculated using the following formulae:-

$$\text{Yield} = \text{Selectivity} \times \text{Conversion}.$$

$$\text{Selectivity} = [\text{Product} / \text{Sum of Products}] \text{ (corrected for carbon number).}$$

$$\text{Conversion} = [(\text{n-butene in} - \text{n-butene out}) / \text{n-butene in}] \times 100 \text{ (corrected for carbon number).}$$

Where n-butene in is 1-butene, cis-2-butene or trans-2-butene. The n-butene “in” is obtained by summing the products and the unreacted n-butene since no carbon is being laid down and all products are being measured.

Impurities within 1-butene were isobutane, butane, cis-2-butene, trans-2-butene and isobutene. Conversion calculations were only done on 1-butene, isobutane and butane since isobutene is a product of isobutane dehydrogenation and cis-2-butene and trans-2-butene are isomerisation products and 1,3-butadiene is a dehydrogenation product.

Impurities within cis-2-butene were 1-butene, trans-2-butene and 1,3-butadiene. The conversion calculation was only done on cis-2-butene since 1-butene and trans-2-butene are isomerisation products and 1,3-butadiene is a dehydrogenation product.

Figure 3.18 below shows a typical 1-butene conversion profile, which has a 24 hour cyclic nature. This cyclic nature is a consequence of daily temperature variations within the laboratory and their effect on the alkene cylinder pressure and hence the flow through the reactor. All reaction comparisons are carried out in the trough of the cycle since this represents the temperature at which the rotameters were checked and calibrated to given the correct reaction flow rates.

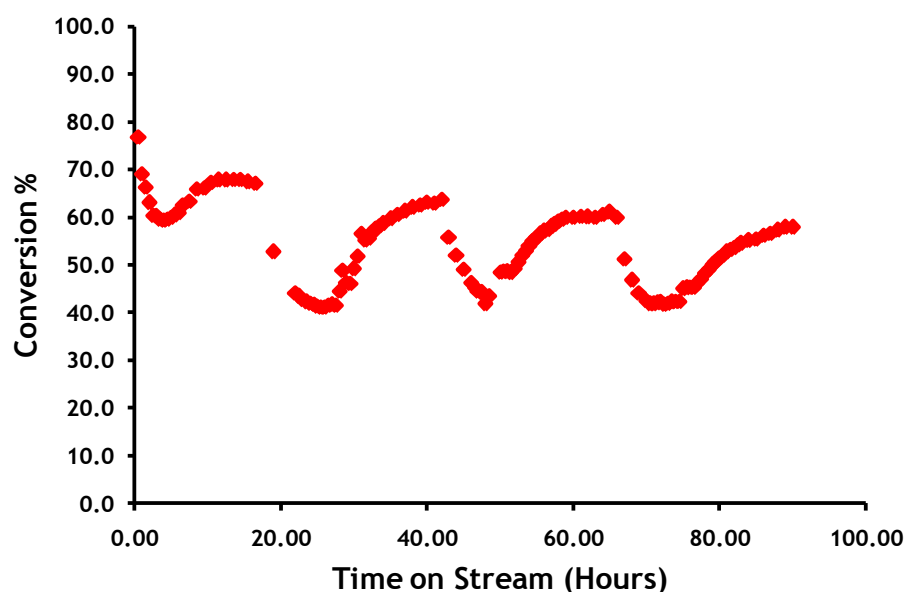


Figure 3.18 Typical Conversion Profile.

### 3.7.5 Acid Site Analysis

Identification of acid sites on the catalysts was carried out in a glass line as shown in figure 3.19 under flow conditions at atmospheric pressure; using propionitrile as the absorbate, toluene as the inert marker and helium as the carrier gas. An ESS Gensys quadrupole mass spectrometer was used to analysis the glass line off gases. Desorption temperatures were recorded using a Comark Dilgence EV N2014 datalogger.

Catalyst, typically 1 g, was placed in the U-tube glass reactor which was attached to the test unit. Oxygen (2 %) balance argon gas mixture was flowed over the catalyst at  $20 \text{ cm}^3 \text{ min}^{-1}$ , the catalyst was heated from ambient

temperature to 748 K at 10 Kmin<sup>-1</sup> and held for 1 hour. The catalyst was then allowed to cool under oxygen (2 %) balance argon gas mixture to ambient temperature. The reactor tube was isolated from the line and helium passed through the bubbler, which was maintained at 293 K, containing the propionitrile/toluene mixture (9:1) at 20 cm<sup>3</sup>min<sup>-1</sup>. The propionitrile/toluene vapour passing through the line was analysed by mass spectrometry following m/e 54 and m/e 92. Once the mass spectrometer trace showed steady state the propionitrile/toluene/helium mixture was passed over the catalyst. When the steady state was re-established for both m/e 52 and m/e 92 this indicated that no more propionitrile was being adsorbed. Subsequently the bubbler was isolated and the reactor flushed with helium until the mass spectrometer trace showed that no more propionitrile/toluene was being evolved. The reactor was then heated from ambient to 873 K at 20 Kmin<sup>-1</sup>. The reactor eluant was analysed by mass spectrometry and m/e 16, m/e 17, m/e 18, m/e 28, m/e 30, m/e 32, m/e 44 and temperature were recorded. The reactor was then cooled to ambient temperature under helium.

Acid site strength is defined as follows:- 250 K to 500 K weak, 500 K to 720 K medium and 720 K to 850 K strong.

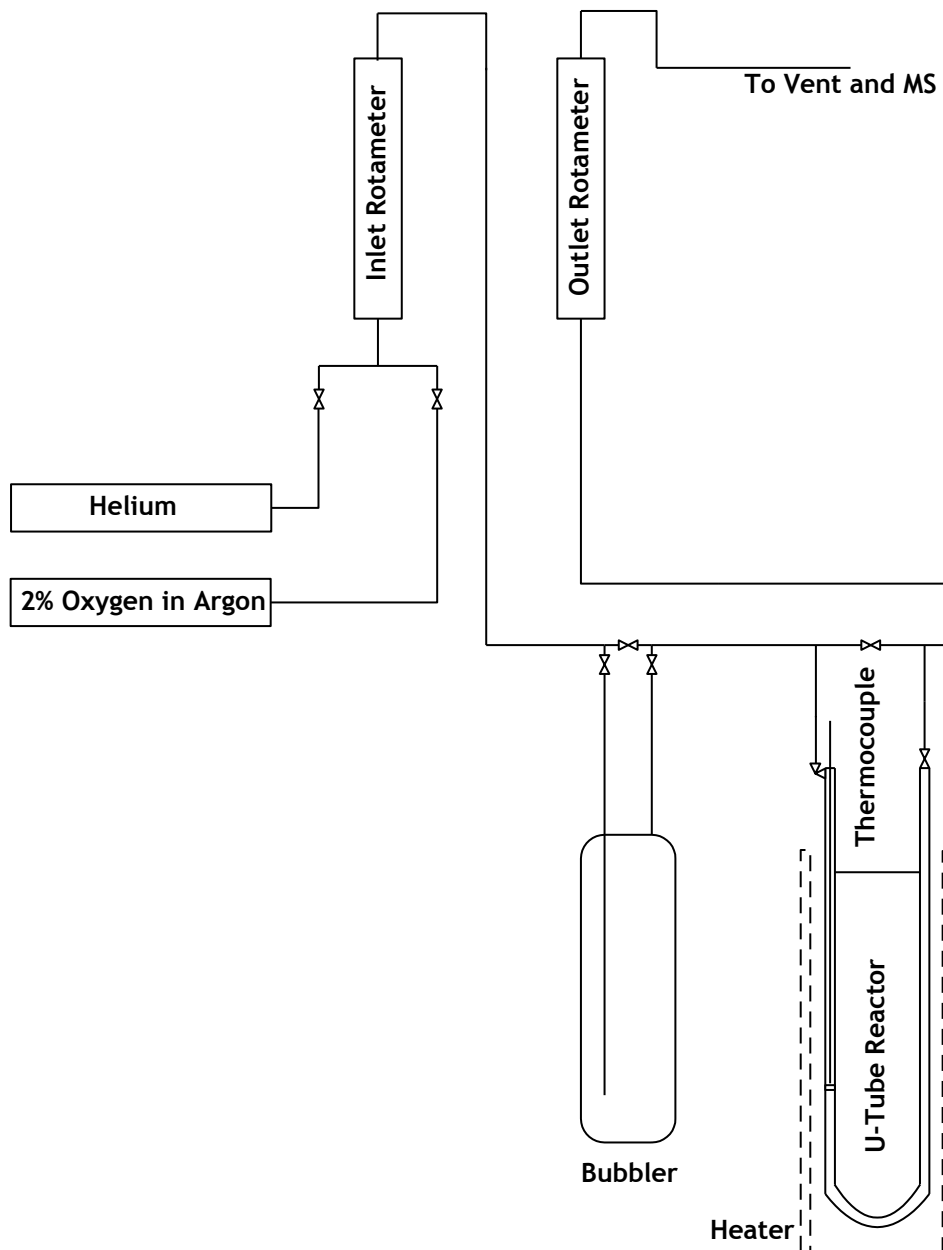


Figure 3.19: Acid Site Analysis Test Unit

### **3.7.6 Magnetic Analysis.**

#### **3.7.6.1 SQUID (Superconducting QUantum Interference Device).**

Magnetic measurements were carried out using a Quantum Design MBMS SQUID fitted with a 5 Tesla magnet using MultiVu version 1.61.82 software. The sample was immobilised with eicosane in a gelatine capsule. Magnetisation vs. field measurements in the range of 0.01 T to 3 T at 290 K and 100 K were carried out on samples of fresh and used catalyst. Data was corrected for the diamagnetic contribution of the capsule and the eicosane.

#### **3.7.6.2 EPR (Electron Paramagnetic Resonance).**

A Bruker ELEXSYS E500 spectrometer was used to produce the X-band EPR spectra of zinc ferrite. The zinc ferrite samples were diluted 1:200 with zinc oxide. The experimental conditions were frequency 9.4325 GHz; modulation 0.1 mT; power 6.3  $\mu$ W, temperature 293 K.

## 4. Results.

### 4.1 $\theta$ -Alumina Support.

#### 4.1.1 Pre-Reaction Characterisation $\theta$ -Alumina.

##### 4.1.1.1 Pre-Reaction X-Ray Diffraction Analysis $\theta$ -Alumina.

Hot stage X-Ray Diffraction was carried out as described in section 3.5.3.

XRD profiles were recorded at 303 K, 373 K, 473 K, 573 K, 673 K, 773 K and 873 K. Examination of the profiles showed a sharpening of the peaks; otherwise no difference was observed.

Figure 4.1 below shows the XRD profiles of  $\theta$ -alumina at 303 K, 573 K and 873 K, which show the presence of  $\alpha$ -alumina,  $\delta$ -alumina,  $\gamma$ -alumina,  $\kappa$ -alumina and  $\theta$ -alumina.

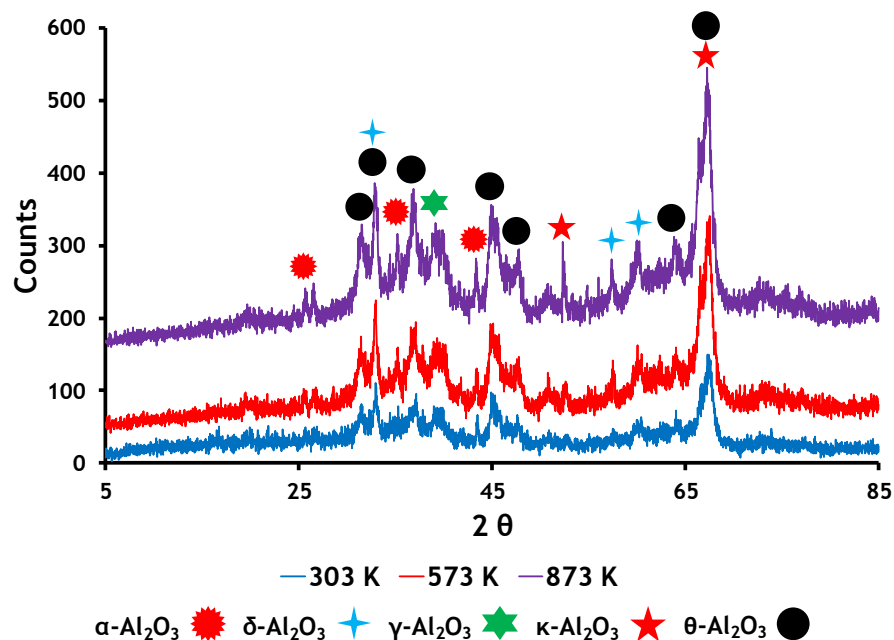


Figure 4.1 Pre-Reaction XRD Spectra of  $\theta$ -Alumina at 303 K, 573 K and 873 K.

#### 4.1.1.2 Pre-Reaction Raman Spectroscopy Analysis $\theta$ -Alumina.

Hot stage Raman spectroscopy was carried out as described in section 3.5.4.

Raman profiles were recorded at 303 K, 373 K, 473 K, 573 K, 673 K, 773 K and 873 K. Examination of the profiles showed a sharpening of the bands; otherwise no difference was observed.

Figure 4.2 below shows the Raman profiles of  $\theta$ -alumina at 303 K, 673 K and 873 K. The Raman bands are tabulated in table 4.1 below to allow comparison.

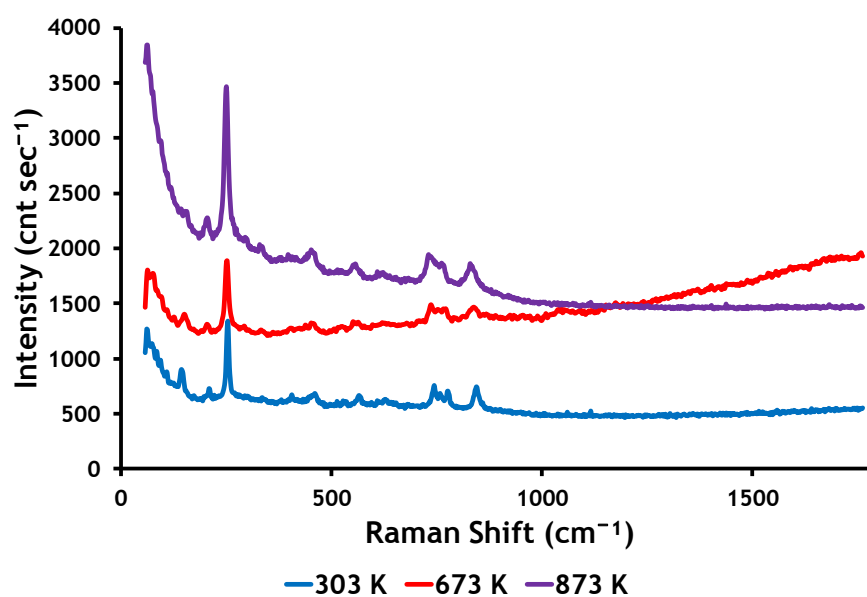


Figure 4.2 Pre-Reaction Raman Spectra of  $\theta$ -Alumina at 303 K, 673 K and 873 K.

Table 4.1 Comparison of Pre-Reaction Raman Shift Bands of  $\theta$ -Alumina compared to literature values.

Raman Shift Bands ( $\text{cm}^{-1}$ )														
	$\theta$ -Alumina[40]													
<b>Literature</b>	244	289	317	327	401	442	453	527	562	619	687	737	772	840
<b><math>\theta</math>-Alumina</b>	251	298		331	397	452	461		557	609		731	762	829

#### 4.1.1.3 Pre-Reaction Surface Area Analysis $\theta$ -Alumina.

Surface area determination was carried out as described in section 3.5.1.

Table 4.2 below shows the surface area, pore diameter and cumulative pore volume of pre-reaction  $\theta$ -alumina.

**Table 4.2 Pre-Reaction Surface Area Results  $\theta$ -Alumina.**

Catalyst	Surface Area ( $\text{m}^2\text{g}^{-1}$ )	Pore Diameter (nm)	Cumulative Pore Volume ( $\text{cm}^3\text{g}^{-1}$ )
$\theta$ -Alumina	95	22	0.511

#### 4.1.1.4 Pre-Reaction Thermo-gravimetric Analysis-Differential Scanning Calorimetry Analysis $\theta$ -Alumina.

Thermo-gravimetric analysis/differential scanning calorimetry was carried out as described in section 3.5.2.

Figure 4.3 below shows a total weight loss of 4 % from pre-reaction  $\theta$ -alumina over the temperature range 290 K to 970 K.

No exothermic or endothermic events were seen on the DSC measurement. The weight loss shown below is likely due to desorption of physisorbed water.

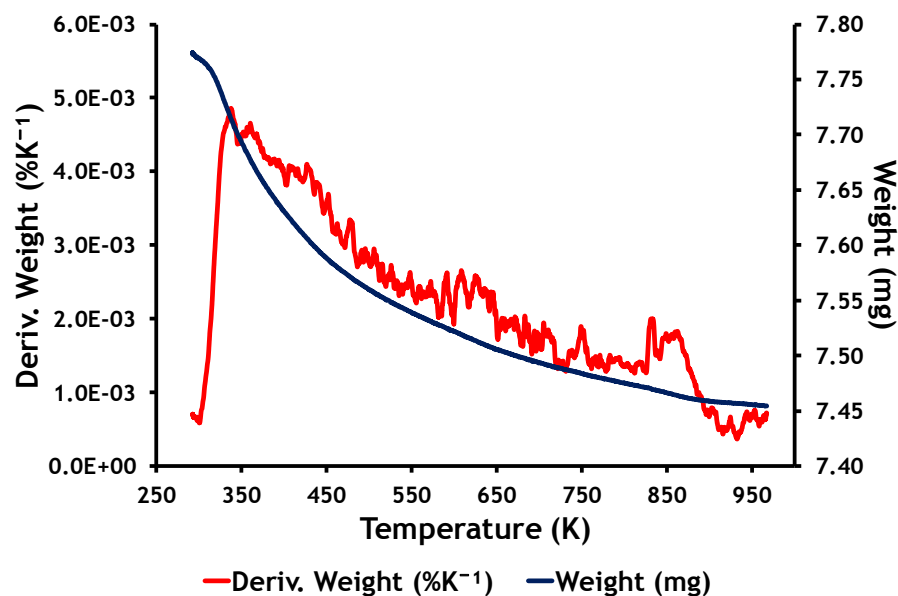


**Figure 4.3** Pre-Reaction  $\theta$ -Alumina TGA and Derivative Weight.

#### 4.1.2 Catalyst Testing $\theta$ -Alumina.

The  $\theta$ -alumina testing is detailed in table 3.7 in section 3.6.3 part of which is reproduced below in table 4.4: the test procedures are given in sections 3.6.2 and 3.6.3.

**Table 4.3** Catalyst Testing List  $\theta$ -Alumina.

Reaction No	Catalyst Code	Bed Vol (cm <sup>3</sup> )	Weight (g)
19	Alumina R	3	1.9703
30	Alumina	1	0.6914

Prior to any catalyst testing blank reactions were run on an empty reactor and a reactor filled with  $\alpha$ -alumina. In both cases no reaction products were observed, only unreacted 1-butene.

Figures 4.4 and 4.5 below show the product selectivities and 1-butene conversion obtained when passing 1-butene over  $\theta$ -alumina with a bed volume of 3 cm<sup>3</sup>.

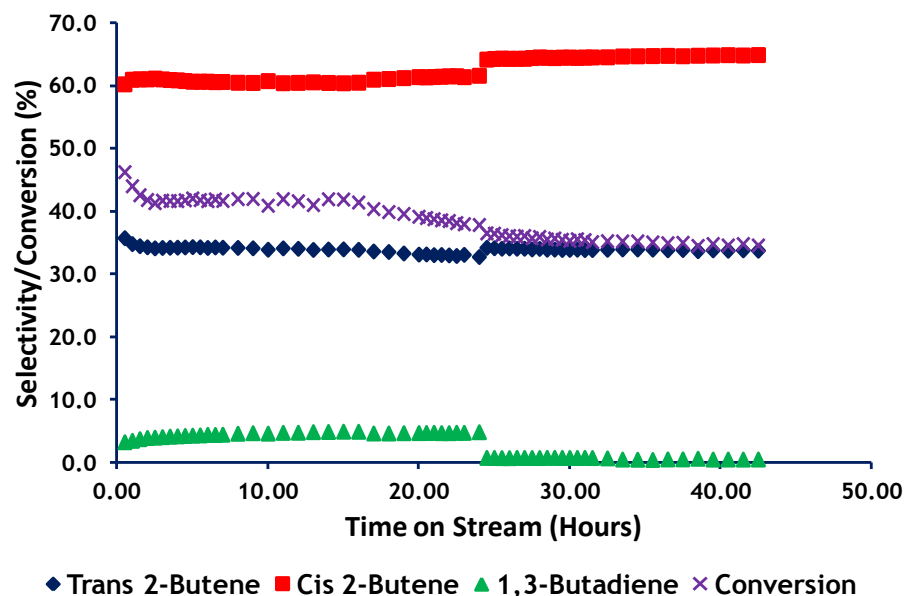


Figure 4.4 Selectivity/Conversion Major Components  $\theta$ -Alumina Bed Volume 3 cm<sup>3</sup>.

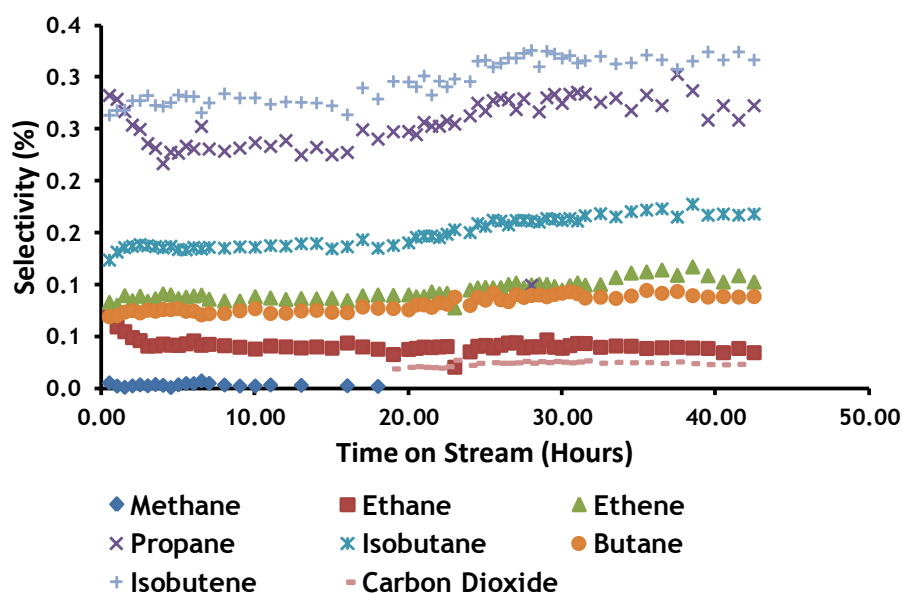


Figure 4.5 Selectivity Minor Components  $\theta$ -Alumina Bed Volume 3 cm<sup>3</sup>.

Figures 4.6 and 4.7 below show the yields, selectivities and conversion obtained when passing 1-butene over  $\theta$ -alumina bed volume of 1 cm<sup>3</sup>.

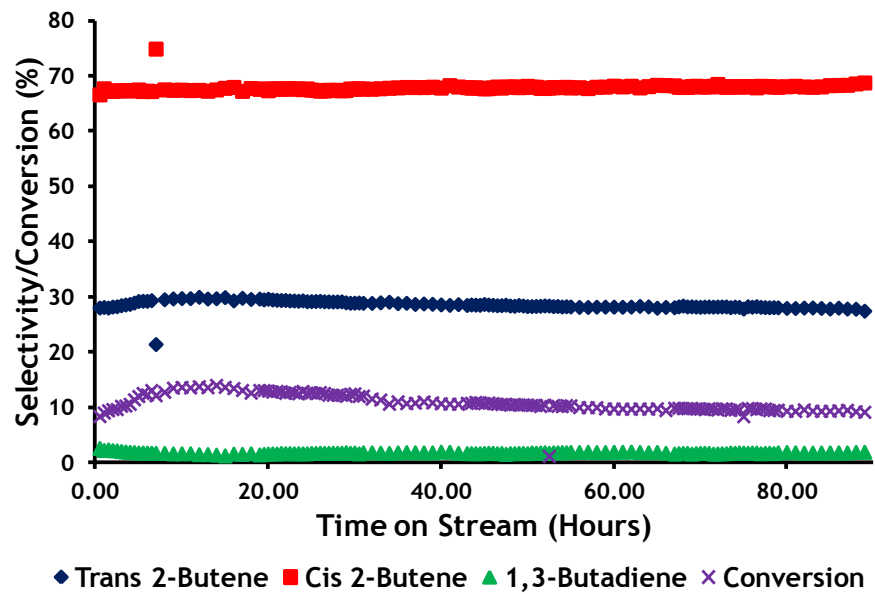


Figure 4.6 Selectivity/Conversion Major Components  $\theta$ -Alumina Bed Volume 1 cm<sup>3</sup>.

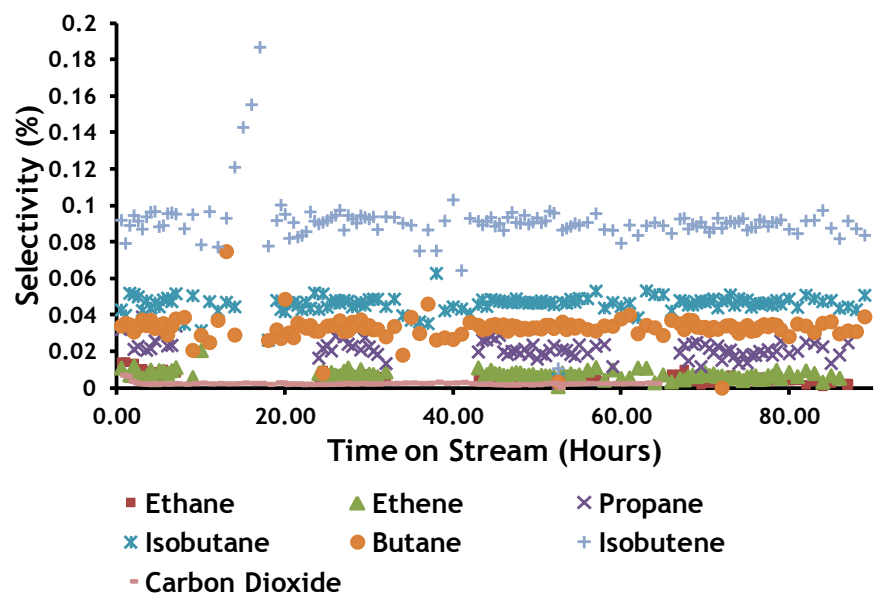


Figure 4.7 Selectivity Minor Components  $\theta$ -Alumina Bed Volume 1 cm<sup>3</sup>.

### 4.1.3 Post Reaction Characterisation $\theta$ -Alumina.

#### 4.1.3.1 Post Reaction X-Ray Diffraction Analysis $\theta$ -Alumina.

Ambient temperature X-Ray Diffraction was carried out as described in section 3.5.3.

Figure 4.8 below shows the ambient temperature XRD profile of  $\theta$ -alumina, which show the presence of  $\alpha$ -alumina,  $\delta$ -alumina,  $\gamma$ -alumina,  $\kappa$ -alumina and  $\theta$ -alumina.

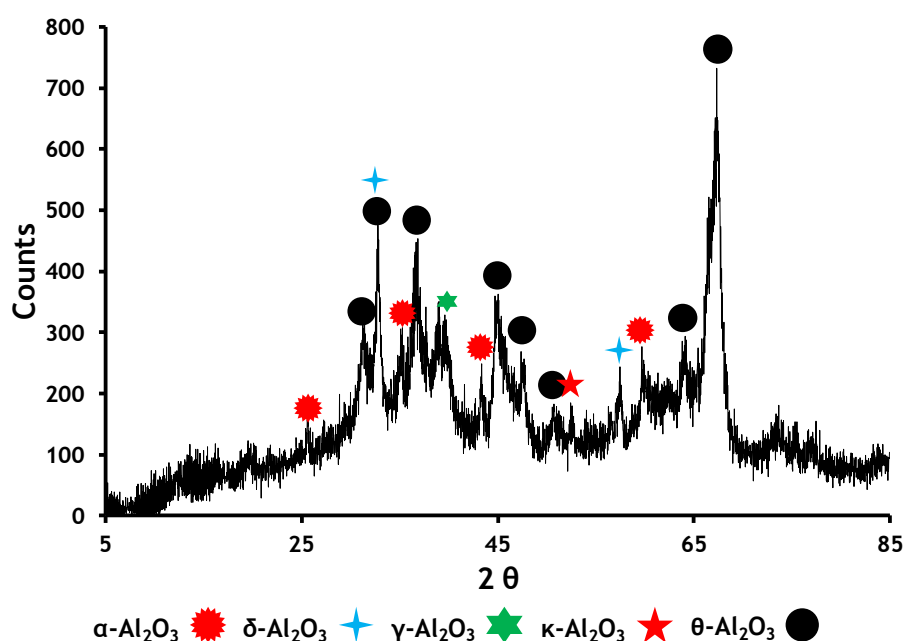


Figure 4.8 Post Reaction Ambient Temperature XRD Spectra of  $\theta$ -Alumina.

#### 4.1.3.2 Post Reaction Raman Spectroscopy Analysis $\theta$ -Alumina.

Ambient temperature Raman spectroscopy was carried out as described in section 3.5.4. however no post reaction Raman spectra for  $\theta$ -Alumina was able to be recorded.

#### 4.1.3.3 Post Reaction Surface Area Analysis $\theta$ -Alumina.

Surface area determination was carried out as described in section 3.5.1.

Table 4.5 below shows the surface area, pore diameter and cumulative pore volume of post reaction  $\theta$ -alumina.

**Table 4.4 Post Reaction Surface Area Results  $\theta$ -Alumina.**

Catalyst	Surface Area ( $\text{m}^2\text{g}^{-1}$ )	Pore Diameter (nm)	Cumulative Pore Volume ( $\text{cm}^3\text{g}^{-1}$ )
$\theta$ -Alumina	93	21	0.477

Comparison of the pre and post reaction surface areas of  $\theta$ -alumina showed no significant change.

#### 4.1.3.4 Post Reaction Thermo-gravimetric Analysis-Differential Scanning Calorimetry Analysis $\theta$ -Alumina.

Thermo-gravimetric analysis/differential scanning calorimetry was carried out as described in section 3.5.2.

Figure 4.9 below shows a total weight loss of 4 % from post reaction  $\theta$ -alumina over the temperature range 290 K to 970 K

No exothermic or endothermic events were seen on the DSC measurement. The weight loss shown below is likely due to desorption of physisorbed water

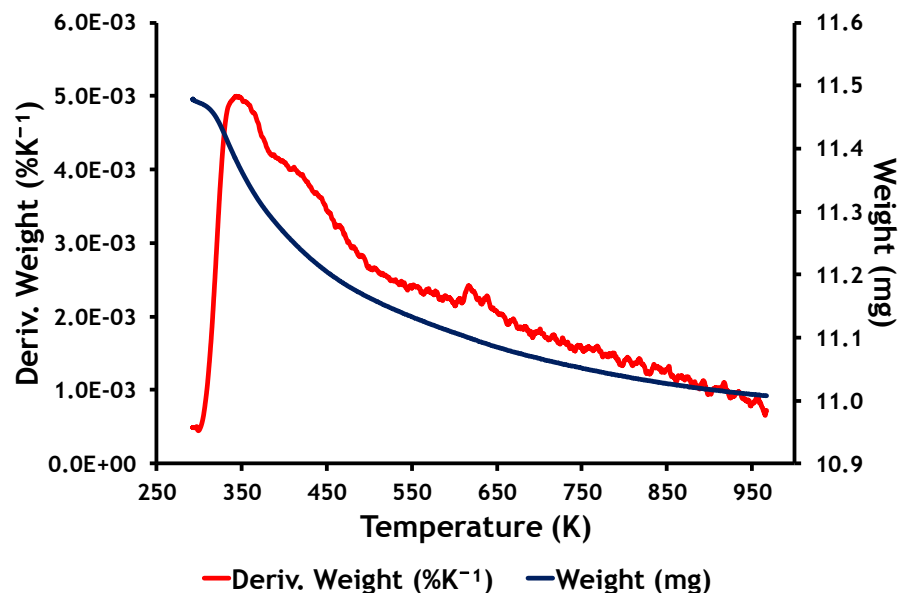


Figure 4.9 Post Reaction  $\theta$ -Alumina TGA and Derivative Weight.

## 4.2 Zinc Ferrite Supported on $\theta$ -Alumina.

### 4.2.1 Pre-Reaction Characterisation Zinc Ferrite on $\theta$ -Alumina.

A total of three zinc ferrite catalysts supported on  $\theta$ -alumina were prepared as outlined in the experimental section 3.3.

#### 4.2.1.1 Pre-Reaction AA Analysis Zinc Ferrite $\theta$ -Alumina.

Table 4.5 below shows the true versus the calculated catalyst loading and the iron:zinc ratio in the case of the supported zinc ferrite catalysts.

Table 4.5 Pre- Reaction Atomic Adsorption Results Zinc Ferrite  $\theta$ -Alumina.

Catalyst	Fe:Zn Mole Ratio	Catalyst Loading
8 % ZF on Alumina	2.07:1	3.45 % ZnFe <sub>2</sub> O <sub>4</sub>
15 % ZF on Alumina	9.57:1	3.2 % Fe/0.39 % Zn
25 % ZF on Alumina	2.56:1	8.81 % ZnFe <sub>2</sub> O <sub>4</sub> /0.49 % Fe

In the table above zinc is assumed to be in the form of zinc oxide and the iron is in the form of an undetermined iron oxide.

#### 4.2.1.2 Pre-Reaction X-Ray Diffraction Analysis Zinc Ferrite $\theta$ -Alumina.

Hot stage X-Ray Diffraction was carried out as described in section 3.5.3.

XRD profiles of 3.45 % zinc ferrite on  $\theta$ -alumina and 3.2 % Fe/0.39 % Zn on  $\theta$ -alumina were recorded at 303 K, 373 K, 473 K, 573 K, 673 K, 773 K and 873 K. Examination of the profiles showed a sharpening of the peaks otherwise no difference was observed. There was no evidence of zinc ferrite or oxides of iron or zinc in either 3.45 % zinc ferrite on alumina or 3.2 % Fe/0.39 % Zn on  $\theta$ -alumina profiles.

Figures 4.10 and 4.11 below show the XRD profiles of 3.45 % zinc ferrite on  $\theta$ -alumina and 3.2 % Fe/0.39 % Zn on  $\theta$ -alumina at 303 K, 573 K and 873 K.

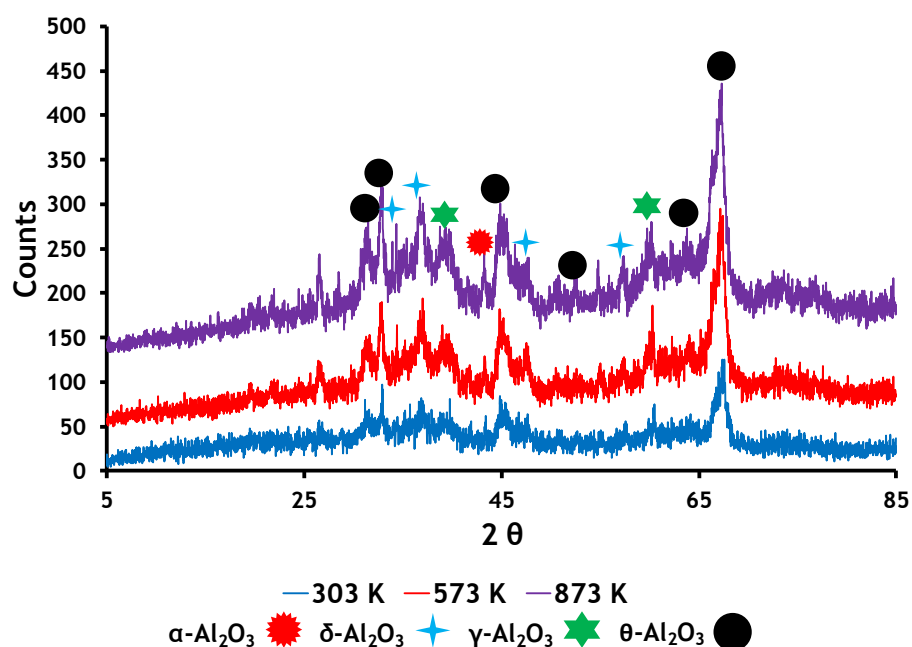
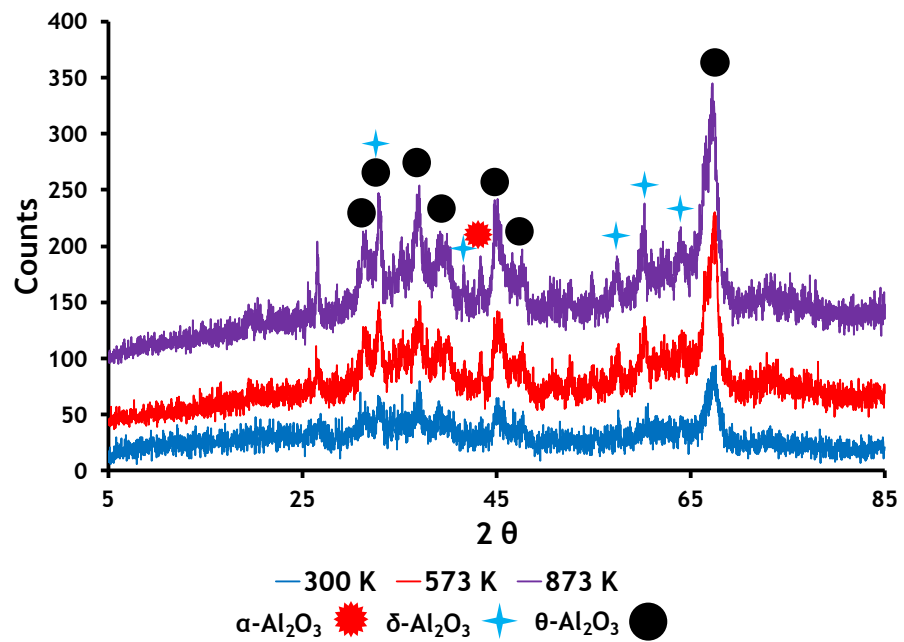


Figure 4.10 Pre-Reaction XRD Spectra of 3.45 % Zinc Ferrite on  $\theta$ -Alumina at 303 K, 573 K and 873 K.



**Figure 4.11** Pre-Reaction XRD Spectra of 3.2 % Fe/0.39 % Zn on  $\theta$ -Alumina at 303 K, 573 K and 873 K.

Ambient temperature X-Ray Diffraction was carried out as described in section 3.5.3.

Figure 4.12 below show the room temperature XRD spectra of calcined 8.81 % ZnFe<sub>2</sub>O<sub>4</sub>/0.49 % Fe on  $\theta$ -alumina which shows no evidence of zinc ferrite, iron oxide or zinc oxide.

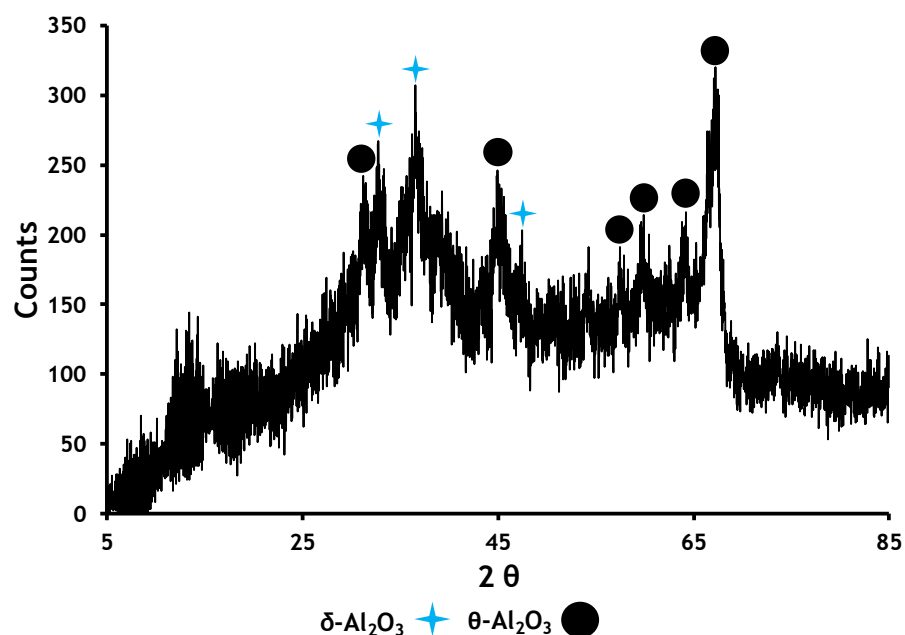


**Figure 4.12** Pre-Reaction Room Temperature XRD Spectra of 8.81 % ZnFe<sub>2</sub>O<sub>4</sub>/0.49 % Fe on θ-Alumina.

#### 4.2.1.3 Pre-Reaction Raman Spectroscopy Analysis Zinc Ferrite on θ-Alumina.

Ambient temperature and hot stage Raman spectroscopy were carried out as described in section 3.5.4.

Raman profiles of 3.45 % zinc ferrite on θ-alumina and 3.2 % Fe/0.39 % Zn on θ-alumina were recorded at 303 K, 373 K, 473 K, 573 K, 673 K, 773 K and 873 K. Examination of the profiles showed sharpening of the bands and loss of the band at 1052 cm<sup>-1</sup>.

Figures 4.13 and 4.14 below show the pre-reaction temperature programmed Raman spectra of 3.45 % zinc ferrite on θ-alumina and 3.2 % Fe/0.39 % Zn on θ-alumina. The Raman bands are tabulated in table 4.6 below to allow comparison.

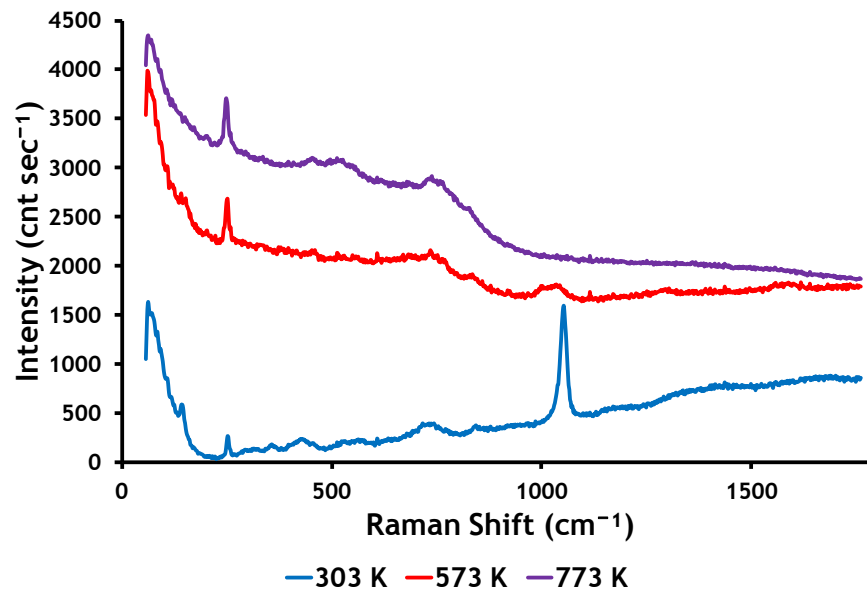


**Figure 4.13** Pre-Reaction Raman Spectra of 3.45 % Zinc Ferrite on  $\theta$ -Alumina at 303 K, 573 K and 773 K.

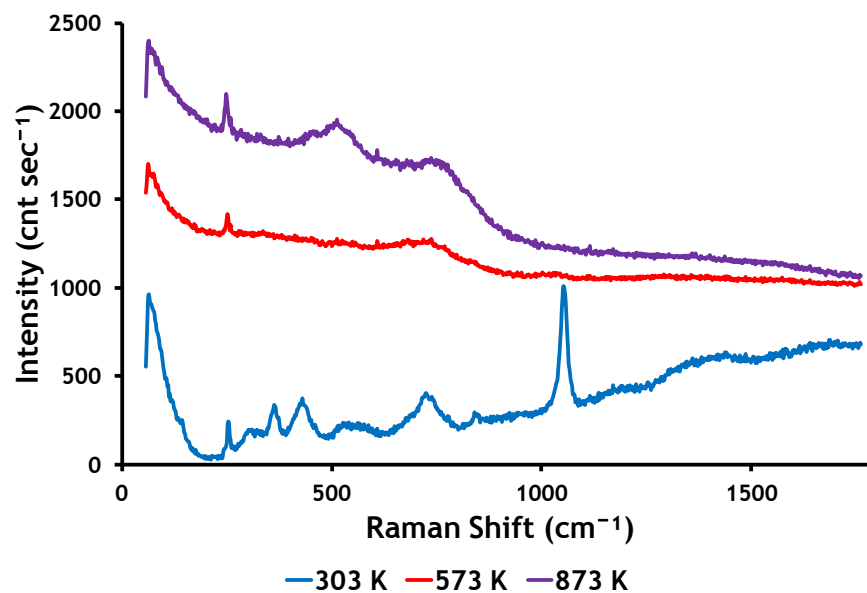


**Figure 4.14** Pre-Reaction Raman Spectra of 3.2 % Fe/0.39 % Zn on  $\theta$ -Alumina at 303 K, 573 K and 873K.

Figure 4.15 below shows the pre-reaction ambient temperature Raman spectra of 8.81 % ZnFe<sub>2</sub>O<sub>4</sub>/0.49 % Fe on  $\theta$ -alumina. The Raman bands are tabulated in table 4.6 below to allow comparison.

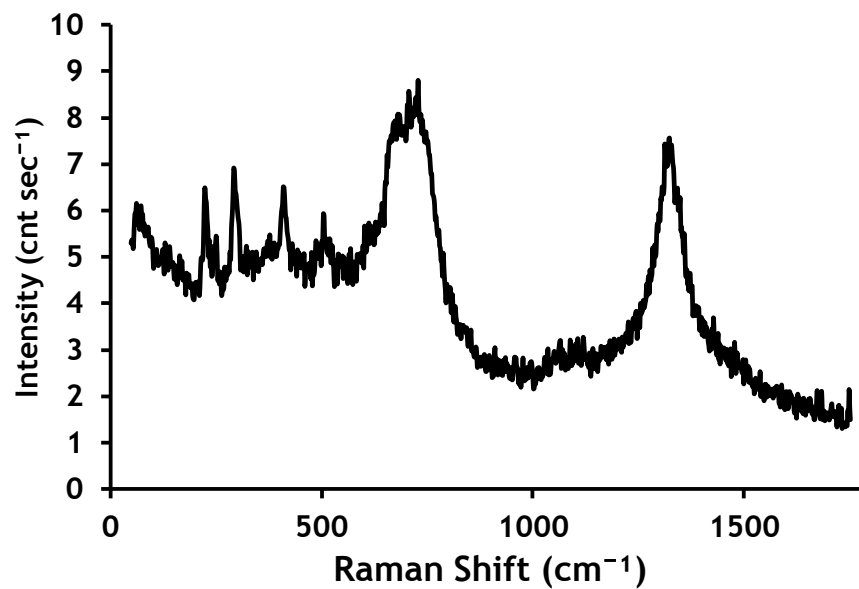


Figure 4.15 Pre-Reaction Ambient Temperature Raman Spectra of 8.81 % ZnFe<sub>2</sub>O<sub>4</sub>/0.49 % Fe on  $\theta$ -Alumina.

Table 4.6 Comparison of Pre-Reaction Raman Shift Bands of Zinc Ferrites on  $\theta$ -Alumina to Literature.

Raman Shift Bands ( $\text{cm}^{-1}$ )																
	$\theta$ -Alumina[40]														Nitrate[41, 42]	$\text{Fe}_2\text{O}_3$ [43]
Literature	244	289	317	327	401	442	453	527	562	619	687	737	772	840	1050	
3.45 % $\text{ZnFe}_2\text{O}_4$ on $\text{Al}_2\text{O}_3$	252			358		426			565			722		843	1054	
3.2 % Fe/0.39 % Zn on $\text{Al}_2\text{O}_3$	254	299		338	406		461	530	566	628		745	776	844	1054	
8.81 % $\text{ZnFe}_2\text{O}_4$ / 0.49 % Fe on $\text{Al}_2\text{O}_3$	249	290		373	408			503			683	728				1324

#### 4.2.1.4 Pre-Reaction Surface Area Measurements Zinc Ferrite on $\theta$ -Alumina.

BET analysis was carried out as described in section 3.5.1. Table 4.7 below shows the supported zinc ferrite results.

Table 4.7 below shows surface area, pore diameter and cumulative pore volume for  $\theta$ -alumina supported catalysts 3.45%  $\text{ZnFe}_2\text{O}_4$  on alumina, 8.81%  $\text{ZnFe}_2\text{O}_4/0.49\%$  Fe on alumina and 3.2% Fe/0.39% Zn on alumina.

Table 4.7 Pre-Reaction Surface Area Results, Zinc Ferrite on  $\theta$ -Alumina.

Catalyst	Surface Area ( $\text{m}^2\text{g}^{-1}$ )	Pore Diameter (nm)	Cumulative Pore Volume ( $\text{cm}^3\text{g}^{-1}$ )
3.45 % $\text{ZnFe}_2\text{O}_4$ on Alumina	82	24	0.4778
3.2 % Fe/0.39 % Zn on Alumina	98	19	0.4542
8.81 % $\text{ZnFe}_2\text{O}_4/0.49\%$ Fe on Alumina	85	17	0.3645

#### 4.2.1.5 Pre-Reaction Thermo-gravimetric Analysis-Differential Scanning Calorimetry Analysis, Zinc Ferrite on $\theta$ -Alumina.

Thermo-gravimetric analysis/differential scanning calorimetry was carried out as described in section 3.5.5.

Figure 4.16 below shows a total weight loss of 12 % from pre-reaction 3.45 % zinc ferrite on  $\theta$ -alumina over a temperature range of 295 K and 870 K.

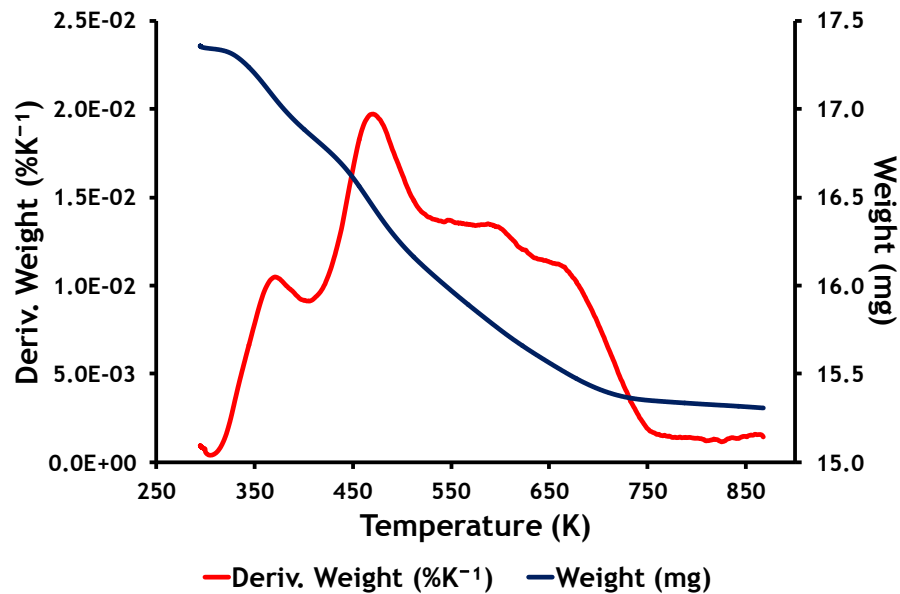


Figure 4.16 Pre-Reaction 3.45 % Zinc Ferrite on  $\theta$ -Alumina TGA/DSC Weight Loss.

Figure 4.17 below shows the evolution of nitrous oxide over the temperature range 480 K to 705 K, relative to the derivative weight.

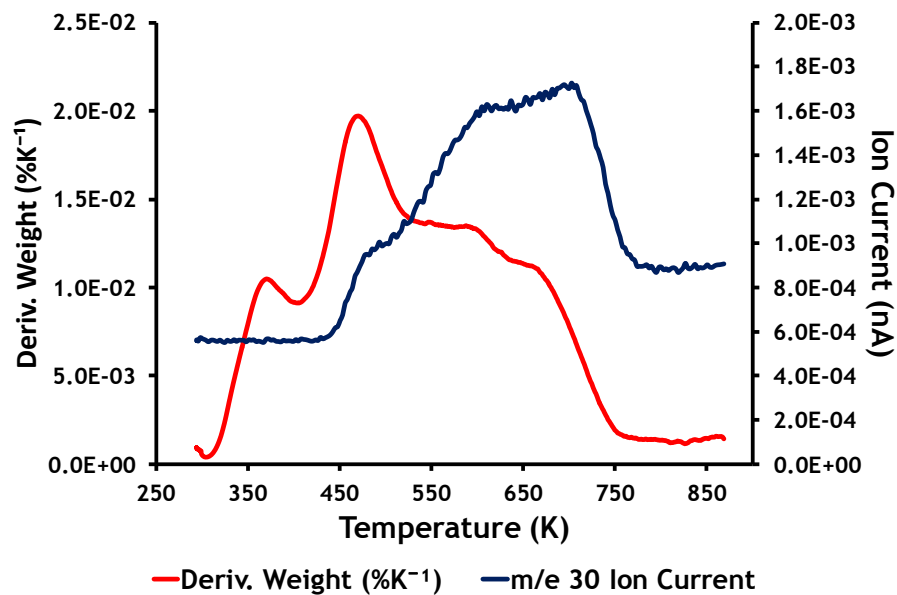


Figure 4.17 Pre-Reaction TGA/DSC Mass Spectrometer Profile from 3.45 % Zinc Ferrite on  $\theta$ -Alumina m/e 30.

Figure 4.18 below shows the evolution of m/e 44, relative to the derivative weigh, at 510 K. This would normally be assigned as carbon dioxide but since the

catalyst was produced from metal nitrates it is more likely to be di-nitrogen oxide.

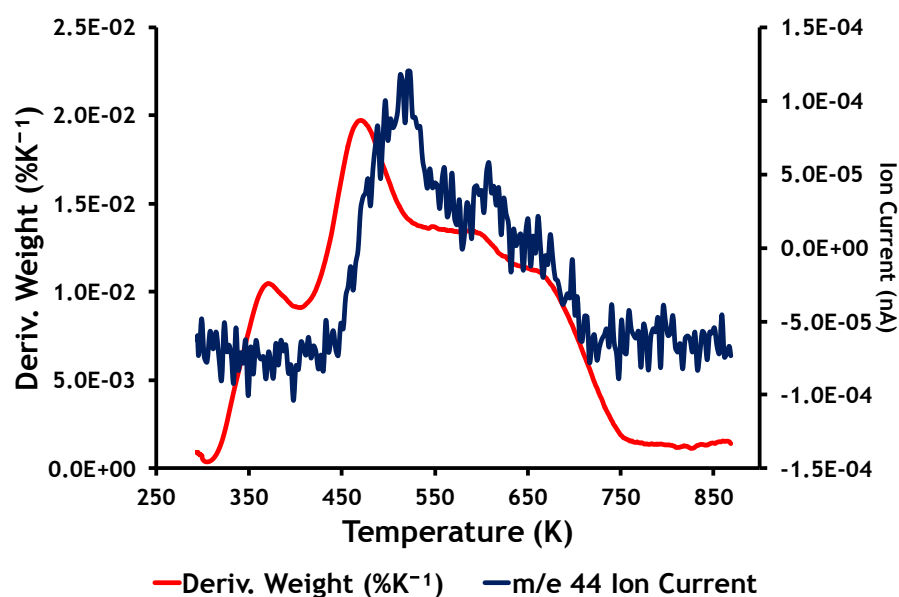


Figure 4.18 Pre-Reaction TGA/DSC Mass Spectrometer Profile from 3.45 % Zinc Ferrite on  $\theta$ -Alumina m/e 44.

Figure 4.19 below shows the evolution of nitric oxide, relative to the derivative weight, at 620 K.

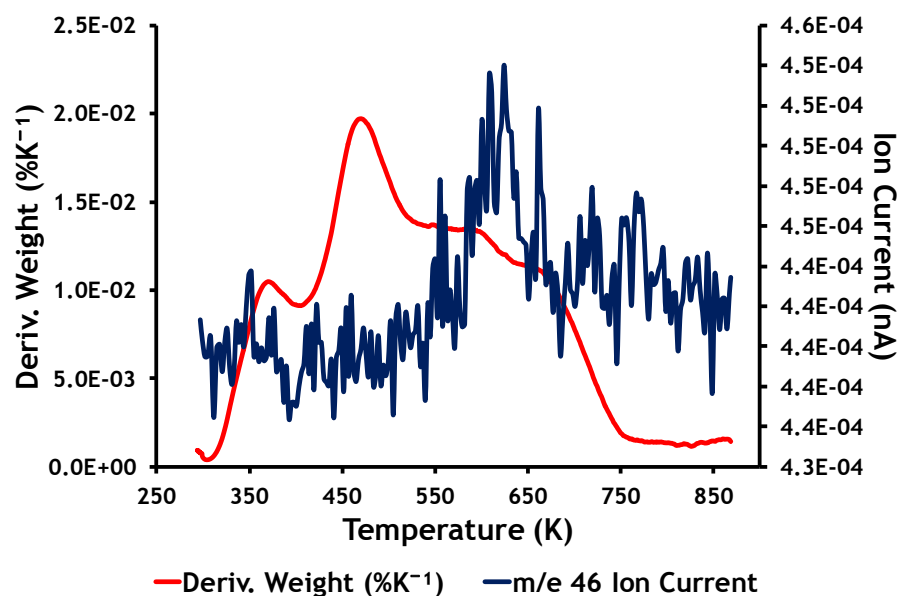


Figure 4.19 Pre-Reaction TGA/DSC Mass Spectrometer Profile from 3.45 % Zinc Ferrite on  $\theta$ -Alumina TGA/DSC m/e 46.

Figure 4.20 below shows a weight loss of 10 % from the pre-reaction 3.2 % Fe/0.39 % Zn on  $\theta$ -alumina over the temperature range of 295 K to 870 K.

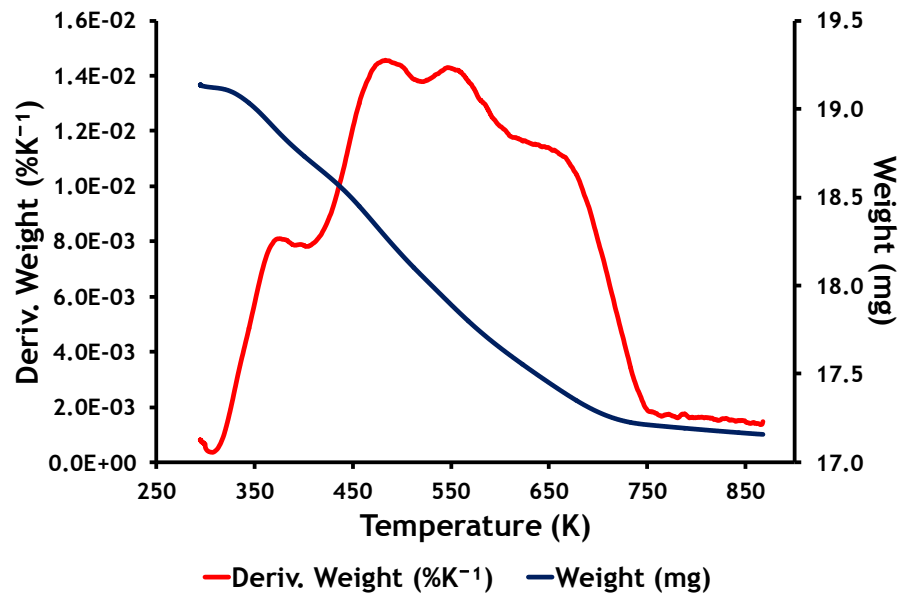


Figure 4.20 Pre-Reaction 3.2 % Fe/0.39 % Zn on  $\theta$ -Alumina TGA/DSC Weight Loss.

Figure 4.21 below shows the evolution of nitric oxide over the temperature range 570 K to 710 K, relative to the derivative weight.

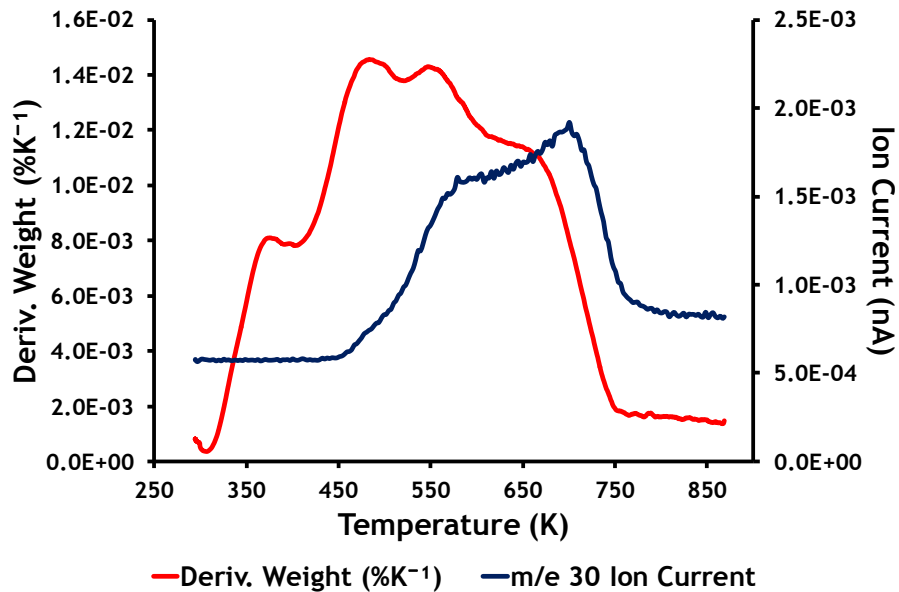


Figure 4.21 Pre-Reaction TGA/DSC Mass Spectrometer Profile from 3.2 % Fe/0.39 % Zn on  $\theta$ -Alumina m/e 30.

Figure 4.22 below shows the evolution of m/e 44, relative to the derivative weight, at 500 K. This would normally be assigned as carbon dioxide but since the catalyst was produced from metal nitrates it is more likely to be di-nitrogen oxide.

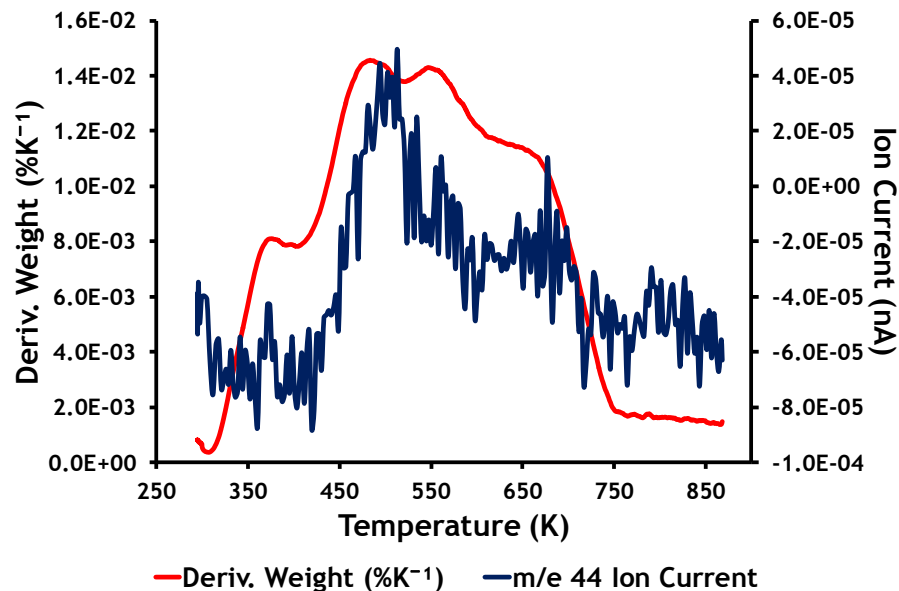


Figure 4.22 Pre-Reaction TGA/DSC Mass Spectrometer Profile from 3.2 % Fe/0.39 % Zn on  $\theta$ -Alumina m/e 44.

Figure 4.23 below shows a total weight loss of 19 % from the pre-reaction 8.81 % ZnFe<sub>2</sub>O<sub>4</sub>/0.49 % Fe on  $\theta$ -alumina over the temperature range 295 K to 890 K.

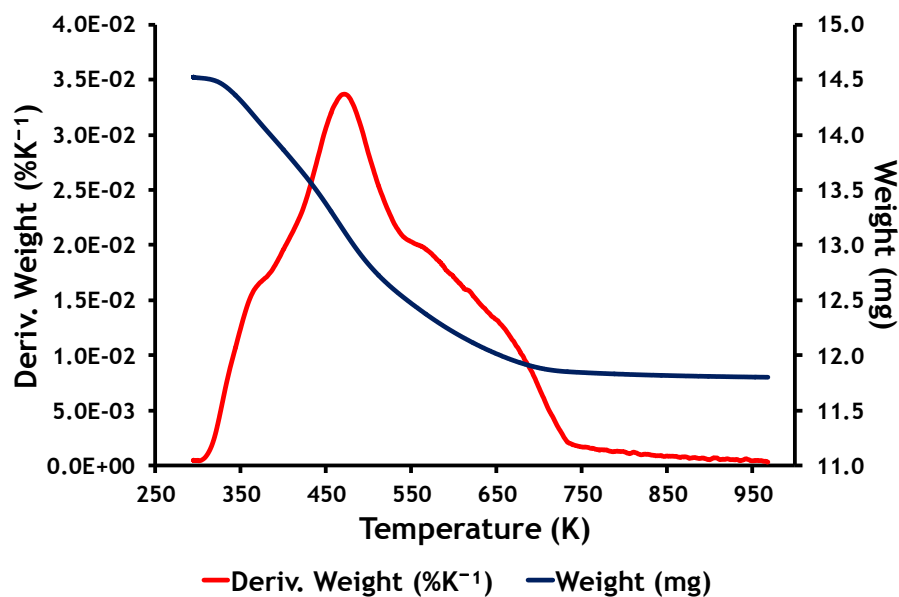


Figure 4.23 Pre-Reaction 8.81% ZnFe<sub>2</sub>O<sub>4</sub>/0.49% Fe on  $\theta$ -Alumina TGA/DSC Weight Loss.

Figure 4.24 below shows the evolution of nitrous oxide over the temperature range 510 K to 680 K, relative to the derivative weight.

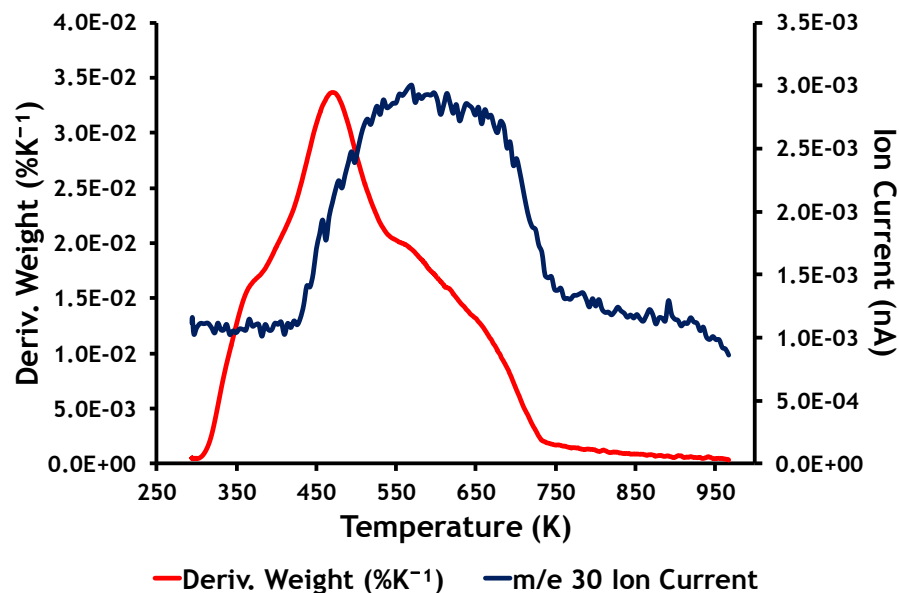


Figure 4.24 Pre-Reaction TGA/DSC Mass Spectrometer Profile from 8.81 % ZnFe<sub>2</sub>O<sub>4</sub>/0.49 % Fe on  $\theta$ -Alumina m/e 30.

#### 4.2.1.6 Pre-Reaction Scanning Electron microscopy Analysis Zinc Ferrite on $\theta$ -Alumina.

Figures 4.25 to 4.27 below show mapped EDX micrographs of the three supported zinc ferrite catalysts. Zinc and iron are represented by green and red dots respectively. The micrographs clearly identify the different coverage of both elements.

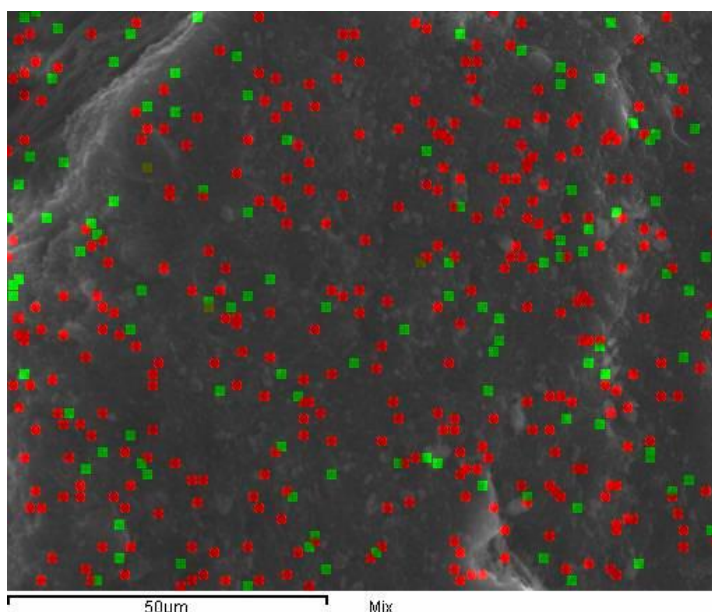
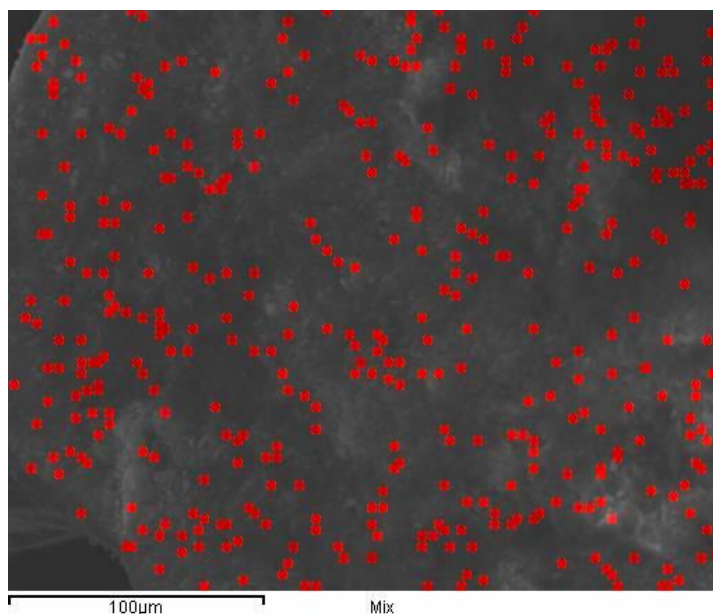
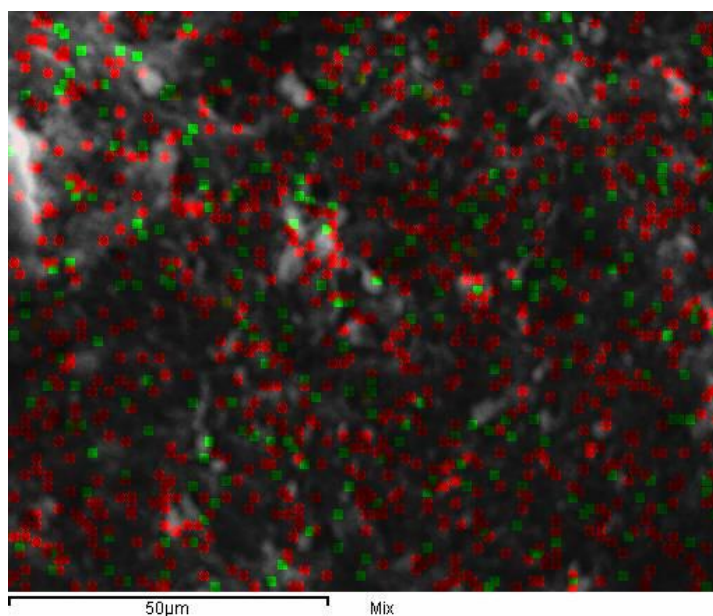


Figure 4.25 Pre-Reaction 3.45 % Zinc Ferrite on  $\theta$ -Alumina SEM Micrograph.

The absence of green dots in figure 4.26 below confirms the very low level of zinc indentified by atomic adsorption analysis.



**Figure 4.26** Pre-Reaction 3.2 % Fe/0.39 % on  $\theta$ -Alumina SEM Micrograph.



**Figure 4.27** Pre-Reaction 8.81 % ZnFe<sub>2</sub>O<sub>4</sub>/0.49 % Fe on  $\theta$ -Alumina SEM Micrograph.

#### 4.2.2 Catalyst Testing Supported Zinc Ferrite on $\theta$ -Alumina.

The supported catalysts tested are detailed in table 3.7 in section 3.6.3, part of which is reproduced below in table 4.8. The test procedures are given in sections 3.6.2 and 3.6.3.

Table 4.8 Catalyst Testing List Supported Zinc Ferrite Catalyst.

Reaction No	Catalyst Code	Bed Vol (cm <sup>3</sup> )	Weight (g)
3	3.2 % Fe/0.39 %Zn/Al <sub>2</sub> O <sub>3</sub>	3	1.9981
4	3.45 % ZF/Al <sub>2</sub> O <sub>3</sub>	3	2.2867
6	8.81 % ZnFe <sub>2</sub> O <sub>4</sub> /0.49 % Fe /Al <sub>2</sub> O <sub>3</sub>	3	2.2698

Figures 4.28 and 4.29 below show the product selectivities and 1-butene conversion obtained when passing 1-butene over 3.45 % zinc ferrite on  $\theta$ -Alumina with a bed volume of 3 cm<sup>3</sup>.

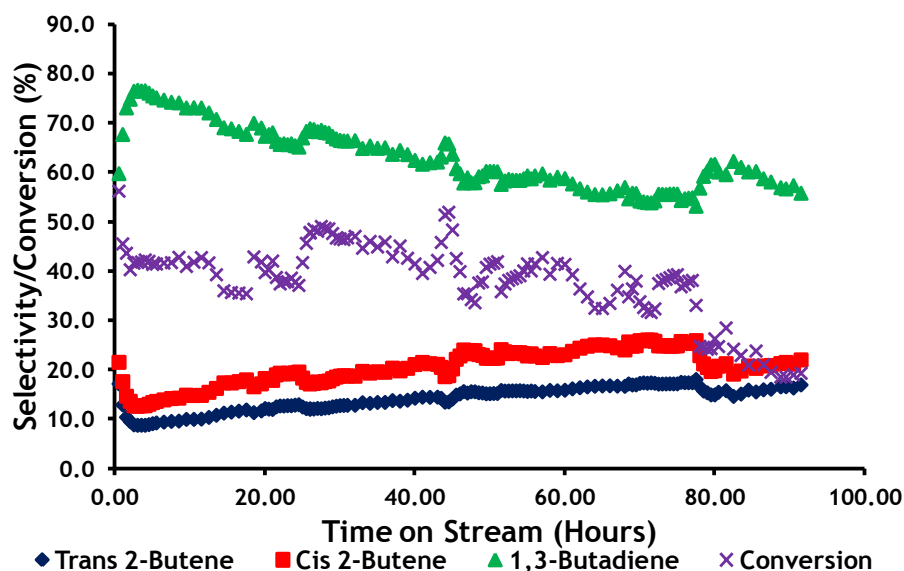


Figure 4.28 Selectivity/Conversion Major Components 3.45 % Zinc Ferrite on  $\theta$ -Alumina.

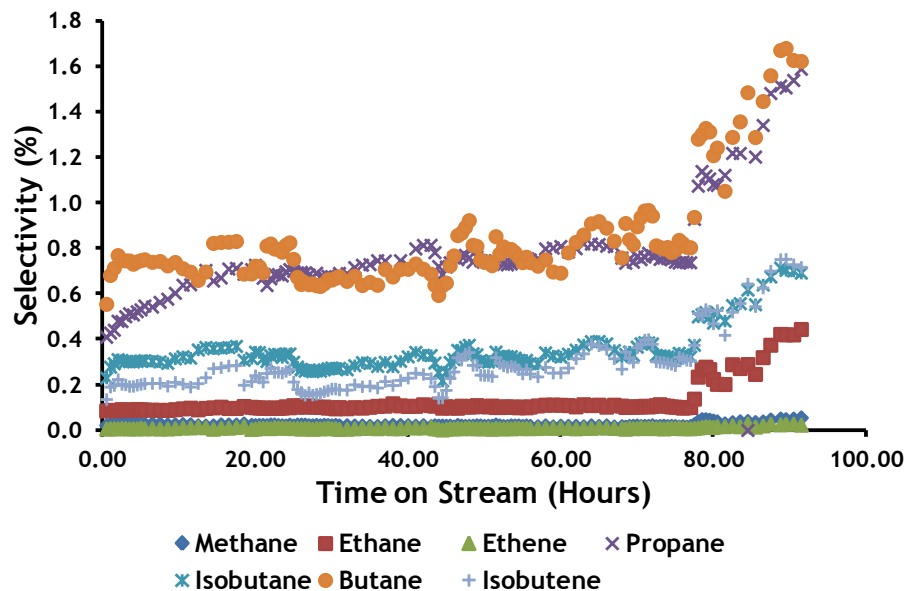


Figure 4.29 Selectivity Minor Components 3.45 % Zinc Ferrite on  $\theta$ -Alumina.

Figures 4.30 and 4.31 below show the product selectivities and 1-butene conversion obtained when passing 1-butene over 3.2 % Fe/0.39 % Zn on  $\theta$ -Alumina with a bed volume of 3 cm<sup>3</sup>.

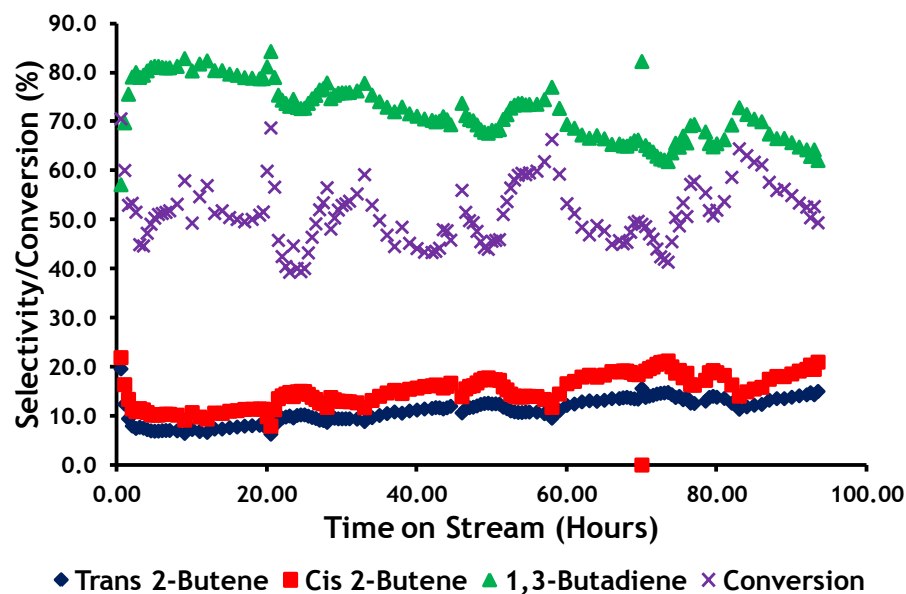


Figure 4.30 Selectivity/Conversion Major Components 3.2 % Fe/0.39 % Zn on  $\theta$ -Alumina.

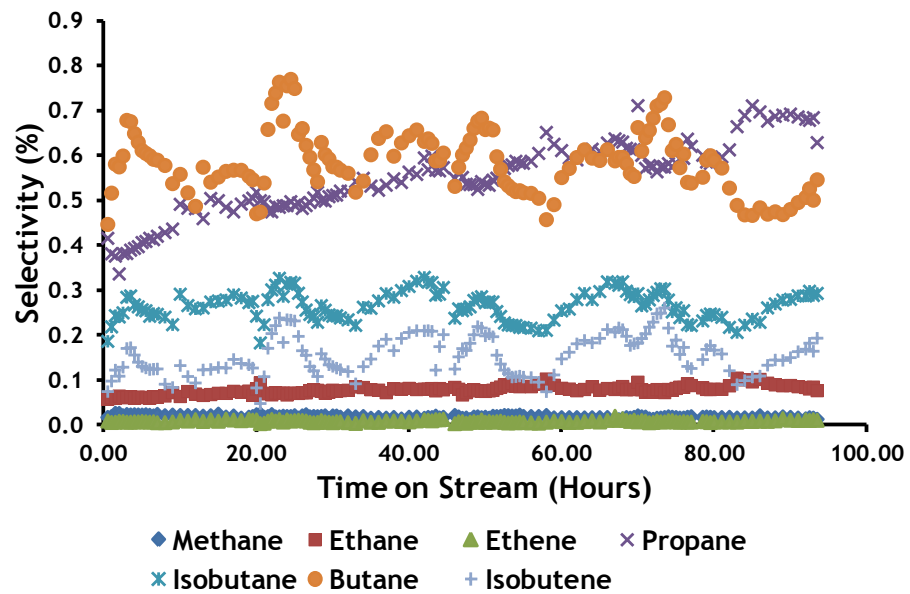


Figure 4.31 Selectivity Minor Components 3.2 % Fe/0.39 % Zn on  $\theta$ -Alumina.

Figures 4.32 and 4.33 below show the product selectivities and 1-butene conversion obtained when passing 1-butene over 8.81 %  $\text{ZnFe}_2\text{O}_4$ /0.49 % Fe on  $\theta$ -Alumina with a bed volume of  $3 \text{ cm}^3$ .

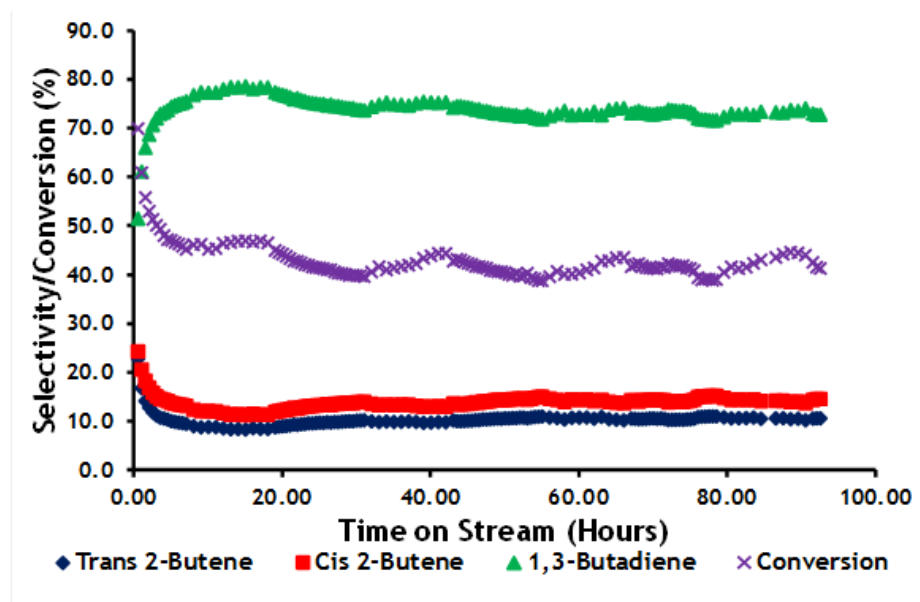


Figure 4.32 Selectivity/Conversion Major Components 8.81 %  $\text{ZnFe}_2\text{O}_4$ /0.49 % Fe on  $\theta$ -Alumina.

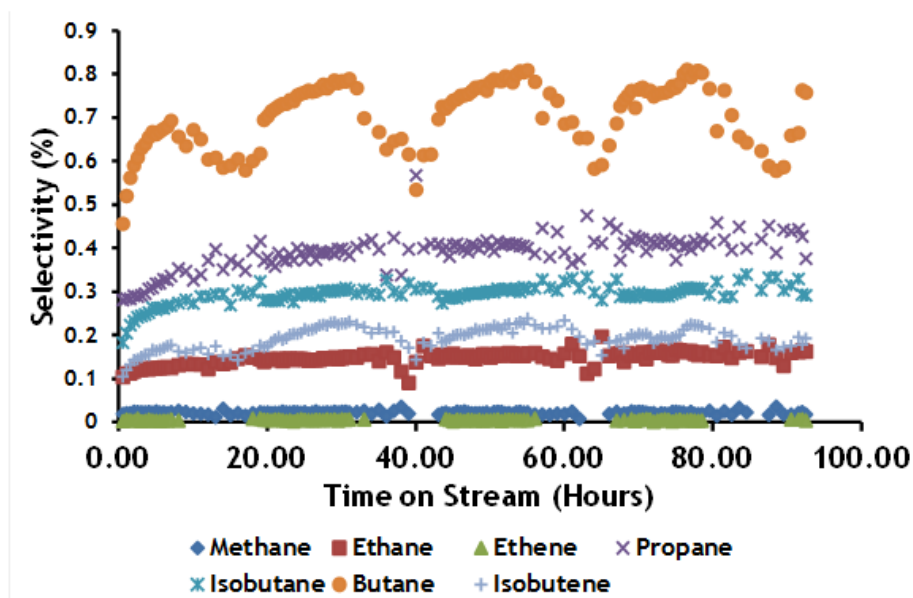


Figure 4.33 Selectivity Minor Components 8.81 % ZnFe<sub>2</sub>O<sub>4</sub>/0.49 % Fe on  $\theta$ -Alumina.

#### 4.2.3 Post Reaction Characterisation Zinc Ferrite on $\theta$ -Alumina.

##### 4.2.3.1 Post Reaction X-Ray Diffraction Analysis Zinc Ferrite on $\theta$ -Alumina.

Ambient temperature X-Ray Diffraction was carried out as described in section 3.5.3.

Figures 4.34 to 4.36 below show the ambient temperature XRD spectra of 3.45 % zinc ferrite  $\theta$ -alumina, 3.2 % Fe/0.39 % Zn on  $\theta$ -alumina and 8.81 % ZnFe<sub>2</sub>O<sub>4</sub>/0.49 % Fe on  $\theta$ -alumina.

Figure 4.34 below shows a typical  $\theta$ -alumina XRD profile with no zinc ferrite, iron oxides or zinc oxide detectable.

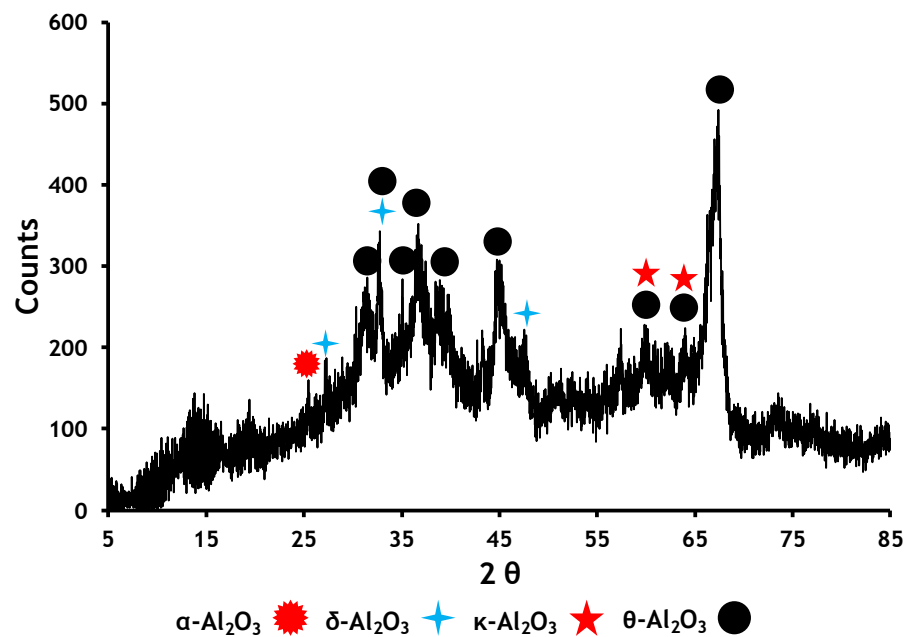


Figure 4.34 Post Reaction Ambient Temperature XRD Spectra of 3.45 % Zinc Ferrite on  $\theta$ -Alumina.

Figure 4.35 below shows a typical  $\theta$ -alumina XRD profile with no zinc ferrite, iron oxides or zinc oxide detectable.

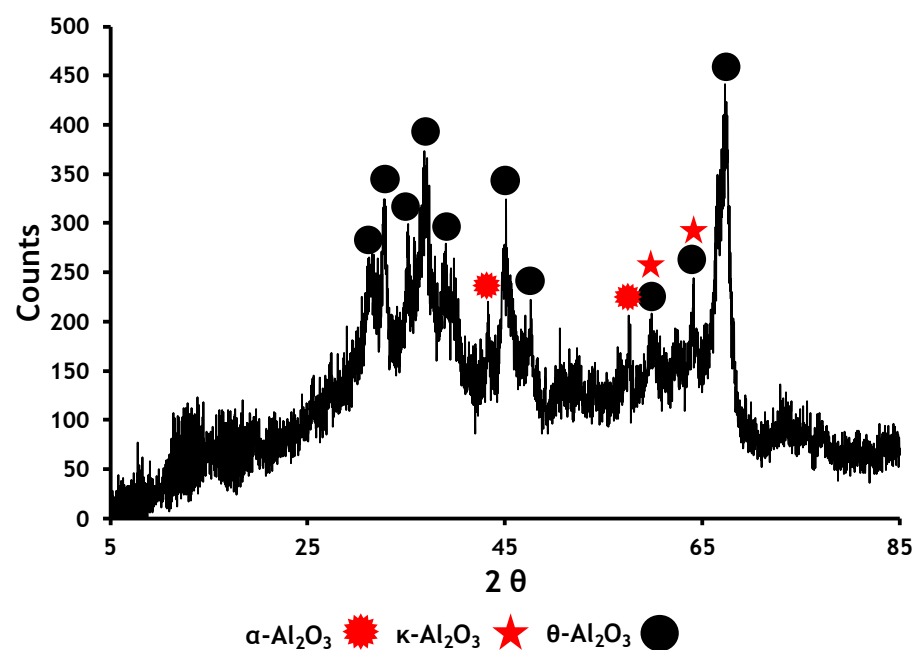
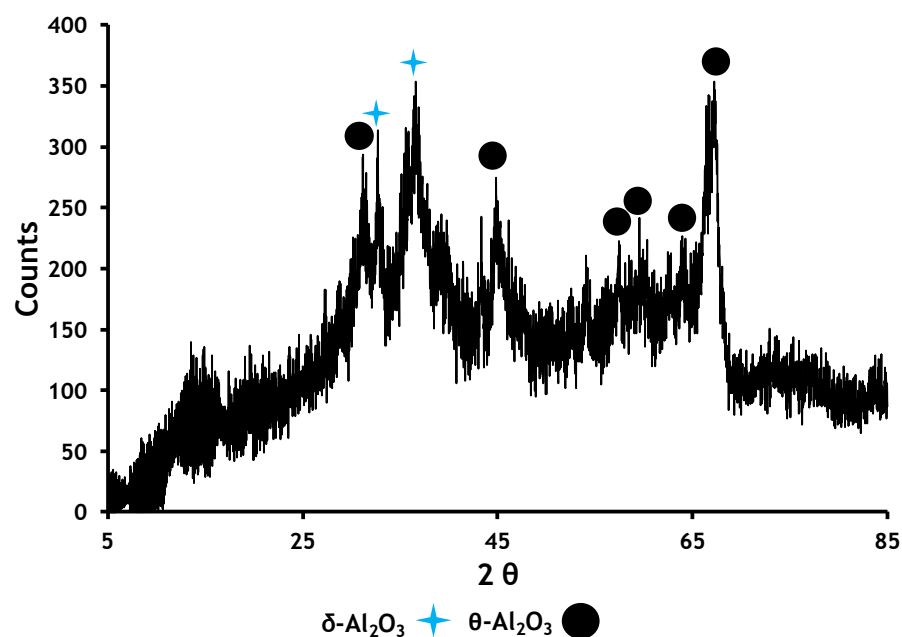


Figure 4.35 Post Reaction Ambient Temperature XRD Spectra of 3.2 % Fe/0.39 % Zn on  $\theta$ -Alumina.

Figure 4.36 below shows a typical  $\theta$ -alumina XRD profile with no zinc ferrite, iron oxides or zinc oxide detectable.



**Figure 4.36** Post Reaction Ambient Temperature XRD Spectra of 8.81 % ZnFe<sub>2</sub>O<sub>4</sub>/0.49 % Fe on  $\theta$ -Alumina.

#### 4.2.3.2 Post Reaction Raman Spectroscopy Analysis Zinc Ferrite on $\theta$ -Alumina.

Figures 4.37 to 4.39 below show the post reaction ambient temperature Raman spectra of 3.45 % zinc ferrite on  $\theta$ -alumina, 3.2 % Fe/0.39 % Zn  $\theta$ -on alumina and 8.81 % ZnFe<sub>2</sub>O<sub>4</sub>/0.49 % Fe on  $\theta$ -alumina. The Raman bands are tabulated in table 4.9 below to allow comparison.

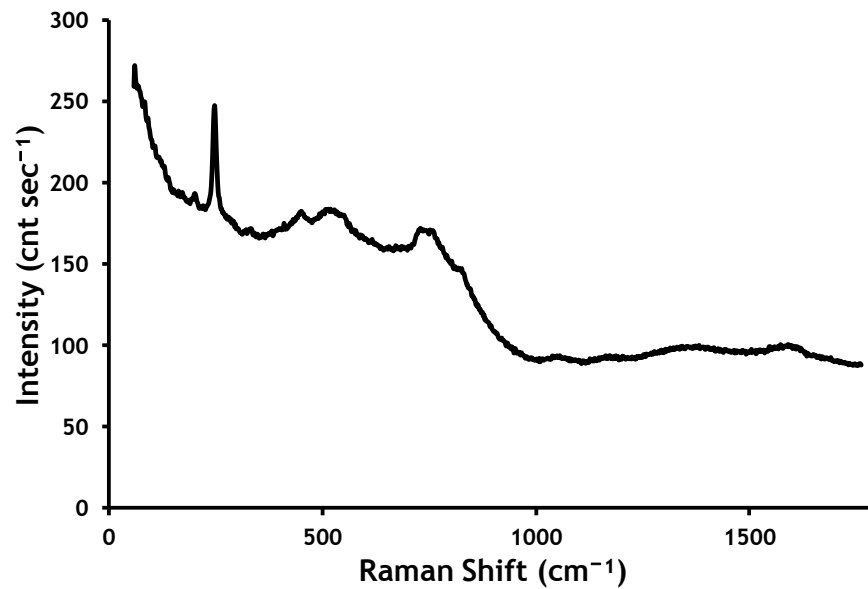


Figure 4.37 Post Reaction Ambient Temperature Raman Spectra of 3.45 % Zinc Ferrite on  $\theta$ -Alumina.

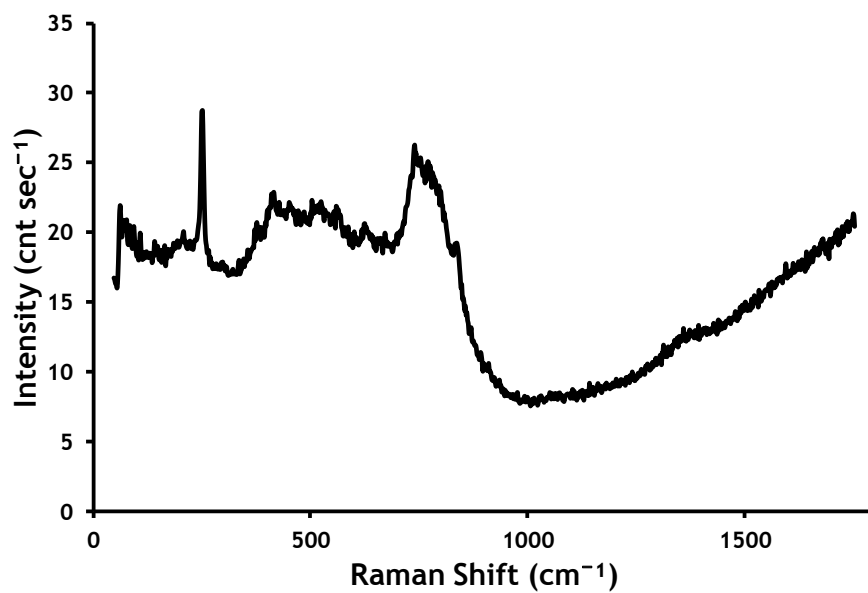
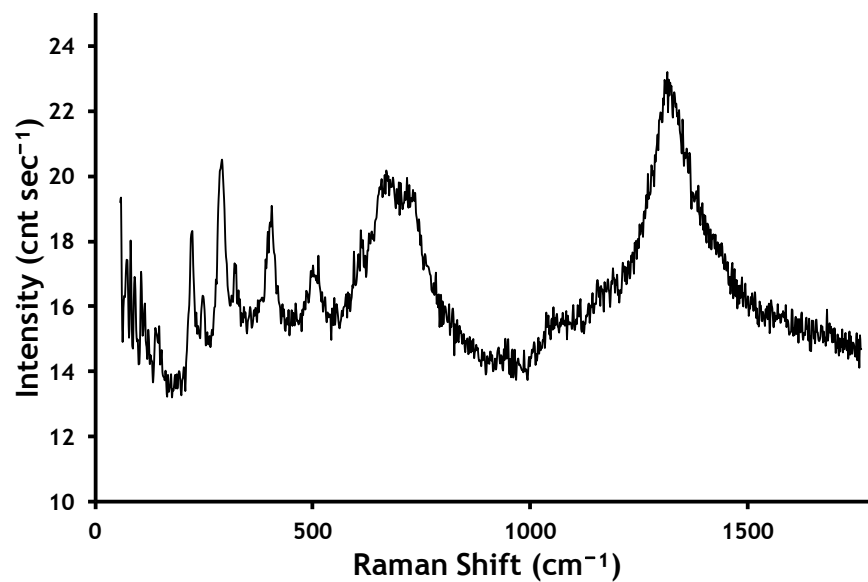


Figure 4.38 Post Reaction Ambient Temperature Raman Spectra of 3.2 % Fe/0.39 % Zn on  $\theta$ -Alumina.



**Figure 4.39** Post Reaction Ambient Temperature Raman Spectra of 8.81 % ZnFe<sub>2</sub>O<sub>4</sub>/0.49 % Fe on  $\theta$ -Alumina.

Table 4.9 Comparison of Post Reaction Raman Shift Bands of Zinc Ferrites on  $\theta$ -Alumina to Literature.

Raman Shift Bands ( $\text{cm}^{-1}$ )															
	$\theta$ -Alumina[40]														$\text{Fe}_2\text{O}_3$ [43]
	244	289	317	327	401	442	453	527	562	619	687	737	772	840	
3.45 % $\text{ZnFe}_2\text{O}_4$ on $\text{Al}_2\text{O}_3$	247			331			450	519			671	729		821	
3.2 % Fe/0.39 % Zn on $\text{Al}_2\text{O}_3$	251	297			415			503	563	624	670	740	773	840	
8.81 % $\text{ZnFe}_2\text{O}_4$ / 0.49 % Fe on $\text{Al}_2\text{O}_3$	248	292		321	406			500	554	613	699				1316

#### 4.2.3.3 Post Reaction Surface Area Measurements Zinc Ferrite on $\theta$ -Alumina.

BET analysis was carried out as described in section 2.5.1. Table 4.10 below shows surface area, pore diameter and cumulative pore volume for  $\theta$ -alumina supported catalysts 3.45 %  $\text{ZnFe}_2\text{O}_4$  on alumina, 8.81 %  $\text{ZnFe}_2\text{O}_4/0.49\%$  Fe on alumina and 3.2 % Fe/0.39 % Zn on alumina.

**Table 4.10 Post Reaction Surface Area Measurements Zinc Ferrite on  $\theta$ -Alumina.**

Catalyst	Surface Area ( $\text{m}^2\text{g}^{-1}$ )	Pore Diameter (nm)	Cumulative Pore Volume ( $\text{cm}^3\text{g}^{-1}$ )
3.45 % $\text{ZnFe}_2\text{O}_4$ on Alumina	89	22	0.4765
3.2 % Fe/0.39 % Zn on Alumina	100	19	0.4913
8.81 % $\text{ZnFe}_2\text{O}_4/0.49\%$ Fe on Alumina	78	19	0.3697

Comparison of pre and post reaction surface areas of the  $\theta$ -alumina supported catalysts shows no significant change.

#### 4.2.3.4 Post Reaction Thermo-gravimetric Analysis-Differential Scanning Calorimetry Analysis Zinc Ferrite on $\theta$ -Alumina.

Figure 4.40 below shows a total weight loss of 6 % from the post reaction 3.45 % zinc ferrite on  $\theta$ -alumina over the temperature range 295 K to 890 K.

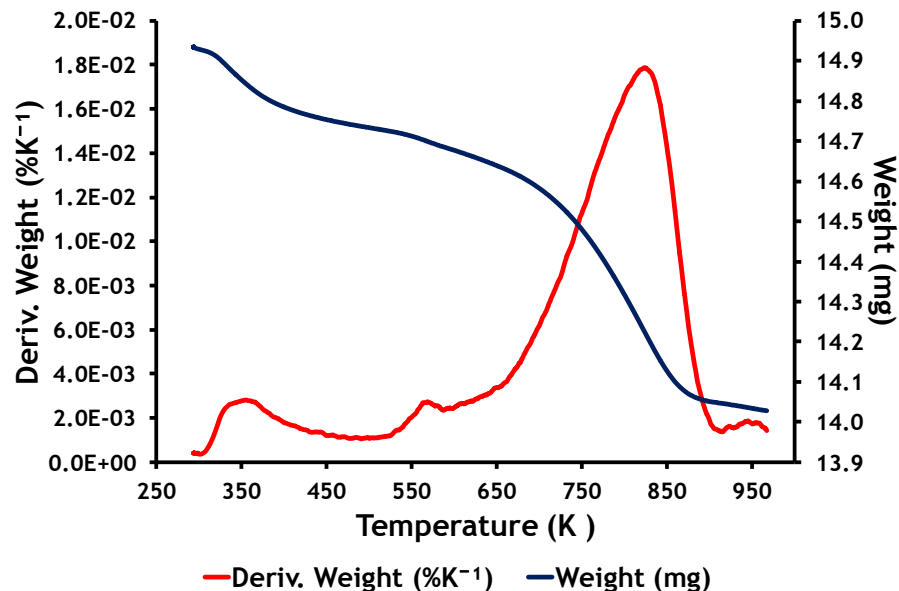


Figure 4.40 Post Reaction 3.45 % Zinc Ferrite on  $\theta$ -Alumina TGA/DSC Weight Loss.

Figure 4.41 below shows the evolution of carbon dioxide at 775 K, relative to the derivative weight.

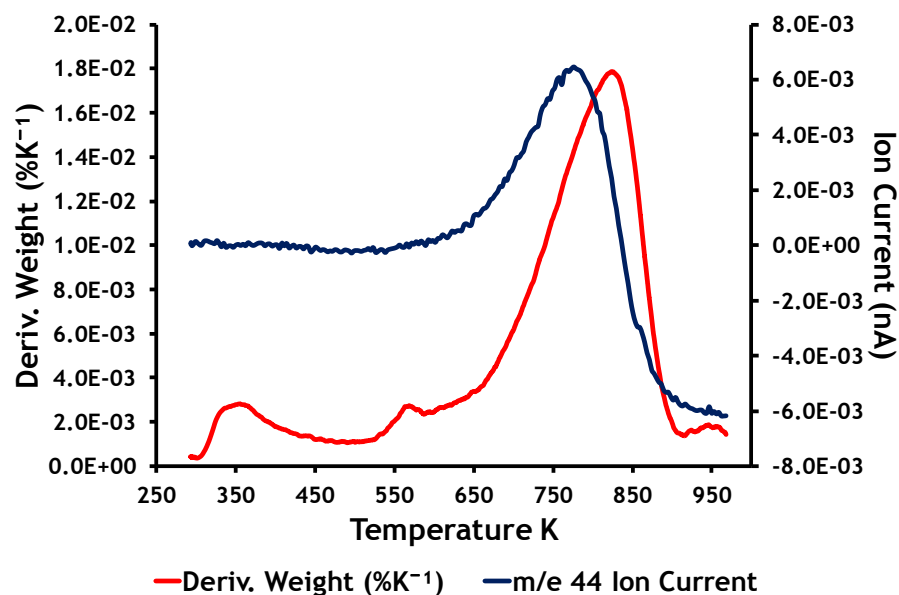


Figure 4.41 Post Reaction TGA/DSC Mass Spectrometer Profile from 3.45 % Zinc Ferrite on  $\theta$ -Alumina m/e 44.

Figure 4.42 below shows a weight loss of 11 % from the post reaction 3.2 % Fe/0.39 % Zn on  $\theta$ -alumina over the temperature range 295 K to 895 K.

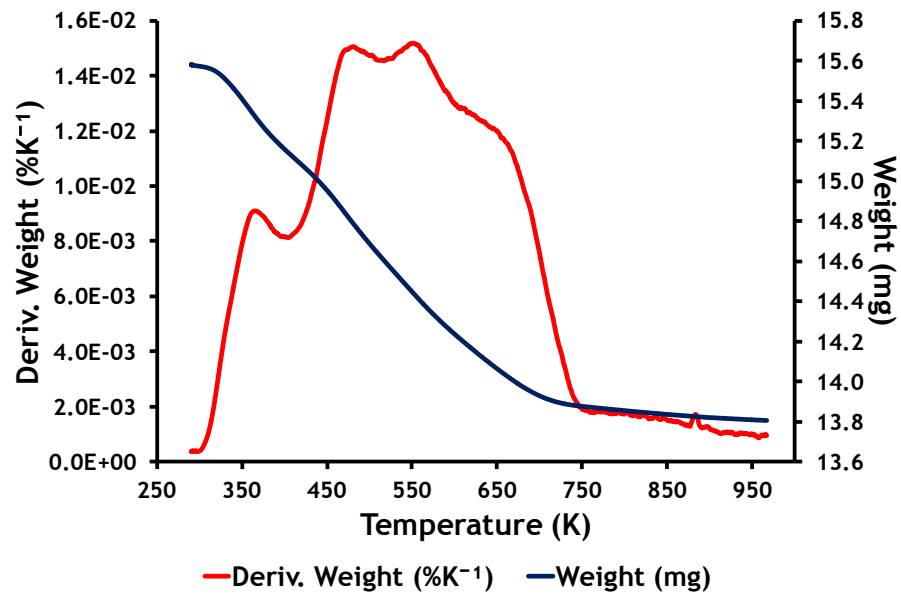


Figure 4.42 Post Reaction 3.2 % Fe/0.39 % Zn on  $\theta$ -Alumina TGA/DSC Weight Loss.

Figure 4.43 below shows the evolution of nitrous oxide over the temperature range 560 K to 690 K, relative to the derivative weight.

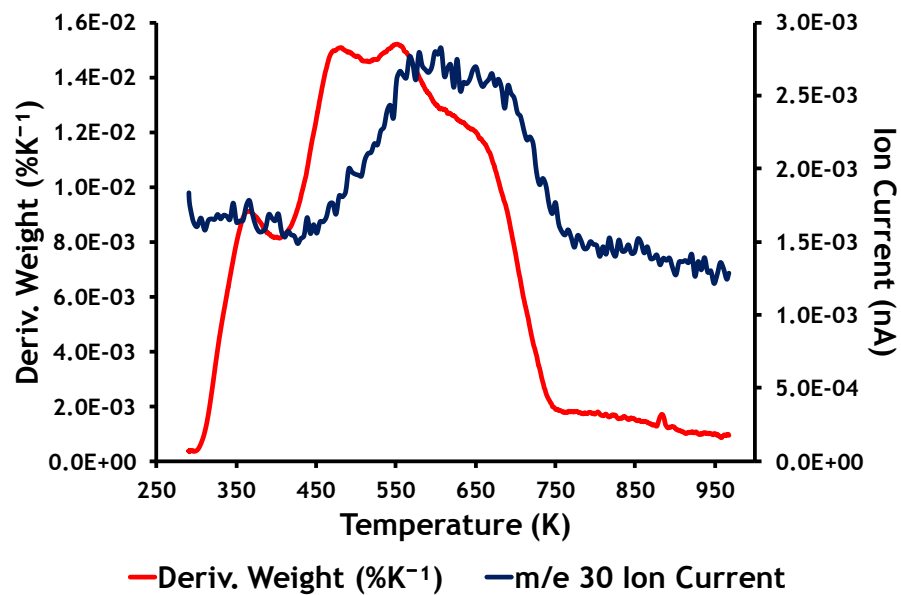


Figure 4.43 Post Reaction TGA/DSC Mass Spectrometer Profile from 3.2 % Fe/0.39 % Zn on  $\theta$ -Alumina m/e 30.

Figure 4.44 below shows a weight loss of 2 % from the post reaction 8.81 % ZnFe<sub>2</sub>O<sub>4</sub>/0.49 % Fe on  $\theta$ -alumina over the temperature range 295 K to 890 K.

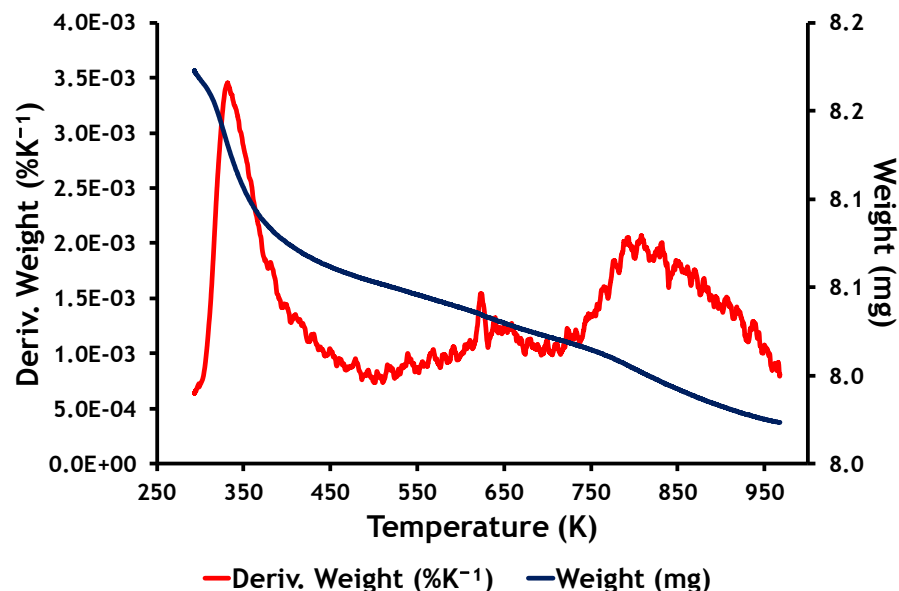


Figure 4.44 Post Reaction 8.81 % ZnFe<sub>2</sub>O<sub>4</sub>/0.49 % Fe on  $\theta$ -Alumina TGA and Derivative Weight.

### 4.3 Vanadia Supported on $\theta$ -Alumina.

#### 4.3.1 Pre-Reaction Characterisation Vanadia on $\theta$ -Alumina.

A total of two vanadia catalysts supported on  $\theta$ -alumina were prepared as outlined in the experimental section 3.3.

##### 4.3.1.1 Pre-Reaction AA Analysis Vanadia on $\theta$ -Alumina.

Table 4.11 below shows the true versus the calculated vanadia loading.

Table 4.11 Pre- Reaction Atomic Adsorption Results Vanadia on  $\theta$ -Alumina.

Calculated Vanadia Loading	True Vanadia Loading
0.5 % VO <sub>x</sub> on Alumina	0.5 % VO <sub>x</sub> on Alumina
3.5 % VO <sub>x</sub> on Alumina	3.3 % VO <sub>x</sub> on Alumina

#### 4.3.1.2 Pre-Reaction X-Ray Diffraction Analysis Vanadia on $\theta$ -Alumina.

Hot stage X-Ray Diffraction was carried out as described in section 3.5.3.

XRD profiles were recorded at 303 K, 373 K, 473 K, 573 K, 673 K, 773 K and 873 K. Examination of the profiles showed that there was no difference between the profiles.

Figure 4.45 below shows the temperature programmed XRD profile of 0.5 % vanadia on  $\theta$ -alumina at 303 K, 573 K and 873 K, which shows the presence of  $\delta$ -alumina and  $\theta$ -alumina.

Ambient temperature X-Ray Diffraction was carried out as described in section 3.5.3.

Figure 4.46 below shows the ambient temperature XRD profile of 3.3 % vanadia on  $\theta$ -alumina at ambient temperature, which shows the presence of  $\delta$ -alumina and  $\theta$ -alumina.

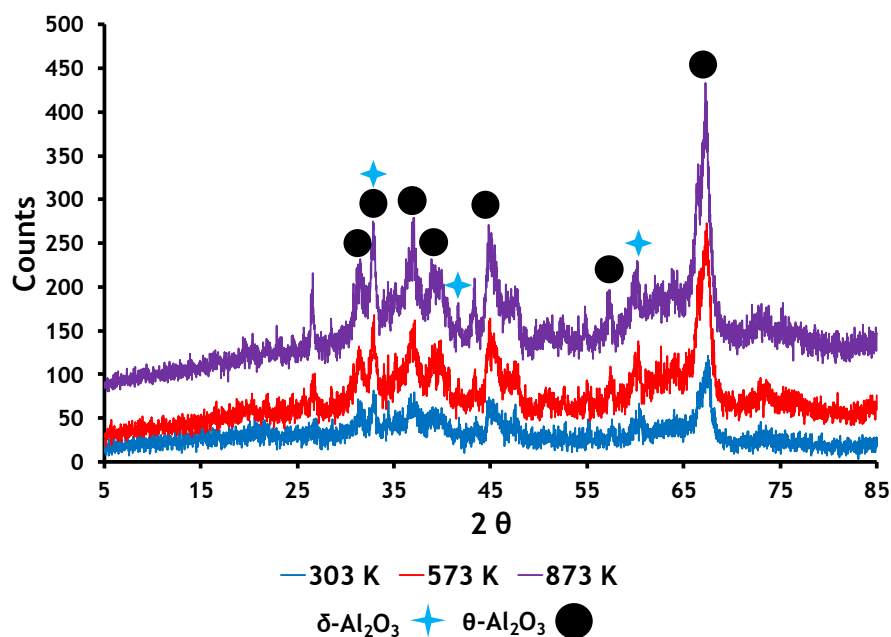
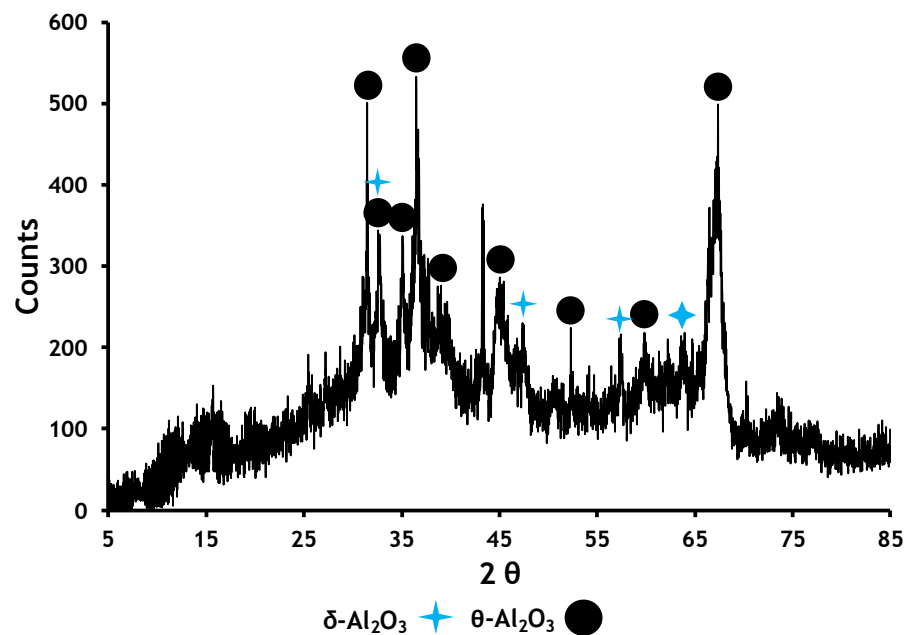


Figure 4.45 Pre-Reaction Temperature Programmed XRD Spectra of 0.5 % Vanadia on  $\theta$ -Alumina at 303 K, 573 K and 873 K.



**Figure 4.46** Pre-Reaction Ambient Temperature XRD Spectra of 3.3 % Vanadia on  $\theta$ -Alumina.

#### 4.3.1.3 Pre-Reaction Raman Spectroscopy Analysis Vanadia.

Ambient temperature and hot stage Raman spectroscopy were carried out as described in section 3.5.4.

Raman profiles of 0.5 % vanadia on  $\theta$ -alumina were recorded at 303 K, 373 K, 473 K, 573 K, 673 K, 773 K and 873 K

Figure 4.47 below shows the pre-reaction temperature programmed Raman spectra of 0.5 % vanadia on  $\theta$ -alumina and figure 4.48 below shows the ambient temperature Raman spectra of 3.3 % vanadia on  $\theta$ -alumina. The Raman bands are tabulated in table 4.12 below to allow comparison. Examination of the pre-reaction temperature profiles showed sharpening of the bands, the loss the band at  $1423\text{ cm}^{-1}$  and the shift of the band at  $1054\text{ cm}^{-1}$  to  $1016\text{ cm}^{-1}$ .

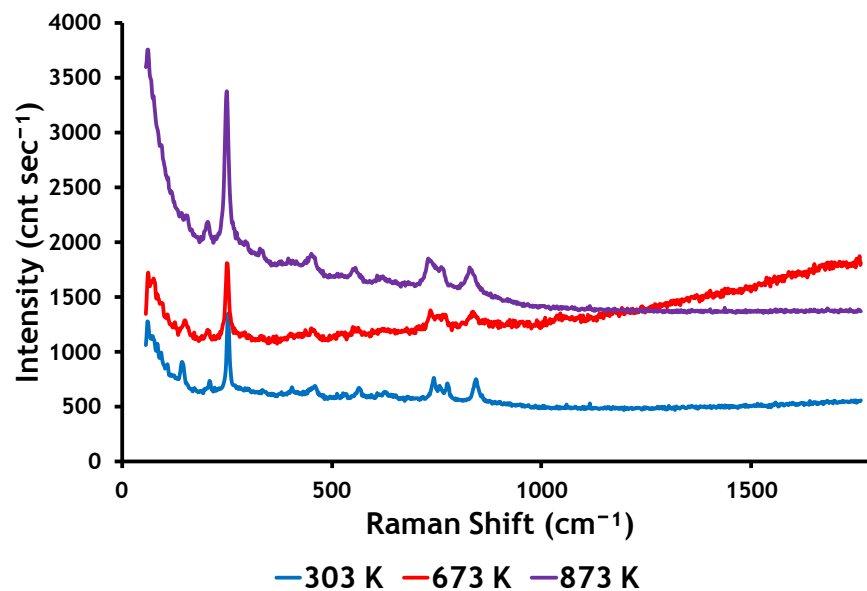


Figure 4.47 Pre-Reaction Temperature Programmed Raman Spectra of 0.5 % Vanadia on  $\theta$ -Alumina at 303 K, 373 K and 873 K.

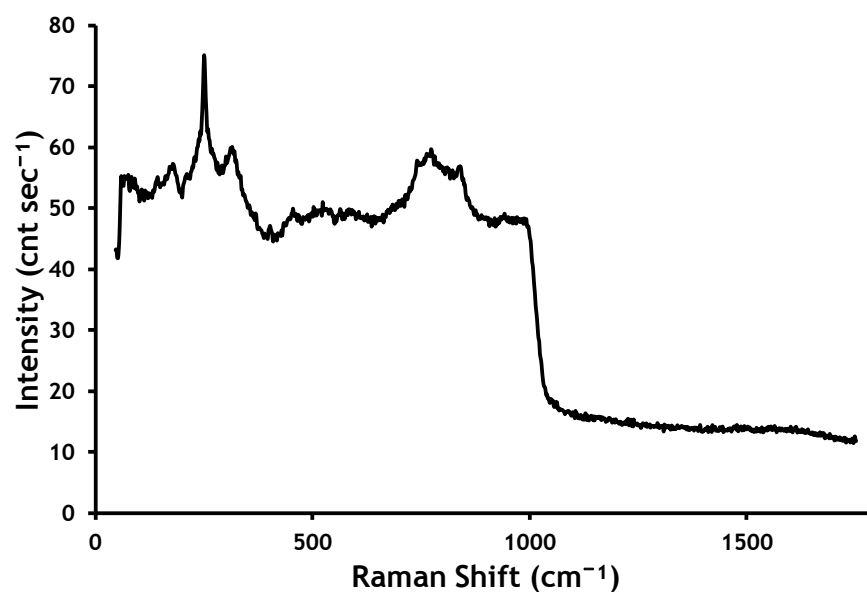


Figure 4.48 Pre-Reaction Ambient Temperature Raman Spectra of 3.3 % Vanadia on  $\theta$ -Alumina.

Table 4.12 Comparison of Pre-Reaction Raman Shift Bands Vanadia on  $\theta$ -Alumina to Literature.

Raman Shift Bands ( $\text{cm}^{-1}$ )																
	$\theta$ -Alumina[40]															$\text{V}_2\text{O}_5$ [40]
Literature	244	289	317	327	401	442	453	527	562	619	687	737		772	840	994
0.5 % Vanadia on $\text{Al}_2\text{O}_3$	251	293		330			450		557	609	680	736	764		834	1019
3.3 % Vanadia on $\text{Al}_2\text{O}_3$	251		316		406		456	524	588			740		774	841	

#### 4.3.1.4 Pre-Reaction Surface Area Measurements Vanadia on $\theta$ -Alumina.

BET analysis was carried out as described in section 2.5.1. Table 4.13 below shows the supported vanadia results.

Table 4.13 below shows surface area, pore diameter and cumulative pore volume for  $\theta$ -alumina supported vanadia 0.5 % VOx on alumina and 3.3 % VOx on alumina.

Table 4.13 Pre-Reaction Surface Area Results Vanadia on  $\theta$ -Alumina.

Catalyst	Surface Area ( $\text{m}^2\text{g}^{-1}$ )	Pore Diameter (nm)	Cumulative Pore Volume ( $\text{cm}^3\text{g}^{-1}$ )
0.5 % VOx on Alumina	91	20	0.4564
3.3 % VOx on Alumina	68	21	0.3517

#### 4.3.1.5 Pre-Reaction Thermo-gravimetric Analysis-Differential Scanning Calorimetry Analysis Vanadia on $\theta$ -Alumina

Thermo-gravimetric analysis/differential scanning calorimetry was carried out as described in section 3.5.5.

Figure 4.49 below shows a total weight loss of 5 % from pre-reaction 0.5 % vanadia on  $\theta$ -alumina over the temperature range 295 K to 870 K.

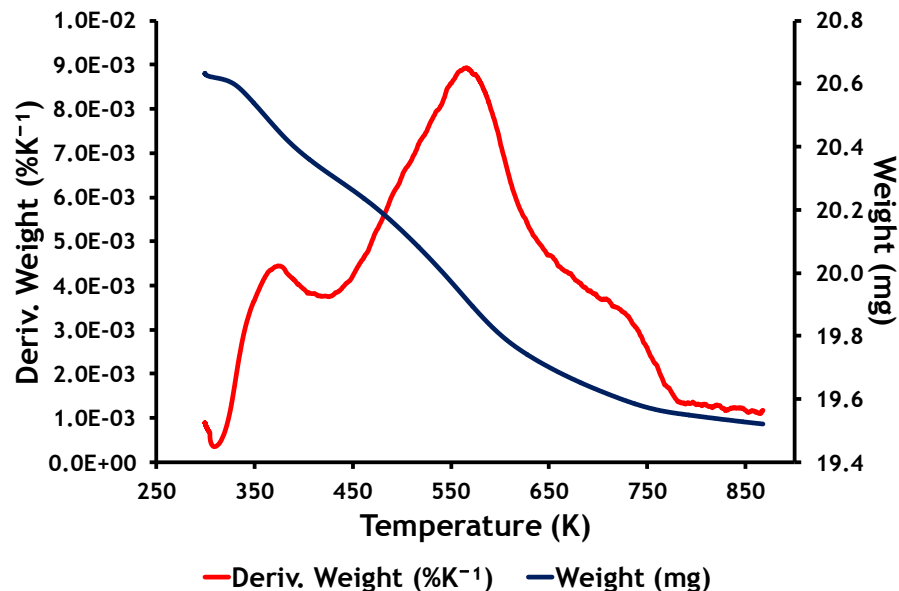


Figure 4.49 Pre-Reaction 0.5 % Vanadia on  $\theta$ -Alumina TGA and Derivative Weight.

Figure 4.50 below shows the evolution of carbon dioxide at 580 K, relative to the derivative weight.

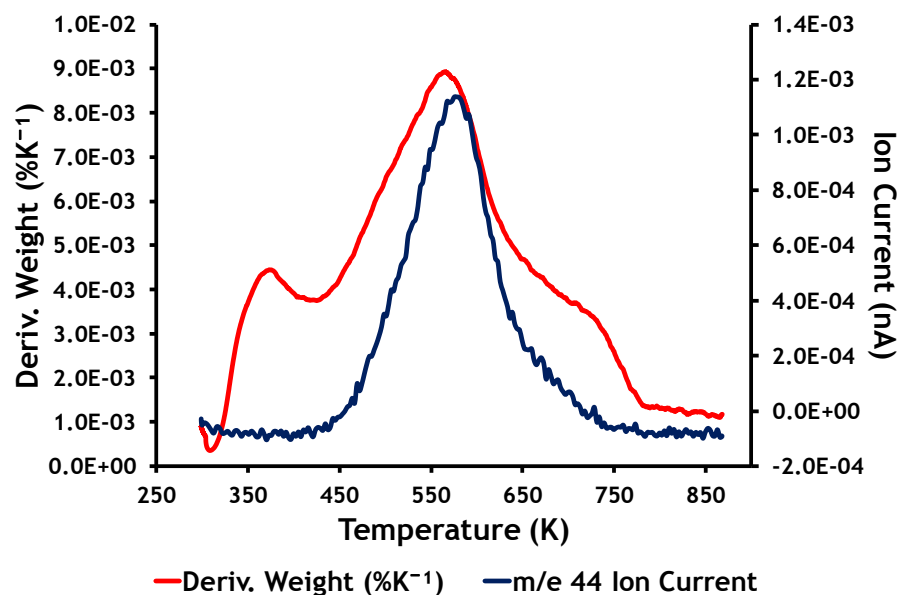


Figure 4.50 Pre-Reaction TGA/DSC Mass Spectrometer Profile from 0.5 % Vanadia on  $\theta$ -Alumina m/e 44.

Figure 4.51 below shows the evolution of nitric oxide at 735 K, relative to the derivative weight.

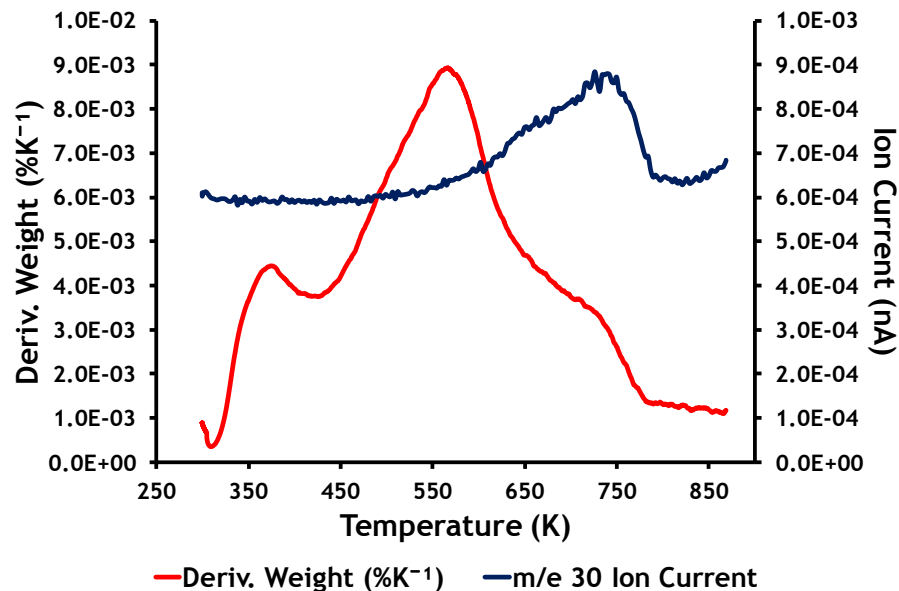


Figure 4.51 Pre-Reaction TGA/DSC Mass Spectrometer Profile from 0.5 % Vanadia on  $\theta$ -Alumina m/e 30.

Figure 4.52 below shows a total weight loss of 11 % from the pre-reaction 3.3 % vanadia on  $\theta$ -alumina over the temperature range 295 K to 870 K.

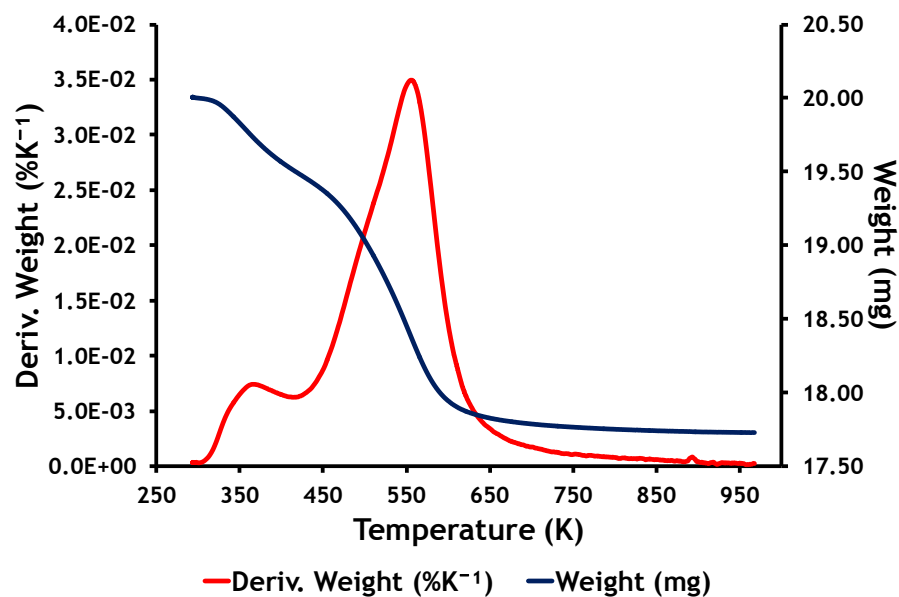
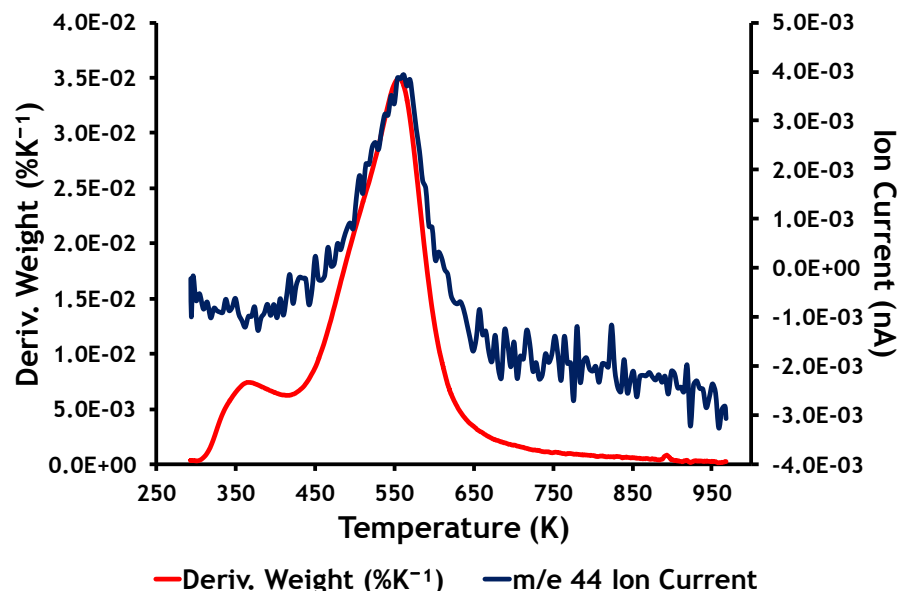


Figure 4.52 Pre-Reaction 3.3 % Vanadia on  $\theta$ -Alumina TGA and Derivative Weight.

Figure 4.53 below shows the evolution of carbon dioxide at 560 K, relative to the derivative weight.



**Figure 4.53** Pre-Reaction TGA/DSC Mass Spectrometer Profile from 3.3 % Vanadia on  $\theta$ -Alumina m/e 44.

#### 4.3.2 Catalyst Testing Supported Vanadia on $\theta$ -Alumina.

The supported catalysts tested are detailed in table 3.7 in section 3.6.3 part of which is reproduced in table 4.14 below and the test procedures are given in sections 3.6.2 and 3.6.3.

**Table 4.14** Catalyst Testing List Supported Vanadia Catalyst on  $\theta$ -Alumina.

Reaction No	Catalyst Code	Bed Vol (cm <sup>3</sup> )	Weight (g)
9	0.5 % VO <sub>x</sub> /Al <sub>2</sub> O <sub>3</sub>	3	1.9218
14	3.3 % VO <sub>x</sub> /Al <sub>2</sub> O <sub>3</sub>	3	2.0732

Figures 4.54 and 4.55 below show the product selectivities and 1-butene conversion obtained when passing 1-butene over 0.5 % vanadia on  $\theta$ -alumina with a bed volume of 3 cm<sup>3</sup>.

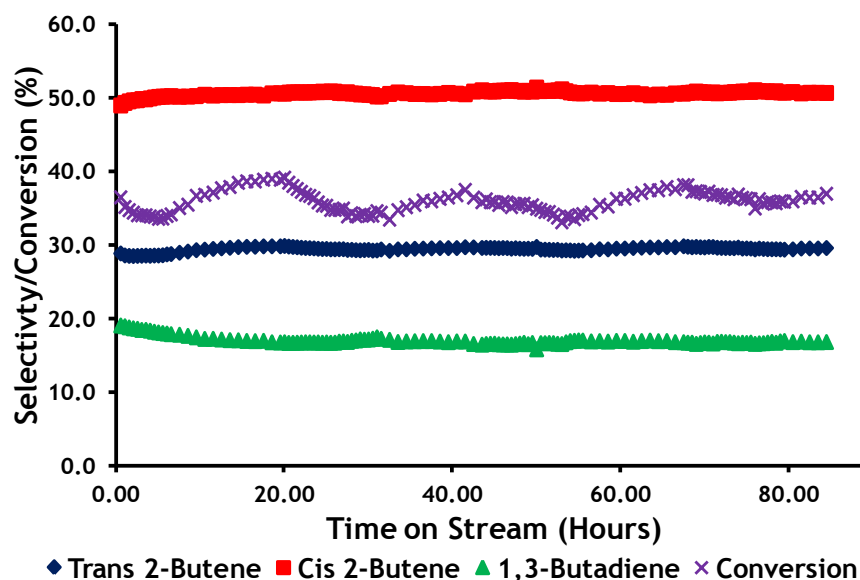


Figure 4.54 Selectivity/Conversion Major Components 0.5 % Vanadia on  $\theta$ -Alumina.

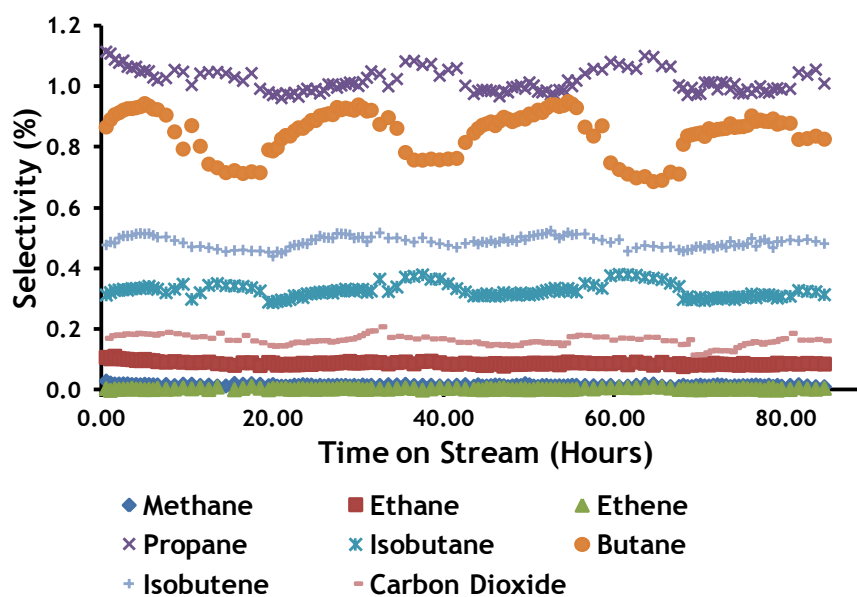


Figure 4.55 Selectivity Minor Components 0.5 % Vanadia on  $\theta$ -Alumina.

Figures 4.56 and 4.57 below show the product selectivities and 1-butene conversion obtained when passing 1-butene over 3.3 % vanadia on  $\theta$ -alumina with a bed volume of 3 cm<sup>3</sup>.

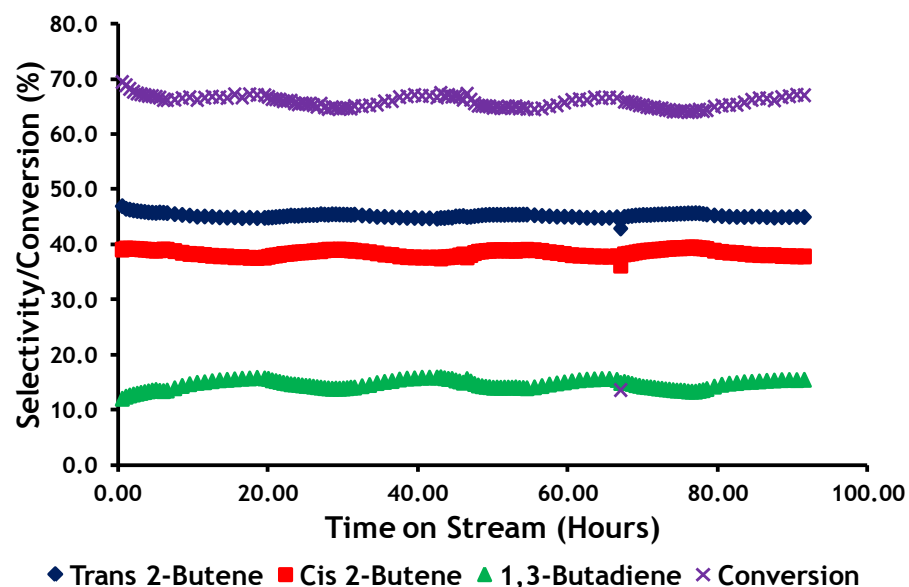


Figure 4.56 Selectivity/Conversion Major Components 3.3 % Vanadia on  $\theta$ -Alumina.

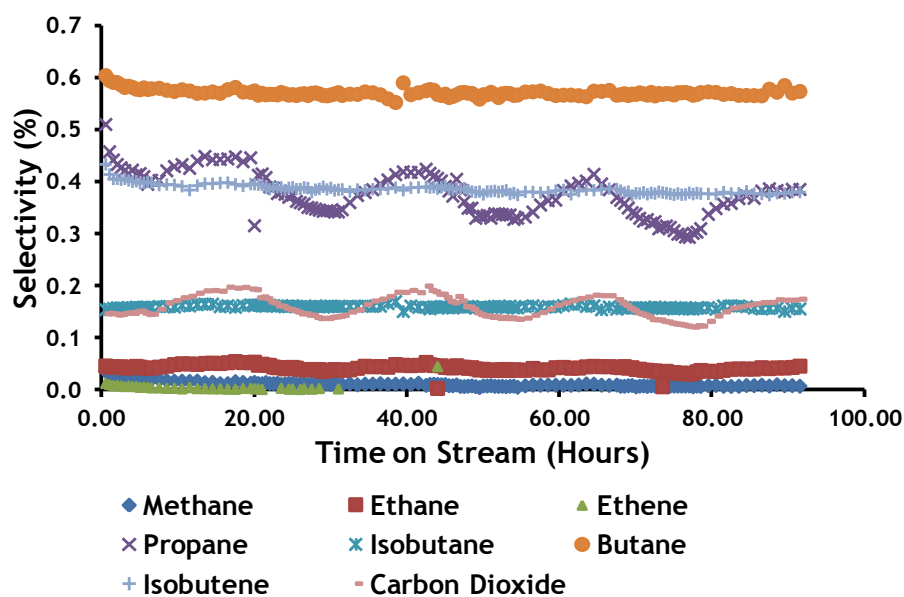


Figure 4.57 Selectivity Minor Components 3.3 % Vanadia on  $\theta$ -Alumina.

### 4.3.3 Post Reaction Characterisation Vanadia on $\theta$ -Alumina.

#### 4.3.3.1 Post Reaction X-Ray Diffraction Analysis of Vanadia $\theta$ -Alumina.

Ambient temperature X-Ray Diffraction was carried out as described in section 3.5.3.

Figure 4.58 below shows the ambient temperature XRD spectra of 0.5 % vanadia on  $\theta$ -alumina, which shows the presence of  $\delta$ -alumina,  $\kappa$ -alumina and  $\theta$ -alumina.

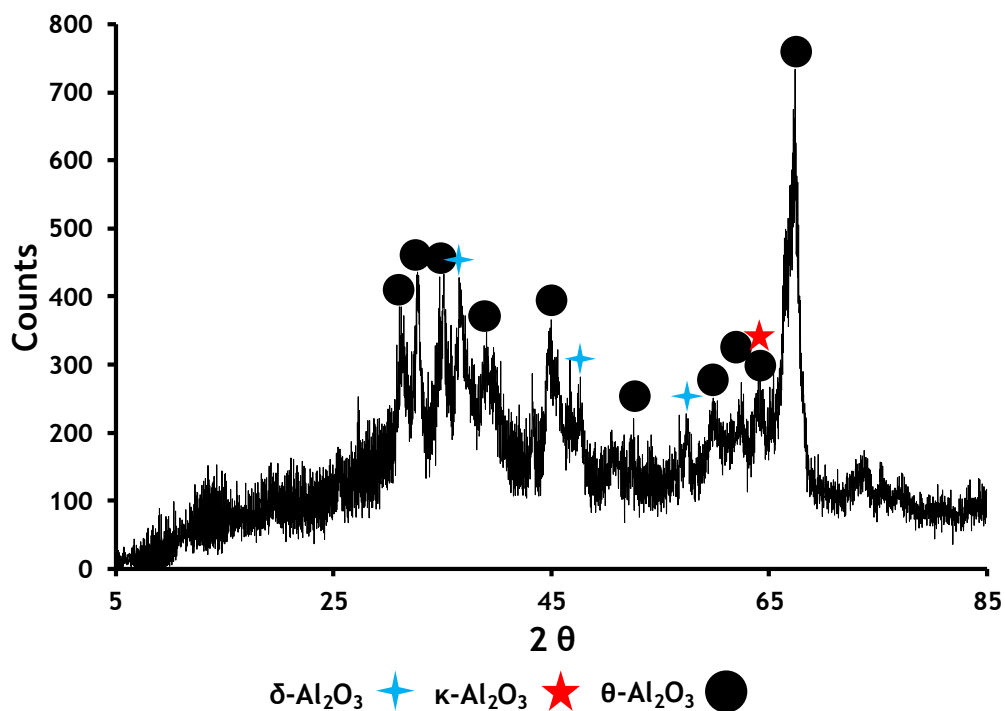


Figure 4.58 Post Reaction Ambient Temperature XRD Spectra of 0.5 % Vanadia on  $\theta$ -Alumina.

Figure 4.59 below shows the ambient temperature XRD spectra of 3.3 % vanadia on  $\theta$ -alumina, which shows the presence of delta, kappa, theta alumina;  $V_3O_7$ ,  $V_5O_9$  and  $V_5O_9$

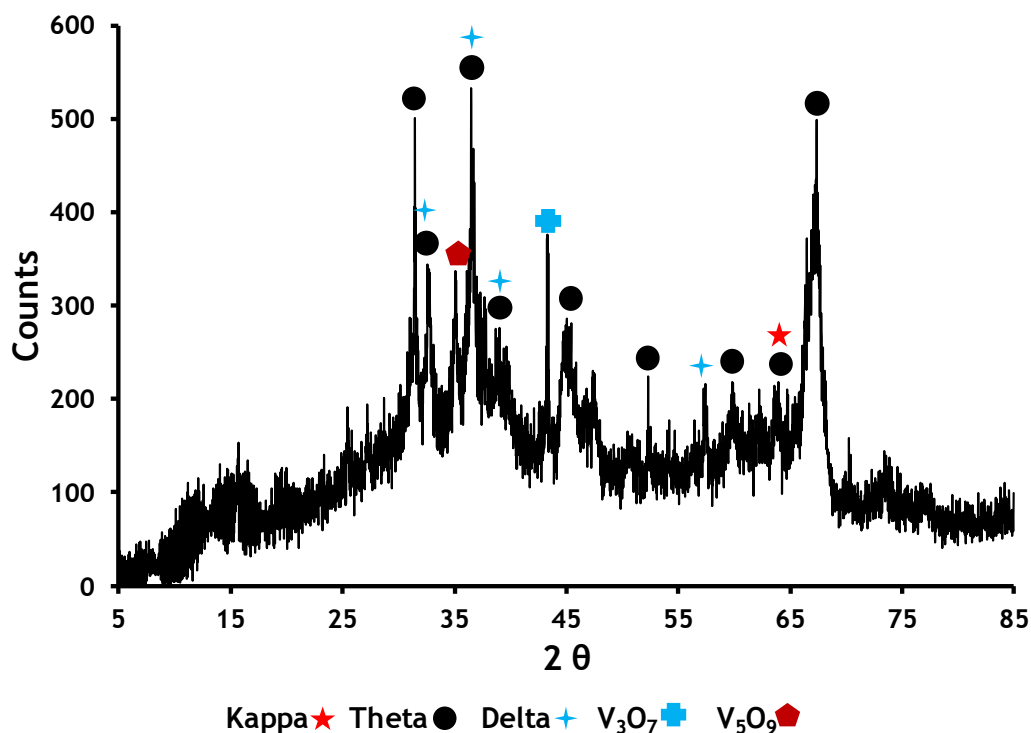


Figure 4.59 Post Reaction Ambient Temperature XRD Spectra of 3.3 % Vanadia on  $\theta$ -Alumina.

#### 4.3.3.2 Post Reaction Raman Spectroscopy Analysis Vanadia on $\theta$ -Alumina.

No post reaction Raman spectra for either 0.5 % or 3.3 % Vanadia on  $\theta$ -Alumina was obtained due to excessive fluorescence.

#### 4.3.3.3 Post Reaction Surface Area Measurements Vanadia on $\theta$ -Alumina.

Table 4.15 below shows surface area, pore diameter and cumulative pore volume for  $\theta$ -alumina supported vanadia 0.5 % VO<sub>x</sub> on alumina and 3.3 % VO<sub>x</sub> on alumina.

**Table 4.15 Post Reaction Surface Area Measurements Vanadia on  $\theta$ -Alumina.**

<b>Catalyst</b>	<b>Surface Area (<math>\text{m}^2\text{g}^{-1}</math>)</b>	<b>Pore Diameter (nm)</b>	<b>Cumulative Pore Volume (<math>\text{cm}^3\text{g}^{-1}</math>)</b>
<b>0.5 % VO<sub>x</sub> on Alumina</b>	97	19	0.4729
<b>3.3 % VO<sub>x</sub> on Alumina</b>	68	21	0.3517

Comparison of pre and post reaction surface areas of the supported vanadia on  $\theta$ -alumina catalysts shows no significant change.

#### **4.3.3.4 Post Reaction Thermo-gravimetric Analysis-Differential Scanning Calorimetry Analysis Vanadia on $\theta$ -Alumina.**

Thermo-gravimetric analysis/differential scanning calorimetry was carried out as described in section 3.5.2.

No exothermic or endothermic events were seen on the DSC measurement. The weight loss shown below is likely due to desorption of physisorbed water at 350 K and to carbon burn off at 750 K.

Figure 4.60 below shows a total weight loss of 3 % from the post reaction 0.5 % vanadia on  $\theta$ -alumina over the temperature range 290 K to 970 K.

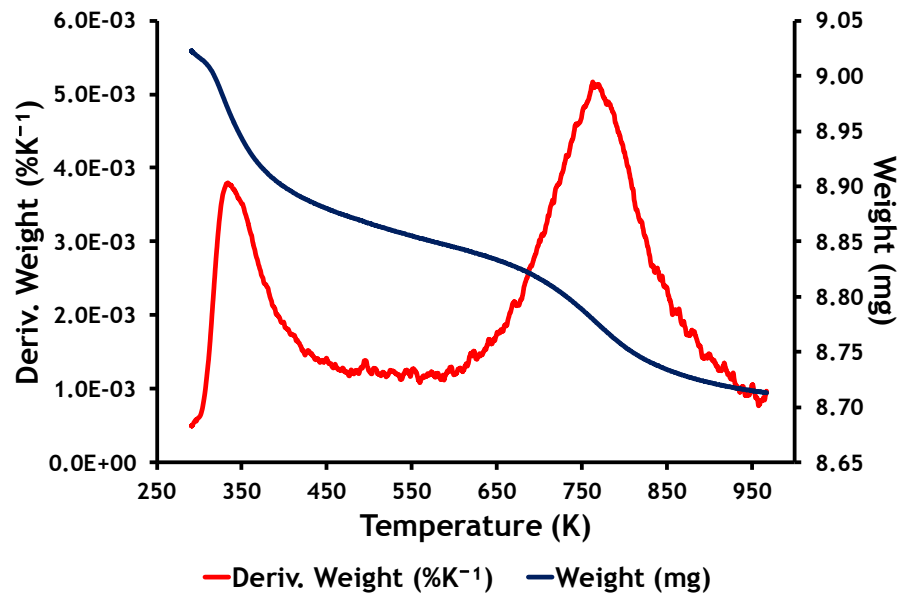


Figure 4.60 Post Reaction 0.5 % Vanadia on  $\theta$ -Alumina TGA and Derivative Weight.

Figure 4.61 below shows a total weight loss of 3 % from the post reaction 3.3 % vanadia on  $\theta$ -alumina over the temperature range 290 K to 970 K.

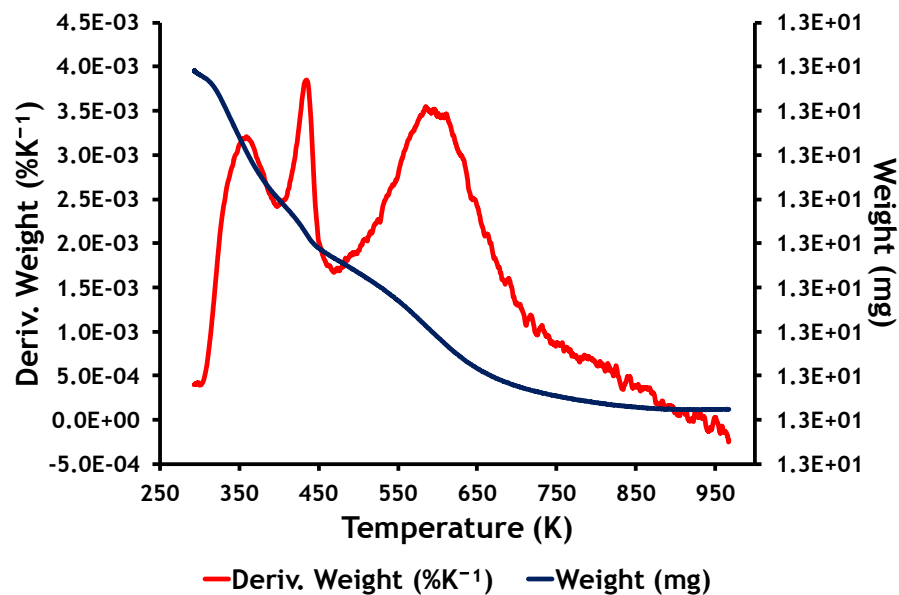


Figure 4.61 Post Reaction 3.3 % Vanadia on  $\theta$ -Alumina TGA and Derivative Weight.

A total of eleven bulk catalysts were prepared as described in section 3.4, tables 3.4 and 3.5. Four zinc ferrite catalysts ZF0.6MP, ZF0.6MBP, ZF3MBPC and ZF3MBPD; three iron enriched zinc ferrite catalysts ZFFeNaOHP, ZFFeNH3P,

ZFFeNH3PD; two iron oxide catalysts Fe2O3NH3P, Fe2O3NaOHP and one citrate precursor zinc ferrite.

#### 4.4 Zinc Ferrite ZF0.6MBP Bulk Catalyst.

##### 4.4.1 Pre-Reaction Characterisation of Zinc Ferrite ZF0.6MBP.

##### 4.4.1.1 Pre-Reaction AA Analysis of Zinc Ferrite ZF0.6MBP.

Atomic adsorption analysis was carried out as described in section 3.5.5.

**Table 4.16 Pre-Reaction AA Analysis of Zinc Ferrite ZF0.6MBP.**

Table 4.16 below shows the atomic adsorption analysis results for the iron and zinc concentrations in zinc ferrite ZF0.6MBP. The expected Fe:Zn ratio was 2.0:1.0.

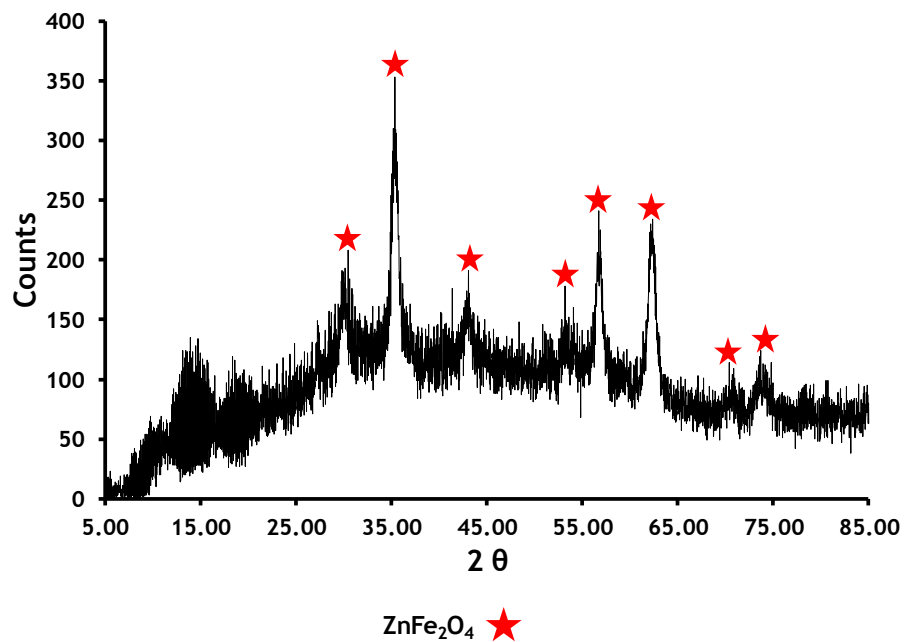
Catalyst	Iron Conc (mmg <sup>-1</sup> )	Zinc Conc (mgg <sup>-1</sup> )	Fe:Zn Mole Ratio
ZF0.6MBP	406.01	214.35	2.2:1.0

Prior to testing, a sample of the catalyst zinc ferrite ZF0.6MBP (6 cm<sup>3</sup>) was placed in the test reactor and subjected to steam at 693 K for 24 hours. This sample was designated as zinc ferrite ZF0.6MBP 24HSPT.

##### 4.4.1.2 Pre-Reaction X-Ray Diffraction Analysis of Zinc Ferrite ZF0.6MBP.

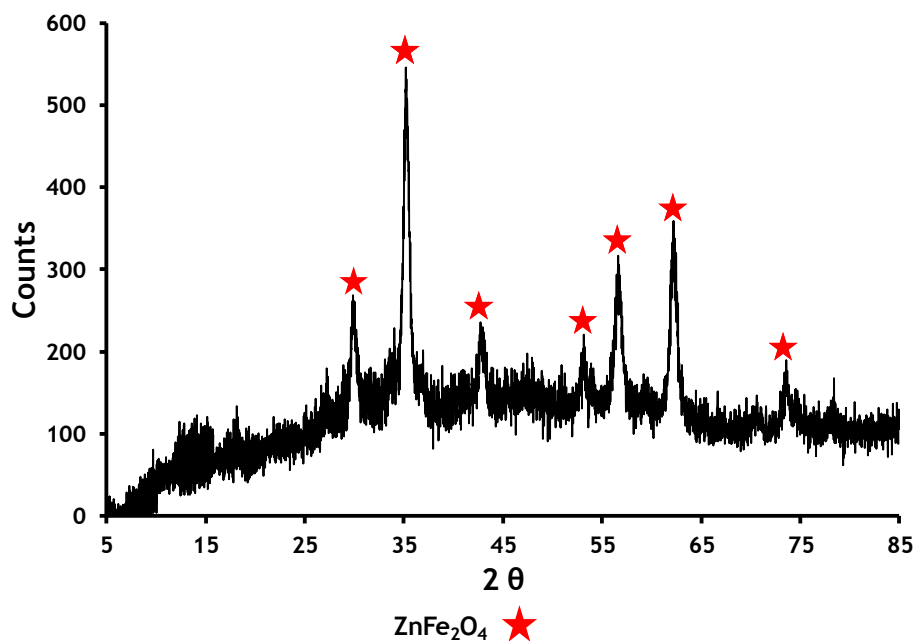
Ambient temperature X-Ray Diffraction was carried out as described in section 3.5.3.

Figure 4.62 below shows the ambient temperature XRD profile of zinc ferrite ZF0.6MBP with a size of 12 nm calculated from the reflection at 35.3 2θ.



**Figure 4.62** Pre-Reaction Ambient Temperature XRD Spectra of Zinc Ferrite ZF0.6MBP.

Figure 4.63 below shows the ambient temperature XRD profile of zinc ferrite ZF0.6MBP 24HSPT with a particle size of 15 nm calculated from the reflection at 35.3  $2\theta$ .



**Figure 4.63** Pre-Reaction Ambient Temperature XRD Spectra of Zinc Ferrite ZF0.6MBP 24HSPT.

From these results it is clear that steam pre-treatment has very little effect on the particle size.

#### 4.4.1.3 Pre-Reaction Raman Spectroscopy Analysis of Zinc Ferrite ZFO.6MBP.

Ambient temperature Raman spectroscopy was carried out as described in section 3.5.4.

Figures 4.64 and 4.65 below show the pre-reaction Raman bands for zinc ferrite ZFO.6MBP and ZFO.6MBP 24HSPT.

The Raman bands are tabulated in table 4.17 below to allow comparison.

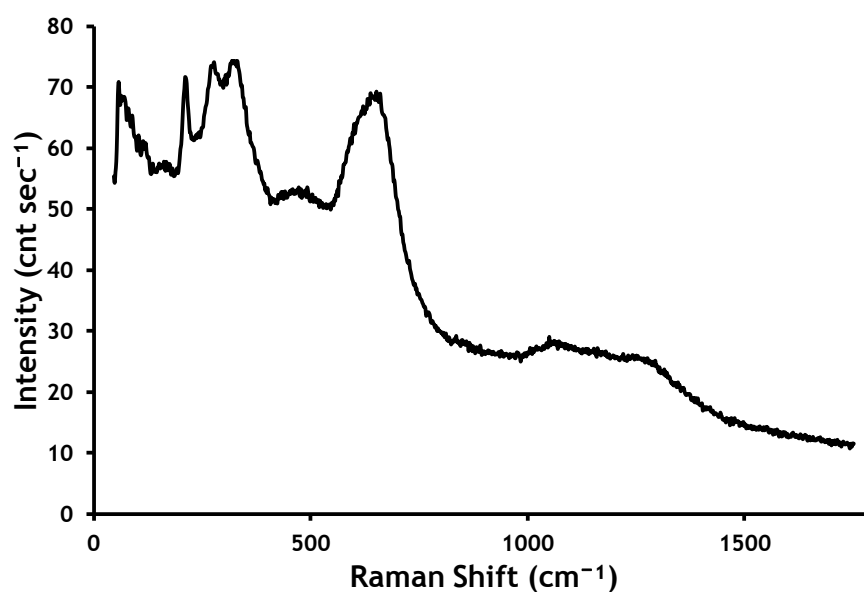
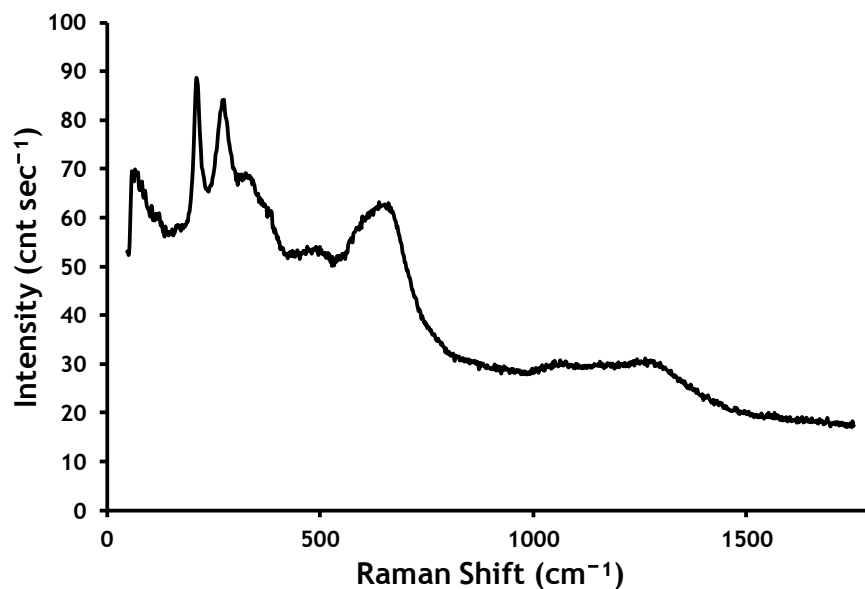


Figure 4.64 Pre-Reaction Ambient Temperature Raman Spectra of Zinc Ferrite ZFO.6MBP.



**Figure 4.65** Pre-Reaction Ambient Temperature Raman Spectra of Zinc Ferrite ZF0.6MBP 24HSPT.

**Table 4.17** Comparison of Pre-Reaction Raman Shift Bands Zinc Ferrite ZF0.6MBP and ZF0.6MBP 24HSPT to Literature.

Raman Shift Bands (cm <sup>-1</sup> )							
	Zinc Ferrite[36]						
Literature	221	246	330-355	451-498	647-659	1091-1106	1271-1298
Zinc Ferrite ZF0.6MBP	211	278	319	473	653	1069	1250
Zinc Ferrite ZF0.6MBP 24HSPT	209	274	330	470	649	1064	1263

#### 4.4.1.4 Pre-Reaction Surface Area Measurements of Zinc Ferrite ZF0.6MBP.

Surface area determination was carried out as described in section 3.5.1.

Table 4.18 below shows the surface area, pore diameter and cumulative pore volume for zinc ferrite ZF0.6MBP and ZF0.6MBP 24HSPT.

**Table 4.18 Pre-Reaction Surface Area Measurements of Zinc Ferrite ZFO.6MBP and ZFO.6MBP 24HSPT.**

Catalyst	Surface Area (m <sup>2</sup> g <sup>-1</sup> )	Pore Diameter (nm)	Cumulative Pore Volume (cm <sup>3</sup> g <sup>-1</sup> )
Zinc Ferrite ZFO.6MBP	84	9	0.2030
Zinc Ferrite ZFO.6MBP 24HSPT	81	9	0.1891

**4.4.1.5 Pre-Reaction Thermo-gravimetric Analysis-Differential Scanning Calorimetry Analysis of Zinc Ferrite ZFO.6MBP.**

Thermo-gravimetric analysis/differential scanning calorimetry was carried out as described in section 3.5.2.

Figure 4.66 below shows a total weight loss of 6 % from the pre-reaction zinc ferrite ZFO.6MBP over a temperature range 295 K to 750 K.

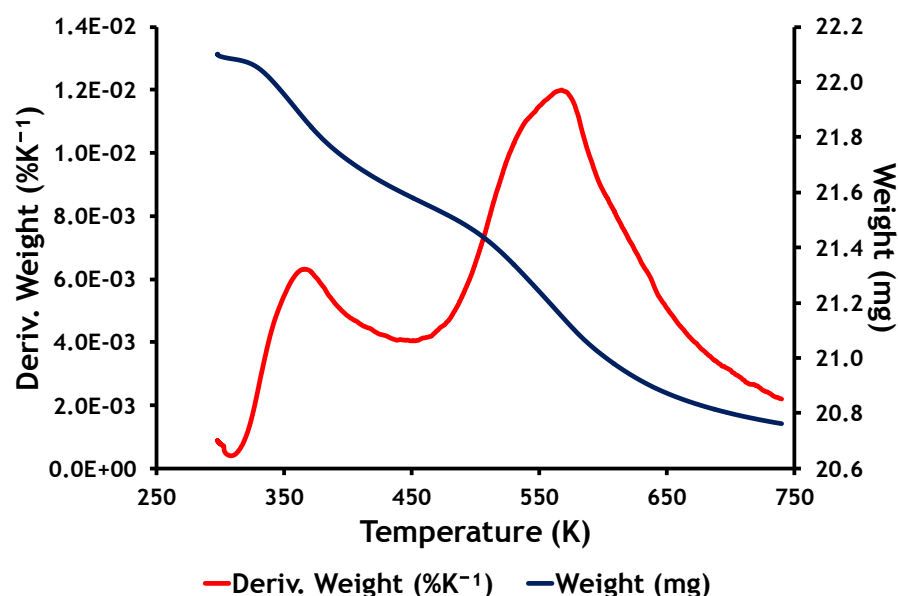


**Figure 4.66 Pre-Reaction Zinc Ferrite ZFO.6MBP TGA and Derivative Weight.**

The DSC profile in figure 4.67 below shows two exothermic events at 340 K and 560 K associated with the evolution of carbon dioxide.

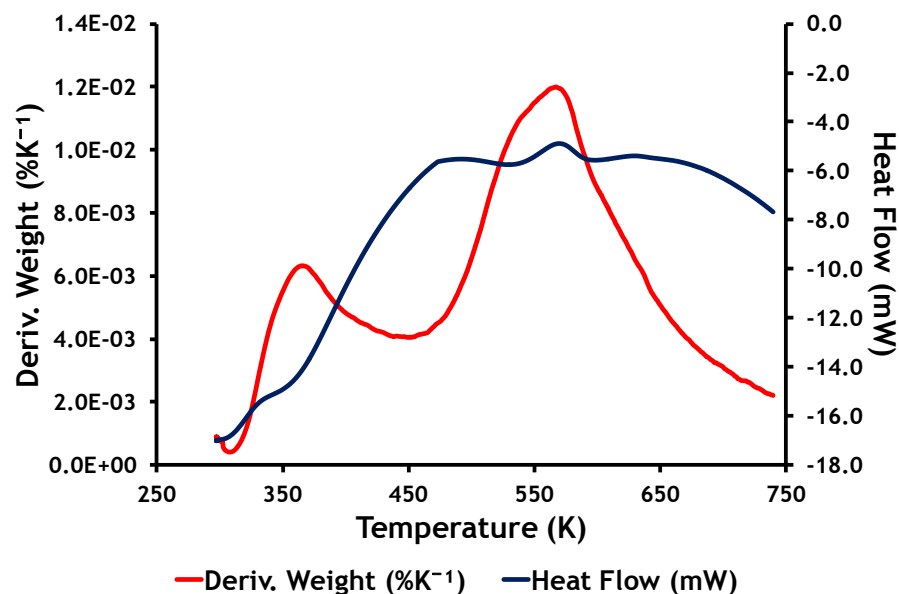


Figure 4.67 Pre-Reaction Zinc Ferrite ZF0.6MBP TGA/DSC DSC.

Figure 4.68 below shows the evolution of carbon dioxide at 365 K and 570 K, relative to the derivative weight.

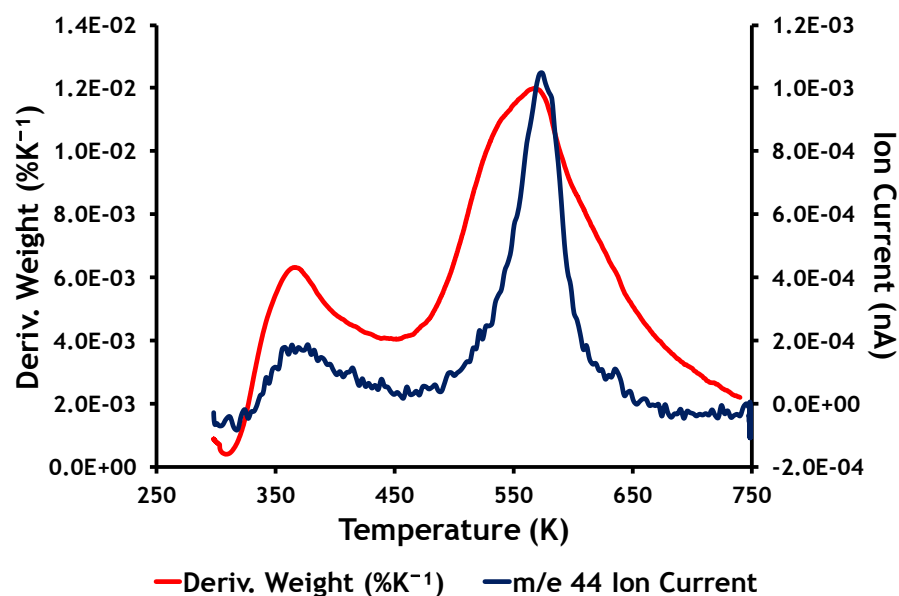
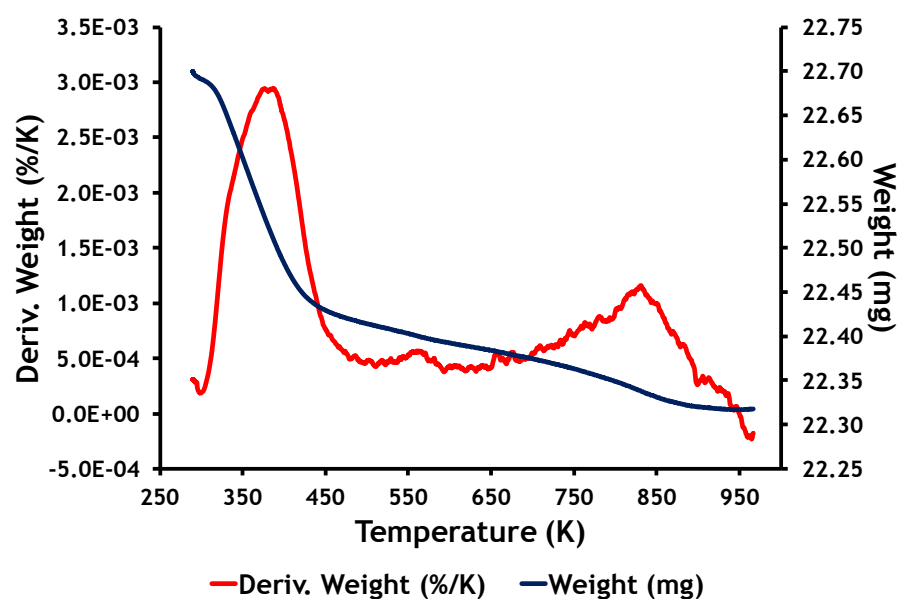


Figure 4.68 Pre-Reaction TGA/DSC Mass Spectrometer Profile from Zinc Ferrite ZF0.6MBP TGA/DSC m/e 44.

Figure 4.69 below shows a total weight loss of 2 % from the pre-reaction zinc ferrite ZF0.6MBP 24HSPT over a temperature range 285 K to 970 K.



**Figure 4.69** Pre-Reaction Zinc Ferrite ZF0.6MBP 24HSPT TGA and Derivative Weight.

No exothermic or endothermic events were seen on the DSC measurement. The weight loss shown above is likely mainly due to desorption of physisorbed water at 375 K and evolution of a small amount of carbon dioxide at 830 K; due to the small amount of material desorbed the mass spectrometer did not show any peaks for water or carbon dioxide.

#### 4.4.1.6 Acid Site Analysis of Zinc Ferrite ZF0.6MBP.

Acid site analysis was carried out as described in section 3.7.5.

Figure 4.70 below shows four acid sites on zinc ferrite ZF0.6MBP; two weak acid sites, one medium acid site and one strong acid site.

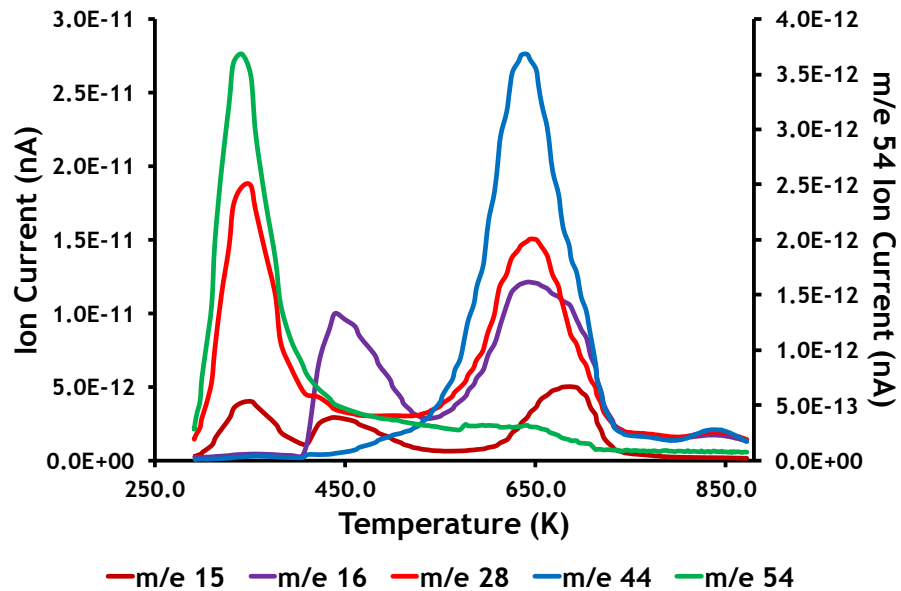


Figure 4.70 Pre-Reaction Zinc Ferrite ZF0.6MBP Acid Site Analysis.

#### 4.4.1.7 Pre-Reaction Electron Paramagnetic Resonance Measurements of Zinc Ferrite ZF0.6MBP.

Electron Paramagnetic Resonance measurement analysis was carried out as described in section 3.7.6.2.

Figures 4.71 and 4.72 below show the EPR profile of pre-reaction zinc ferrite ZF0.6MBP and steamed pre-reaction ZF0.6MBP 24HSPT.

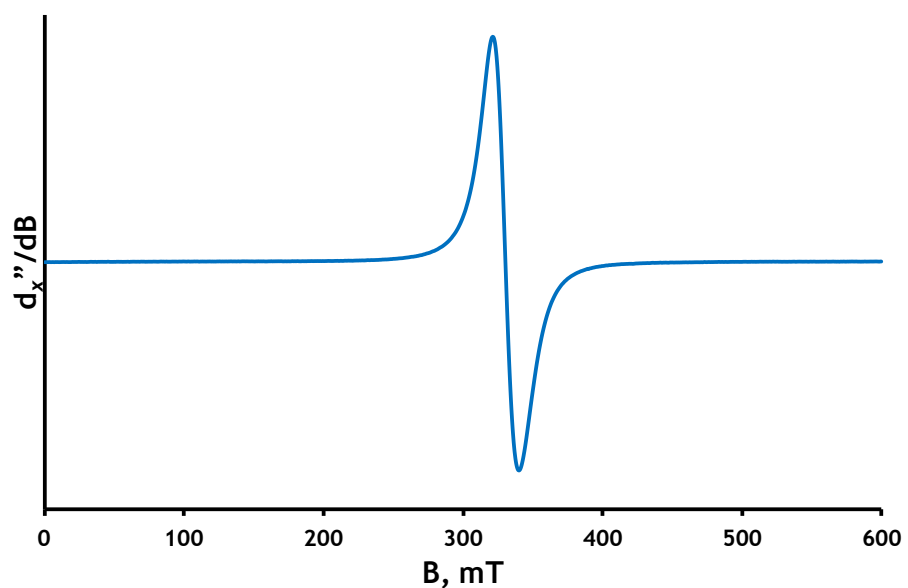
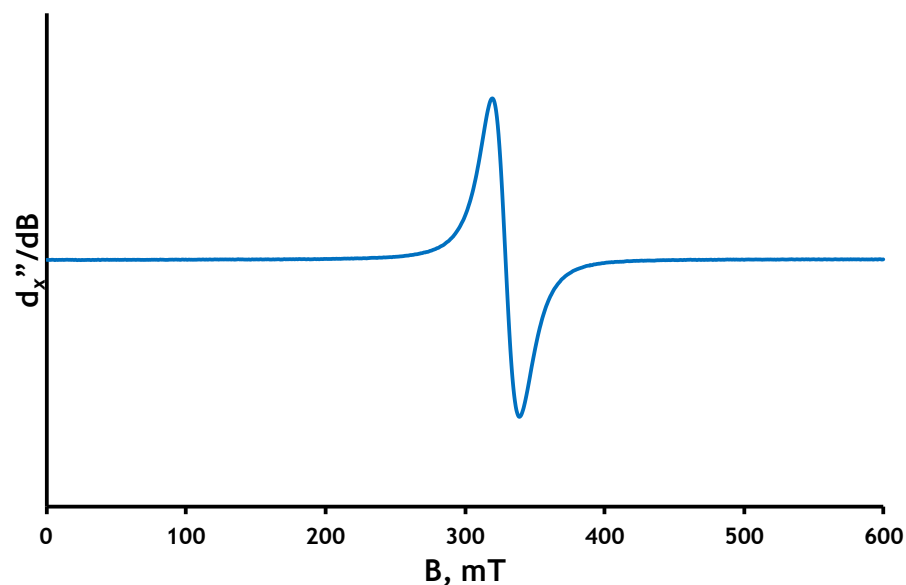


Figure 4.71 EPR Profile of Pre-Reaction Zinc Ferrite ZF0.6MBP.



**Figure 4.72 EPR Profile of Steamed Pre-Reaction Zinc Ferrite ZF0.6MBP 24HSPT.**

#### **4.4.1.8 Pre-Reaction Scanning Electron Microscopy Analysis of Zinc Ferrite ZF0.6MBP.**

Scanning electron microscopy analysis was carried out as described in section 3.7.1.

The SEM micrograph of zinc ferrite ZF0.6MBP in figure 4.73 below shows the pores in the bulk catalyst.

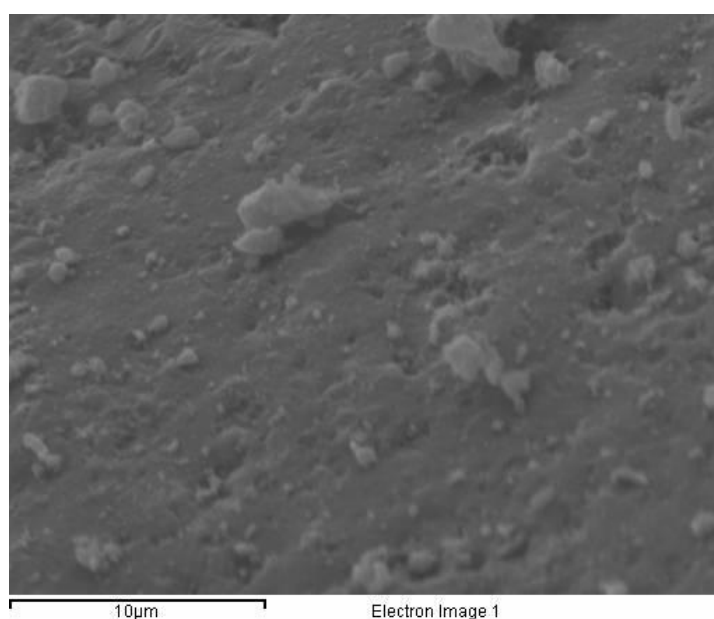


**Figure 4.73 Pre-Reaction Zinc Ferrite ZF0.6MBP SEM Micrograph.**

#### 4.4.2 Catalyst Testing Zinc Ferrite ZF0.6MBP.

The zinc ferrites are detailed in table 3.7 in section 3.6.3, part of which is reproduced below in table 4.19 and the test procedures are given in sections 3.6.2 and 3.6.3.

Prior to any bulk catalyst testing two blank reactions were carried out to study the effect of steam on the bulk catalyst, one for 67 hours and the second for 196 hours. The catalyst used was zinc ferrite 0.6MBP, 1-butene was omitted from the reaction mixture outlined in section 3.6.2. The surface area decreased from  $84 \text{ m}^2\text{g}^{-1}$  to  $40 \text{ m}^2\text{g}^{-1}$  and  $57 \text{ m}^2\text{g}^{-1}$  for 67 hours and 196 hours steam treatment respectively.

**Table 4.19 Catalyst Testing of Zinc Ferrite ZF0.6MBP.**

Reaction No	Catalyst Code	Bed Vol (cm <sup>3</sup> )	Weight (g)
5	ZF0.6MBP	3	3.8695
11	ZF0.6MBP 24HSPT	3	4.0215

Figures 4.74 and 4.75 below show the product selectivities and 1-butene conversion obtained when passing 1-butene over zinc ferrite ZF0.6MBP with a bed volume of 3 cm<sup>3</sup>.

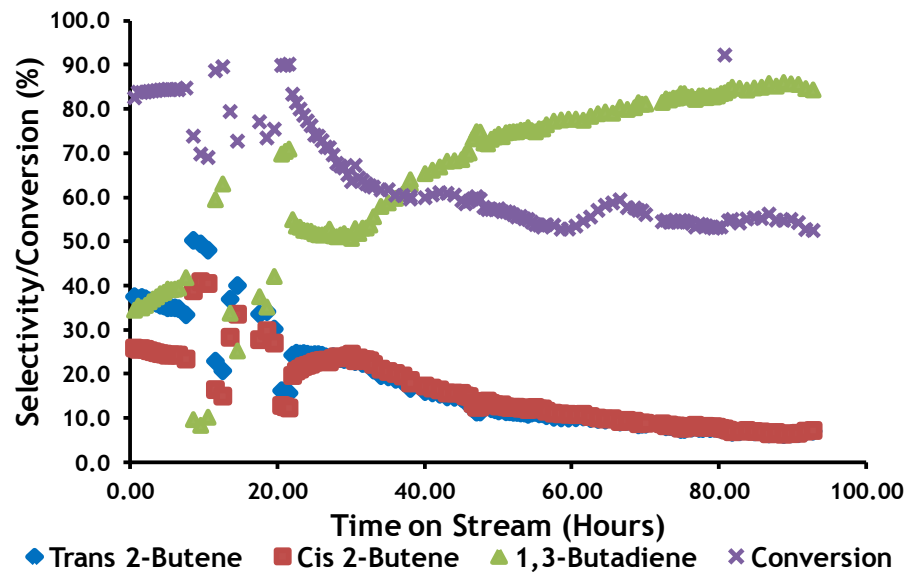


Figure 4.74 Selectivity/Conversion Major Components Zinc Ferrite ZF0.6MBP.

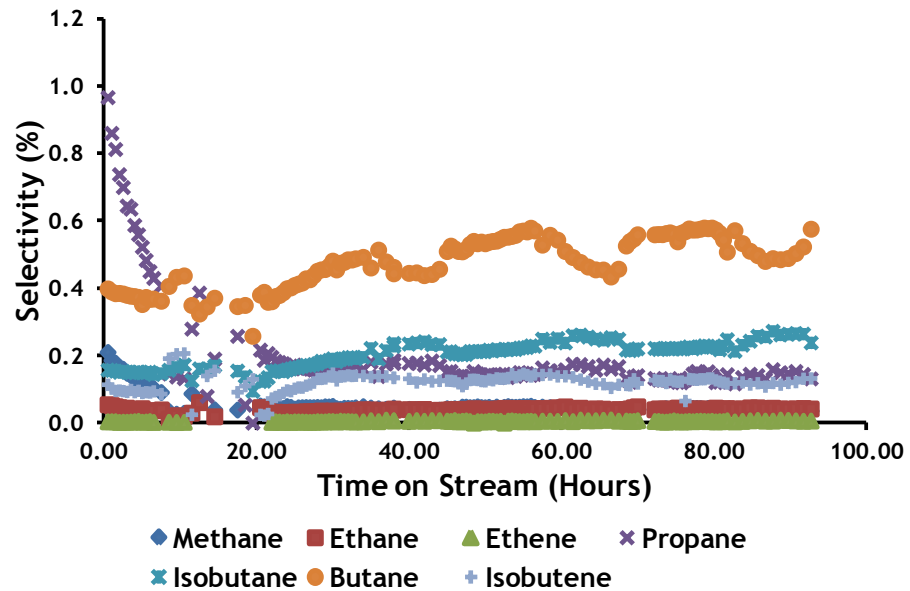


Figure 4.75 Selectivity Minor Components Zinc Ferrite ZF0.6MBP.

Figures 4.76 and 4.77 below show the product selectivities and 1-butene conversion obtained when passing 1-butene over zinc ferrite ZF0.6MBP 24HSPT with a bed volume of 3 cm<sup>3</sup>.

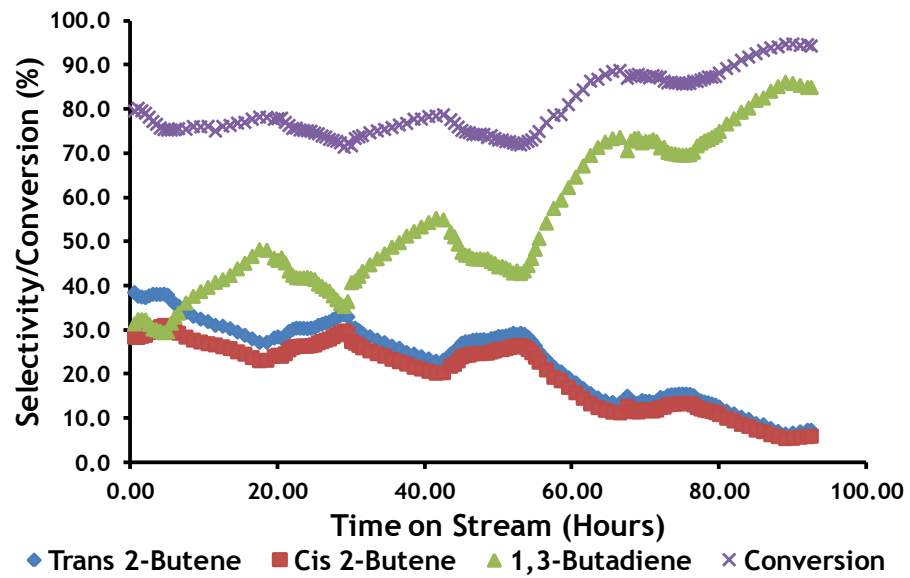


Figure 4.76 Selectivity/Conversion Major Components Zinc Ferrite ZF0.6MBP 24HSPT.

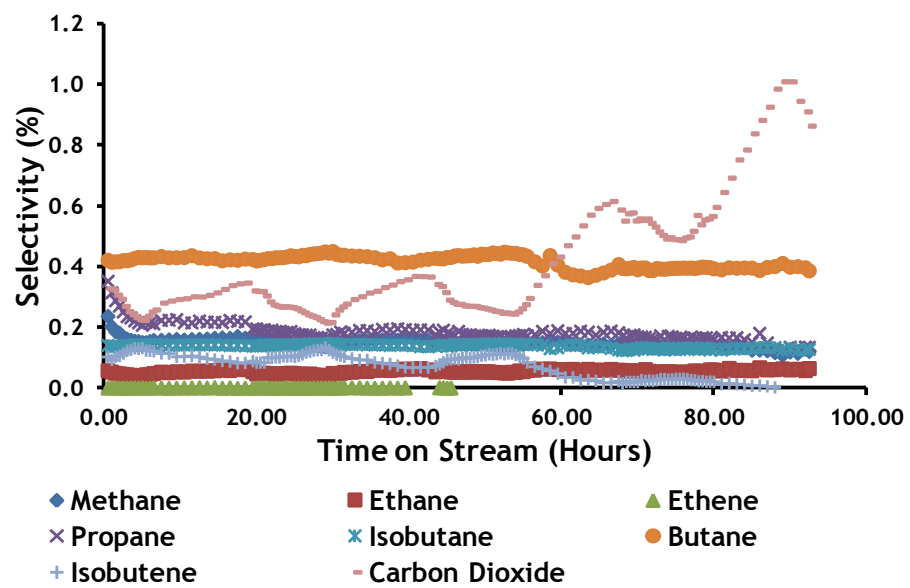


Figure 4.77 Selectivity Minor Components Zinc Ferrite ZF0.6MBP 24HSPT.

#### 4.4.3 Post Reaction Characterisation of Zinc Ferrite ZF0.6MBP.

##### 4.4.3.1 Post Reaction X-Ray Diffraction Analysis of Zinc Ferrite ZF0.6MBP.

Ambient temperature X-Ray Diffraction was carried out as described in section 3.5.3.

Figure 4.78 below shows the post reaction XRD profile of zinc ferrite ZF0.6MBP with a particle size of 16 nm calculated from the reflection at 35.2 2θ.

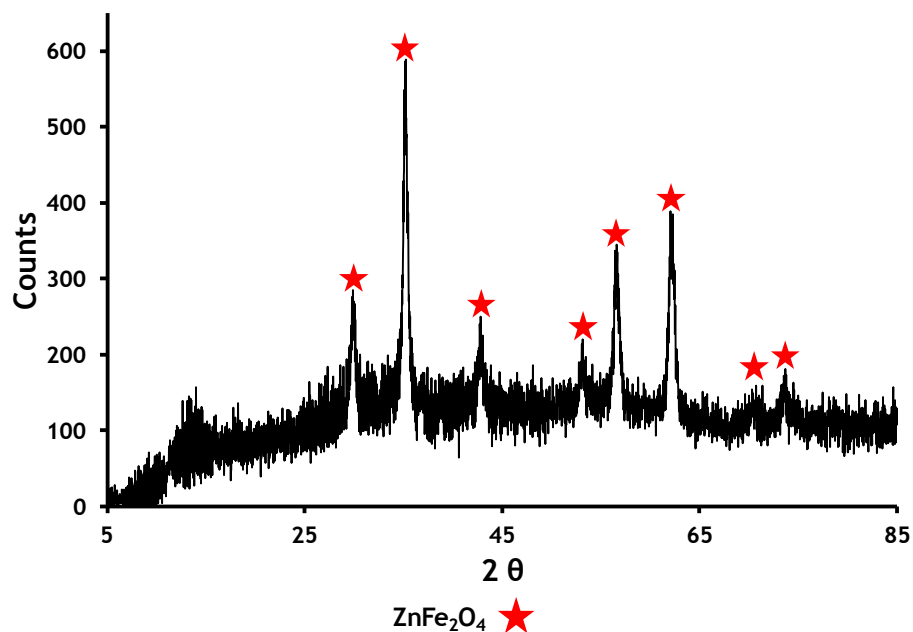


**Figure 4.78 Post Reaction Ambient Temperature XRD Spectra of Zinc Ferrite ZF0.6MBP.**

Comparison of the pre and post reaction particle size of ZF0.6MBP shows a slight increase in particle size from 12 nm to 16 nm.

Figure 4.79 below shows the post reaction XRD profile of zinc ferrite ZF0.6MBP 24HSPT with a particle size of 15 nm calculated from the reflection at 35.3 2θ.

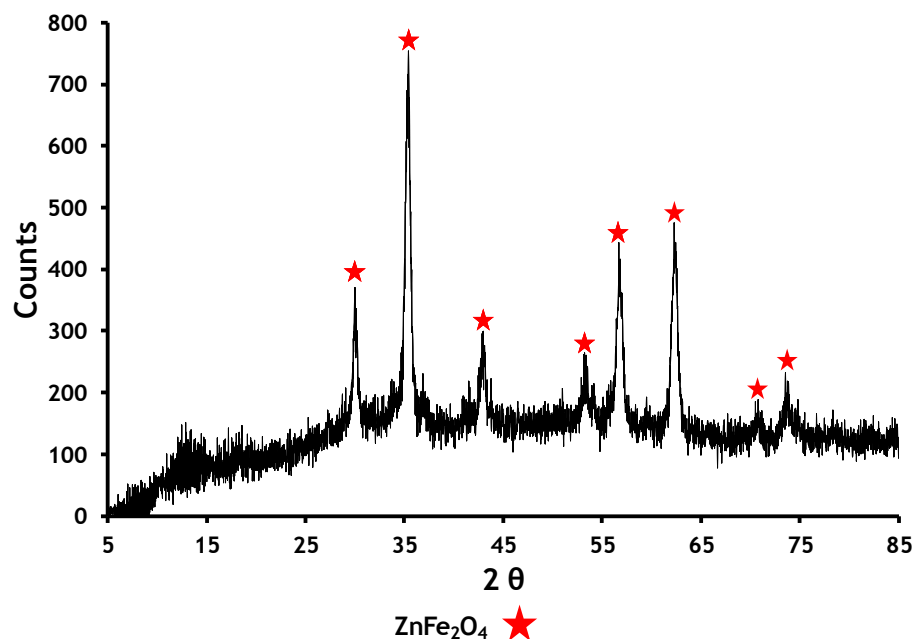


**Figure 4.79** Post Reaction Ambient Temperature XRD Spectra of Zinc Ferrite ZF0.6MBP 24HSPT.

Comparison of the pre and post reaction particle size of ZF0.6MBP24HSPT shows no change in particle size.

#### 4.4.3.2 Post Reaction Ambient Temperature Raman Spectroscopy Analysis of Zinc Ferrite ZF0.6MBP.

Ambient temperature Raman spectroscopy was carried out as described in section 3.5.4.

Figures 4.80 and 4.81 below show the post reaction Raman bands for zinc ferrite ZF0.6MBP and ZF0.6MBP 24HSPT. The Raman bands are tabulated in table 4.20 below to allow comparison.

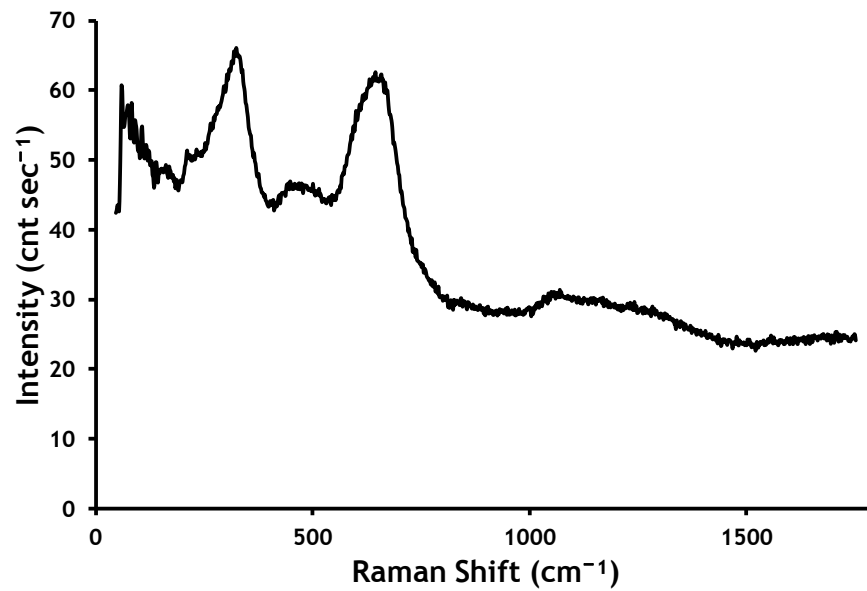


Figure 4.80 Post Reaction Ambient Temperature Raman Spectra of Zinc Ferrite ZF0.6MBP.

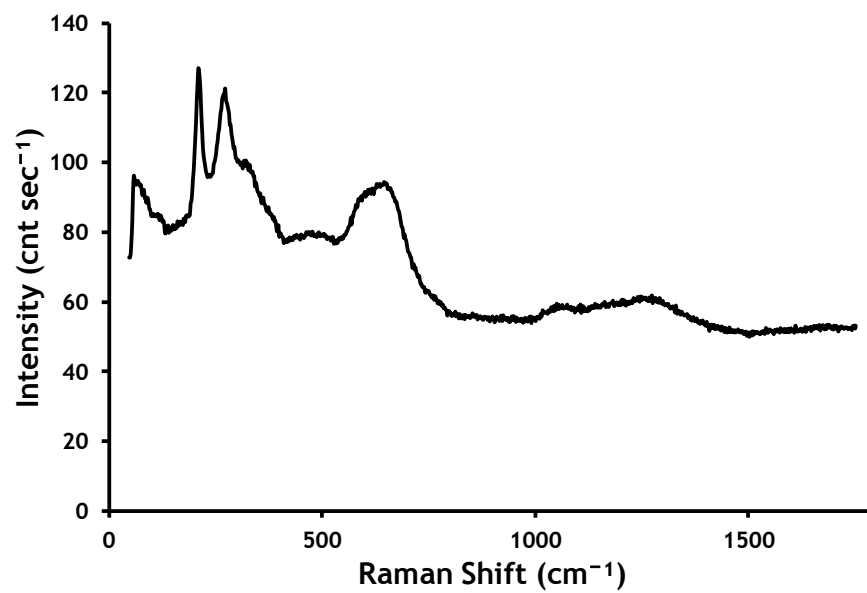


Figure 4.81 Post Reaction Ambient Temperature Raman Spectra of Zinc Ferrite ZF0.6MBP 24HSPT.

**Table 4.20 Comparison of Post Reaction Raman Shift Bands Zinc Ferrite ZF0.6MBP and ZF0.6MBP 24HSPT to Literature.**

Raman Shift Bands ( $\text{cm}^{-1}$ )							
	Zinc Ferrite[36]						
Literature	221	246	330-355	451-498	647-659	1091-1106	1271-1298
Zinc Ferrite ZF0.6MBP			324	472	645	1070	1284
Zinc Ferrite ZF0.6MBP 24HSPT	209	274	320	478	654	1050	1274

Comparison of pre and post reaction Raman profiles for ZF0.6MBP shows a loss of bands associated with zinc ferrite at  $211 \text{ cm}^{-1}$  and  $278 \text{ cm}^{-1}$ .

Comparison of pre and post reaction Raman profiles for ZF0.6MBP 24HSPT shows no loss of bands associated with zinc ferrite.

#### **4.4.3.3 Post Reaction Surface Area Measurements of Zinc Ferrite ZF0.6MBP.**

Surface area determination was carried out as described in section 3.5.1.

Table 4.21 below shows the surface area, pore diameter and cumulative pore volume for zinc ferrite ZF0.6MBP and ZF0.6MBP 24HSPT.

**Table 4.21 Post Reaction Surface Area Measurements of Zinc Ferrite ZF0.6MBP.**

<b>Catalyst</b>	<b>Surface Area (m<sup>2</sup>g<sup>-1</sup>)</b>	<b>Pore Diameter (nm)</b>	<b>Cumulative Pore Volume (cm<sup>3</sup>g<sup>-1</sup>)</b>
<b>Zinc Ferrite ZF0.6MBP</b>	37	19	0.1739
<b>Zinc Ferrite ZF0.6MBP 24HSPT</b>	39	18	0.1735

Comparison of the pre and post reaction surface areas of the zinc ferrites ZF0.6MBP and ZF0.6MBP 24HSPT shows a decrease from 84 m<sup>2</sup>g<sup>-1</sup> to 37 m<sup>2</sup>g<sup>-1</sup> for ZFF0.6MBP and a decrease from 81 m<sup>2</sup>g<sup>-1</sup> to 39 m<sup>2</sup>g<sup>-1</sup> for ZFF0.6MBP 24HSPT.

#### **4.4.3.4 Post Reaction Thermo-gravimetric Analysis-Differential Scanning Calorimetry Analysis of Zinc Ferrite 0.6MBP.**

Thermo-gravimetric analysis/differential scanning calorimetry was carried out as described in section 3.5.2.

Figure 4.82 below shows a weight loss of 1 % from the post reaction zinc ferrite ZF0.6MBP over the temperature range 285 K to 970K.

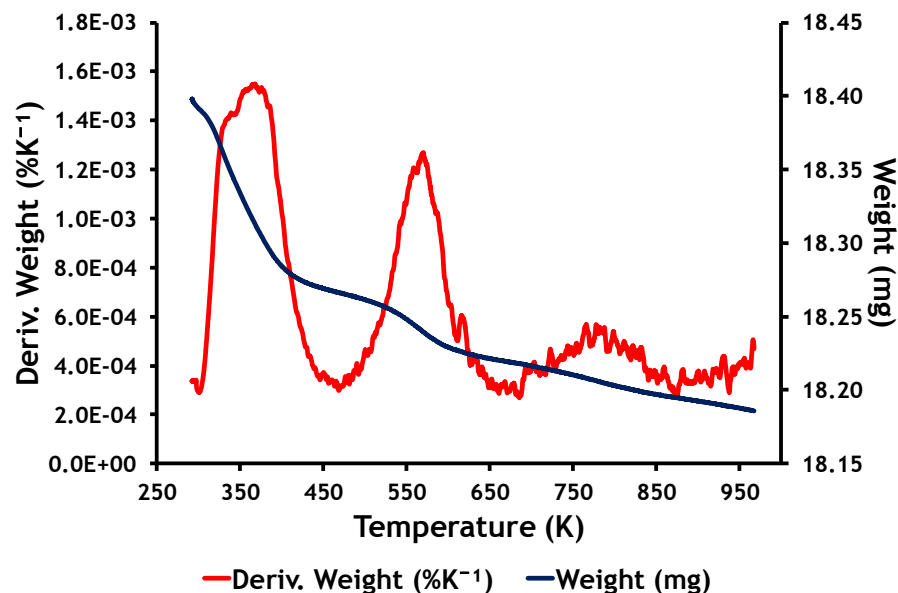


**Figure 4.82 Post Reaction Zinc Ferrite ZF0.6MBP TGA and Derivative Weight.**

No exothermic or endothermic events were seen on the DSC measurement. The weight loss shown above is likely due to desorption of physisorbed water at 350 K and to carbon burn off at 550 K and 800 K.

The post reaction zinc ferrite ZF0.6MBP 24HSPT TGA and Derivative Weight profile was featureless therefore no profiles are shown.

#### 4.4.3.5 Post Reaction Acid Site Analysis of Zinc Ferrite ZF0.6MBP.

Acid site analysis was carried out as described in section 3.7.5.

Figure 4.83 below shows two acid sites on zinc ferrite ZF0.6MBP; one weak acid site, and one medium acid site showing the loss of one weak acid site and the strong acid site from pre-reaction zinc ferrite ZF0.6MBP.

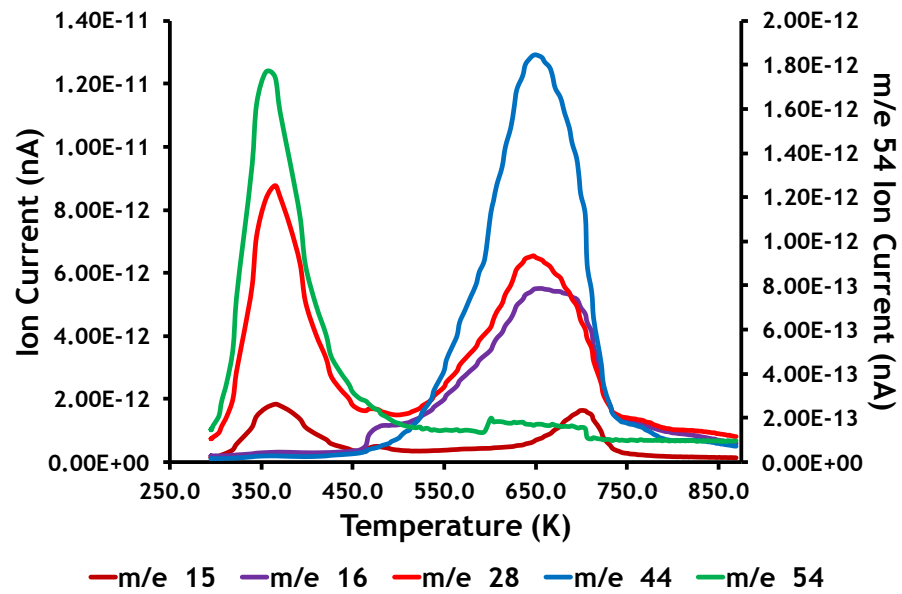


Figure 4.83 Post Reaction Zinc Ferrite ZF0.6MBP Acid Site Analysis.

#### 4.4.3.6 Post Reaction Electron Paramagnetic Resonance Measurements of Zinc Ferrite ZF0.6MBP.

Electron Paramagnetic Resonance measurement analysis was carried out as described in section 3.7.6.2.

Figures 4.84 and 4.85 below show the ERP profiles of post-reaction zinc ferrite ZF0.6MBP and steamed post-reaction ZF0.6MBP 24HSPT.

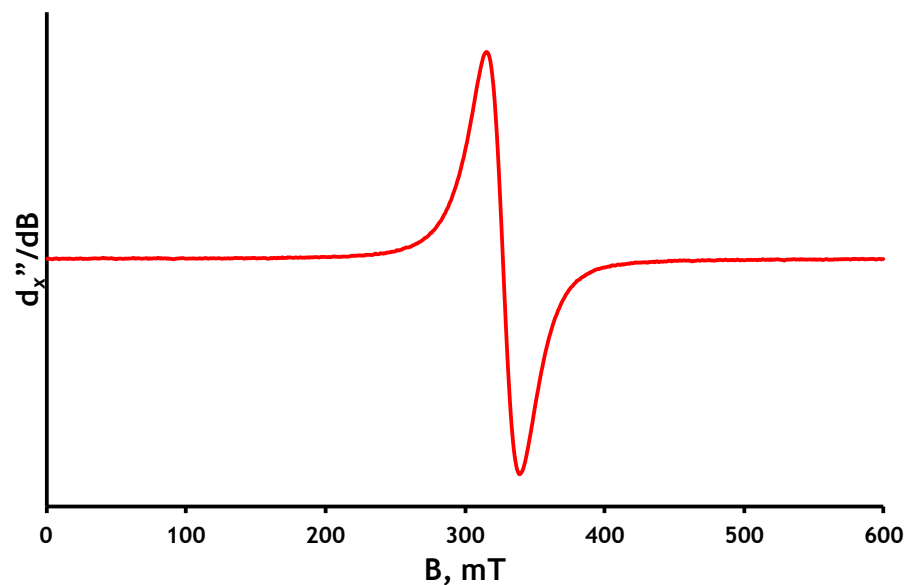
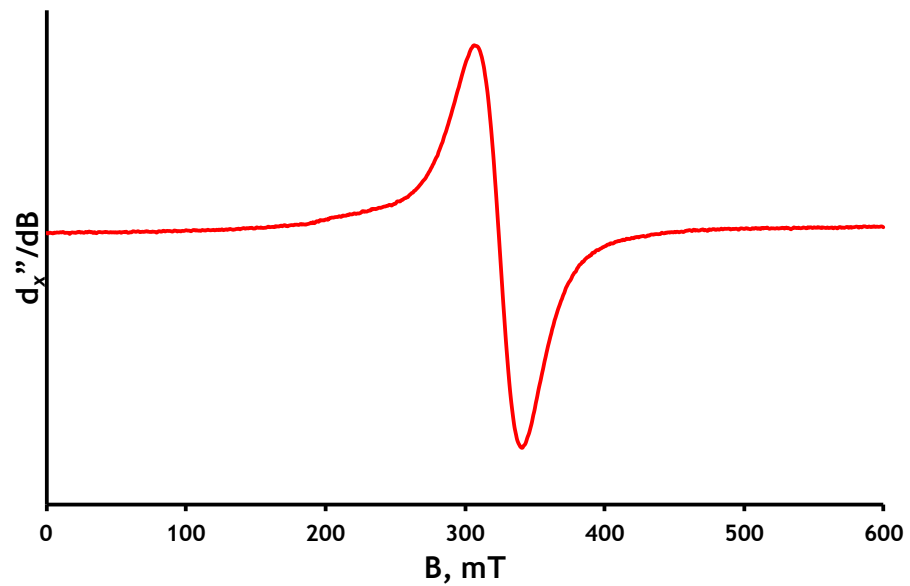


Figure 4.84 EPR Profile of Post Reaction Zinc Ferrite ZF0.6MBP.



**Figure 4.85 EPR Profile of Post Reaction Zinc Ferrite ZF0.6MBP 24HSPT.**

#### **4.4.3.7 Post Reaction Scanning Electron Microscopy Analysis of Zinc Ferrite ZF0.6MBP.**

Scanning electron microscopy analysis was carried out as described in section 3.7.1.

Figure 4.86 below shows the SEM micrograph of post reaction zinc ferrite ZF0.6MBP.

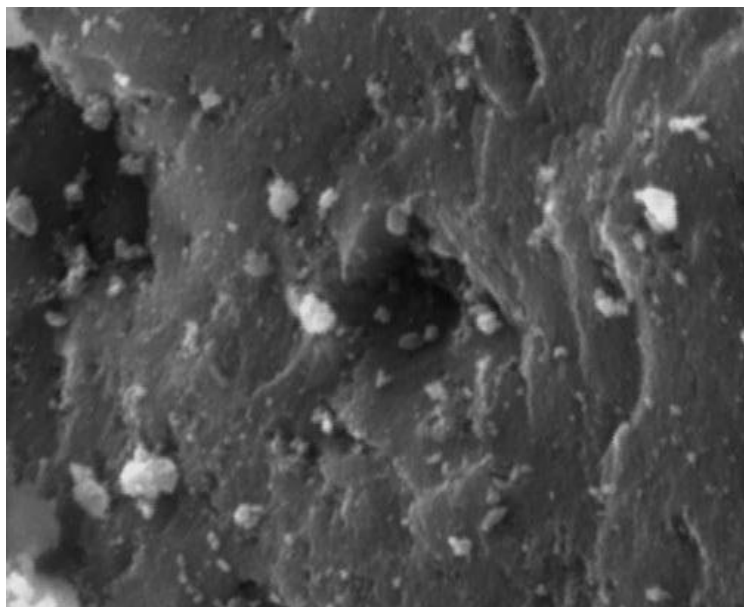


**Figure 4.86** Post Reaction Zinc Ferrite 0.6MBP SEM Micrograph 67 Hours.

#### **4.5 Zinc Ferrite ZF3MBPC Bulk Catalyst.**

##### **4.5.1 Pre-Reaction Characterisation of Zinc Ferrite ZF3MBPC.**

Atomic adsorption analysis was carried out as described in section 3.5.5.

##### **4.5.1.1 Pre-Reaction AA Analysis of Zinc Ferrite ZF3MBPC.**

Table 4.22 below shows the atomic adsorption analysis results for the iron and zinc concentrations in zinc ferrite ZF3MBPC.

**Table 4.22** Pre-Reaction AA Analysis of Zinc Ferrite ZF3MBPC.

Catalyst	Iron Conc ( $\text{mgg}^{-1}$ )	Zinc Conc ( $\text{mgg}^{-1}$ )	Fe:Zn Mole Ratio
ZF3MBPC	400.61	238.34	2:1

##### **4.5.1.2 Pre-Reaction X-Ray Diffraction Analysis of ZF3MBPC.**

Ambient temperature X-Ray Diffraction was carried out as described in section 3.5.3.

Figure 4.87 below shows the pre reaction ambient temperature XRD profile of zinc ferrite ZF3MBPC with a particle size of 18 nm calculated from the reflection at 35.22 2θ.

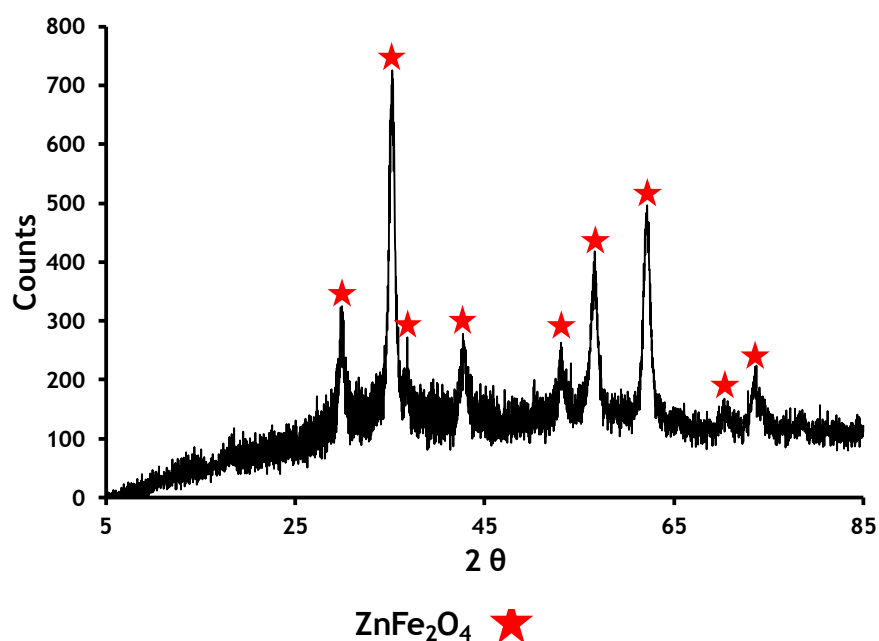


**Figure 4.87** Pre-Reaction Ambient Temperature XRD Spectra of Zinc Ferrite ZF3MBPC.

#### 4.5.1.3 Pre-Reaction Raman Spectroscopy Analysis of Zinc Ferrite ZF3MBPC.

Ambient temperature Raman spectroscopy was carried out as described in section 3.5.4.

Figure 4.88 below shows the pre-reaction Raman bands for zinc ferrite ZF3MBPC. The Raman bands are tabulated in table 4.23 below to allow comparison.

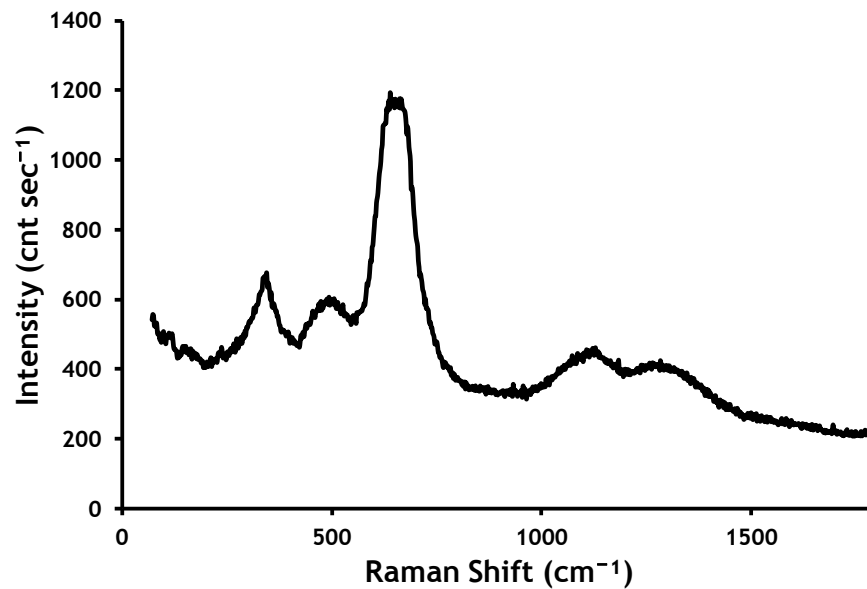


**Figure 4.88** Pre-Reaction Ambient Temperature Raman Spectra of Zinc Ferrite ZF3MBPC.

**Table 4.23** Comparison of Pre-Reaction Raman Shift Bands Zinc Ferrite ZF3MBPC to Literature.

Raman Shift Bands (cm <sup>-1</sup> )							
	Zinc Ferrite[36]						
Literature	221	246	330-355	451-498	647 659	1091-1106	1271-1298
Zinc Ferrite ZF3MBPC			346	494	652	1122	1270

#### 4.5.1.4 Pre-Reaction Surface Area Measurements of Zinc Ferrite ZF3MBPC.

Surface area determination was carried out as described in section 3.5.1.

Table 4.24 below shows surface area, pore diameter and cumulative pore volume for zinc ferrite ZF3MBPC.

Table 4.24 Pre-Reaction Surface Area Analysis of Zinc Ferrite ZF3MBPC.

Catalyst	Surface Area (m <sup>2</sup> g <sup>-1</sup> )	Pore Diameter (nm)	Cumulative Pore Volume (cm <sup>3</sup> g <sup>-1</sup> )
Zinc Ferrite ZF3MBPC	38	12	0.1179

#### 4.5.1.5 Pre-Reaction Thermo-gravimetric Analysis-Differential Scanning Calorimetry Analysis of Zinc Ferrite ZF3MBPC.

Thermo-gravimetric analysis/differential scanning calorimetry was carried out as described in section 3.5.2.

Figure 4.89 below shows a total weight loss of 7 % from the pre-reaction zinc ferrite ZF3MBPC over the temperature range 290 K to 750 K.

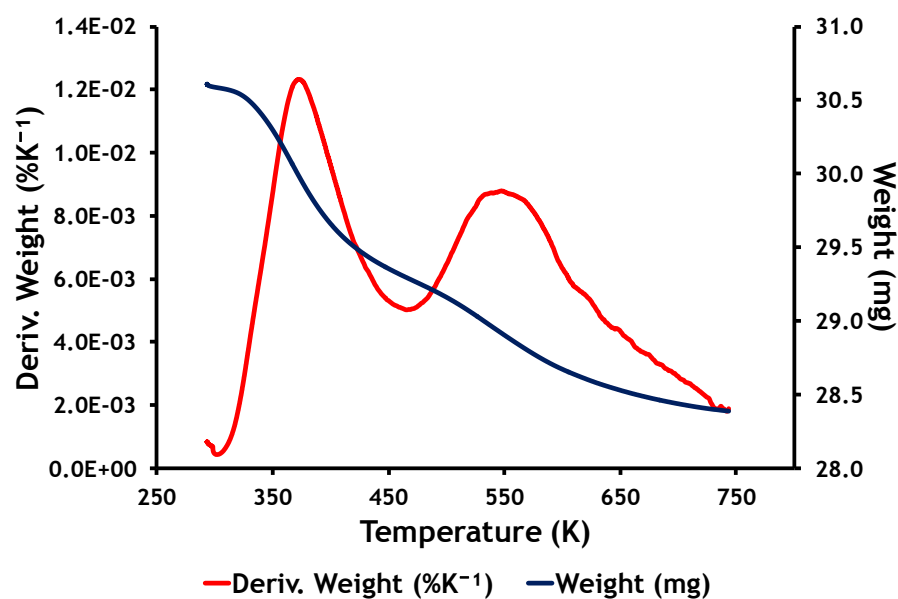


Figure 4.89 Pre-Reaction Zinc Ferrite ZF3MBPC TGA and Derivative Weight.

The DSC profile in figure 4.90 below shows two endothermic events at 327 K to 362 K and 485 K to 526 K associated with the evolution of carbon dioxide.

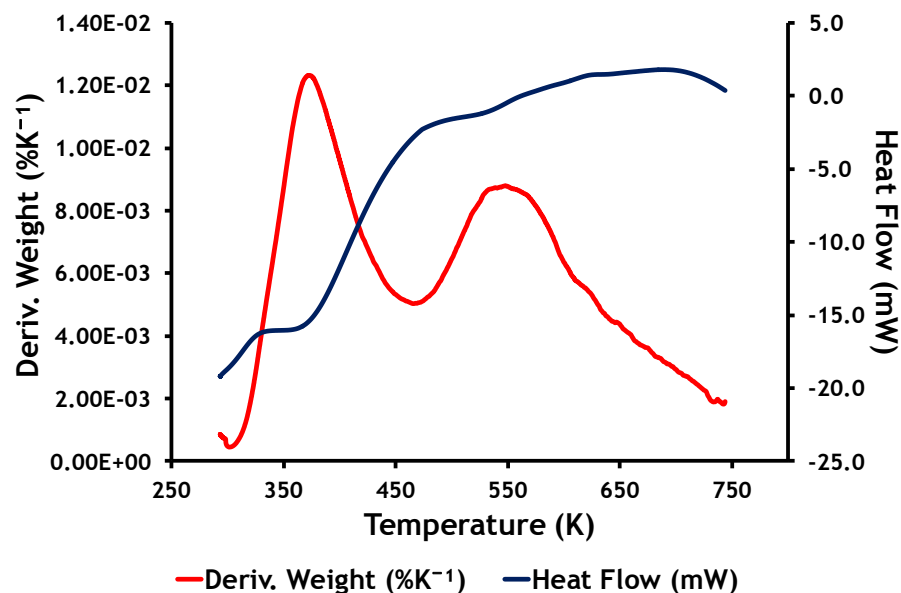


Figure 4.90 Pre-Reaction Zinc Ferrite ZF3MBPC TGA/DSC DSC.

Figure 4.91 below shows the evolution of carbon dioxide at 327 K to 362 K and 485 K to 526 K, relative to the derivative weight.

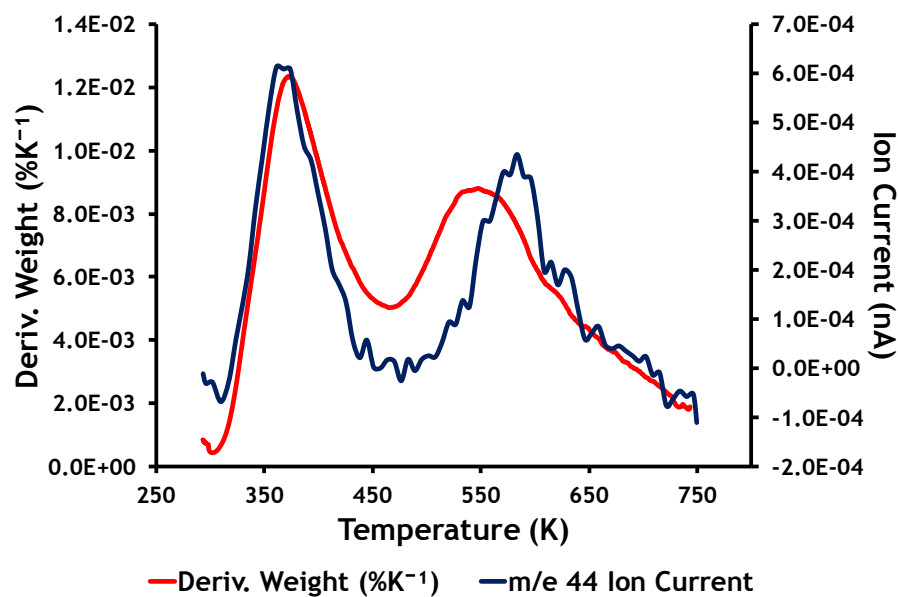


Figure 4.91 Pre-Reaction TGA/DSC Mass Spectrometer Profile from Zinc Ferrite ZF3MBPC m/e 44.

#### 4.5.1.6 Pre-Reaction Acid Site Analysis of Zinc Ferrite ZF3MBPC.

Acid site analysis was carried out as described in section 3.7.5.

Figure 4.92 below shows four acid sites on zinc ferrite ZF3MBPC; one weak acid site, two medium acid sites and one strong acid site.

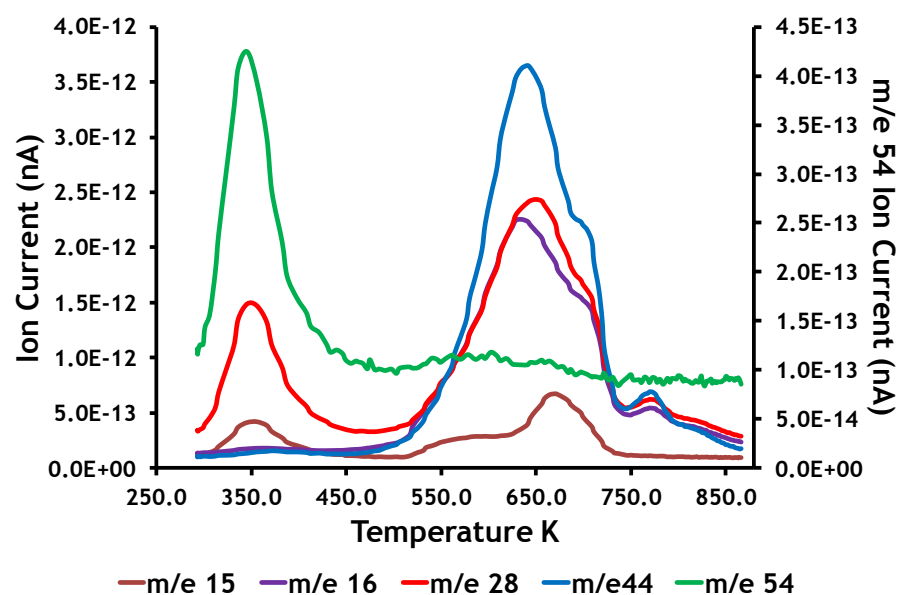
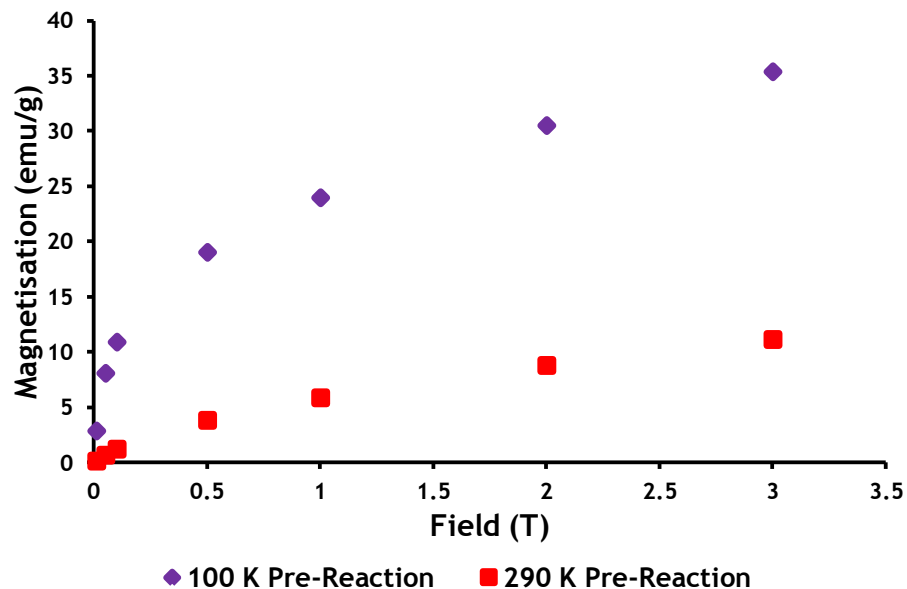


Figure 4.92 Pre-Reaction Zinc Ferrite ZF3MBPC Acid Site Analysis.

#### 4.5.1.7 Pre-Reaction Magnetic and Electron Paramagnetic Resonance Measurements of Zinc Ferrite ZF3MBPC.

Magnetic measurement analysis was carried out as described in section 3.7.6.1. Figure 4.93 below shows the magnetic property of pre-reaction zinc ferrite ZF3MBPC.



**Figure 4.93 Pre-Reaction Zinc Ferrite ZF3MBPC SQUID Magnetic Measurement.**

Electron Paramagnetic Resonance measurement analysis was carried out as described in section 3.7.6.2.

Figure 4.94 below shows the EPR profile of pre-reaction zinc ferrite ZF3MBPC.

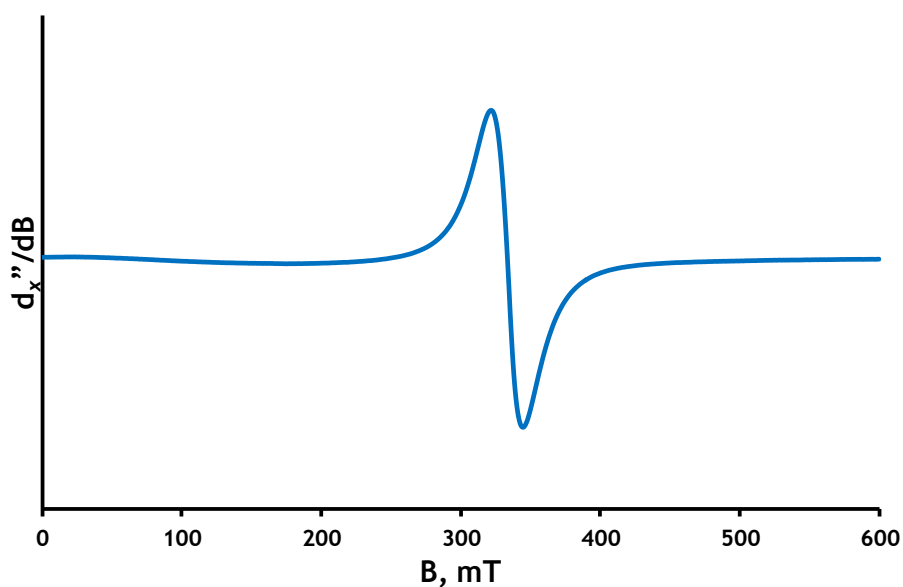


**Figure 4.94 EPR Profile Pre-Reaction Zinc Ferrite ZF3MBPC.**

#### 4.5.2 Catalyst Testing Zinc Ferrite ZF3MBPC.

The reactions involving zinc ferrite ZF3MBPC are detailed in table 3.7 in section 3.6.3 part of which is reproduced below in table 4.25 and the test procedures are given in sections 3.6.2 and 3.6.3.

Table 4.25 Catalyst Testing List Zinc Ferrite ZF3MBPC.

Reaction No	Catalyst Code	Bed Vol (cm <sup>3</sup> )	Weight (g)
8	ZF3MBPC	3	3.7896
12	ZF3MBPC	2	2.5316
13	ZF3MBPC	1	1.2942
16	ZF3MBPC	3	3.875
17	ZF3MBPC	1	1.2277
22	ZF3MBPC	1	1.1478
23	ZF3MBPC	1	1.1632
24	Al <sub>2</sub> O <sub>3</sub> /ZF3MBPC	3:1	1.8529:1.1170
31	Al <sub>2</sub> O <sub>3</sub> /ZF3MBPC	1:1	0.6820:1.0920
33	Al <sub>2</sub> O <sub>3</sub> /ZF3MBPC	1:1 (Mixed)	0.6490/1.1718
34	ZF3MBPC	0.5	0.6927

Figures 4.95 and 4.96 below show the product selectivities and 1-butene conversion obtained when passing 1-butene over zinc ferrite ZF3MBPC with a bed volume of 3 cm<sup>3</sup>.

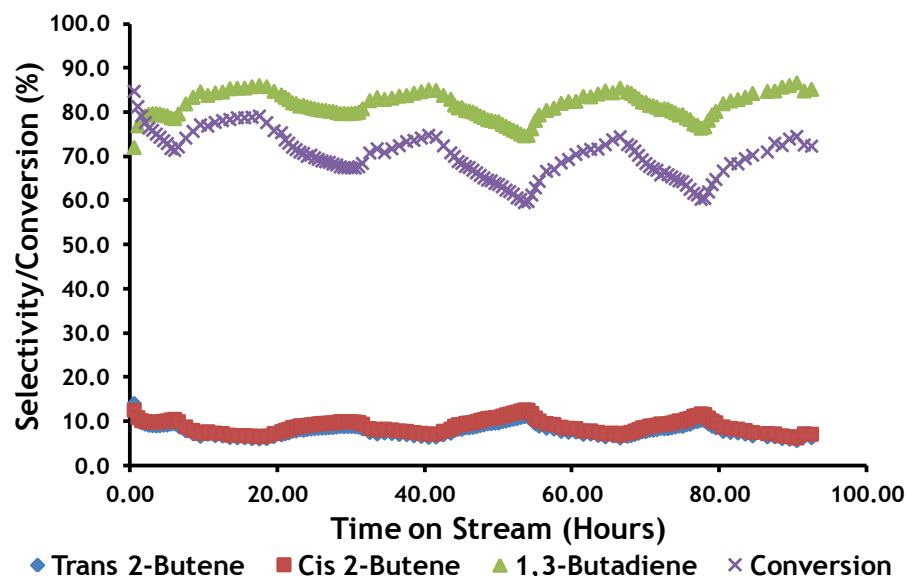


Figure 4.95 Selectivity/Conversion Major Components Zinc Ferrite ZF3MBPC Bed Volume 3 cm<sup>3</sup>.

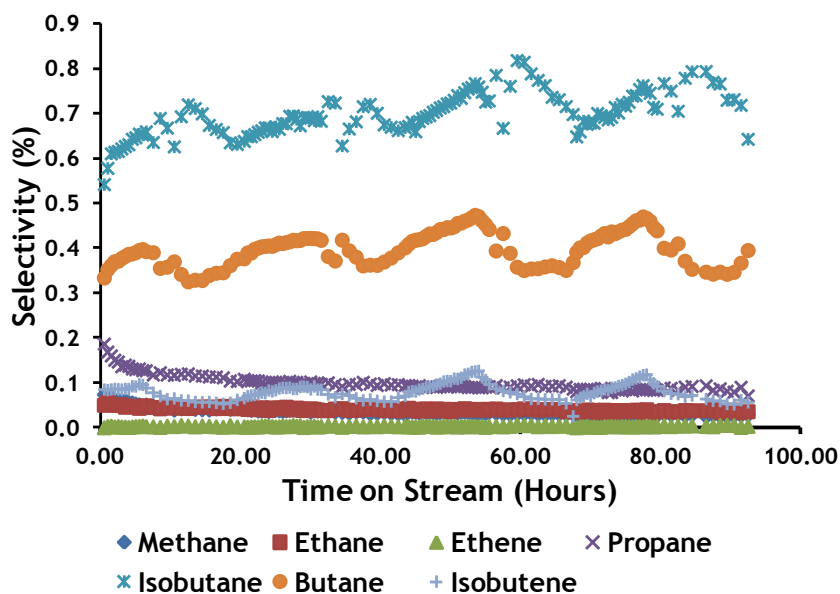


Figure 4.96 Selectivity Minor Components Zinc Ferrite ZF3MBPC Bed Volume 3 cm<sup>3</sup>.

Figures 4.97 and 4.98 below show the product selectivities and 1-butene conversion obtained when passing 1-butene over zinc ferrite ZF3MBPC with a bed volume of 2 cm<sup>3</sup>.

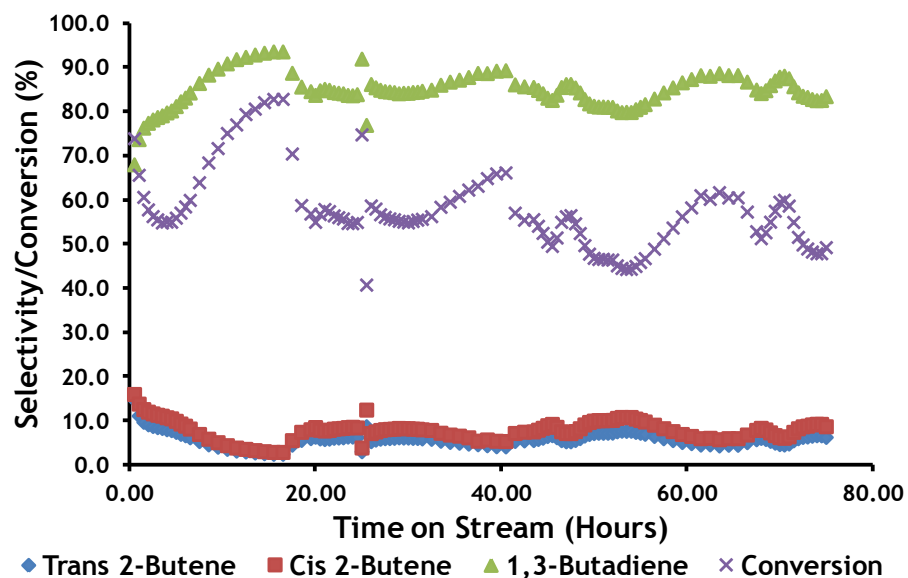


Figure 4.97 Selectivity/Conversion Major Components Zinc Ferrite ZF3MBPC Bed Volume 2 cm<sup>3</sup>.

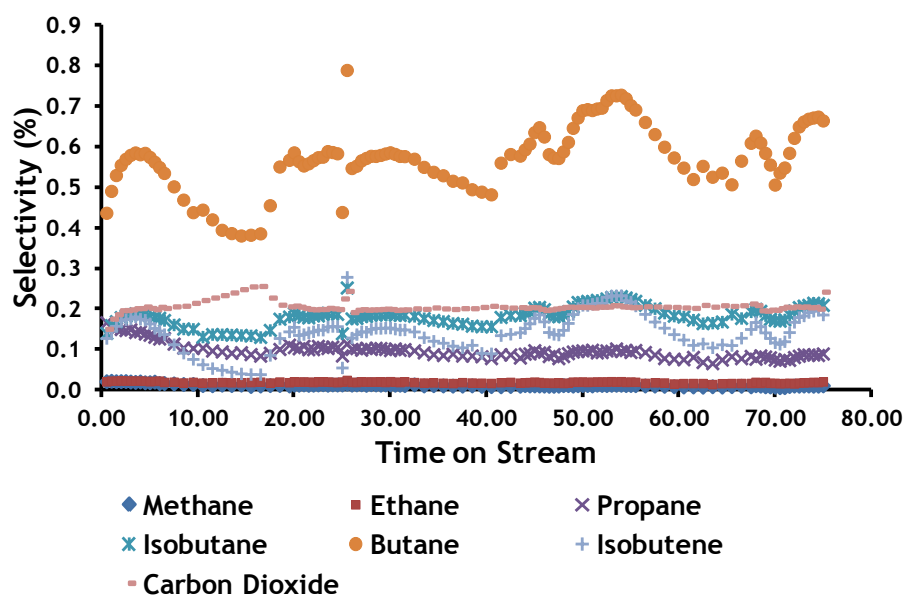


Figure 4.98 Selectivity Minor Components Zinc Ferrite ZF3MBPC Bed Volume 2 cm<sup>3</sup>.

Figures 4.99 and 4.100 below show the product selectivities and 1-butene conversion obtained when passing 1-butene over zinc ferrite ZF3MBPC with a bed volume of 1 cm<sup>3</sup>.

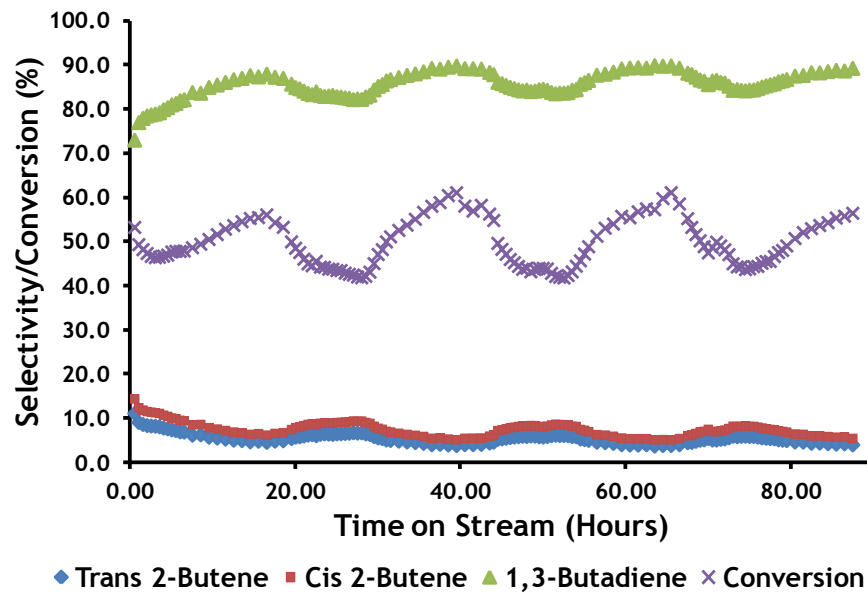


Figure 4.99 Selectivity/Conversion Major Components Zinc Ferrite ZF3MBPC Bed Volume 1 cm<sup>3</sup>

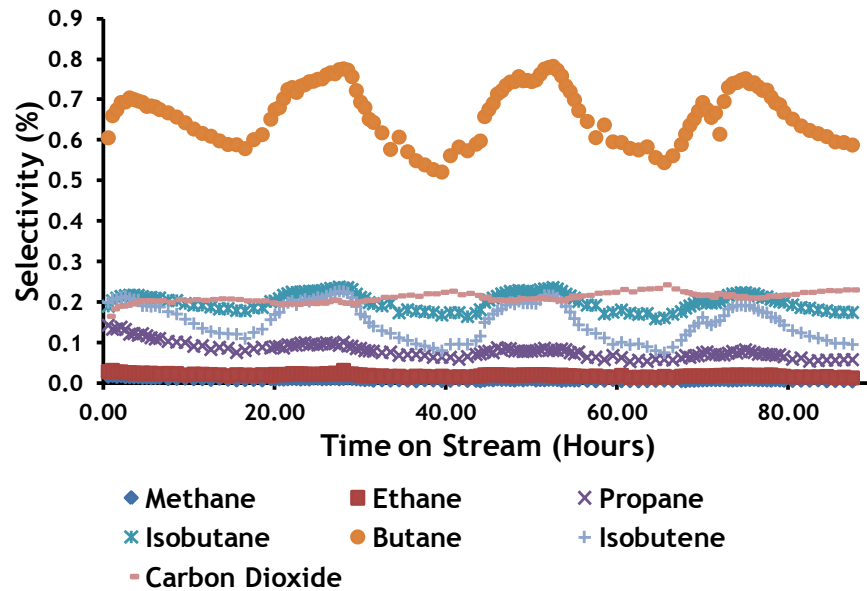


Figure 4.100 Selectivity Minor Components Zinc Ferrite ZF3MBPC Bed Volume 1 cm<sup>3</sup>.

Figures 4.101 and 4.102 below show the product selectivities and 1-butene conversion obtained when passing 1-butene over zinc ferrite ZF3MBPC with a bed volume of 0.5 cm<sup>3</sup>.

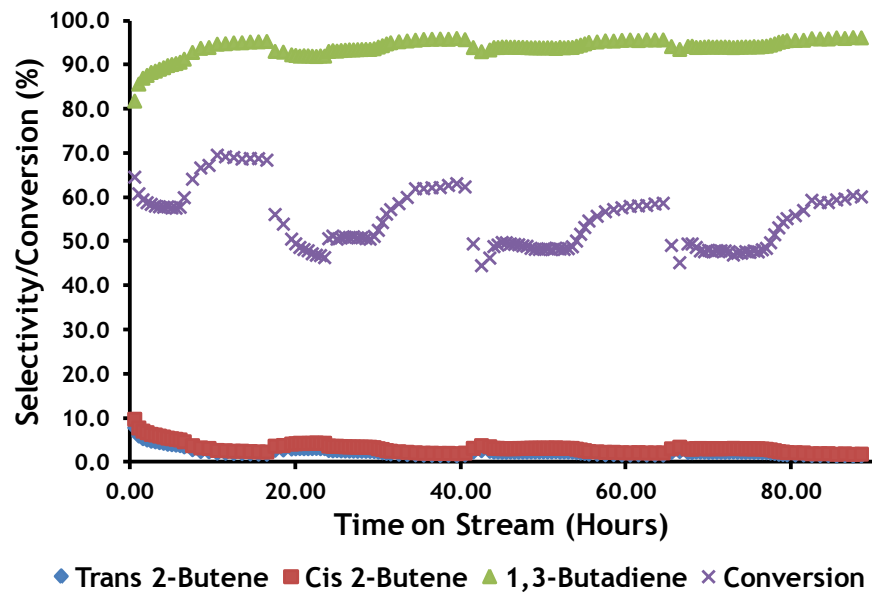


Figure 4.101 Selectivity/Conversion Major Components Zinc Ferrite ZF3MBPC Bed Volume 0.5 cm<sup>3</sup>.

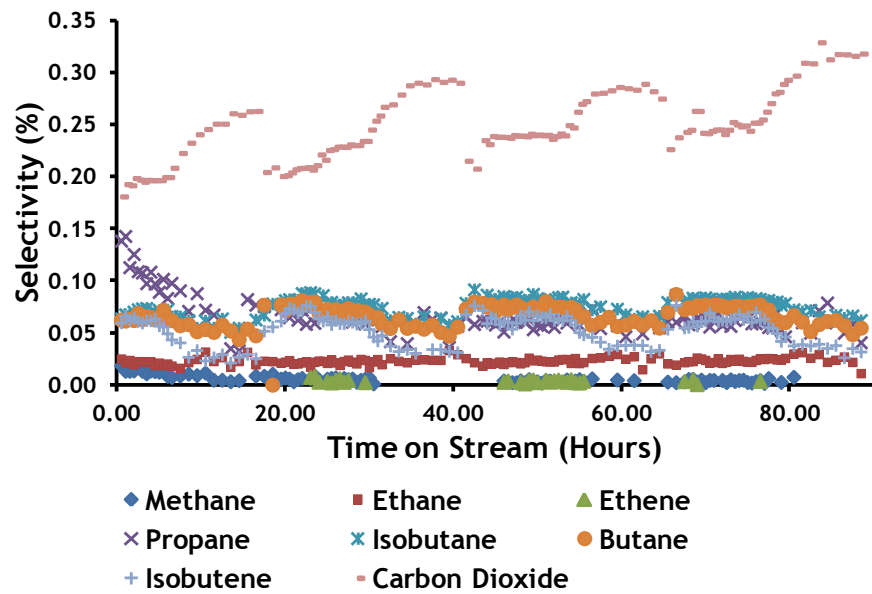


Figure 4.102 Selectivity Minor Components Zinc Ferrite ZF3MBPC Bed Volume 0.5 cm<sup>3</sup>.

Figure 4.103 and table 4.26 below show the variation in product selectivity and 1-butene conversion at 50 hours on stream zinc ferrite ZF3MBPC with differing bed volume.

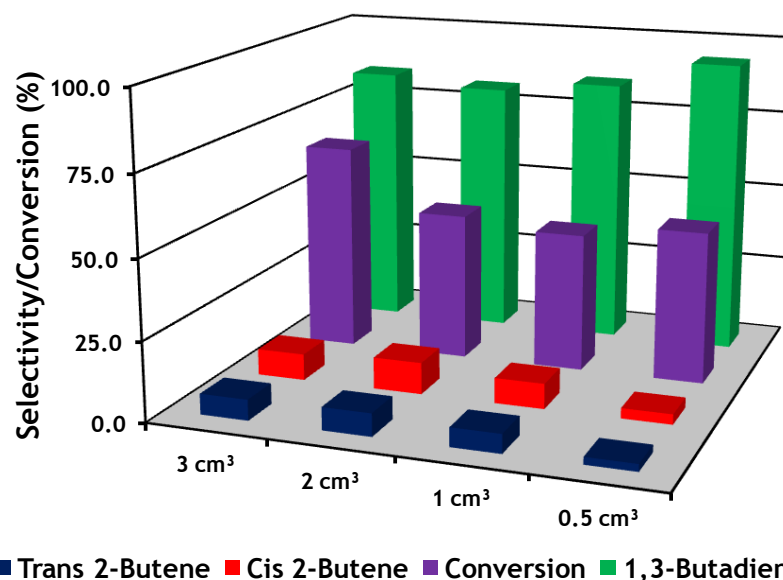


Figure 4.103 Bed Volume Comparison of Selectivities and Conversion at 50 Hours on Stream Zinc Ferrite ZF3MBPC.

Table 4.26 Bed Volume Comparison of Selectivities and Conversion at 50 Hours on Stream Zinc Ferrite ZF3MBPC.

	3 cm <sup>3</sup>	2 cm <sup>3</sup>	1 cm <sup>3</sup>	0.5 cm <sup>3</sup>
Trans 2-Butene	7	7	6	2
Cis 2-Butene	8	10	8	3
1,3-Butadiene	84	81	85	94
Conversion	66	47	44	48

Figures 4.104 to 4.110 below show the product selectivities and 1-butene conversion obtained when passing 1-butene over zinc ferrite ZF3MBPC with varying reactor temperatures.

Normal operating temperature used in the catalyst testing regime is 693 K. Reaction temperatures were raised or lowered to determine the effect on conversion and selectivities. After each temperature change the reaction temperature was returned to 693 K to ascertain if the conversion and selectivities returned to normal.

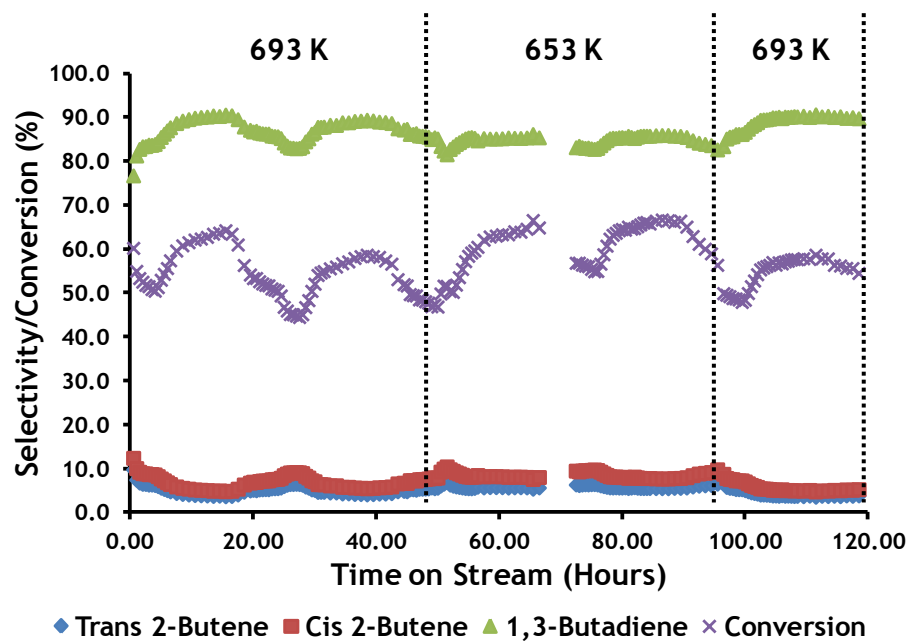


Figure 4.104 Selectivity/Conversion Major Components Zinc Ferrite ZF3MBPC Temperature Variation 693 K - 653 K - 693 K.

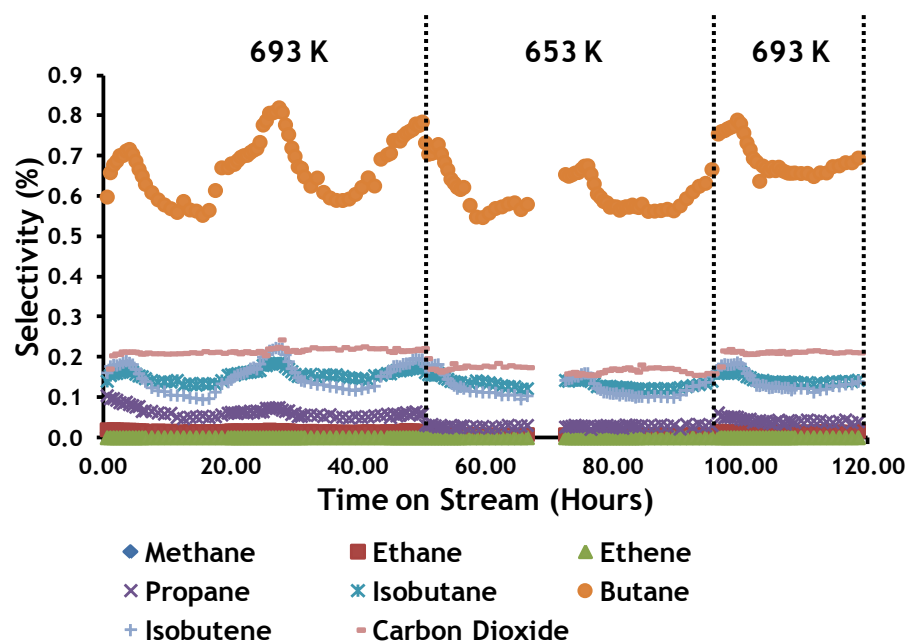


Figure 4.105 Selectivity Minor Components Zinc Ferrite ZF3MBPC Temperature Variation 693 K - 653 K - 693 K.

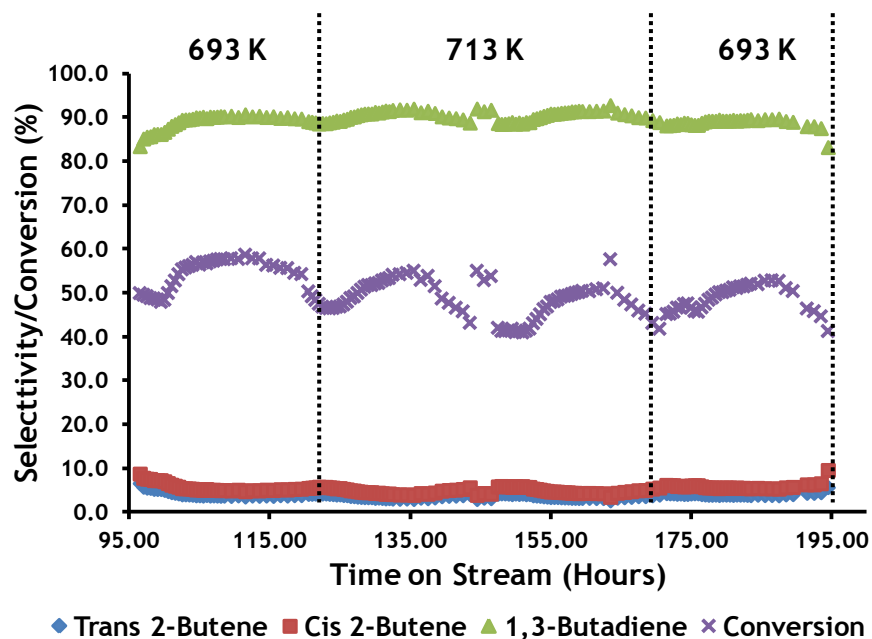


Figure 4.106 Selectivity/Conversion Major Components Zinc Ferrite ZF3MBPC Temperature Variation 693 K - 713 K - 693 K.

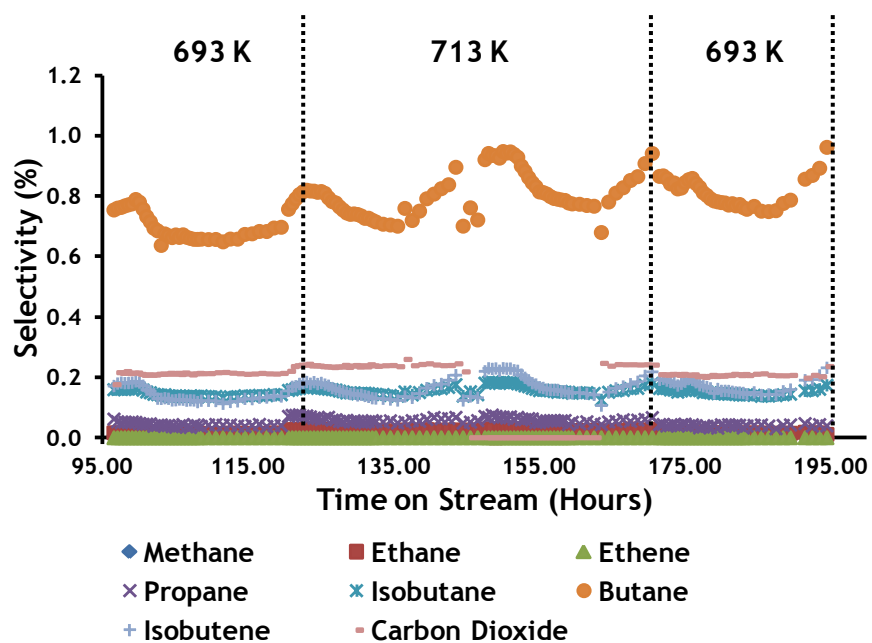


Figure 4.107 Selectivity Minor Components Zinc Ferrite ZF3MBPC Temperature Variation 693 K - 713 K - 693 K.

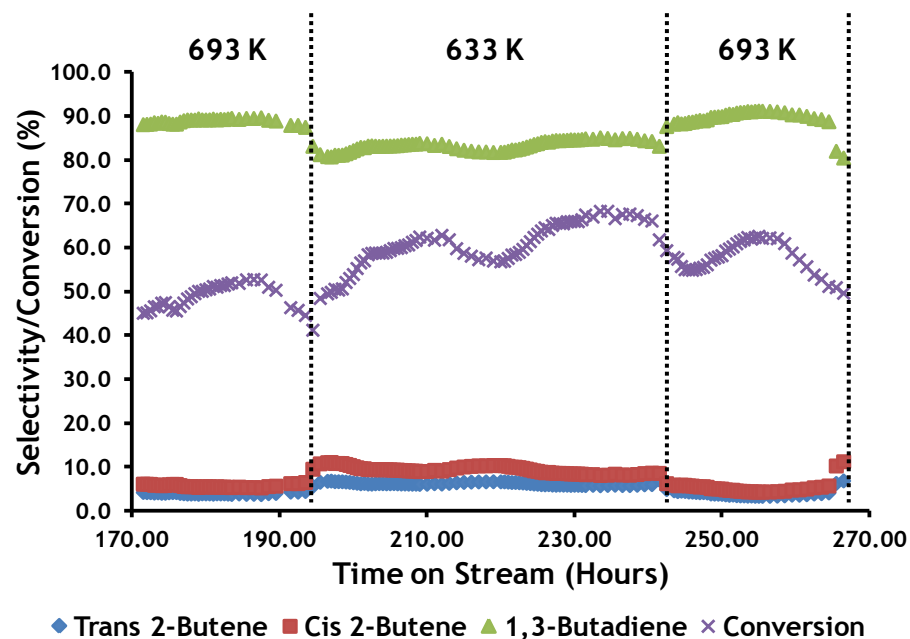


Figure 4.108 Selectivity/Conversion Major Components Zinc Ferrite ZF3MBPC Temperature Variation 693 K - 633 K - 693 K.

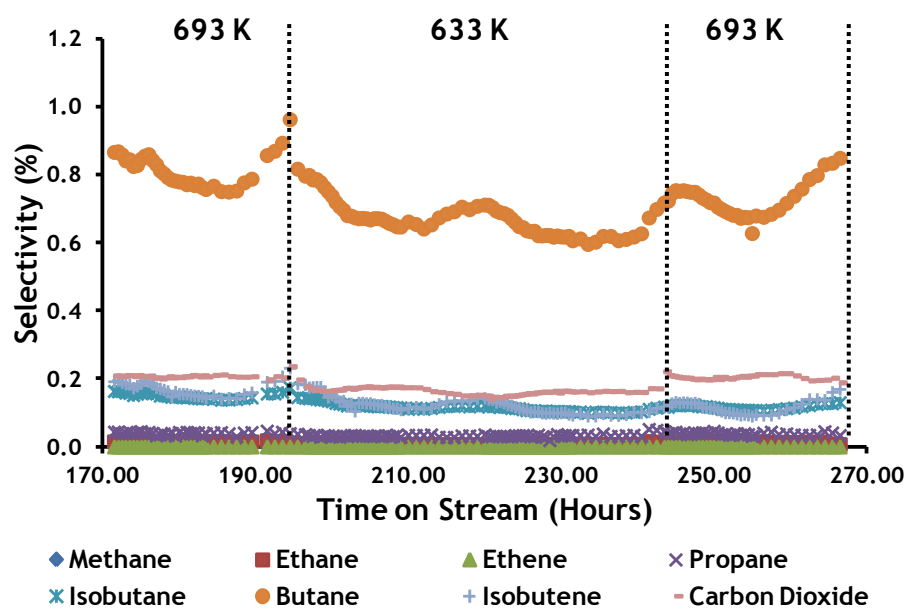


Figure 4.109 Selectivity Minor Components Zinc Ferrite ZF3MBPC Temperature Variation 693 K - 633 K - 693 K.

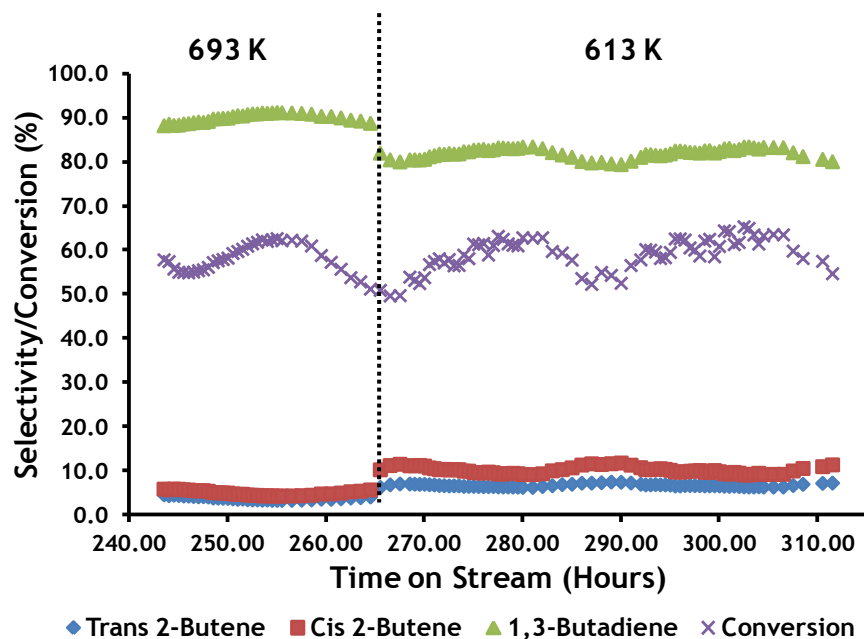


Figure 4.110 Selectivity/Conversion Major Components Zinc Ferrite ZF3MBPC Temperature Variation 693 K - 613 K.

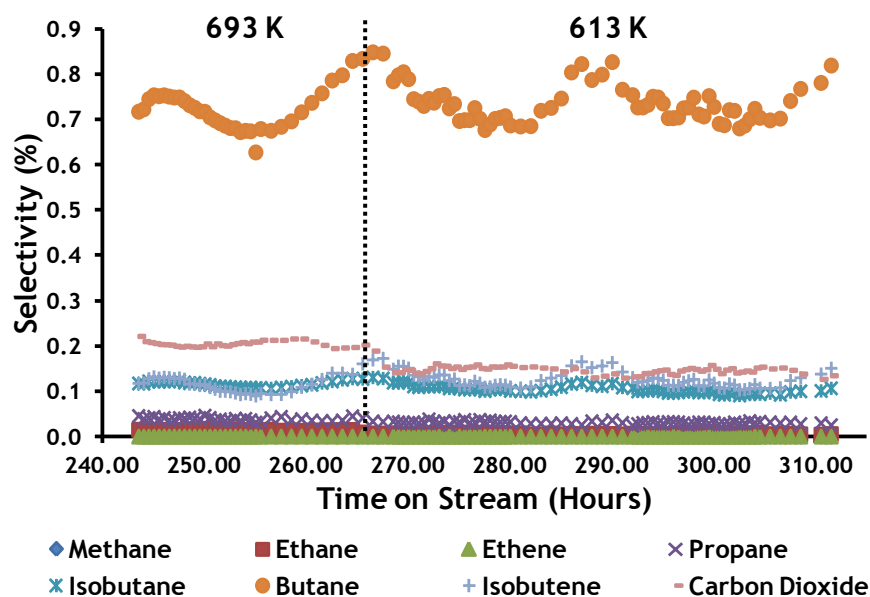


Figure 4.111 Selectivity Minor Components Zinc Ferrite ZF3MBPC Temperature Variation 693 K - 613 K.

Table 4.27 below shows the average 1-butene conversion, cis-2-butene, trans-2-butene and 1,3-butadiene over zinc ferrite catalyst at 693K.

Table 4.27 Average 1-Butene Conversion and Selctivities of Major Products.

	Trans 2-Butene	Cis 2-Butene	1,3-Butadiene	Conversion
Average	4.5	6.2	88.0	53.6
St. Dev.	1.0	1.5	2.5	5.1

Figures 4.112 to 4.117 below show the product selectivities and 1-butene conversion obtained when passing 1-butene over zinc ferrite ZF3MBPC with differing linear velocities. Increasing the linear velocity was achieved by either doubling original gas mix flow or by the inclusion of an equivalent flow of argon gas. Gaps in figures 4.112 to 4.113 below are due to problems with analysis equipment.

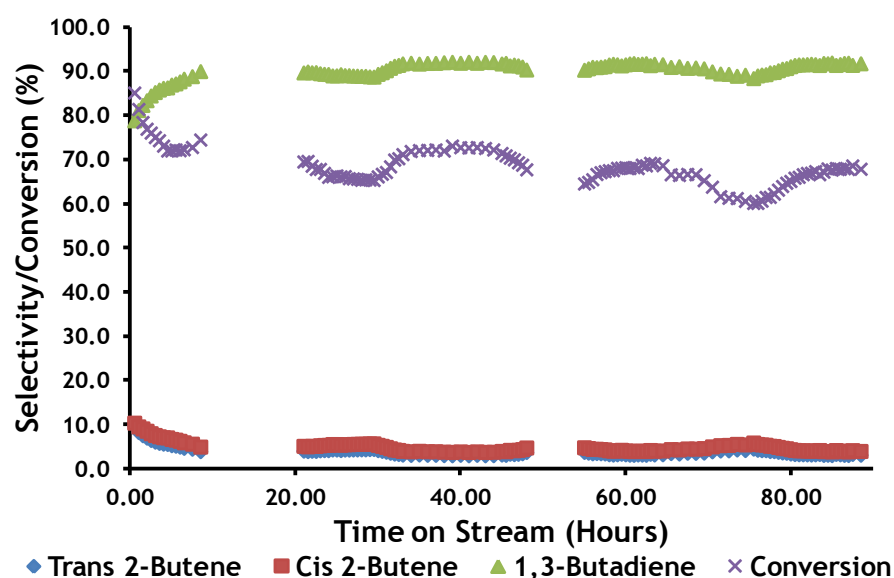


Figure 4.112 Selectivity/Conversion Major Components Zinc Ferrite ZF3MBPC Double Flow Bed Volume 3 cm<sup>3</sup>.

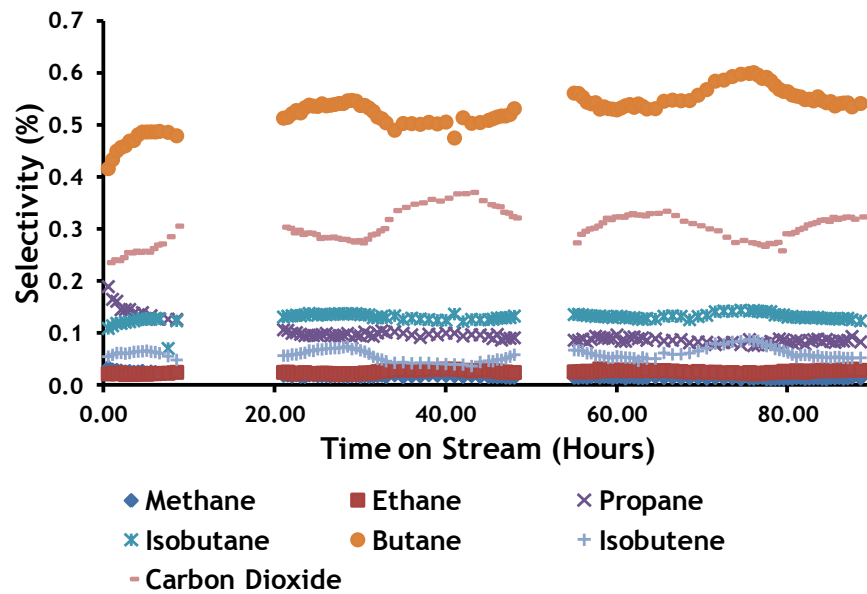


Figure 4.113 Selectivity Minor Components Zinc Ferrite ZF3MBPC Double Flow Bed Volume 3 cm<sup>3</sup>.

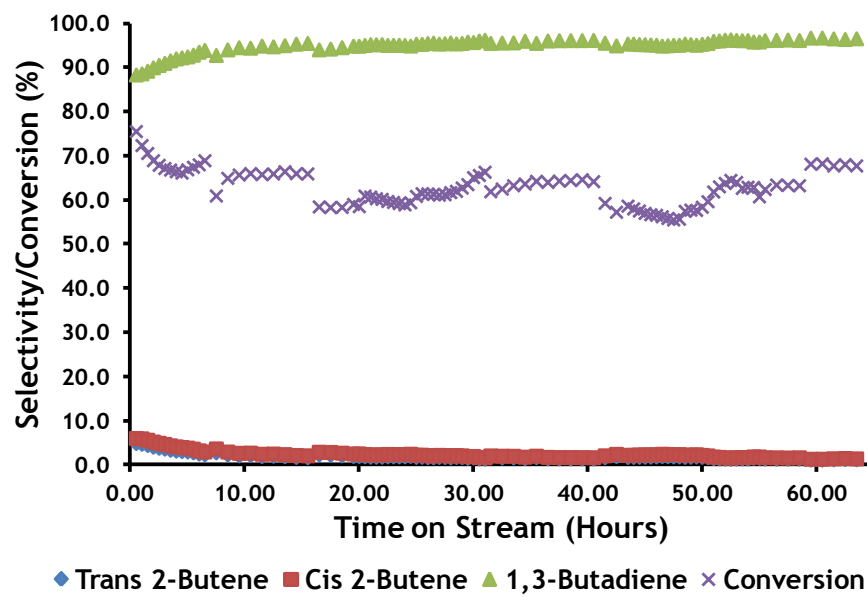


Figure 4.114 Selectivity/Conversion Major Components Zinc Ferrite ZF3MBPC Double Flow Bed Volume 1 cm<sup>3</sup>.

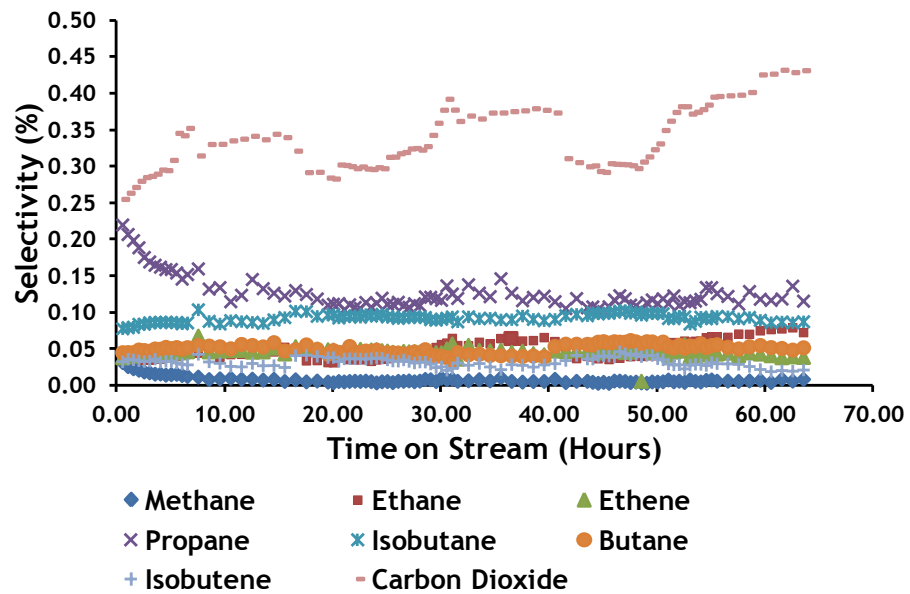


Figure 4.115 Selectivity Minor Components Zinc Ferrite ZF3MBPC Double Flow Bed Volume 1 cm<sup>3</sup>.

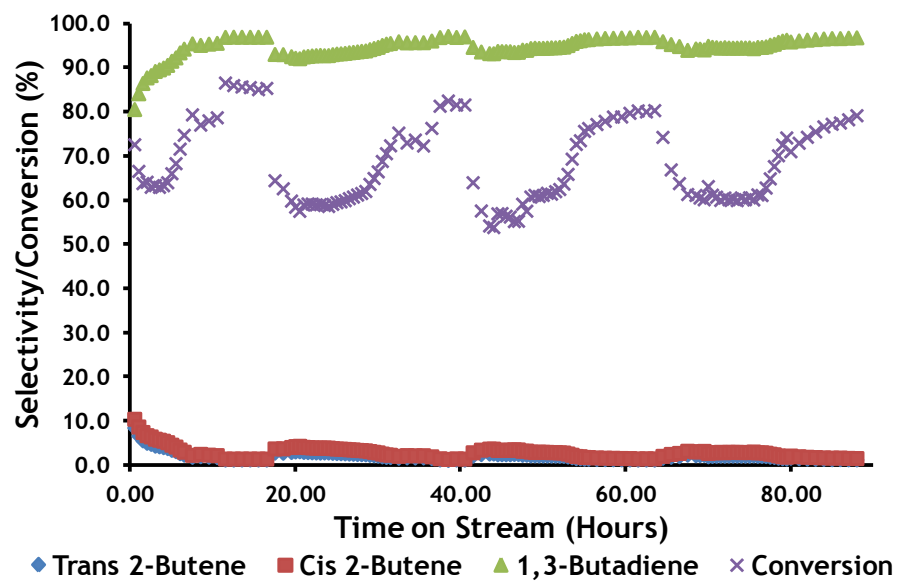


Figure 4.116 Selectivity/Conversion Major Components Zinc Ferrite ZF3MBPC Normal Flow Bed + Argon Bed Volume 1 cm<sup>3</sup>.

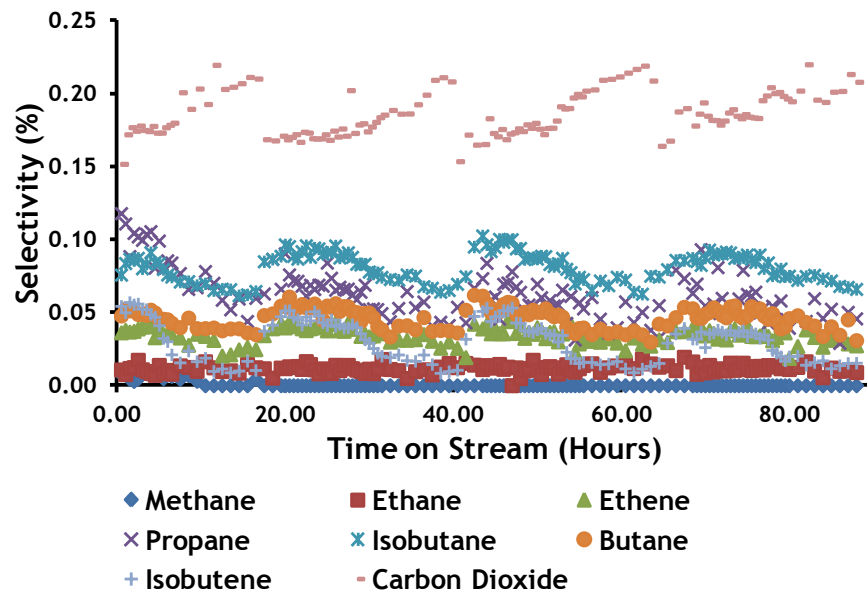


Figure 4.117 Selectivity Minor Components Zinc Ferrite ZF3MBPC Normal Flow Bed + Argon Bed Volume 1 cm<sup>3</sup>.

Figure 4.118 and table 4.28 below show the comparison of alkene selectivities and 1-butene conversion obtained at 55 hours when passing 1-butene over zinc ferrite ZF3MBPC with a bed volume of 3 cm<sup>3</sup> with normal linear velocity of 11.85 Lh<sup>-1</sup> (NLV) and double linear velocity of 23.70 Lh<sup>-1</sup> (DLV) with no argon dilution.

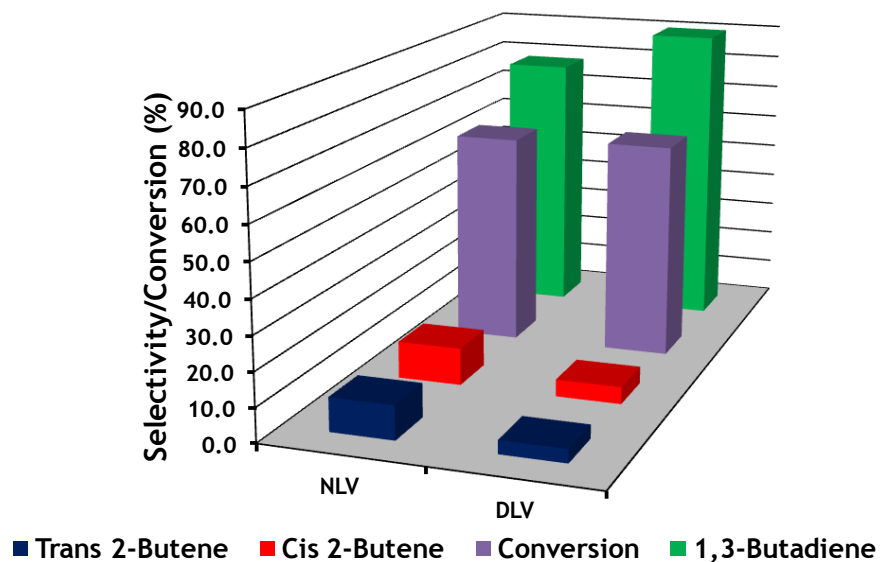
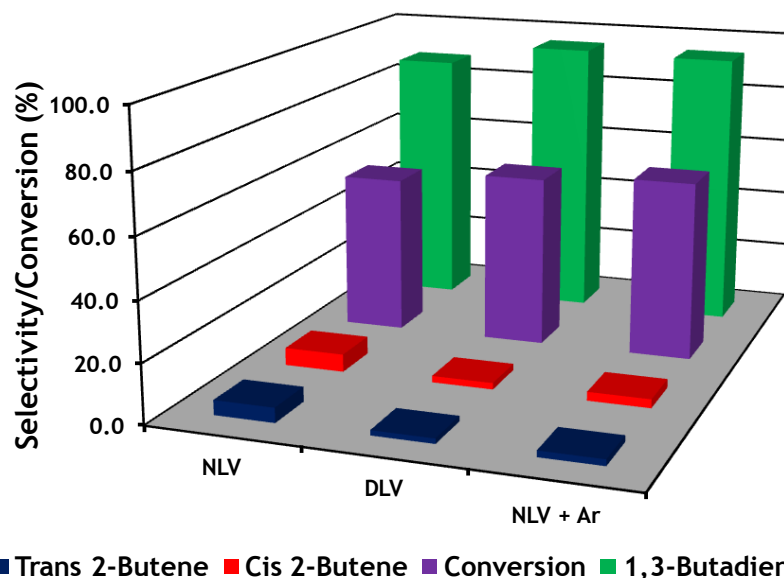


Figure 4.118 Flow Comparison of Selectivities and Conversion at 55 Hours on Stream Zinc Ferrite ZF3MBPC Bed Volume 3 cm<sup>3</sup>.

**Table 4.28** Flow Comparison of Selectivities and Conversion at 55 Hours on Stream Zinc Ferrite ZF3MBPC Bed Volume 3 cm<sup>3</sup>.

	Trans 2-Butene	Cis 2-Butene	1,3-Butadiene	Conversion
NLV	10	11	78	63
DLV	4	5	90	64

Figure 4.119 and table 4.29 below show the comparison of alkene selectivities and 1-butene conversion obtained at 50 hours when passing 1-butene over zinc ferrite ZF3MBPC with a bed volume of 1 cm<sup>3</sup> with a normal linear velocity of 11.85 Lh<sup>-1</sup> (NLV) and double linear velocity of 23.70 Lh<sup>-1</sup> with (NLV + Ar) and without argon dilution (DLV).



**Figure 4.119** Flow Comparison of Selectivities and Conversion at 50 Hours on Stream Zinc Ferrite ZF3MBPC Bed Volume 1 cm<sup>3</sup>.

**Table 4.29** Flow Comparison of Selectivities and Conversion at 50 Hours on Stream Zinc Ferrite ZF3MBPC Bed Volume 1 cm<sup>3</sup>.

	Trans 2-Butene	Cis 2-Butene	1,3-Butadiene	Conversion
NLV	5	6	88	54
DLV	2	2	95	58
NLV + Ar	2	3	94	61

Figures 4.120 to 4.125 below show the product selectivities and 1-butene conversion obtained when passing 1-butene over  $\theta$ -alumina:zinc ferrite ZF3MBPC dual bed with  $\theta$ -alumina:zinc ferrite ZF3MBPC ratios of 3:1, 1:1 and mixed1:1.

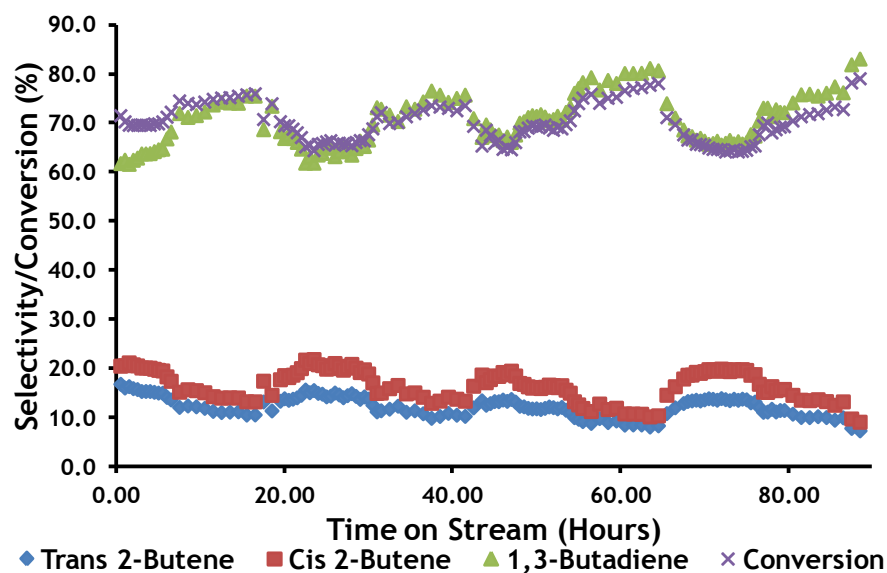


Figure 4.120 Selectivity/Conversion Major Components Dual Bed  $\theta$ -Alumina/Zinc Ferrite ZF3MBPC 3:1.

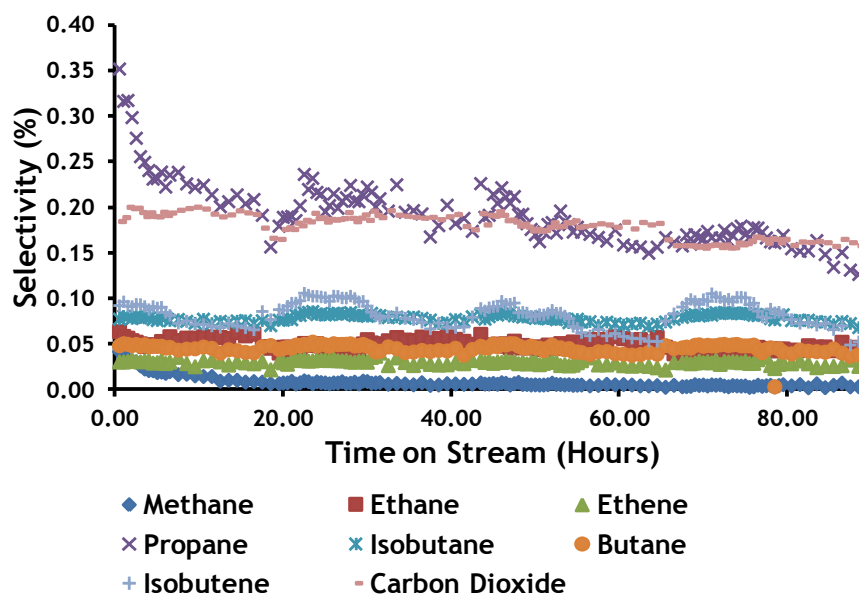


Figure 4.121 Selectivity/Minor Components Dual Bed  $\theta$ -Alumina/Zinc Ferrite ZF3MBPC 3:1.

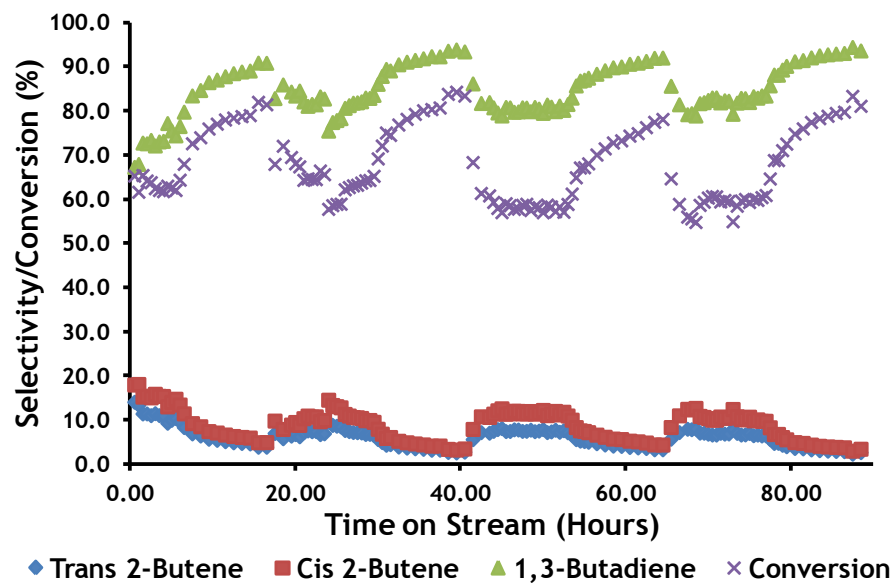


Figure 4.122 Selectivity/Conversion Major Components Dual Bed  $\theta$ -Alumina/Zinc Ferrite ZF3MBPC 1:1.

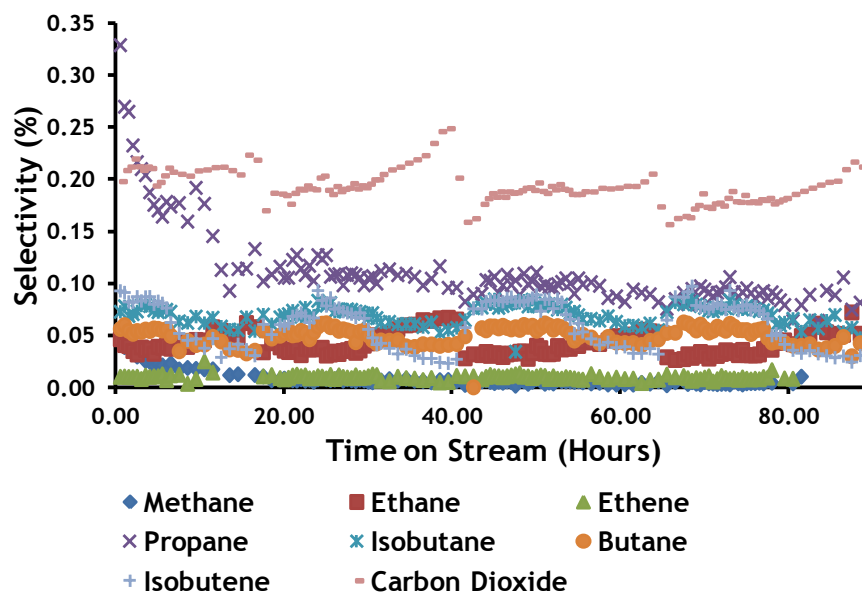


Figure 4.123 Selectivity/Minor Components Dual Bed  $\theta$ -Alumina/Zinc Ferrite ZF3MBPC 1:1.

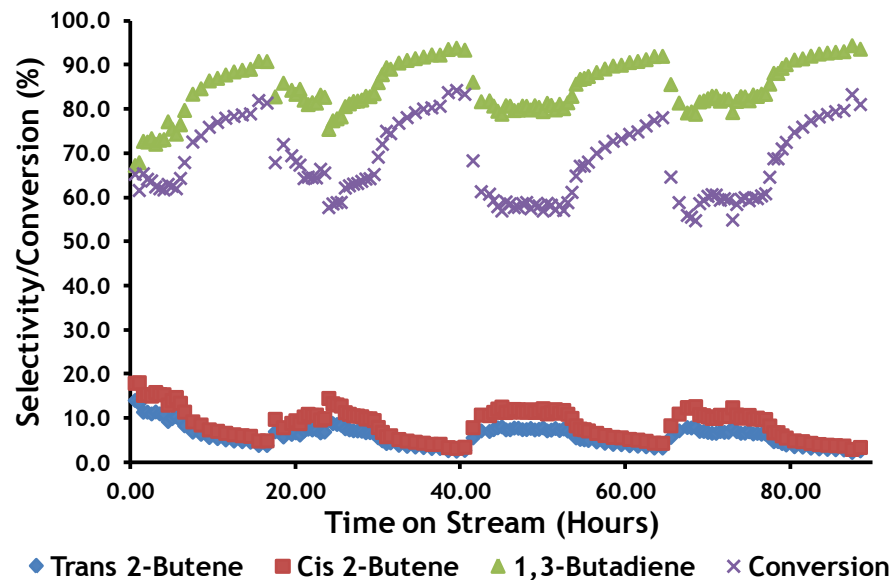


Figure 4.124 Selectivity/Conversion Major Components Dual Bed  $\theta$ -Alumina/Zinc Ferrite ZF3MBPC1:1 Mixed.

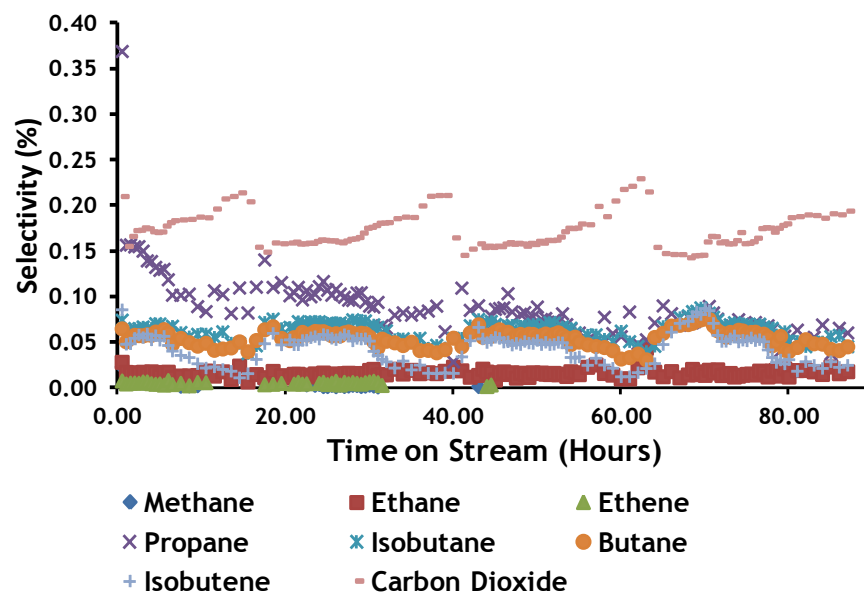


Figure 4.125 Selectivity Minor Components Dual Bed  $\theta$ -Alumina/Zinc Ferrite ZF3MBPC 1:1 Mixed.

Figure 4.126 and table 4.30 below show the comparison of alkene selectivities and 1-butene conversion obtained at 50 hours when passing 1-butene over  $\theta$ -alumina:zinc ferrite ZF3MBPC dual bed with ratios of 3:1, 1:1 and mixed 1:1.

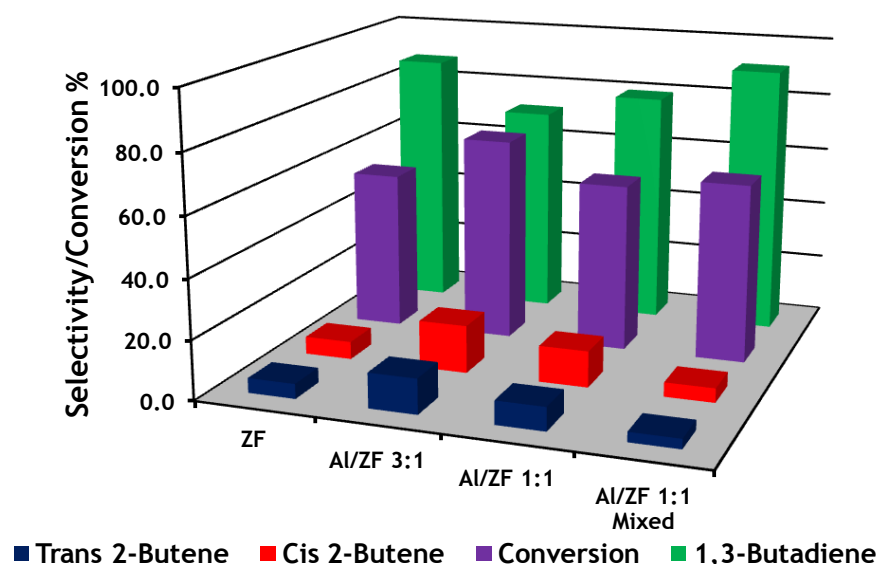


Figure 4.126 Dual Bed Comparison of Selectivities and Conversion at 50 Hours on Stream  $\theta$ -Alumina:Zinc Ferrite ZF3MBPC.

Table 4.30 Dual Bed Comparison of Selectivities and Conversion at 50 Hours on Stream  $\theta$ -Alumina:Zinc Ferrite ZF3MBPC.

	ZF	Al/ZF 3:1	Al/ZF 1:1	Al/ZF 1:1 Mixed
Trans 2-Butene	5	12	8	3
Cis 2-Butene	6	16	12	5
1,3-Butadiene	88	71	79	91
Conversion	54	69	57	61

#### 4.5.3 Post Reaction Characterisation of Zinc Ferrite ZF3MBPC.

##### 4.5.3.1 Post Reaction X-Ray Diffraction Analysis of ZF3MBPC.

Ambient temperature X-Ray Diffraction was carried out as described in section 3.5.3 on zinc ferrite ZF3MBPC bed volume 3 cm<sup>3</sup>.

Figure 4.127 below shows the post reaction ambient temperature XRD profile of zinc ferrite ZF3MBPC with a particle size of 36 nm calculated from the reflection at 35.02 2 $\theta$ .

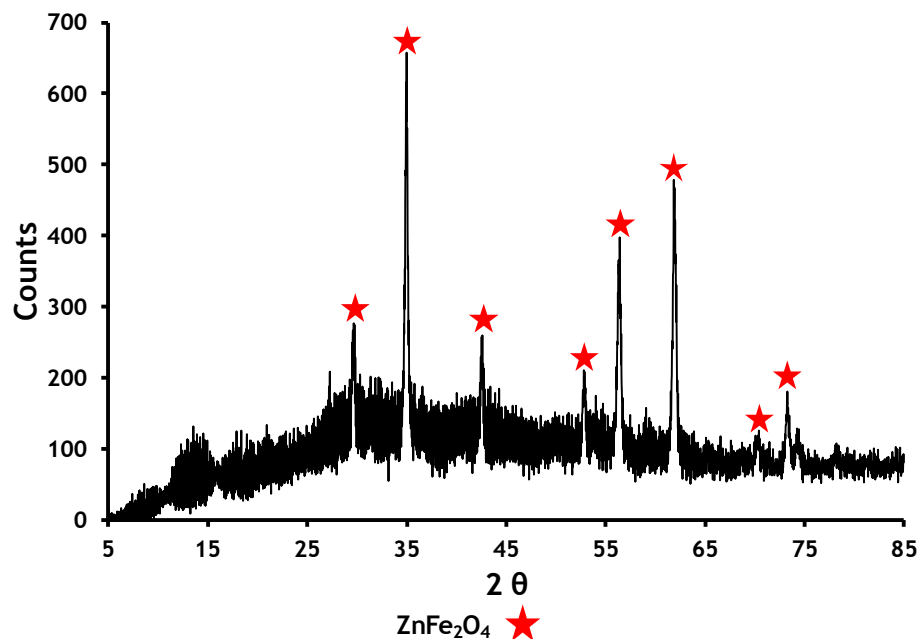


**Figure 4.127** Post Reaction Ambient Temperature XRD Spectra of Zinc Ferrite ZF3MBPC.

#### 4.5.3.2 Post Reaction Raman Spectroscopy Analysis of Zinc Ferrite ZF3MBPC.

Ambient temperature Raman spectroscopy was carried out as described in section 3.5.4 on zinc ferrite ZF3MBPC bed volume 3 cm<sup>3</sup>.

Figure 4.128 below shows the post reaction Raman bands for zinc ferrite ZF3MBPC. The Raman bands are tabulated in table 4.31 below to allow comparison.

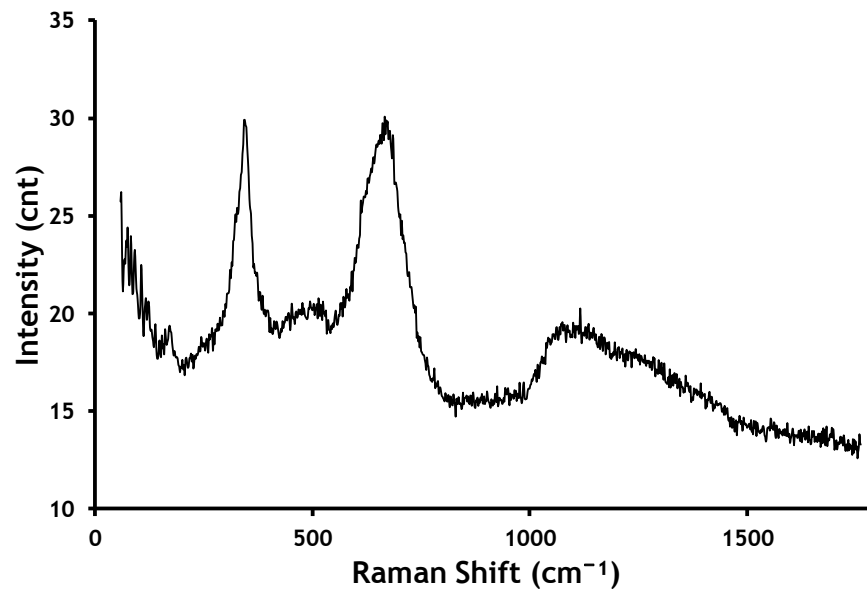


**Figure 4.128** Post Reaction Ambient Temperature Raman Spectra of Zinc Ferrite ZF3MBPC.

**Table 4.31** Comparison of Post Reaction Raman Shift Bands Zinc Ferrite ZF3MBPC to Literature.

Raman Shift Bands (cm <sup>-1</sup> )							
	Zinc Ferrite[36]						
Literature	221	246	330-355	451-498	647-659	1091-1106	1271-1298
Zinc Ferrite ZF3MBPC			344	494	666	1086	

#### 4.5.3.3 Post Reaction Surface Area Measurements of Zinc Ferrite ZF3MBPC.

Surface area determination was carried out as described in section 3.5.1 on zinc ferrite ZF3MBPC bed volume 3 cm<sup>3</sup>.

Table 4.32 below shows surface area, pore diameter and cumulative pore volume for zinc ferrite ZF3MBPC.

**Table 4.32 Post Reaction Surface Area Measurements of Zinc Ferrite ZF3MBPC.**

<b>Catalyst</b>	<b>Surface Area (m<sup>2</sup>g<sup>-1</sup>)</b>	<b>Pore Diameter (nm)</b>	<b>Cumulative Pore Volume (cm<sup>3</sup>g<sup>-1</sup>)</b>
<b>Zinc Ferrite ZF3MBPC</b>	15	33	0.1197

**4.5.3.4 Post Reaction Thermo-gravimetric Analysis-Differential Scanning Calorimetry Analysis of Zinc Ferrite ZF3MBPC.**

Thermo-gravimetric analysis/differential scanning calorimetry was carried out as described in section 3.5.2 on zinc ferrite ZF3MBPC bed volume 3 cm<sup>3</sup>.

No exothermic or endothermic events were seen on the DSC measurement. Figure 4.129 below shows weight losses and gains which happen simultaneously due to the burning off of coke and the oxidation of newly exposed reduced sites within the catalyst.

Figure 4.129 below shows a total weight loss of less than 1 % from the post reaction zinc ferrite ZF3MBPC over the temperature range 290 K to 970 K.

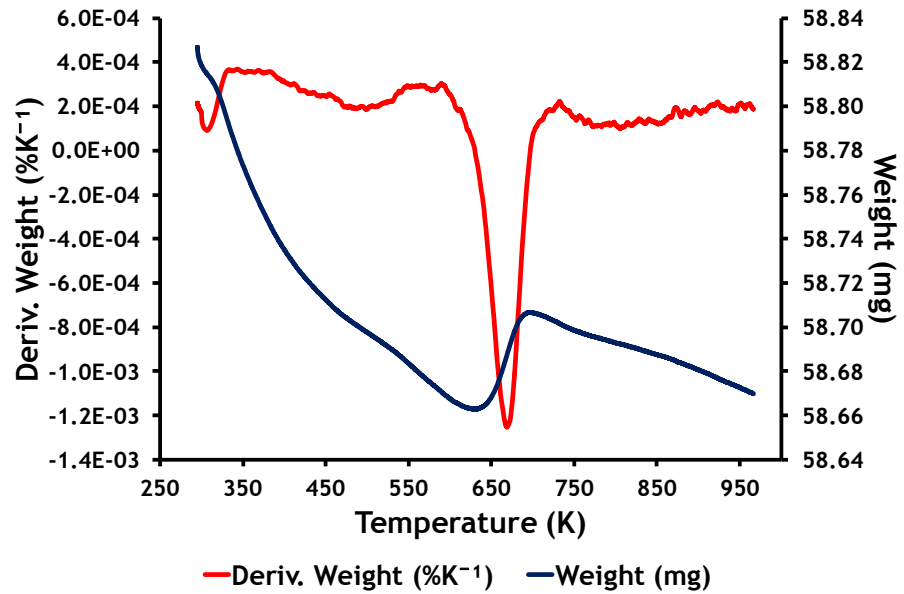


Figure 4.129 Post Reaction Zinc Ferrite ZF3MBPC TGA and Derivative Weight.

Figure 4.130 below shows the evolution of carbon dioxide at 650 K, relative to the derivative weight.

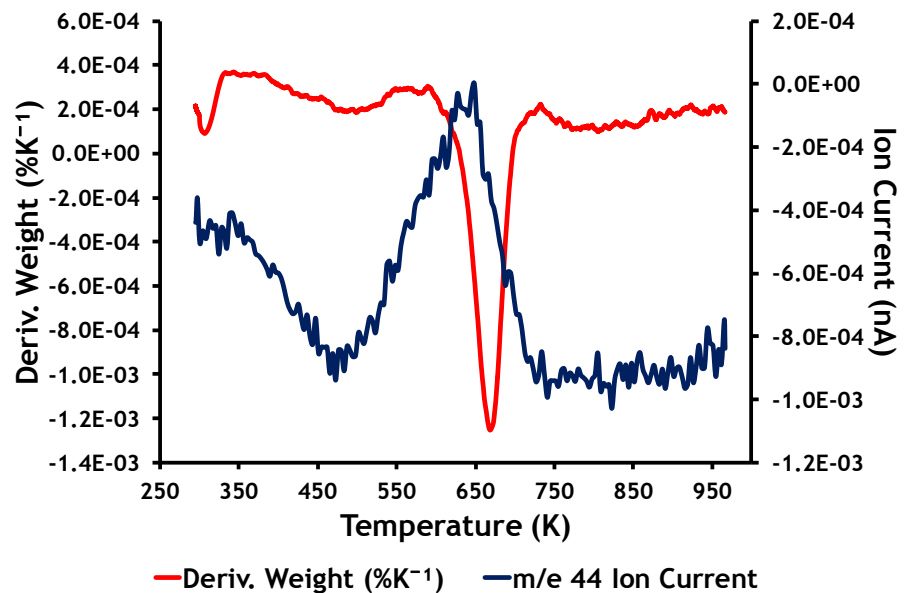


Figure 4.130 Post Reaction TGA/DSC Mass Spectrometer Profile from Zinc Ferrite ZF3MBPC m/e 44.

#### 4.5.3.5 Post Reaction Acid Site Analysis of Zinc Ferrite ZF3MBPC.

Acid site analysis was carried out as described in section 3.7.5 on zinc ferrite ZF3MBPC bed volume 3 cm<sup>3</sup>.

Figure 4.131 below shows two acid sites on zinc ferrite ZF3MBPC; one weak acid site and one medium acid site, showing the loss of one medium acid site and one strong acid site from the pre-reaction ZF3MBPC.

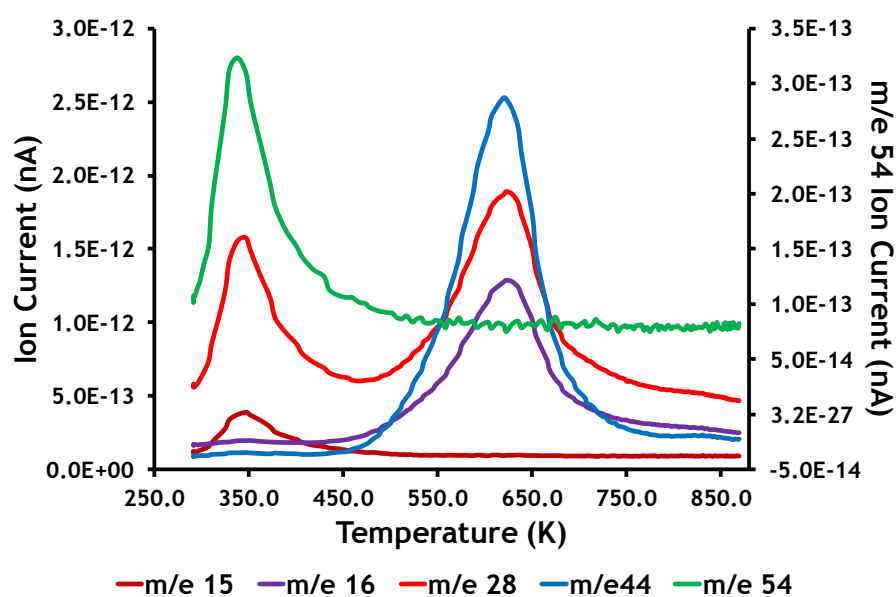
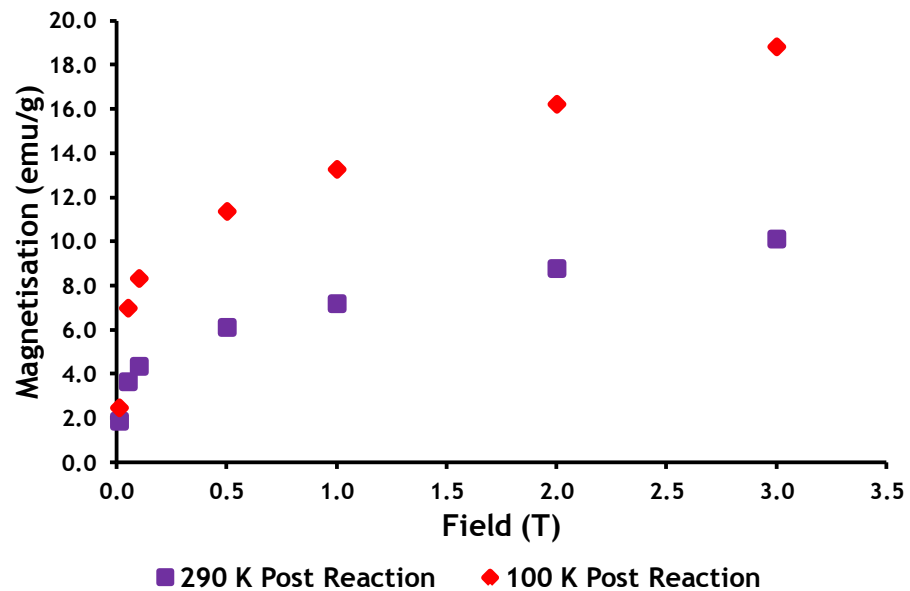


Figure 4.131 Post Reaction Zinc Ferrite ZF3MBPC Acid Site Analysis.

#### 4.5.3.6 Post Reaction Magnetic and Electron Paramagnetic Resonance Measurements of Zinc Ferrite ZF3MBPC.

Magnetic measurement analysis was carried out as described in section 3.7.6.1 on zinc ferrite ZF3MBPC bed volume 3 cm<sup>3</sup>.

Figure 4.132 below shows the magnetic properties of post reaction zinc ferrite ZF3MBPC.



**Figure 4.132 Post Reaction Zinc Ferrite ZF3MBPC SQUID Magnetic Measurement.**

The post-reaction measurement gives a similar result to that observed pre-reaction, however a decrease in the amount of magnetism is observed.

Electron Paramagnetic Resonance measurement analysis was carried out as described in section 3.7.6.2 on zinc ferrite ZF3MBPC bed volume 3 cm<sup>3</sup>.

Figure 4.133 below shows the EPR profile zinc ferrite ZF3MBPC.

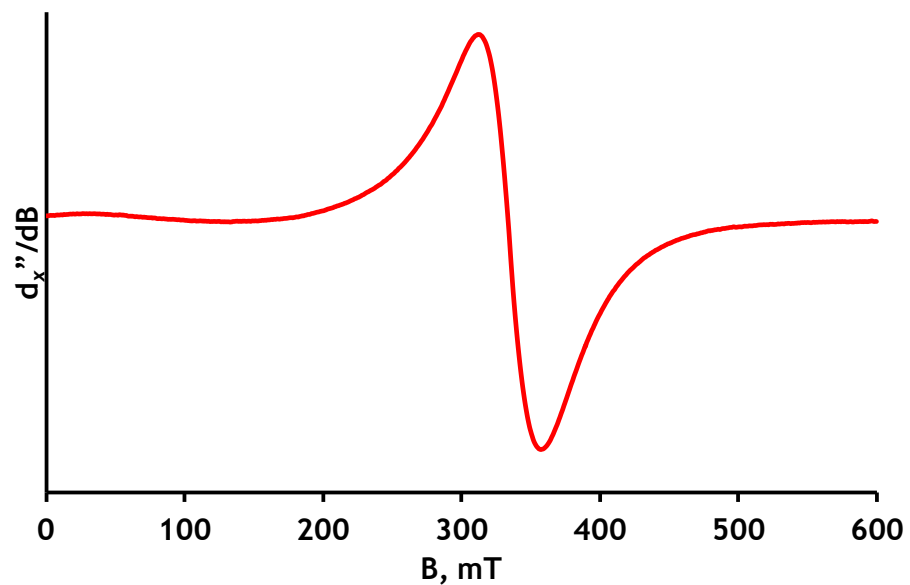


**Figure 4.133 EPR Profile of Post Reaction Zinc Ferrite ZF3MBPC.**

The post-reaction measurement gives a similar result to that observed pre-reaction, however there is a slight broadening of the profile in the post-reaction system.

#### **4.6 Zinc Ferrite ZF3MBPD Bulk Catalyst.**

##### **4.6.1 Pre-Reaction Characterisation of Zinc Ferrite ZF3MBPD.**

###### **4.6.1.1 Pre-Reaction AA Analysis of Zinc Ferrite ZF3MBPD.**

Atomic adsorption analysis was carried out as described in section 3.5.5.

Table 4.33 below shows the atomic adsorption analysis results for the iron and zinc concentrations in zinc ferrite ZF3MBPD.

**Table 4.33 Pre-Reaction AA Analysis of Zinc Ferrite ZF3MBPD.**

<b>Catalyst</b>	<b>Iron Conc (mgg<sup>-1</sup>)</b>	<b>Zinc Conc (mgg<sup>-1</sup>)</b>	<b>Fe:Zn Mole Ratio</b>
<b>ZF3MBPD</b>	412.04	231.48	2.3:1

###### **4.6.1.2 Pre-Reaction X-Ray Diffraction Analysis of ZF3MBPD.**

Ambient temperature X-Ray Diffraction was carried out as described in section 3.5.3.

Figure 4.134 below shows the pre reaction ambient temperature XRD profile of zinc ferrite ZF3MBPD with a particle size of 18 nm calculated from the reflection at 35.08 2θ.

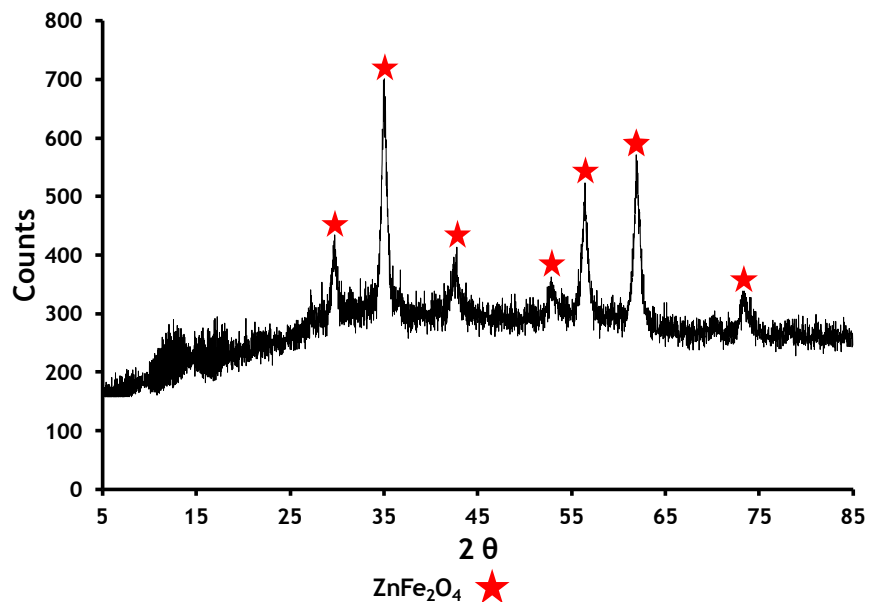


**Figure 4.134 Pre-Reaction Ambient Temperature XRD Spectra of Zinc Ferrite ZF3MBPD.**

#### **4.6.1.3 Pre-Reaction Raman Spectroscopy Analysis of Zinc Ferrite ZF3MBPD.**

Ambient temperature Raman spectroscopy was carried out as described in section 3.5.4.

Figure 4.135 below shows the pre-reaction Raman bands for zinc ferrite ZF3MBPD. The Raman bands are tabulated in table 4.34 below to allow comparison.

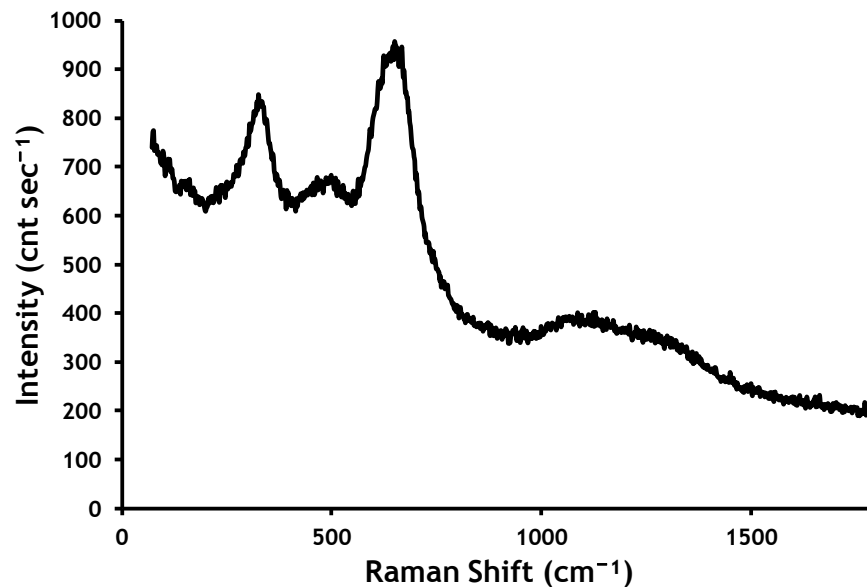


**Figure 4.135** Pre-Reaction Ambient Temperature Raman Spectroscopy of Zinc Ferrite ZF3MBPD.

**Table 4.34** Comparison of Pre-Reaction Raman Shift Bands Zinc Ferrite ZF3MBPD to Literature.

Raman Shift Bands (cm <sup>-1</sup> )							
	Zinc Ferrite[36]						
Literature	221	246	330-355	451-498	647-659	1091-1106	1271-1298
Zinc Ferrite ZF3MBPD			325	499	650	1124	

#### 4.6.1.4 Pre-Reaction Surface Area Measurements of Zinc Ferrite ZF3MBPD.

Surface area determination was carried out as described in section 3.5.1.

Table 4.35 below shows surface area, pore diameter and cumulative pore volume for zinc ferrite ZF3MBPD.

**Table 4.35 Pre-Reaction Surface Area Measurements of Zinc Ferrite ZF3MBPD.**

Catalyst	Surface Area (m <sup>2</sup> g <sup>-1</sup> )	Pore Diameter (nm)	Cumulative Pore Volume (cm <sup>3</sup> g <sup>-1</sup> )
Zinc Ferrite ZF3MBPD	50	13	0.1601

**4.6.1.5 Pre-Reaction Thermo-gravimetric Analysis-Differential Scanning Calorimetry Analysis of Zinc Ferrite ZF3MBPD.**

Thermo-gravimetric analysis/differential scanning calorimetry was carried out as described in section 3.5.2.

Figure 4.136 below shows a total weight loss of less than 1 % which can be attributed to desorption of physisorbed water.

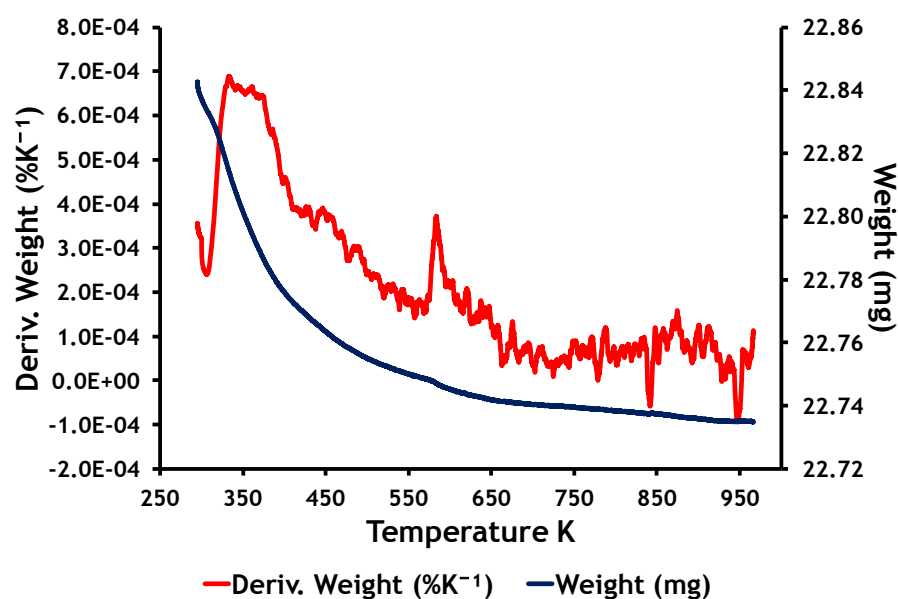


**Figure 4.136 Pre-Reaction Zinc Ferrite ZF3MBPD TGA and Derivative Weight.**

**4.6.1.6 Pre-Reaction Acid Site Analysis of Zinc Ferrite ZF3MBPD.**

Acid site analysis was carried out as described in section 3.7.5.

Figure 4.137 below shows five acid sites on zinc ferrite ZF3MBPC; two weak acid sites, one medium acid site and two strong acid sites.

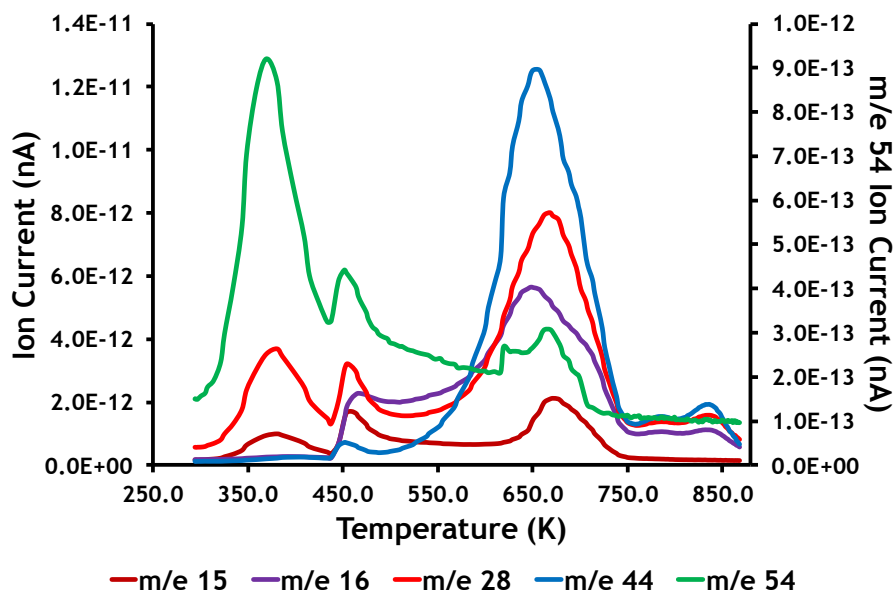


Figure 4.137 Pre-Reaction Zinc Ferrite ZF3MBPD Acid Site Analysis.

#### 4.6.2 Catalyst Testing Zinc Ferrite ZF3MBPD.

The reactions involving zinc ferrite ZF3MBPD are detailed in table 3.7 in section 3.6.3 part of which is reproduced below in table 4.36 and the test procedures are given in sections 3.6.2 and 3.6.3.

Table 4.36 Catalyst Testing List Zinc Ferrite ZF3MBPD.

Reaction No	Catalyst Code	Bed Vol (cm <sup>3</sup> )	Weight (g)
7	ZF3MBPD	3	2.7175
35	ZF3MBPD	1 (1-butene)	0.7148
36	ZF3MBPD	1 (cis-2-butene)	0.708
37	ZF3MBPD	1 (trans-2-butene)	0.6825

Figures 4.138 and 4.139 below show the product selectivities and 1-butene conversion obtained when passing 1-butene over zinc ferrite ZF3MBPD with a bed volume of 3 cm<sup>3</sup>. The gap in figures 4.138 to 4.139 below are due to problems with analysis equipment.

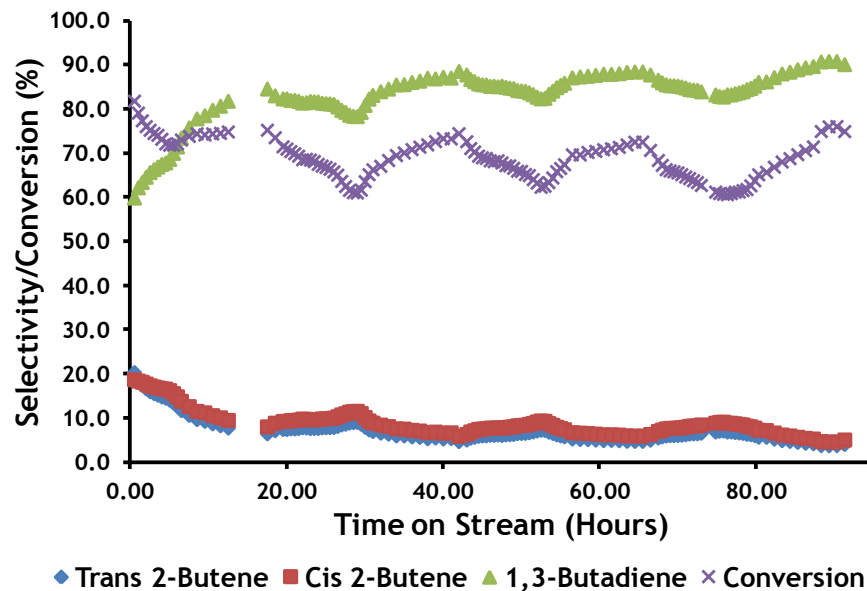


Figure 4.138 Selectivity/Conversion Major Components Zinc Ferrite ZF3MBPD Bed Volume 3 cm<sup>3</sup>.

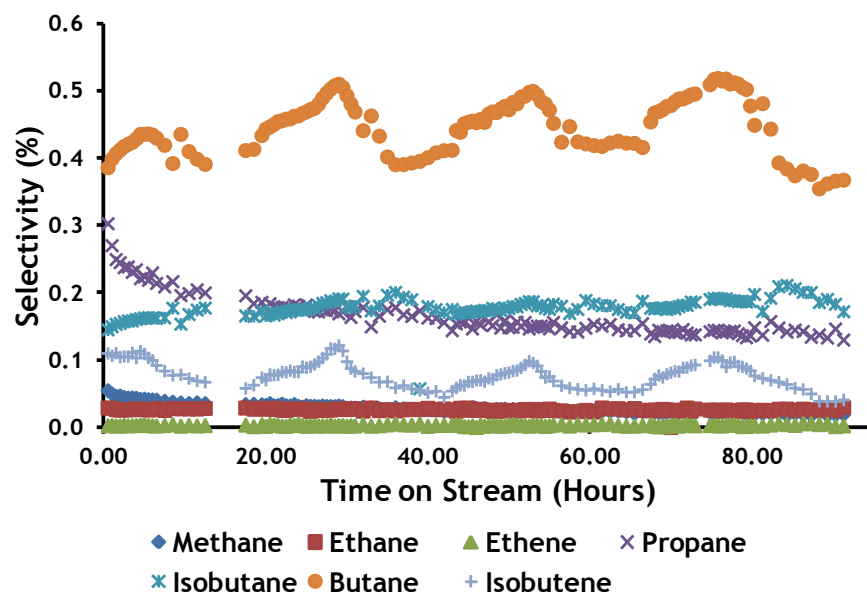


Figure 4.139 Selectivity Minor Components Zinc Ferrite ZF3MBPD Bed Volume 3 cm<sup>3</sup>.

Figures 4.140 and 4.141 below show the product selectivities and 1-butene conversion obtained when passing 1-butene over zinc ferrite ZF3MBPD with a bed volume of 1 cm<sup>3</sup>.

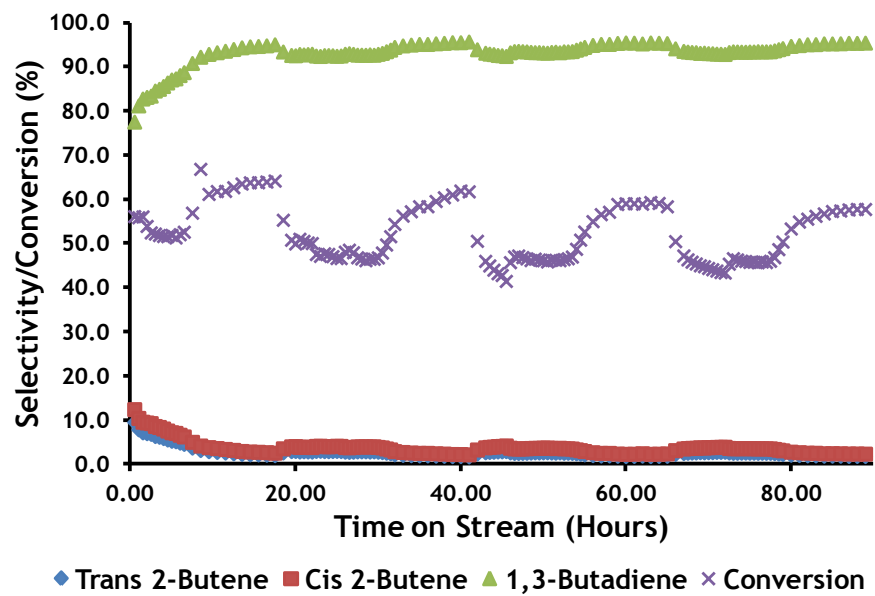


Figure 4.140 Selectivity/Conversion Major Components Zinc Ferrite ZF3MBPD Alkene 1-Butene Bed Volume 1 cm<sup>3</sup>.

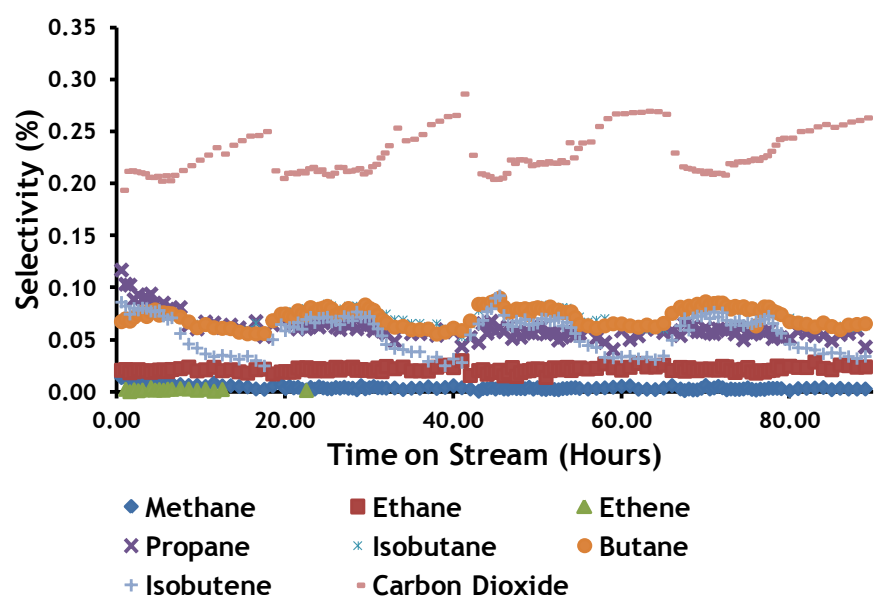


Figure 4.141 Selectivity Minor Components Zinc Ferrite ZF3MBPD Alkene 1-Butene Bed Volume 1 cm<sup>3</sup>.

Figures 4.142 and 4.143 below show the product selectivities and cis-2-butene conversion obtained when passing cis-2-butene over zinc ferrite ZF3MBPD with a bed volume of 1 cm<sup>3</sup>.

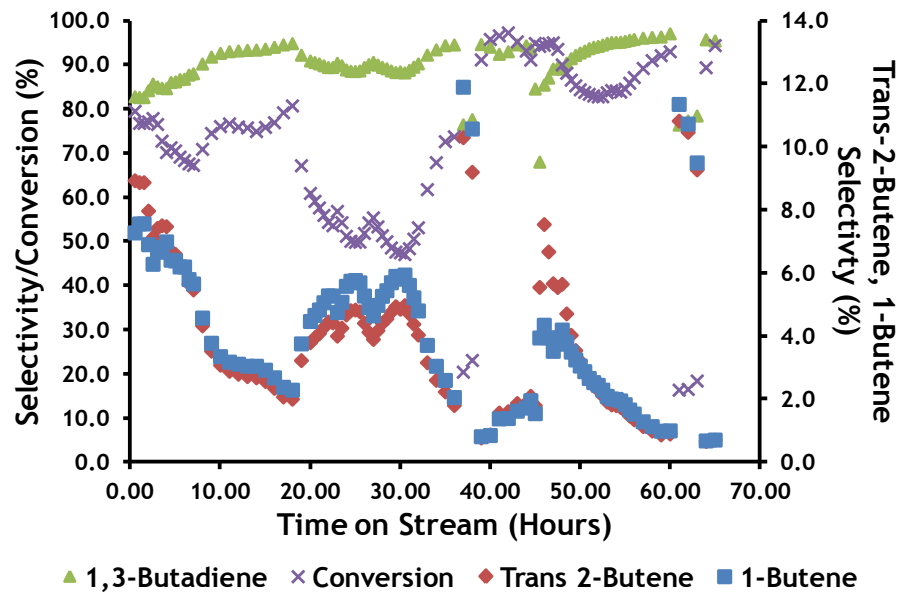


Figure 4.142 Selectivity/Conversion Major Components Zinc Ferrite ZF3MBPD Alkene Cis-2-Butene Bed Volume 1 cm<sup>3</sup>.

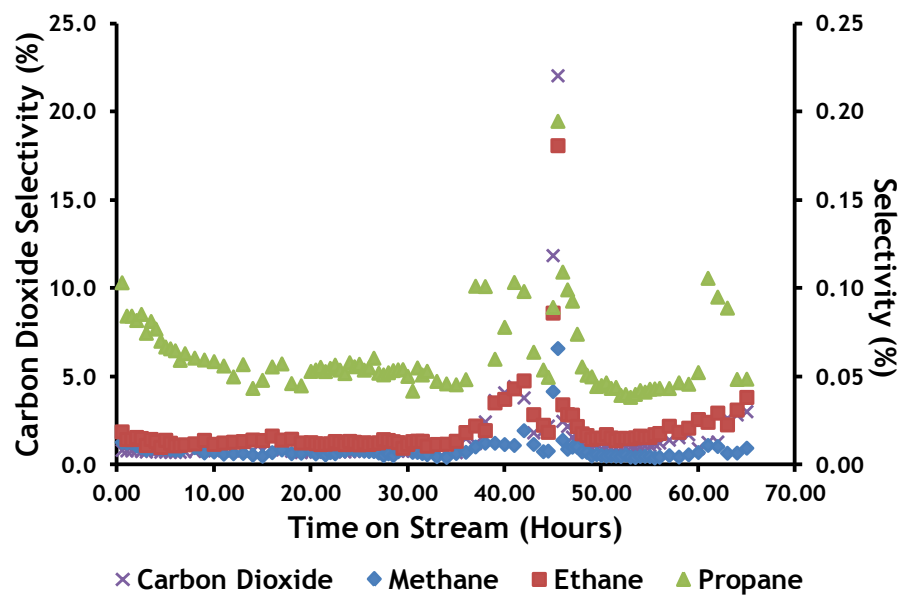


Figure 4.143 Selectivity Minor Components Zinc Ferrite ZF3MBPD Alkene Cis-2-Butene Bed Volume 1 cm<sup>3</sup>.

Figures 4.144 and 4.145 below show the product selectivities and trans-2-butene conversion obtained when passing trans-2-butene over zinc ferrite ZF3MBPD with a bed volume of 1 cm<sup>3</sup>.

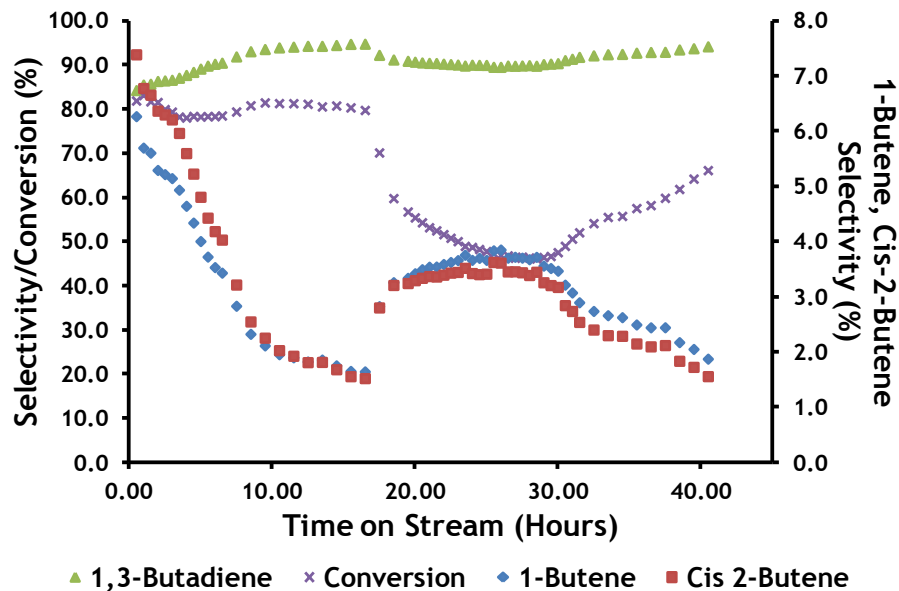


Figure 4.144 Selectivity/Conversion Major Components Zinc Ferrite ZF3MBPD Alkene Trans-2-Butene Bed Volume 1 cm<sup>3</sup>.

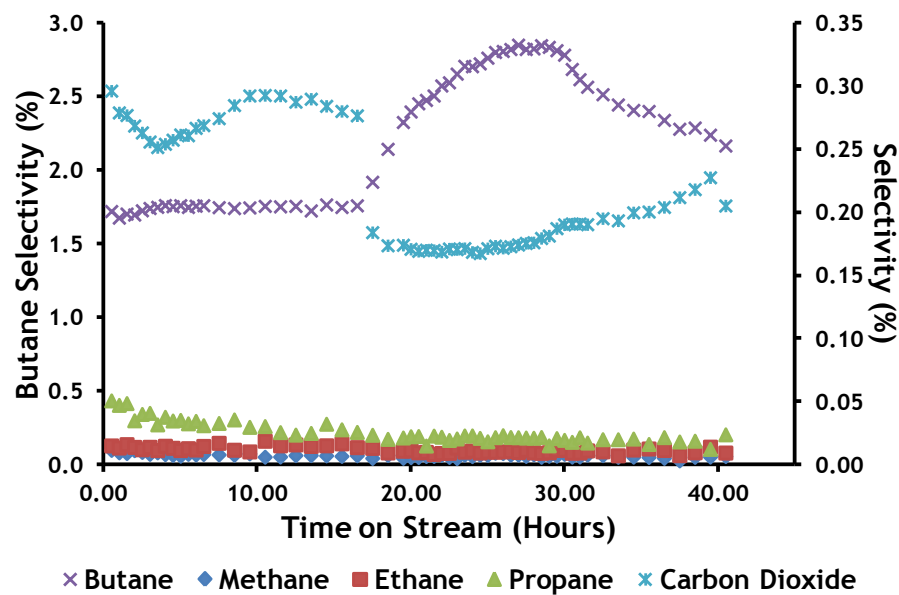


Figure 4.145 Selectivity Minor Components Zinc Ferrite ZF3MBPD Alkene Trans-2-Butene Bed Volume 1 cm<sup>3</sup>.

Figure 4.146 and table 4.37 below show the variation in product selectivity and alkene conversion at 10 hours on stream zinc ferrite ZF3MBPD with differing butane isomers.

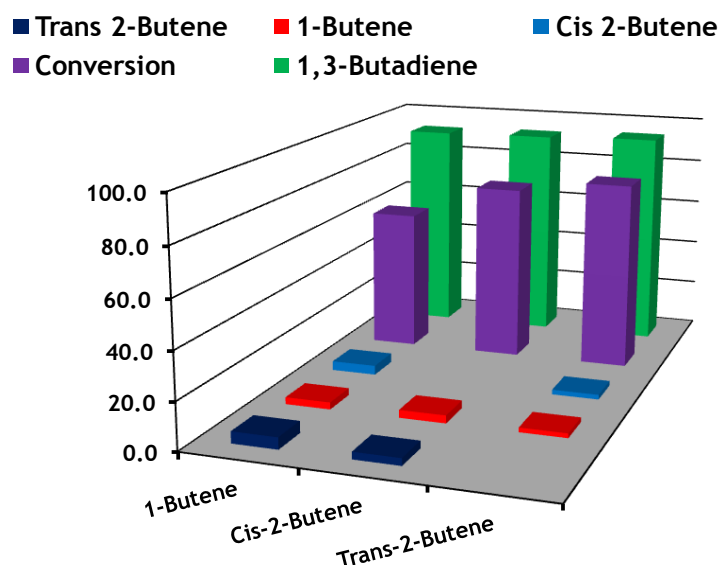


Figure 4.146 Isomer Effect on Selectivities and Conversion at 10 Hours on Stream Zinc Ferrite ZF3MBPD Bed Volume 1 cm<sup>3</sup>.

Table 4.37 Isomer Effect on Selectivities and Conversion at 10 Hours on Stream Zinc Ferrite ZF3MBPD Bed Volume 1 cm<sup>3</sup>.

	1-Butene	Cis-2-Butene	Trans-2-Butene
Trans 2-Butene	3	3	
1-Butene		3	2
Cis 2-Butene	4		2
1,3-Butadiene	92	93	94
Conversion	61	76	81

#### 4.6.3 Post Reaction Characterisation of Zinc Ferrite ZF3MBPD.

##### 4.6.3.1 Post Reaction X-Ray Diffraction Analysis of ZF3MBPD.

Ambient temperature X-Ray Diffraction was carried out as described in section 3.5.3 on zinc ferrite ZF3MBPD bed volume 3 cm<sup>3</sup>.

Figure 4.147 below shows the post reaction ambient temperature XRD profile of zinc ferrite ZF3MBPD with a particle size of 29 nm calculated from the reflection at 35.0 2θ.

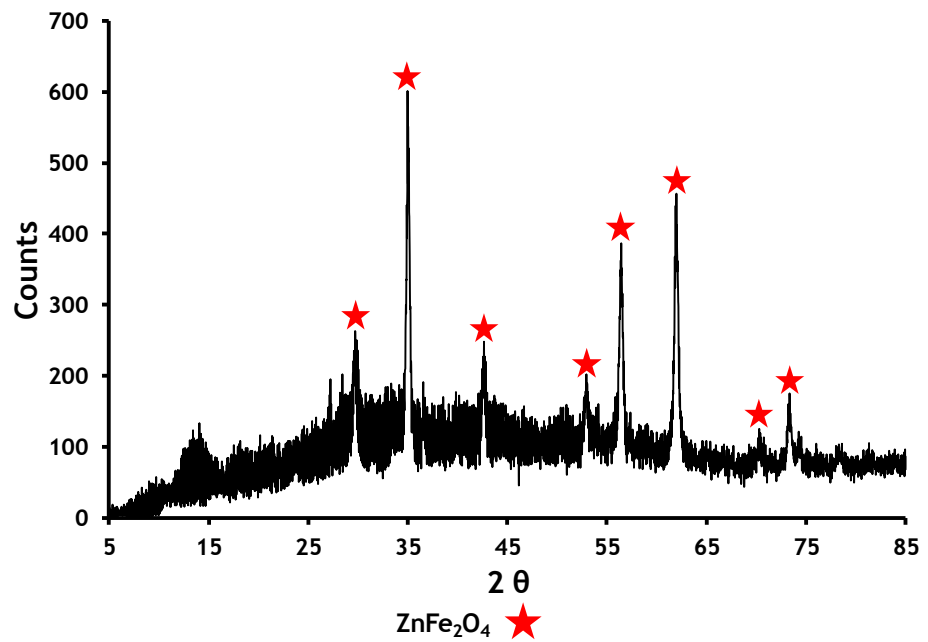


**Figure 4.147** Post Reaction Ambient Temperature XRD Spectra of Zinc Ferrite ZF3MBPD.

#### 4.6.3.2 Post Reaction Raman Spectroscopy Analysis of Zinc Ferrite ZF3MBPD.

Ambient temperature Raman spectroscopy was carried out as described in section 3.5.4 on zinc ferrite ZF3MBPD bed volume 3 cm<sup>3</sup>.

Figure 4.148 below shows the post reaction Raman bands for zinc ferrite ZF3MBPD. The Raman bands are tabulated in table 4.38 below to allow comparison.

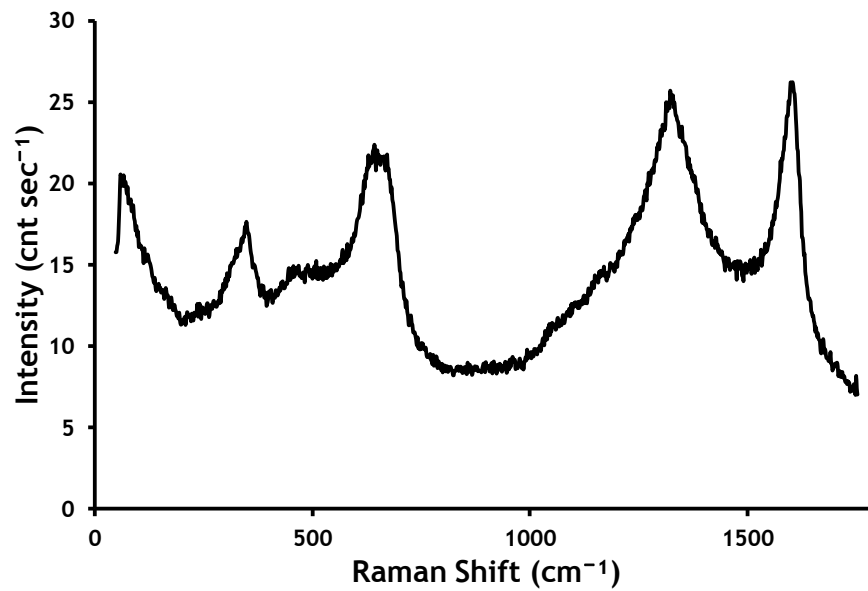


**Figure 4.148** Post Reaction Ambient Temperature Raman Spectroscopy of Zinc Ferrite ZF3MBPD.

Table 4.38 Comparison of Post Reaction Raman Shift Bands Zinc Ferrite ZF3MBPD to Literature.

Raman Shift Bands (cm <sup>-1</sup> )									
	Zinc Ferrite[36]							Carbon Laydown[44]	
Literature	221	246	330-355	451-498	647-659	1091-1106	1271-1298	1350	1600
Zinc Ferrite ZF3MBPD			347	490	641			1322	1603

#### 4.6.3.3 Post Reaction Surface Area Measurements of Zinc Ferrite ZF3MBPD.

Surface area determination was carried out as described in section 3.5.1.

Table 4.39 below shows surface area, pore diameter and cumulative pore volume analysis for zinc ferrite ZF3MBPD bed volume 3 cm<sup>3</sup>.

**Table 4.39 Post Reaction Surface Area Measurements of Zinc Ferrite ZF3MBPD.**

Catalyst	Surface Area (m <sup>2</sup> g <sup>-1</sup> )	Pore Diameter (nm)	Cumulative Pore Volume (cm <sup>3</sup> g <sup>-1</sup> )
Zinc Ferrite ZF3MBPD	15	34	0.1289

#### 4.6.3.4 Post Reaction Thermo-gravimetric Analysis-Differential Scanning Calorimetry Analysis of Zinc Ferrite ZF3MBPD.

Thermo-gravimetric analysis/differential scanning calorimetry was carried out as described in section 3.5.2.

No exothermic or endothermic events were seen on the DSC measurement. Figure 4.149 below shows weight losses and gains which happen simultaneously due to the burning off of coke and the oxidation of newly exposed reduced sites within the catalyst. Figure 4.149 below shows a total weight loss of less than 1 % relative to the derivative weight loss.

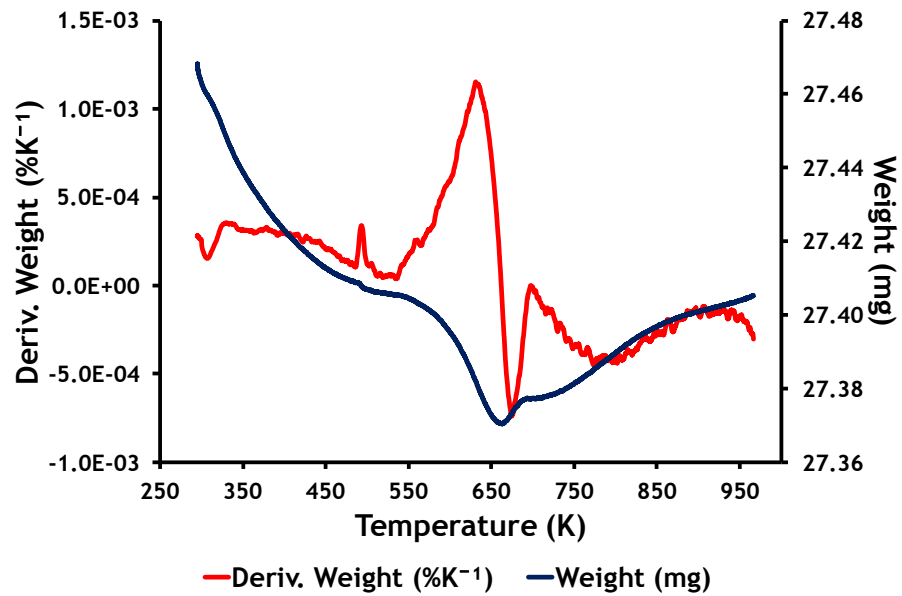


Figure 4.149 Post Reaction Zinc Ferrite ZF3MBPD TGA and Derivative Weight.

Figure 4.150 below shows the evolution of carbon dioxide at 650 K, relative to the derivative weight.

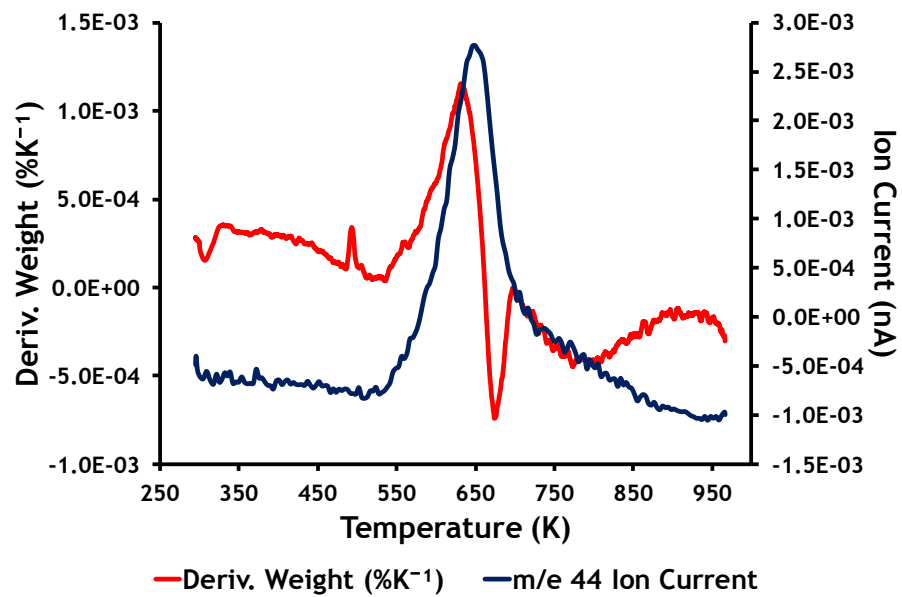


Figure 4.150 Post Reaction TGA/DSC Mass Spectrometer Profile from Zinc Ferrite ZF3MBPD m/e 44.

#### 4.6.3.5 Post Reaction Acid Site Analysis of Zinc Ferrite ZF3MBPD.

Acid site analysis was carried out as described in section 3.7.5 on zinc ferrite ZF3MBPD bed volume 3 cm<sup>3</sup>.

Figure 4.151 below shows two acid sites on zinc ferrite ZF3MBPD; one weak acid site and one medium acid site showing the loss of one weak acid site and two strong acid sites from pre-reaction zinc ferrite ZF3MBPD.

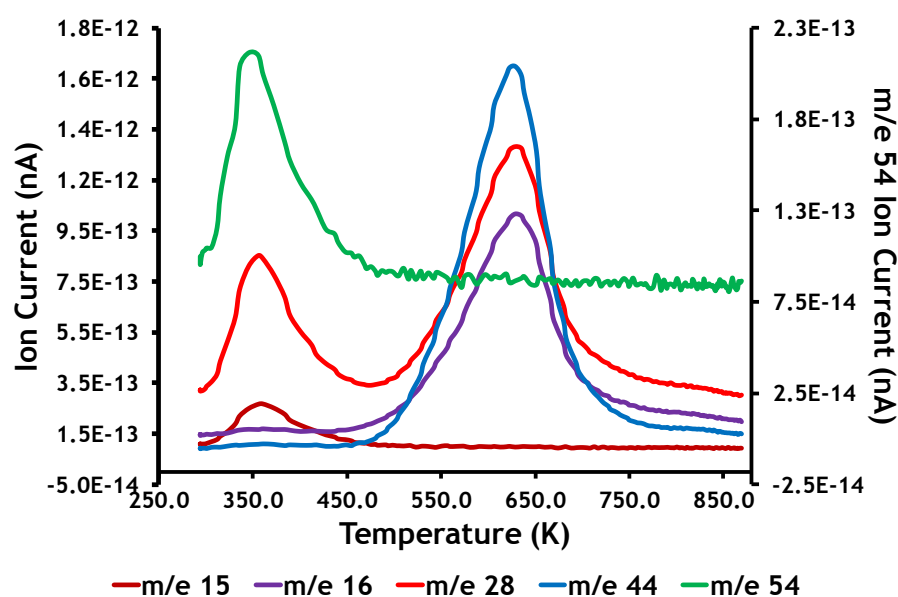


Figure 4.151 Post Reaction Zinc Ferrite ZF3MBPD Acid Site Analysis.

#### 4.7 Iron Enriched Zinc Ferrites Bulk Catalysts ZFFeNH3P, ZFFeNH3P and ZFFeNaOHP.

##### 4.7.1 Pre-Reaction Characterisation of Iron Enriched Zinc Ferrites.

##### 4.7.1.1 Pre-Reaction AA Analysis of Iron Enriched Zinc Ferrites.

Atomic adsorption analysis was carried out as described in section 3.5.5.

Table 4.40 below shows the atomic adsorption analysis results for the iron and zinc concentrations in iron enriched zinc ferrites ZFFeNH3P, ZFFeNH3PD and

ZFFeNaOHP. The expected Fe:Zn ratio was 3.0:1.0 and this was only found in ZFFeNH3PD.

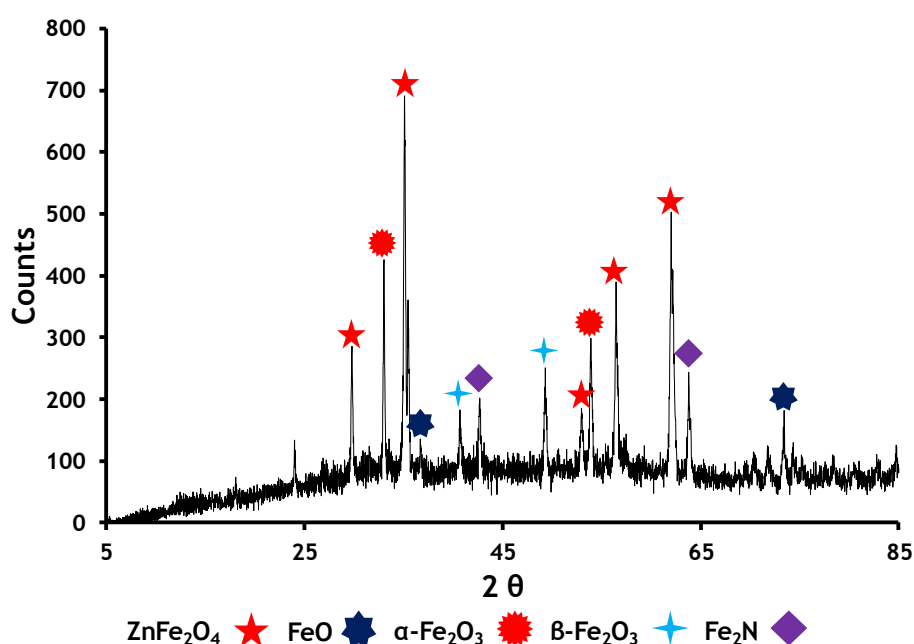
**Table 4.40 Pre-Reaction AA Analysis of Iron Enriched Zinc Ferrites.**

Catalyst	Iron Conc (mg.g <sup>-1</sup> )	Zinc Conc (mg.g <sup>-1</sup> )	Fe:Zn Mole Ratio
ZFFeNH3P	418.86	126.10	3.9:1.0
ZFFeNH3PD	78.44	26.26	3.0:1.0
ZFFeNaOHP	631.55	23.35	31.7:1.0

#### 4.7.1.2 Pre-Reaction X-Ray Diffraction Analysis of Iron Enriched Zinc Ferrites.

Ambient temperature X-Ray Diffraction was carried out as described in section 3.5.3.

Figure 4.152 below shows the pre-reaction ambient temperature XRD profile for iron enriched zinc ferrite ZFFeNH3P.



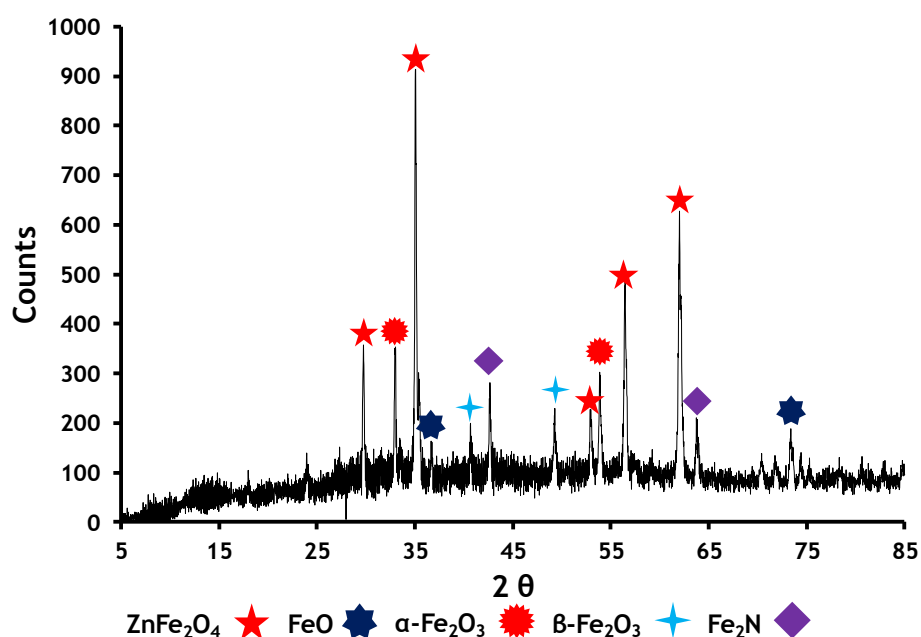
**Figure 4.152 Pre-Reaction Ambient Temperature XRD Spectra of Iron Enriched Zinc Ferrite ZFFeNH3P.**

Table 4.41 below gives the particle sizes and the 2θ angle at which they were measured for ZnFe<sub>2</sub>O<sub>4</sub>, α-Fe<sub>2</sub>O<sub>3</sub> and β-Fe<sub>2</sub>O<sub>3</sub>.

**Table 4.41 Pre-Reaction Iron Enriched Zinc Ferrite ZFFeNH3P Particle Size Measurement.**

	ZnFe <sub>2</sub> O <sub>4</sub>	α-Fe <sub>2</sub> O <sub>3</sub>	β-Fe <sub>2</sub> O <sub>3</sub>
Degrees 2θ	35.1	33.1	49.3
Particle Size nm	48	63	40

Figure 4.153 below shows the pre-reaction ambient temperature XRD profile for iron enriched zinc ferrite ZFFeNH3PD.



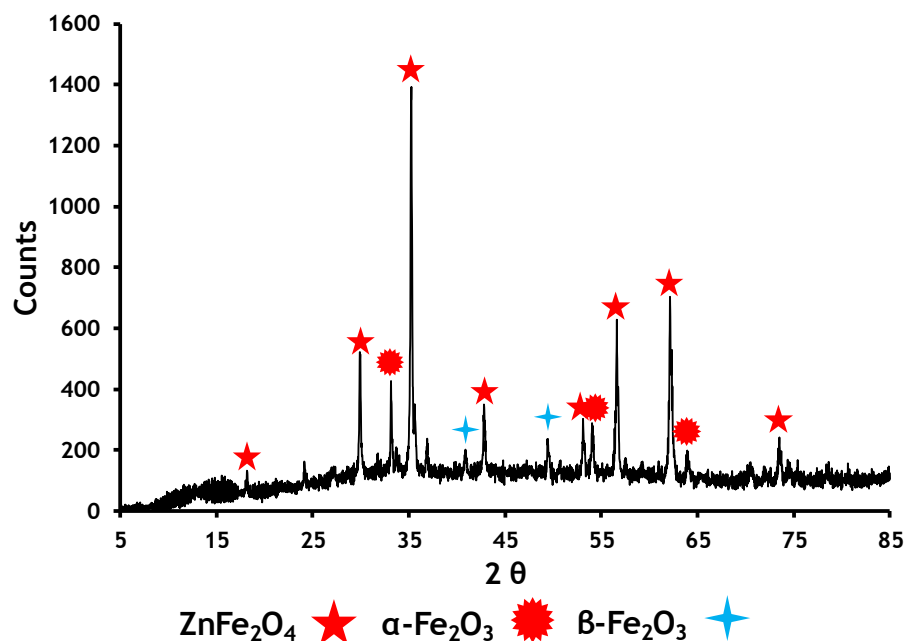
**Figure 4.153 Pre-Reaction Ambient Temperature XRD Spectra of Iron Enriched Zinc Ferrite ZFFeNH3PD.**

Table 4.42 below gives the particle size and the 2θ angle at which they were measured for ZnFe<sub>2</sub>O<sub>4</sub>, α-Fe<sub>2</sub>O<sub>3</sub> and β-Fe<sub>2</sub>O<sub>3</sub>.

**Table 4.42 Pre-Reaction Iron Enriched Zinc Ferrite ZFFeNH3PD Particle Size Measurement.**

	ZnFe <sub>2</sub> O <sub>4</sub>	α-Fe <sub>2</sub> O <sub>3</sub>	β-Fe <sub>2</sub> O <sub>3</sub>
Degrees 2θ	35.1	33.1	49.3
Particle Size nm	48	63	40

Figure 4.154 below shows the pre-reaction ambient temperature XRD profile for iron enriched zinc ferrite ZFFeNaOHP.



**Figure 4.154** Pre-Reaction Ambient Temperature XRD Spectra of Iron Enriched Zinc Ferrite ZFFeNaOHP.

Table 4.43 below gives the particle size and the  $2\theta$  angle at which they were measured for  $\text{ZnFe}_2\text{O}_4$ ,  $\alpha\text{-Fe}_2\text{O}_3$ ,  $\beta\text{-Fe}_2\text{O}_3$  and  $\gamma\text{-Fe}_2\text{O}_3$ .

**Table 4.43** Pre-Reaction Iron Enriched Zinc Ferrite ZFFeNaOHP Particle Size Measurement.

	$\text{ZnFe}_2\text{O}_4$	$\alpha\text{-Fe}_2\text{O}_3$	$\beta\text{-Fe}_2\text{O}_3$
Degrees $2\theta$	35.1	33.2	49.5
Particle Size nm	51	70	45

#### 4.7.1.3 Pre-Reaction Raman Spectroscopy Analysis of Iron Enriched Zinc Ferrites.

Ambient temperature Raman spectroscopy was carried out as described in section 3.5.4.

Figures 4.155 to 4.157 below show the pre-reaction Raman bands for iron enriched zinc ferrite catalysts ZFFeNH3P, ZFFeNH3PD and ZFFeNaOHP. The Raman bands are tabulated in table 4.44 below to allow comparison.

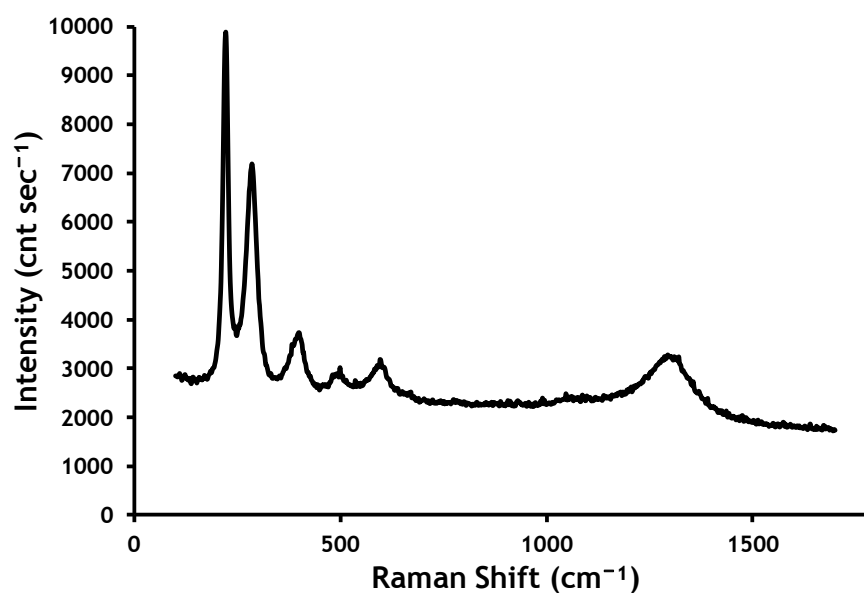


Figure 4.155 Pre-Reaction Ambient Temperature Raman Spectra of Iron Enriched Zinc Ferrite ZFFeNH3P.

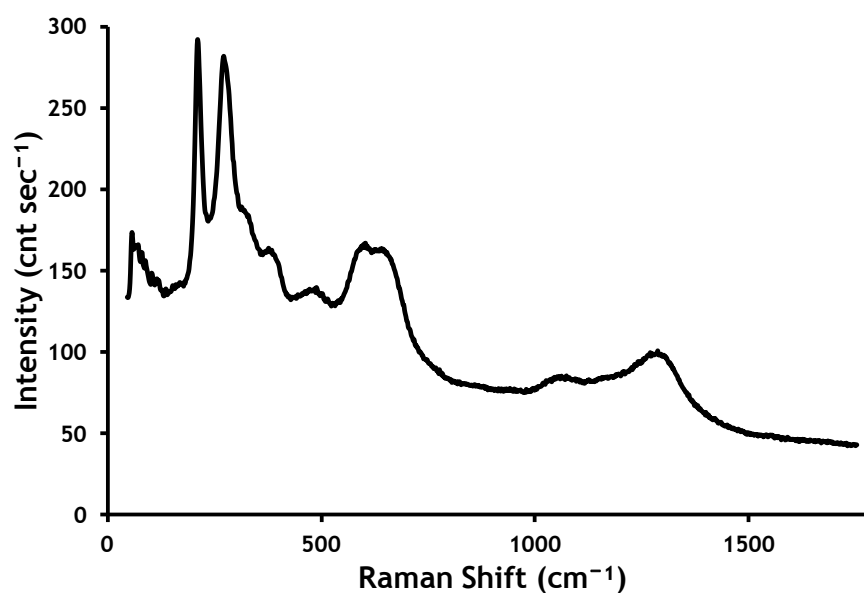
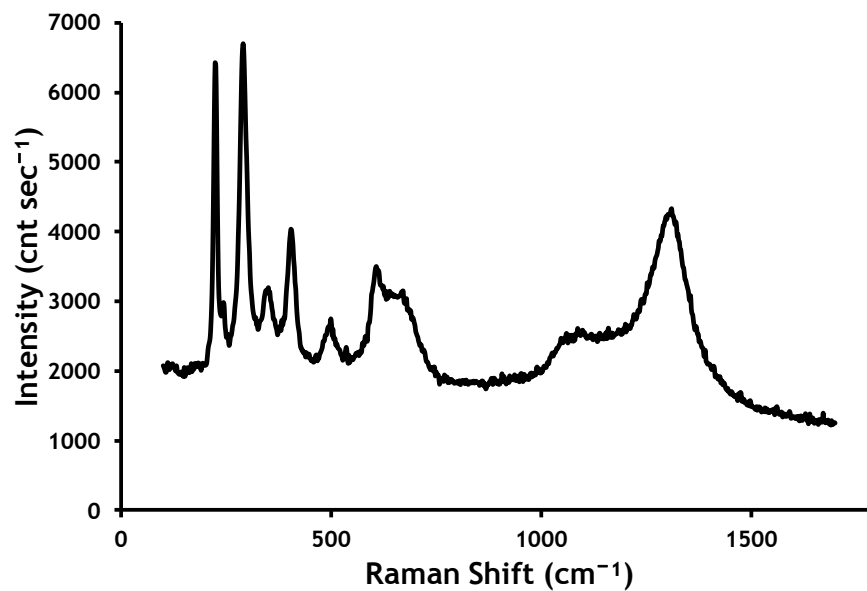


Figure 4.156 Pre-Reaction Ambient Temperature Raman Spectra of Iron Enriched Zinc Ferrite ZFFeNH3PD.



**Figure 4.157** Pre-Reaction Ambient Temperature Raman Spectra of Iron Enriched Zinc Ferrite ZFFeNaOHP.

Table 4.44 Comparison of Pre-Reaction Raman Shift Bands Iron Enriched Zinc Ferrite to Literature.

	Raman Shift Bands (cm <sup>-1</sup> )								
	Zinc Ferrite[36]				Ferric Oxide[43]				Zinc Oxide[46]
Literature	221	246	451-498	647-659	291	410	611	1318	1090
Iron Enriched Zinc Ferrite ZFFeNH3P	211		499		285		596	1294	1074
Iron Enriched Zinc Ferrite ZFFeNH3PD	211		489	638	272		604	1287	1074
Iron Enriched Zinc Ferrite ZFFeNaOHP	224	245	499	671	290	404	608	1311	1087

#### 4.7.1.4 Pre-Reaction Surface Area Measurements of Iron Enriched Zinc Ferrites.

Surface area determination was carried out as described in section 3.5.1.

Table 4.45 below shows surface area, pore diameter and cumulative pore volume for iron enriched zinc ferrite ZFFeNH3P, ZFFeNH3PD and ZFFeNaOHP

**Table 4.45 Pre-Reaction Surface Area Measurements of Iron Enriched Zinc Ferrites.**

Catalyst	Surface Area (m <sup>2</sup> g <sup>-1</sup> )	Pore Diameter (nm)	Cumulative Pore Volume (cm <sup>3</sup> g <sup>-1</sup> )
Iron Enriched Zinc Ferrite ZFFeNH3P	7	12	0.015
Iron Enriched Zinc Ferrite ZFFeNH3PD	<1	66	0.005
Iron Enriched Zinc Ferrite ZFFeNaOHP	<1	65	0.001

#### 4.7.1.5 Pre-Reaction Thermo-gravimetric Analysis-Differential Scanning Calorimetry Analysis of Iron Enriched Zinc Ferrites.

Thermo-gravimetric analysis/differential scanning calorimetry was carried out as described in section 3.5.2.

Figure 4.158 below shows a total weight loss of 11 % from the pre-reaction iron enriched zinc ferrite ZFFeNH3P over the temperature range 290 K to 970K.

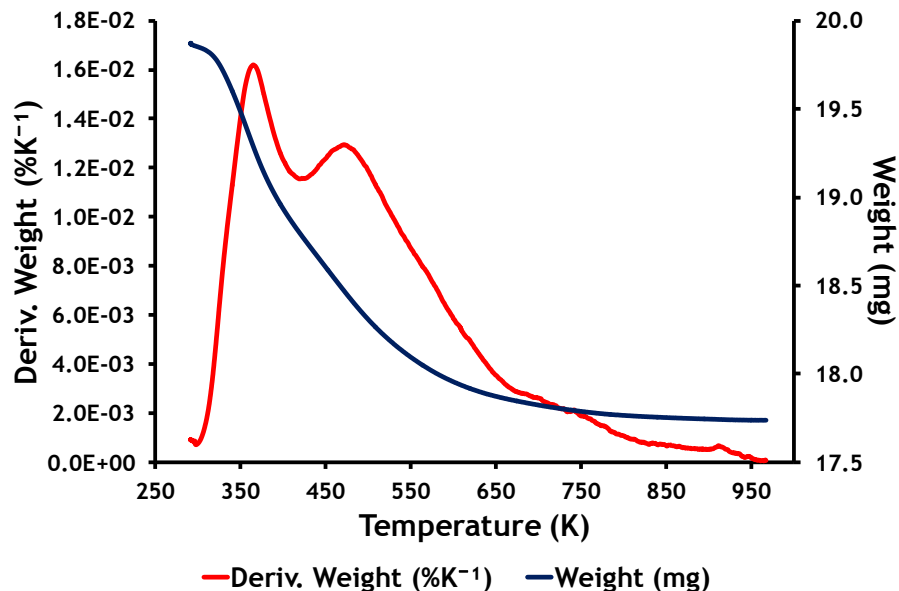


Figure 4.158 Pre-Reaction Iron Enriched Zinc Ferrite ZFFeNH3P TGA and Derivative Weight.

The DSC profile in figure 4.161 below shows an endothermic event at 362 K associated with desorption of physisorbed water. Also shown is an exothermic event at 900 K associated with a small weight loss, this event is not seen with zinc ferrite so the change may be due an iron species.

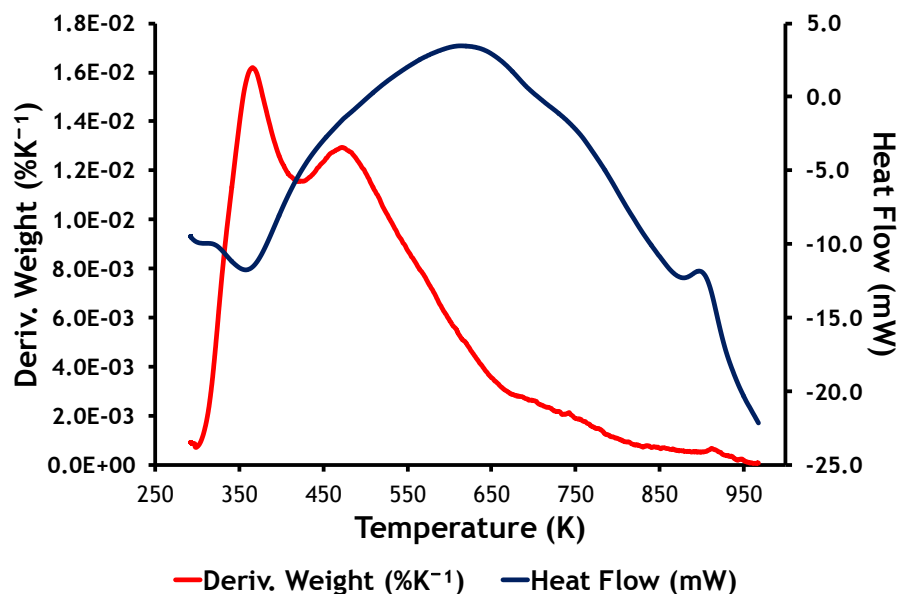


Figure 4.159 Pre-Reaction Iron Enriched Zinc Ferrite ZFFeNH3P TGA/DSC DSC.

Figure 4.160 below shows a total weight loss of 14 % from the pre-reaction iron enriched zinc ferrite ZFFeNH3PD over the temperature range 290 K to 970 K.

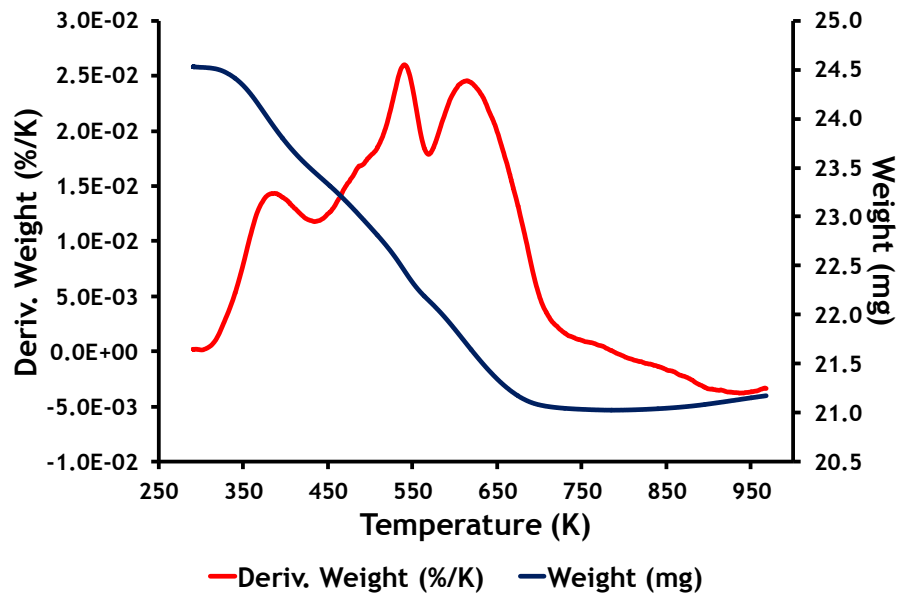


Figure 4.160 Pre-Reaction Iron Enriched Zinc Ferrite ZFFeNH3PD TGA and Derivative Weight.

Figure 161 below shows one endothermic and three exothermic events at 372 K, 540 K, 728 K and 898 K respectively. The events at 372 K and 540 K are associated with desorption of physisorbed water and carbon burn off. The two events at 728 K and 898 K show no real mass change, this may be explained by a phase change.

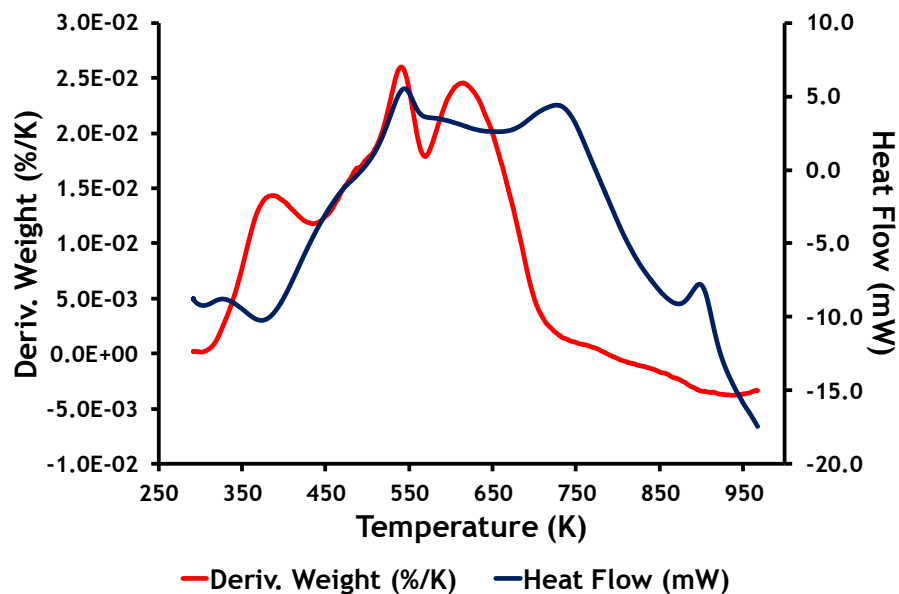


Figure 4.161 Pre-Reaction Iron Enriched Zinc Ferrite ZFFeNH3PD TGA/DSC DSC.

Figure 4.162 below shows the evolution of carbon monoxide at 540 K, relative to the derivative weight.

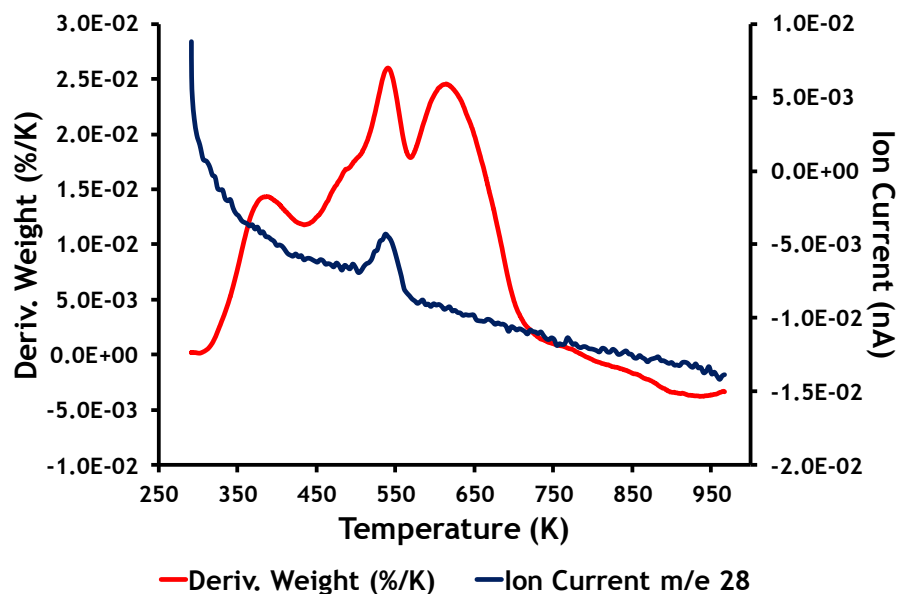


Figure 4.162 Pre-Reaction TGA/DSC Mass Spectrometer Profile from Iron Enriched Zinc Ferrite ZFFeNH3PD m/e 28.

Figure 4.163 below shows the evolution of nitrous oxide at 630 K, relative to the derivative weight.

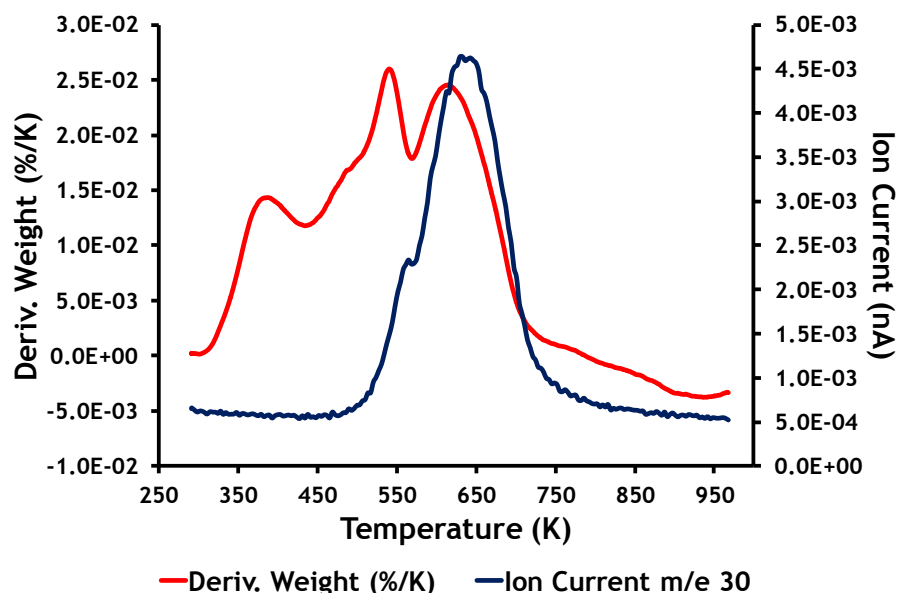


Figure 4.163 Pre-Reaction TGA/DSC Mass Spectrometer Profile from Iron Enriched Zinc Ferrite ZFFeNH3PD m/e 30.

Figure 4.164 below shows a total weight loss of 11 % from the pre-reaction iron enriched zinc ferrite ZFFeNaOHP over a temperature range of 290 K to 970 K.

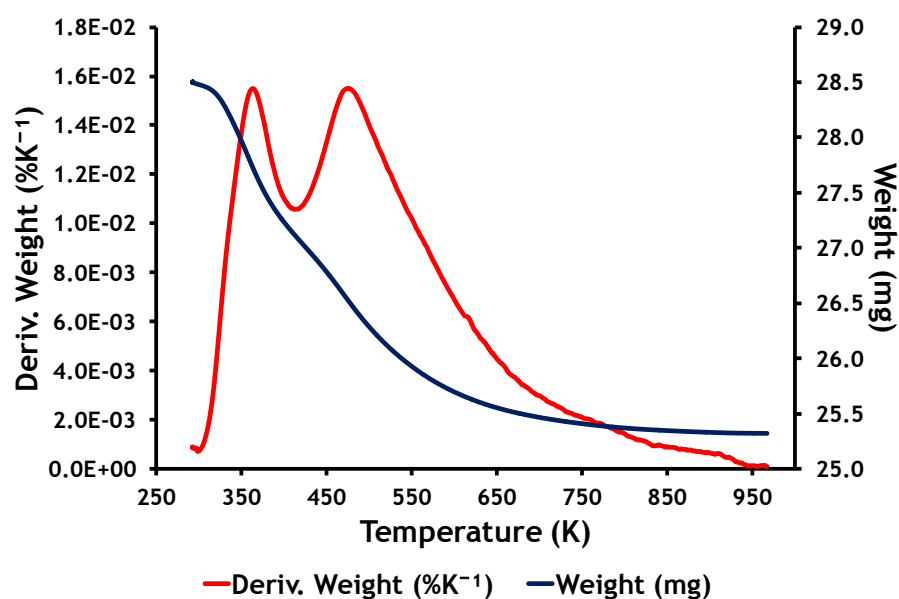


Figure 4.164 Pre-Reaction Iron Enriched Zinc Ferrite ZFFeNaOHP TGA and Derivative Weight.

The DSC profile in figure 4.165 below shows an endothermic event at 362 K associated with desorption of physisorbed water. Also shown is an exothermic event at 900 K associated with a small weight loss, this event is not seen with zinc ferrite so the change may be due an iron species.

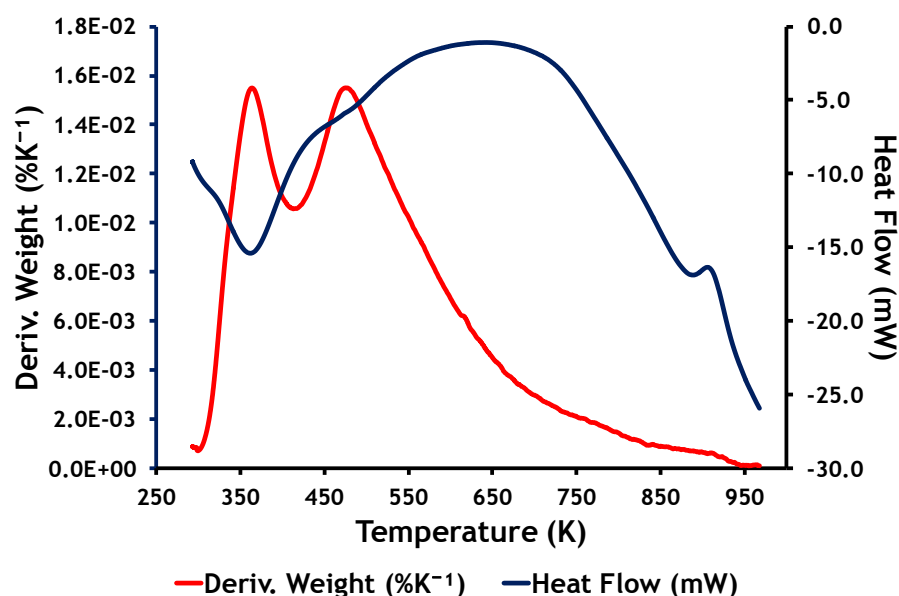


Figure 4.165 Pre-Reaction Iron Enriched Zinc Ferrite ZFFeNaOHP TGA/DSC DSC.

#### 4.7.2 Catalyst Testing Iron Enriched Zinc Ferrites.

The reactions using iron enriched zinc ferrites are detailed in table 3.7 in section 3.6.3 part of which is reproduced below in table 4.46. The test procedures are given in sections 3.6.2 and 3.6.3.

Table 4.46 Catalyst Testing List for Iron Enriched Zinc Ferrites.

Reaction No	Catalyst Code	Bed Vol (cm <sup>3</sup> )	Weight (g)
18	ZFFeNH3P	3	5.8493
20	ZFFeNH3PD	3	7.5162
25	ZFFeNaOHP	1	2.4339

Figures 4.166 and 4.167 below show the product selectivities and 1-butene conversion obtained when passing 1-butene over iron enriched zinc ferrite ZFFeNH3P with a bed volume of 3 cm<sup>3</sup>.

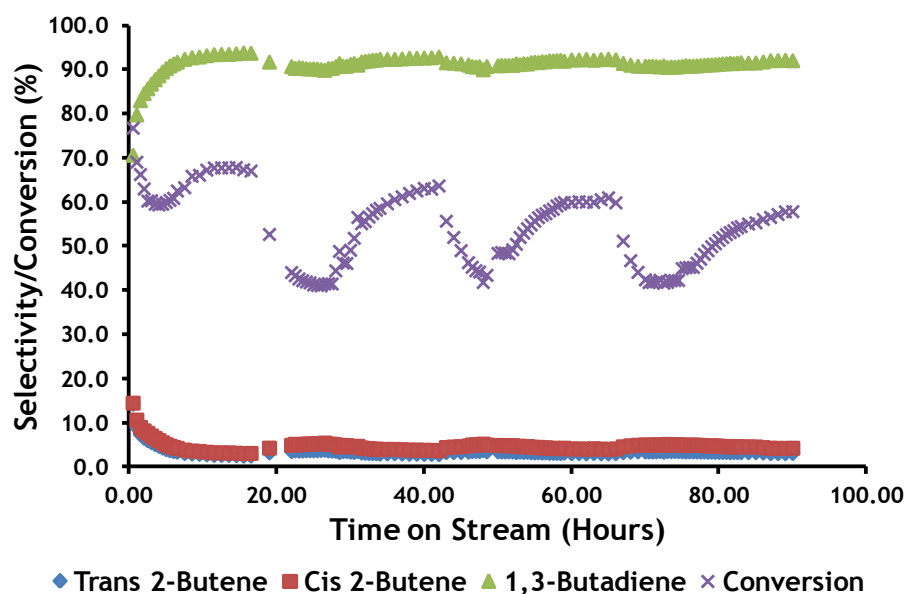


Figure 4.166 Selectivity/Conversion Major Components Iron Enriched Zinc Ferrite ZFFeNH3P Bed Volume 3 cm<sup>3</sup>.

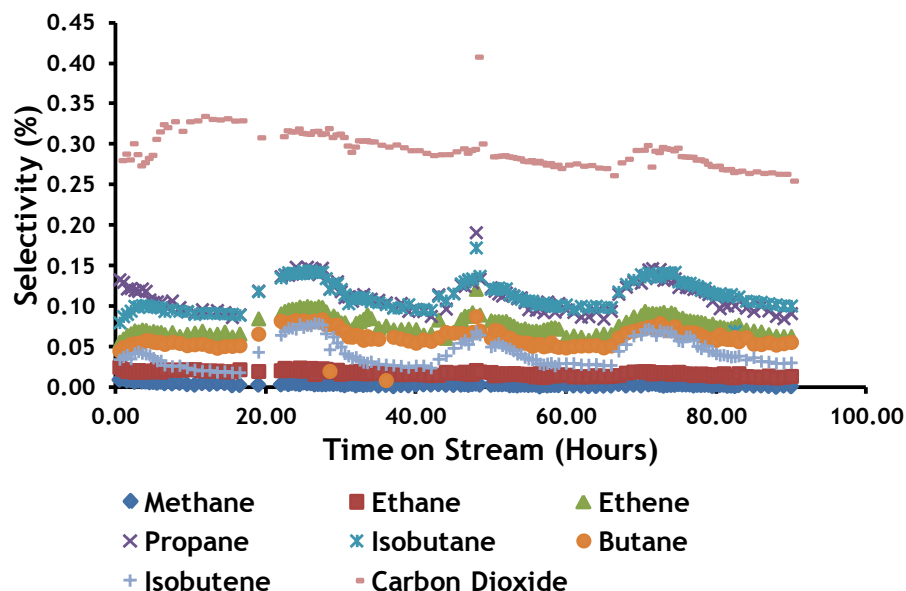


Figure 4.167 Selectivity Minor Components Iron Enriched Zinc Ferrite ZFFeNH3P Bed Volume 3 cm<sup>3</sup>.

Figures 4.168 and 4.169 below show the product selectivities and 1-butene conversion obtained when passing 1-butene over iron enriched zinc ferrite ZFFeNH3PD with a bed volume of 3 cm<sup>3</sup>. The gap in figures 4.168 to 4.169 below is due to problems with analysis equipment.

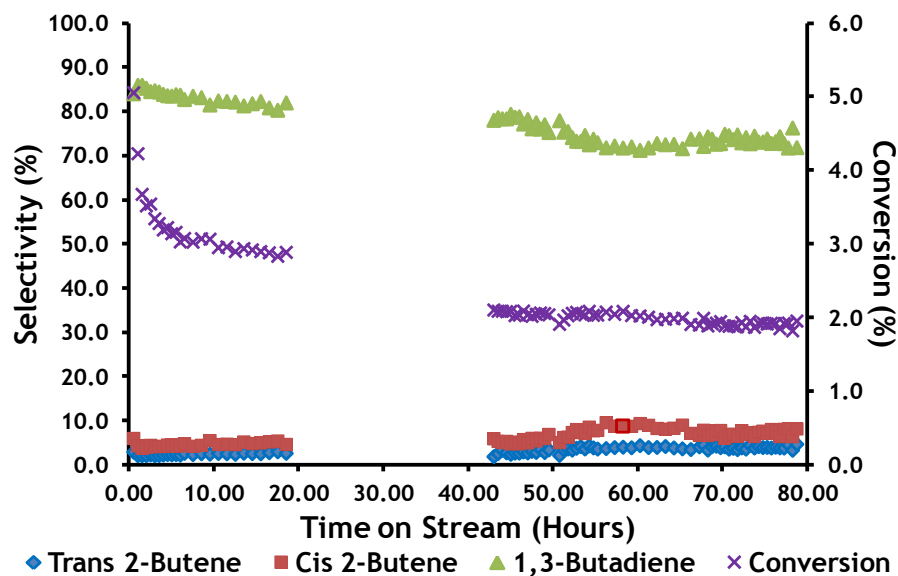


Figure 4.168 Selectivity/Conversion Major Components Iron Enriched Zinc Ferrite ZFFeNH3PD Bed Volume 3 cm<sup>3</sup>.

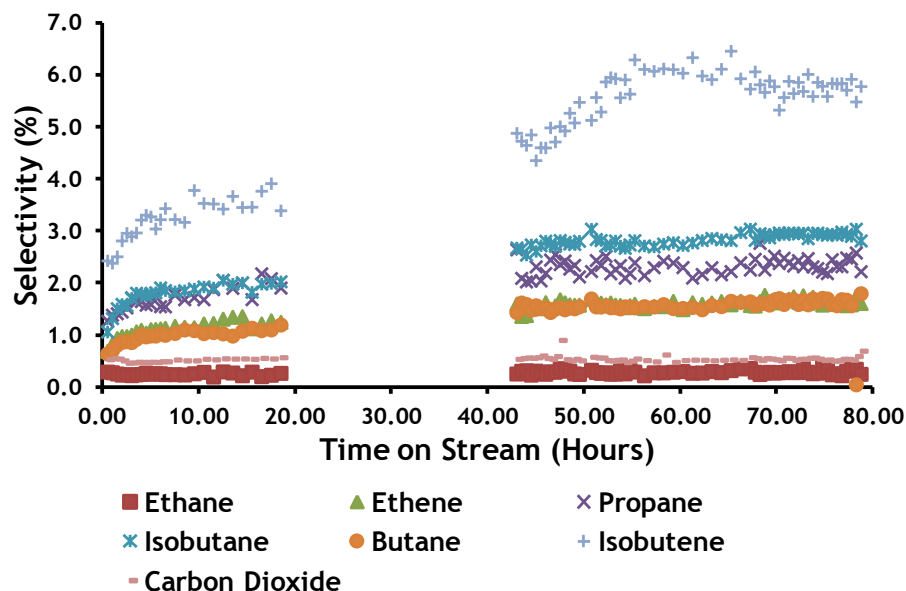


Figure 4.169 Selectivity Minor Components Iron Enriched Zinc Ferrite ZFFeNH3PD Bed Volume 3 cm<sup>3</sup>.

Figures 4.170 and 4.171 below show the product selectivities and 1-butene conversion obtained when passing 1-butene over iron enriched zinc ferrite ZFFeNH3PD with a bed volume of 1 cm<sup>3</sup>.

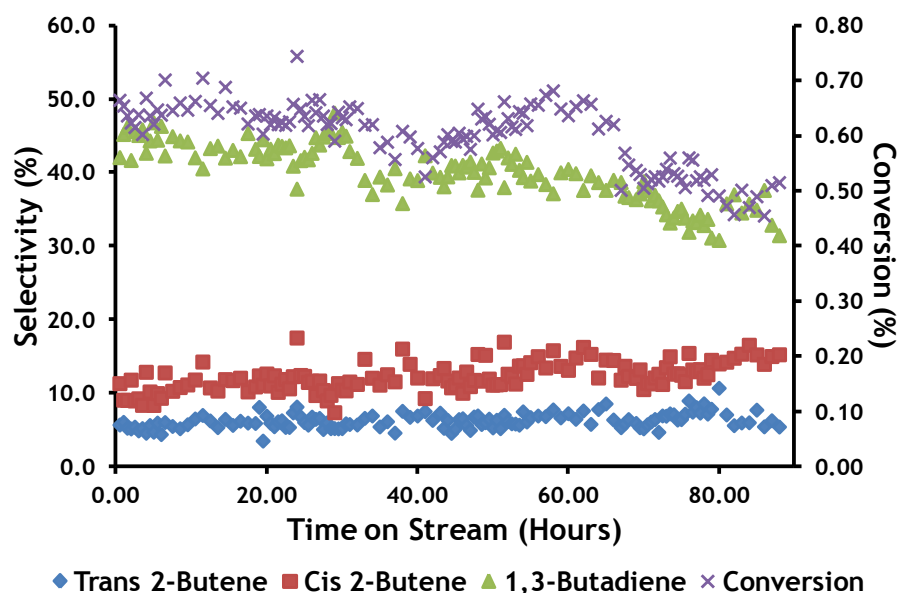


Figure 4.170 Selectivity/Conversion Major Components Iron Enriched Zinc Ferrite ZFFeNaOHP Bed Volume 1 cm<sup>3</sup>.

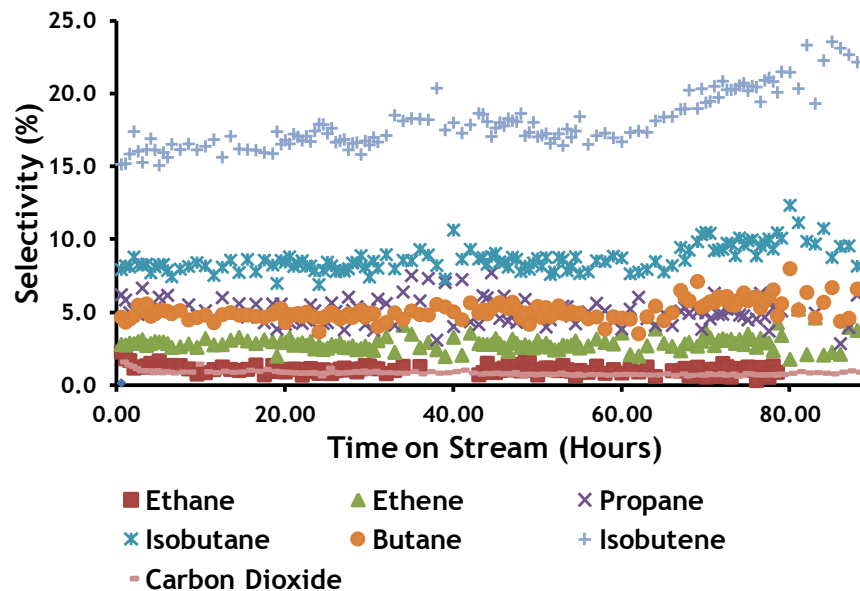


Figure 4.171 Selectivity Minor Components Iron Enriched Zinc Ferrite ZFFeNaOHP Bed Volume 1 cm<sup>3</sup>.

#### 4.7.3 Post Reaction Characterisation of Iron Enriched Zinc Ferrites.

##### 4.7.3.1 Post Reaction X-Ray Diffraction Analysis of Iron Enriched Zinc Ferrites.

Ambient temperature X-Ray Diffraction was carried out as described in section 3.5.3.

Figure 4.172 below shows the loss of FeO and Fe<sub>2</sub>N in the post reaction ambient temperature XRD profile iron enriched zinc ferrite ZFFeNH3P.

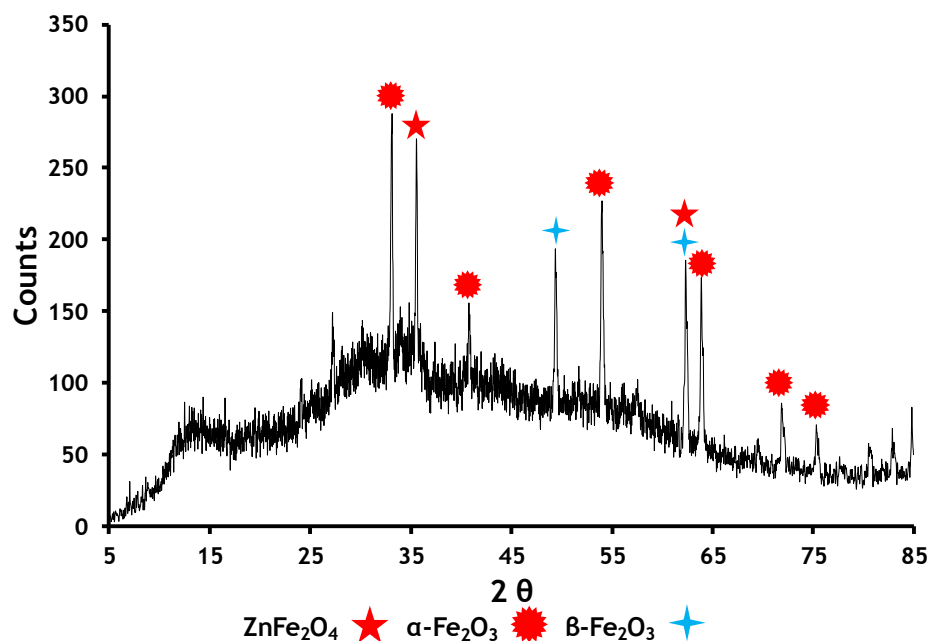


**Figure 4.172 Post Reaction Ambient Temperature XRD Spectra of Iron Enriched Zinc Ferrite ZFFeNH3P.**

Table 4.47 below gives the particle size and the 2θ angle at which they were measured for ZnFe<sub>2</sub>O<sub>4</sub>, α-Fe<sub>2</sub>O<sub>3</sub> and β-Fe<sub>2</sub>O<sub>3</sub>.

**Table 4.47 Post Reaction Iron Enriched Zinc Ferrite ZFFeNH3P Particle Size Measurement.**

	ZnFe <sub>2</sub> O <sub>4</sub>	α-Fe <sub>2</sub> O <sub>3</sub>	β-Fe <sub>2</sub> O <sub>3</sub>
Degrees 2θ	35.6	33.1	49.4
Particle Size nm	61	53	42

Comparison of the pre and post reaction particle size of iron enriched ZFFeNH3P shows an increase in ZnFe<sub>2</sub>O<sub>4</sub> particle size from 48 nm to 61 nm and a decrease in the α-Fe<sub>2</sub>O<sub>3</sub> particle size from 63 nm to 53 nm.

Figure 4.173 below shows the loss of FeO in the post reaction ambient temperature XRD profile iron enriched zinc ferrite ZFFeNH3PD.

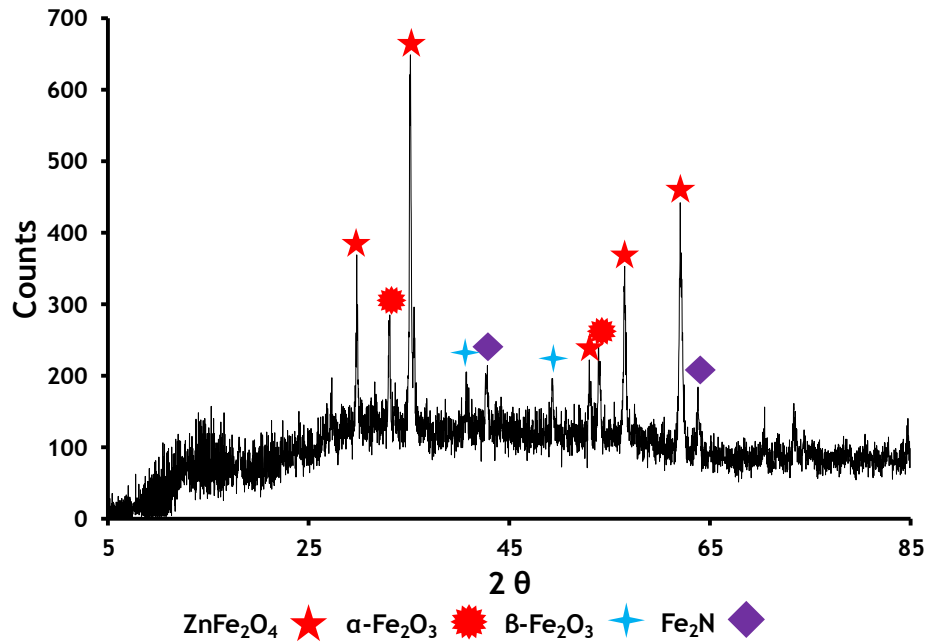


**Figure 4.173 Post Reaction Ambient Temperature XRD Spectra of Iron Enriched Zinc Ferrite ZFFeNH3PD.**

Table 4.48 below gives the particle size and the 2θ angle at which they were measured for ZnFe<sub>2</sub>O<sub>4</sub>, α-Fe<sub>2</sub>O<sub>3</sub> and β-Fe<sub>2</sub>O<sub>3</sub>.

**Table 4.48 Post Reaction Iron Enriched Zinc Ferrite ZFFeNH3PD Particle Size Measurement.**

	ZnFe <sub>2</sub> O <sub>4</sub>	α-Fe <sub>2</sub> O <sub>3</sub>	β-Fe <sub>2</sub> O <sub>3</sub>
Degrees 2θ	35.1	33.0	49.3
Particle Size nm	49	60	56

Comparison of the pre and post reaction particle size of iron enriched ZFFeNH3PD shows an increase in β-Fe<sub>2</sub>O<sub>3</sub> particle size from 40 nm to 56 nm.

Figure 4.174 below shows the loss of γ-Fe<sub>2</sub>O<sub>3</sub> in the post reaction ambient temperature XRD profile of iron enriched zinc ferrite ZFFeNaOHP.

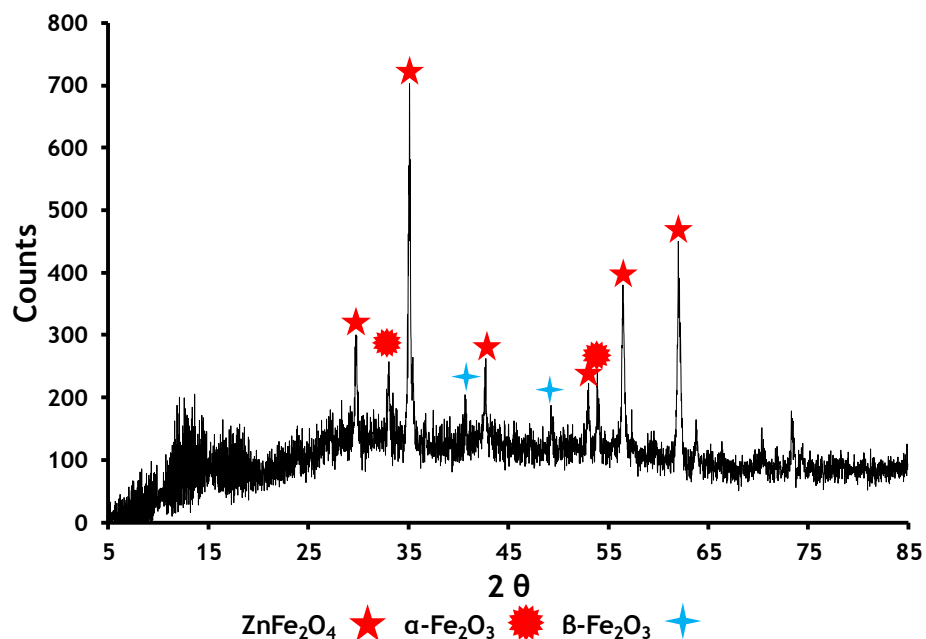


**Figure 4.174** Post Reaction Ambient Temperature XRD Spectra of Iron Enriched Zinc Ferrite ZFFeNaOHP.

Table 4.49 below gives the particle size and the  $2\theta$  angle at which they were measured for  $\text{ZFe}_2\text{O}_4$  and  $\alpha\text{-Fe}_2\text{O}_3$ .

**Table 4.49** Post Reaction Iron Enriched Zinc Ferrite ZFFeNaOHP Particle Size Measurement.

	$\text{ZnFe}_2\text{O}_4$	$\alpha\text{-Fe}_2\text{O}_3$
Degrees $2\theta$	35.1	33.0
Particle Size nm	37	43

Comparison of the pre and post reaction particle size of iron enriched ZFFeNaOHP shows a decrease in  $\text{ZnFe}_2\text{O}_4$  particle size from 51 nm to 42 nm; no change in the  $\alpha\text{-Fe}_2\text{O}_3$  particle size was observed. The particle size of  $\beta\text{-Fe}_2\text{O}_3$  was unable to be calculated and  $\gamma\text{-Fe}_2\text{O}_3$  peak was no longer present.

#### 4.7.3.2 Post Reaction Raman Spectroscopy Analysis of Iron Enriched Zinc Ferrites.

Ambient temperature Raman spectroscopy was carried out as described in section 3.5.4.

Figures 4.175 to 4.177 below show the post reaction Raman bands for iron enriched zinc ferrite catalysts ZFFeNH3P, ZFFeNH3PD and ZFFeNaOHP. The Raman bands are tabulated in table 4.50 below to allow comparison.

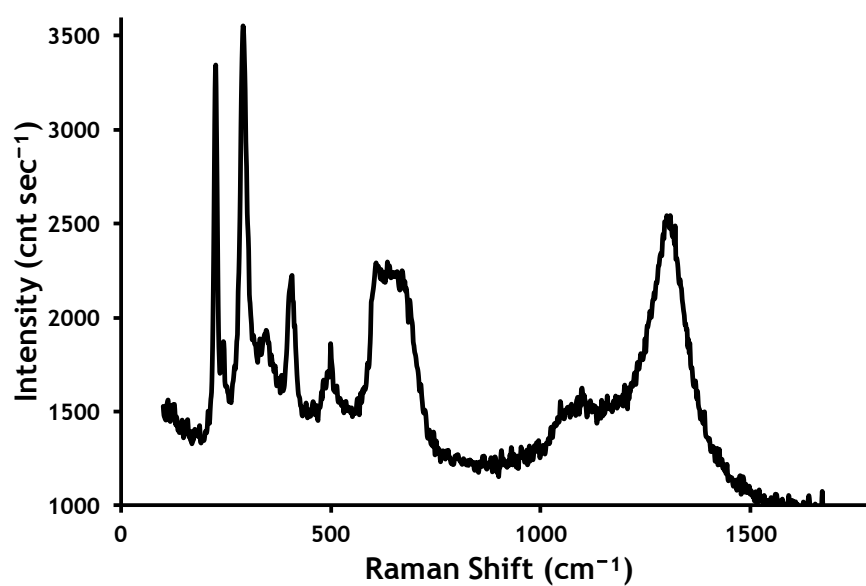


Figure 4.175 Post Reaction Ambient Temperature Raman Spectra of Iron Enriched Zinc Ferrite ZFFeNH3P.

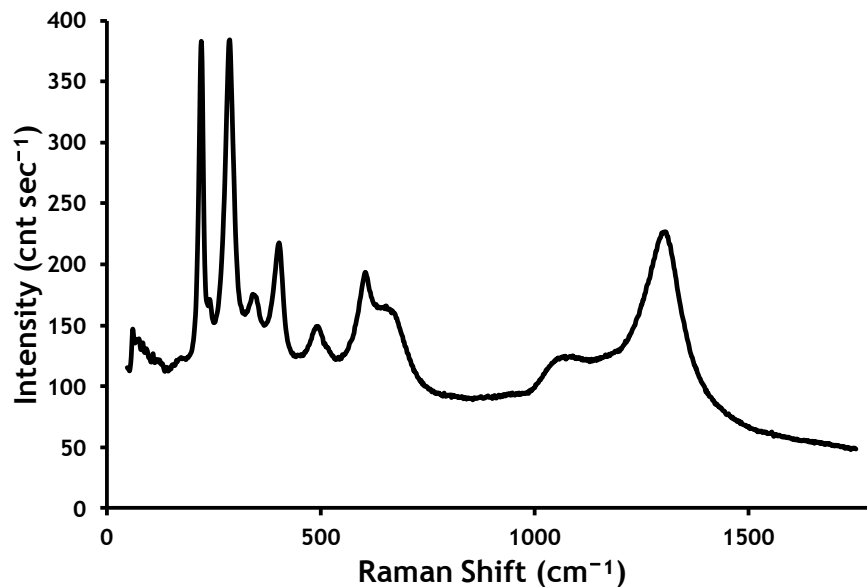


Figure 4.176 Post Reaction Ambient Temperature Raman Spectra of Iron Enriched Zinc Ferrite ZFFeNH3PD.

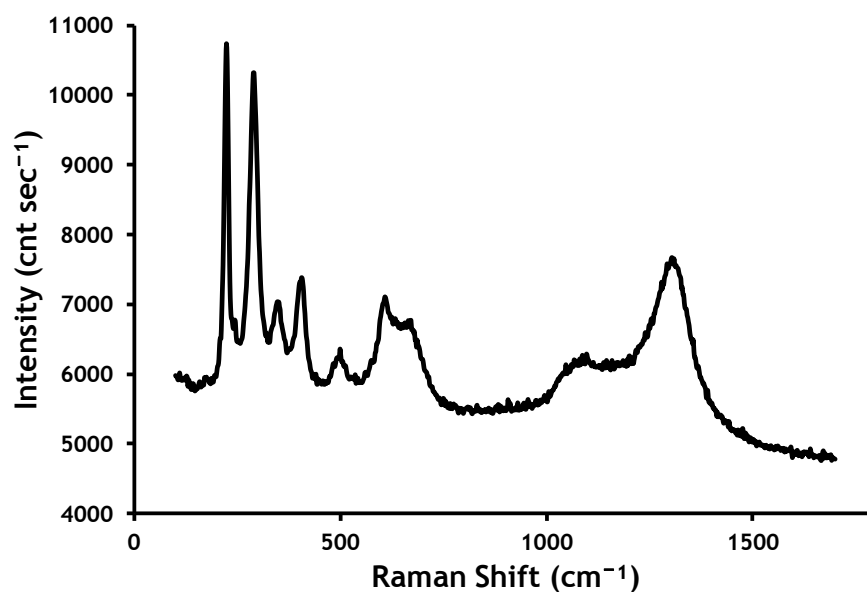


Figure 4.177 Post Reaction Ambient Temperature Raman Spectra of Iron Enriched Zinc Ferrite ZFFeNaOHP.

Table 4.50 Comparison of Post Reaction Raman Shift Bands Iron Enriched Zinc Ferrite to Literature.

Catalyst	Raman Shift Bands (cm <sup>-1</sup> )									
	Zinc Ferrite[36]					Ferric Oxide[43]				Zinc Oxide[46]
Literature	221	246		451-498	647-659	291	410	611	1318	1090
Iron Enriched Zinc Ferrite ZFeNH <sub>3</sub> P	225	255	345	499	634	290	407	607	1309	1058
Iron Enriched Zinc Ferrite ZFeNH <sub>3</sub> PD	225	243	345	499	634	290	407	607	1309	1099
Iron Enriched Zinc Ferrite ZFeNaOHP	224	245	347	499	671	290	406	608	1304	1097

Comparison of the pre and post reaction Raman profiles for iron enriched ZFFeNH3P shows a loss of the band at  $1287\text{ cm}^{-1}$  and addition of bands at  $225\text{ cm}^{-1}$ ,  $255\text{ cm}^{-1}$  and  $345\text{ cm}^{-1}$  associated with  $\text{ZnFe}_2\text{O}_4$ ; loss of the band at  $403\text{ cm}^{-1}$  associated with  $\text{Fe}_2\text{O}_3$  and a shift of the band associated with  $\text{ZnO}$  from  $1059\text{ cm}^{-1}$  to  $1099\text{ cm}^{-1}$ .

Comparison of the pre and post reaction Raman profiles for iron enriched ZFFeNH3PD shows a loss of the band at  $1294\text{ cm}^{-1}$  and addition of bands at  $240\text{ cm}^{-1}$  and  $343\text{ cm}^{-1}$  associated with  $\text{ZnFe}_2\text{O}_4$ ; loss of the band at  $403\text{ cm}^{-1}$  associated with  $\text{Fe}_2\text{O}_3$  and a shift of the band associated with  $\text{ZnO}$  from  $1059\text{ cm}^{-1}$  to  $1099\text{ cm}^{-1}$ .

Comparison of the pre and post reaction Raman profiles for iron enriched ZFFeNaOHP shows a loss of the band at  $244\text{ cm}^{-1}$  and addition of bands at  $348\text{ cm}^{-1}$  and  $671\text{ cm}^{-1}$  associated with  $\text{ZnFe}_2\text{O}_4$ ; loss of the band at  $608\text{ cm}^{-1}$  associated with  $\text{Fe}_2\text{O}_3$  and a loss of the band associated with  $\text{ZnO}$ .

#### **4.7.3.3 Post Reaction Surface Area Measurements of Iron Enriched Zinc Ferrites.**

Surface area determination was carried out as described in section 3.5.1.

Table 4.51 below shows surface area, pore diameter and cumulative pore volume for iron enriched zinc ferrite ZFFeNH3O, ZFFeNH3PD and ZFFeNaOHP.

**Table 4.51 Post Reaction Surface Area Measurements of Iron Enriched Zinc Ferrites.**

Catalyst	Surface Area (m <sup>2</sup> g <sup>-1</sup> )	Pore Diameter (nm)	Cumulative Pore Volume (cm <sup>3</sup> g <sup>-1</sup> )
Iron Zinc Ferrite ZFFeNH3P	8	6	0.008
Iron Zinc Ferrite ZFFeNH3PD	<1	41	0.005
Iron Zinc Ferrite ZFFeNaOHP	<1	10	0.0002

Comparison of pre and post reaction surface areas of the iron enriched zinc ferrite catalysts shows no significant change.

#### **4.7.3.4 Post Reaction Thermo-gravimetric Analysis-Differential Scanning Calorimetry Analysis of Iron Enriched Zinc Ferrites.**

Thermo-gravimetric analysis/differential scanning calorimetry was carried out as described in section 3.5.2.

The post reaction TGA/DSC of ZFFeNH3P showed a weight loss of less than 1 %; ZFFeNH3PD and ZFFeNaOHP both showed weight gains of less than 1 %.

### **4.8 Iron Oxide Bulk Catalysts Fe<sub>2</sub>O<sub>3</sub>NH<sub>3</sub>P and Fe<sub>2</sub>O<sub>3</sub>NaOHP.**

#### **4.8.1 Pre-Reaction Characterisation of Iron Oxide Catalysts.**

##### **4.8.1.1 Pre-Reaction X-Ray Diffraction Analysis of Iron Oxide Catalysts.**

Ambient temperature X-Ray Diffraction was carried out as described in section 3.5.3.

Figure 4.178 below shows the pre-reaction ambient temperature XRD profile of iron oxide catalyst Fe<sub>2</sub>O<sub>3</sub>NaOHP, which shows the presence of the  $\alpha$ ,  $\beta$  and  $\gamma$  phases of Fe<sub>2</sub>O<sub>3</sub>

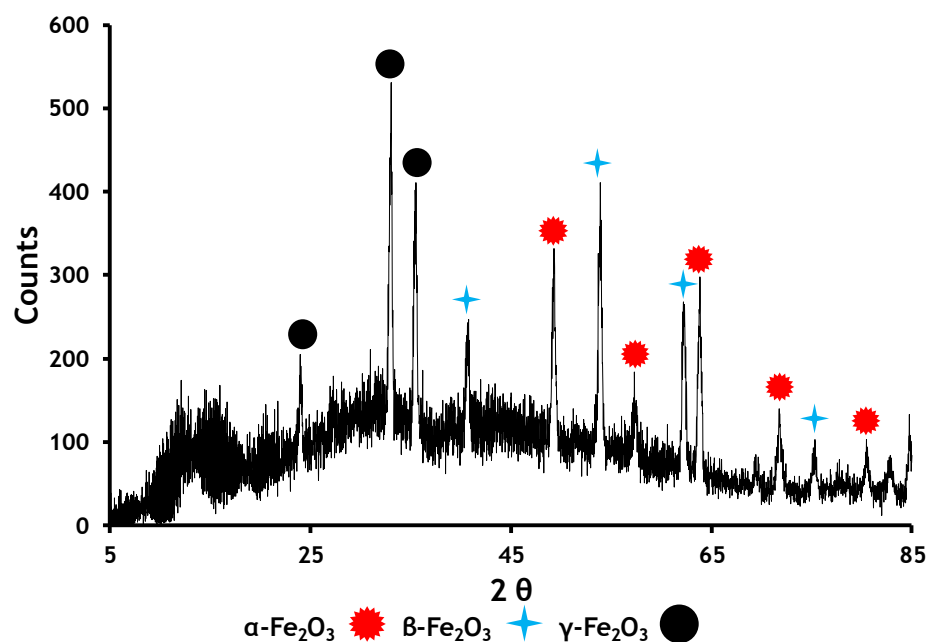


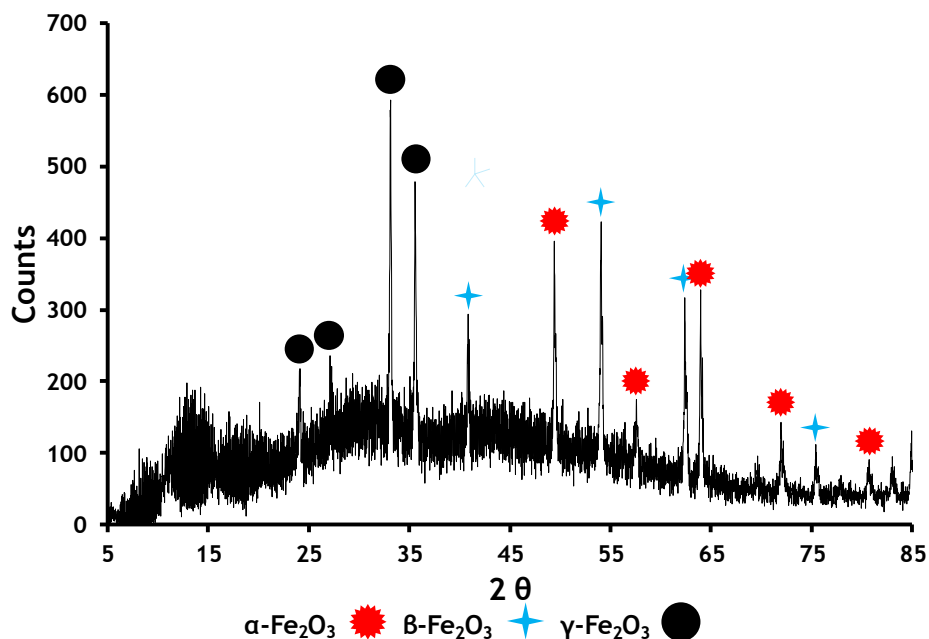
Figure 4.178 Pre-Reaction Ambient Temperature XRD Spectra of Iron Oxide Catalyst Fe<sub>2</sub>O<sub>3</sub>NaOHP.

Table 4.52 below gives the particle size and the 2θ angle at which they were measured for α-Fe<sub>2</sub>O<sub>3</sub>, β-Fe<sub>2</sub>O<sub>3</sub> and γ-Fe<sub>2</sub>O<sub>3</sub>.

Table 4.52 Pre-Reaction Iron Oxide Catalyst Fe<sub>2</sub>O<sub>3</sub>NaOHP Particle Size Measurement.

	α-Fe <sub>2</sub> O <sub>3</sub>	β-Fe <sub>2</sub> O <sub>3</sub>	γ-Fe <sub>2</sub> O <sub>3</sub>
Degrees 2θ	49.2	53.9	33.0
Particle Size nm	28	27	28

Figure 4.179 below shows the pre-reaction ambient temperature XRD profile of iron oxide catalyst Fe<sub>2</sub>O<sub>3</sub>NH<sub>3</sub>P.



**Figure 4.179** Pre-Reaction Ambient Temperature XRD Spectra of Iron Oxide Catalyst Fe<sub>2</sub>O<sub>3</sub>NH<sub>3</sub>P.

Table 4.53 below gives the particle size and the 2θ angle at which they were measured for α-Fe<sub>2</sub>O<sub>3</sub>, β-Fe<sub>2</sub>O<sub>3</sub> and γ-Fe<sub>2</sub>O<sub>3</sub>.

**Table 4.53** Pre-Reaction Iron Oxide Catalyst Fe<sub>2</sub>O<sub>3</sub>NH<sub>3</sub>P Particle Size Measurement.

	α-Fe <sub>2</sub> O <sub>3</sub>	β-Fe <sub>2</sub> O <sub>3</sub>	γ-Fe <sub>2</sub> O <sub>3</sub>
Degrees 2θ	49.4	54.1	33.1
Particle Size nm	41	37	41

Iron oxide catalyst prepared from sodium hydroxide has an average particle size 30% smaller than iron oxide catalysts prepared from ammonia.

#### 4.8.1.2 Pre-Reaction Raman Spectroscopy Analysis of Iron Oxide Catalysts.

Ambient temperature Raman spectroscopy was carried out as described in section 3.5.4.

Figures 4.180 to 4.181 below show the pre-reaction Raman bands for iron oxide catalysts Fe<sub>2</sub>O<sub>3</sub>NaOHP and Fe<sub>2</sub>O<sub>3</sub>NH<sub>3</sub>P. The Raman bands are tabulated in table 4.54 below to allow comparison.

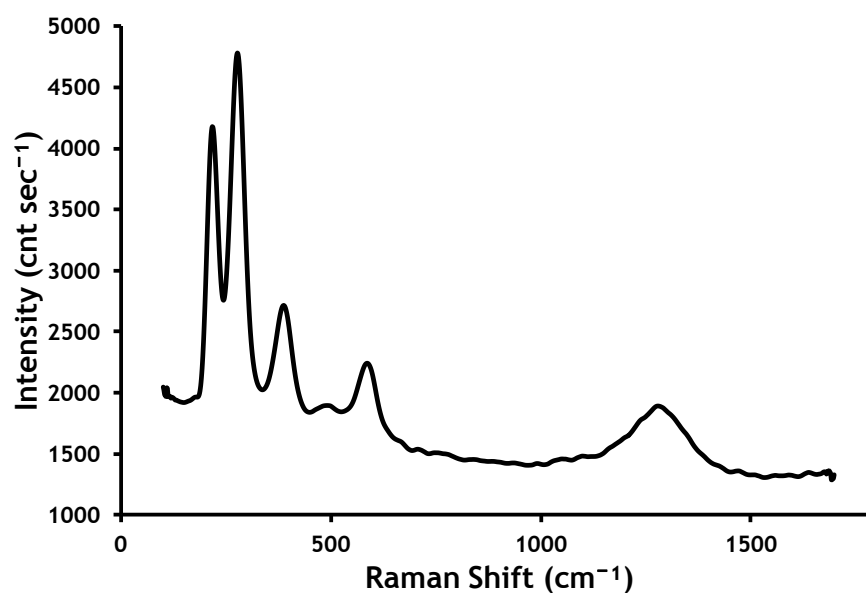


**Figure 4.180** Pre-Reaction Ambient Temperature Raman Spectra of Iron Oxide Catalyst Fe<sub>2</sub>O<sub>3</sub>NaOHP.

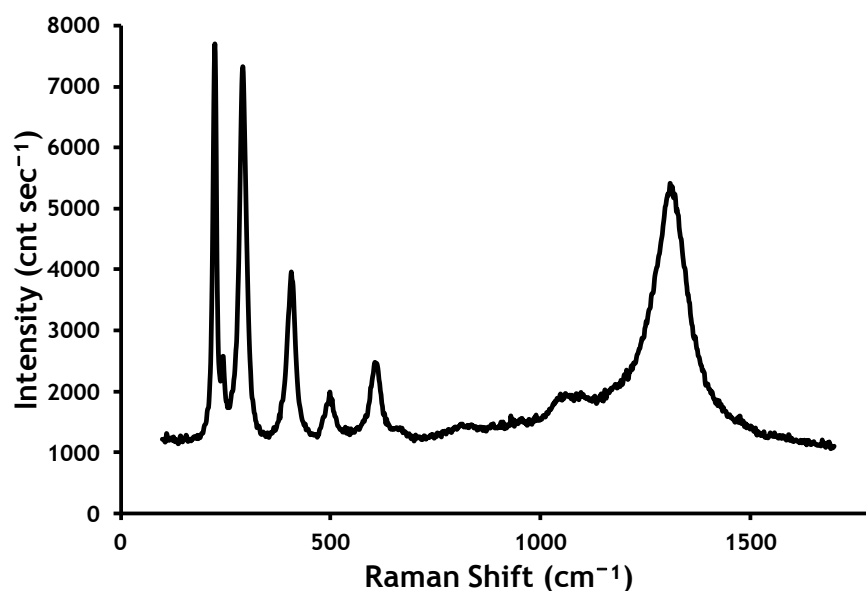


**Figure 4.181** Pre-Reaction Ambient Temperature Raman Spectra of Iron Oxide Catalyst Fe<sub>2</sub>O<sub>3</sub>NH<sub>3</sub>P.

**Table 4.54 Comparison of Pre-Reaction Raman Shift Bands Iron Oxide to Literature.**

Raman Shift Bands $\text{cm}^{-1}$							
	Ferric Oxide[43]						
Literature	225	245	291	410	495	611	1318
Iron Oxide Fe <sub>2</sub> O <sub>3</sub> NaOHP	217		277	387	491	586	1279
Iron Oxide Fe <sub>2</sub> O <sub>3</sub> NH <sub>3</sub> P	225	245	292	407	499	606	1309

#### 4.8.1.3 Pre-Reaction Surface Area Measurements of Iron Oxide Catalysts.

Surface area determination was carried out as described in section 3.5.1.

Table 4.55 below shows surface area, pore diameter and cumulative pore volume for iron oxide Fe<sub>2</sub>O<sub>3</sub>NaOHP and Fe<sub>2</sub>O<sub>3</sub>NH<sub>3</sub>P.

**Table 4.55 Pre-Reaction Surface Area Measurements of Iron Oxide Catalysts.**

Catalyst	Surface Area ( $\text{m}^2\text{g}^{-1}$ )	Pore Diameter (nm)	Cumulative Pore Volume ( $\text{cm}^3\text{g}^{-1}$ )
Fe <sub>2</sub> O <sub>3</sub> NaOHP	11	12	0.0344
Fe <sub>2</sub> O <sub>3</sub> NH <sub>3</sub> P	26	20	0.1398

#### 4.8.1.4 Pre-Reaction Thermo-gravimetric Analysis-Differential Scanning Calorimetry Analysis of Iron Oxide Catalysts.

Thermo-gravimetric analysis/differential scanning calorimetry was carried out as described in section 3.5.2.

Figure 4.182 below shows a total weight loss of 14 % from the pre-reaction iron oxide Fe<sub>2</sub>O<sub>3</sub>NaOHP over the temperature range 290 K to 970K.

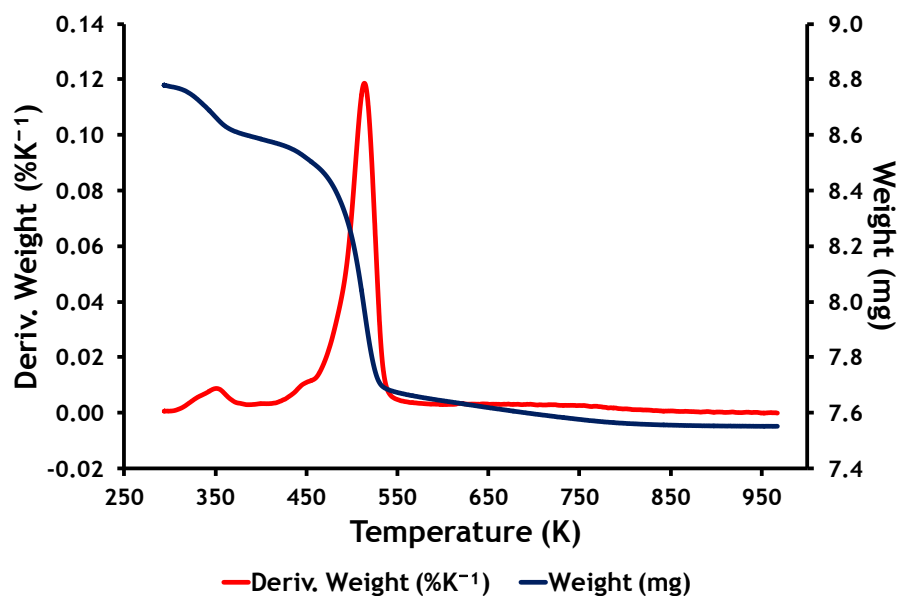


Figure 4.182 Pre-Reaction Iron Oxide Catalysts Fe<sub>2</sub>O<sub>3</sub>NaOHP TGA and Derivative Weight.

The DSC profile in figure 4.183 below shows two endothermic events at 350 K and 500 K associated with the evolution of water.

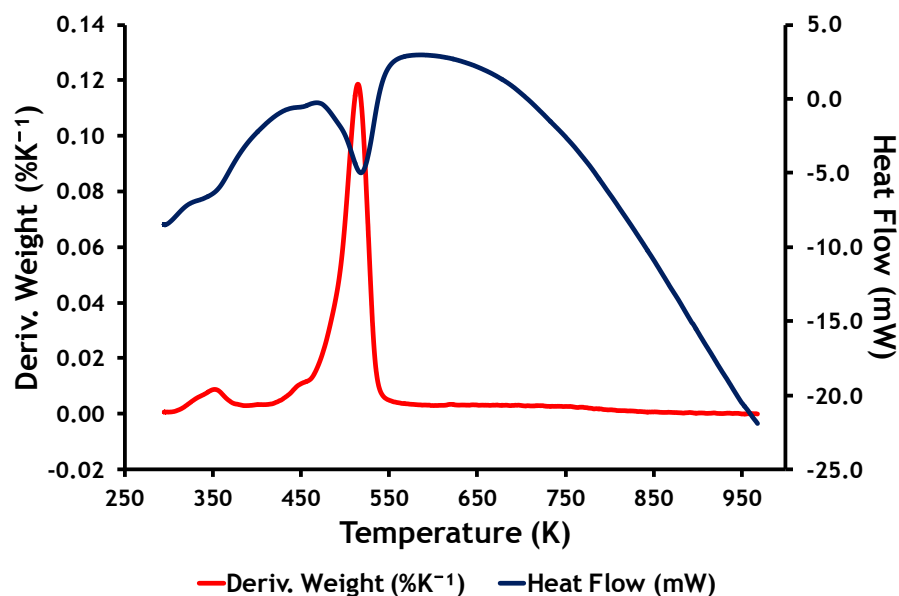


Figure 4.183 Pre-Reaction Iron Oxide Catalysts Fe<sub>2</sub>O<sub>3</sub>NaOHP TGA/DSC DSC.

Figure 4.184 below shows the evolution of water at 530 K, relative to the derivative weight loss.

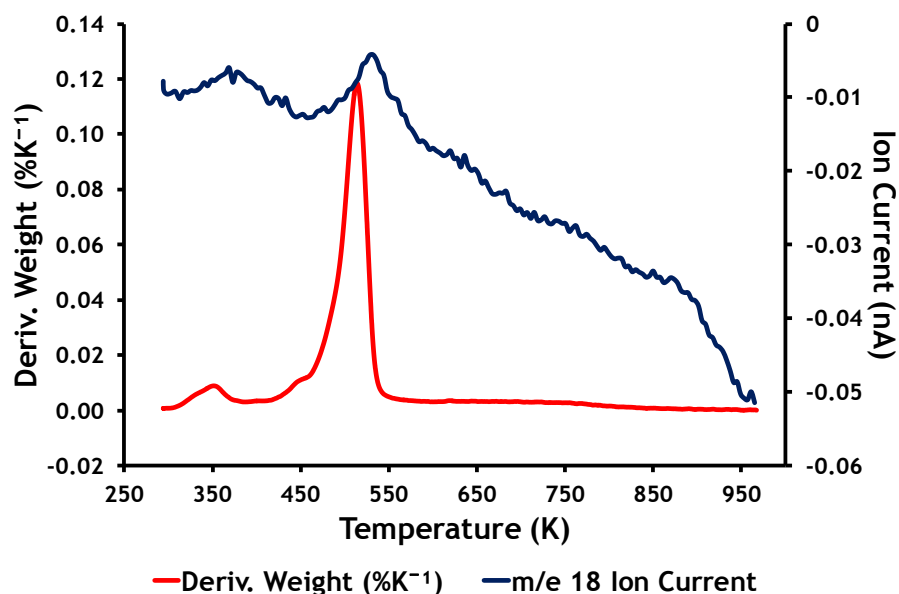


Figure 4.184 Pre-Reaction TGA/DSC Mass Spectrometer Profile from Iron Oxide Catalyst Fe<sub>2</sub>O<sub>3</sub>NaOHP m/e 18.

Figure 4.185 below shows a total weight loss of 8 % from iron oxide Fe<sub>2</sub>O<sub>3</sub>NH<sub>3</sub>P over the temperature range 290 K to 970 K.

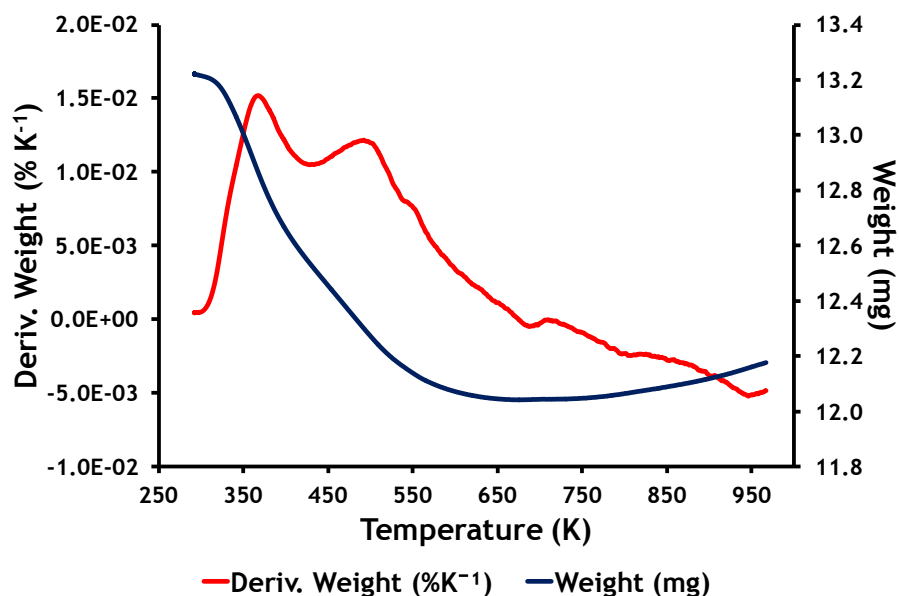


Figure 4.185 Pre-Reaction Iron Oxide Catalysts Fe<sub>2</sub>O<sub>3</sub>NH<sub>3</sub>P TGA and Derivative Weight.

The DSC profile in figure 4.186 below shows two endothermic events at 365 K and 495 K associated with the evolution of water. There is an exothermic event at 700K with no real mass change, this may be explained by a phase change.

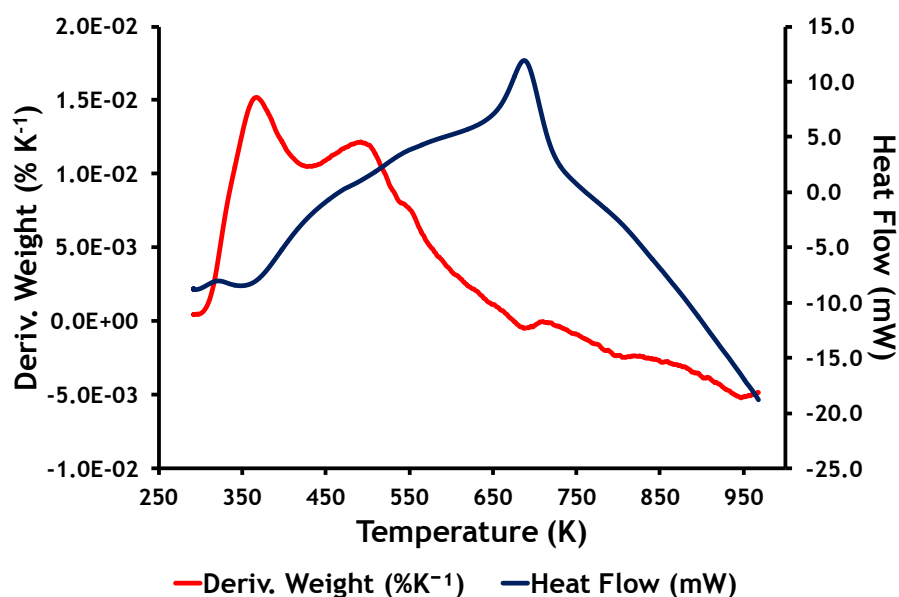


Figure 4.186 Pre-Reaction Iron Oxide Catalysts Fe<sub>2</sub>O<sub>3</sub>NH<sub>3</sub>P TGA/DSC DSC.

#### 4.8.2 Catalyst Testing Iron Oxide Catalysts.

The reactions involving iron oxide catalysts Fe<sub>2</sub>O<sub>3</sub>NaOHP and Fe<sub>2</sub>O<sub>3</sub>NH<sub>3</sub>P are detailed in table 3.7 in section 3.6.3 part of which is reproduced below in table 4.56. The test procedures are given in sections 3.6.2 and 3.6.3.

Table 4.56 Catalyst Testing List Iron Oxide Catalysts.

Reaction No	Catalyst Code	Bed Vol (cm <sup>3</sup> )	Weight (g)
28	Fe <sub>2</sub> O <sub>3</sub> NaOHP	1	0.9612
29	Fe <sub>2</sub> O <sub>3</sub> NH <sub>3</sub> P	1	2.1434

Figures 4.187 and 4.188 below show the product selectivities and 1-butene conversion obtained when passing 1-butene over iron oxide Fe<sub>2</sub>O<sub>3</sub>NaOHP with a bed volume of 1 cm<sup>3</sup>.

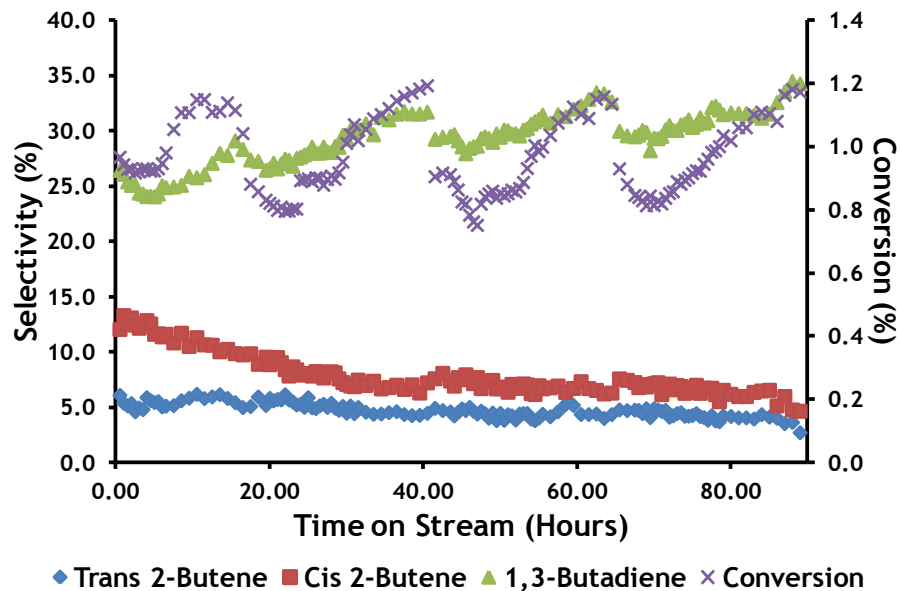


Figure 4.187 Selectivity/Conversion Major Components Iron Oxide Catalyst Fe<sub>2</sub>O<sub>3</sub>NaOHP Bed Volume 1 cm<sup>3</sup>.

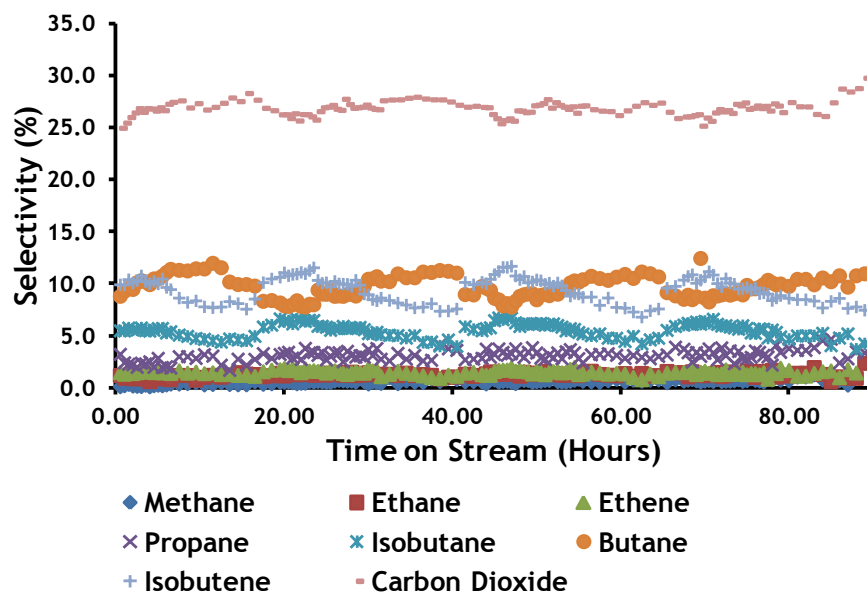


Figure 4.188 Selectivity Minor Components Iron Oxide Catalyst Fe<sub>2</sub>O<sub>3</sub>NaOHP Bed Volume 1 cm<sup>3</sup>.

Figures 4.189 and 4.190 below show the product selectivities and 1-butene conversion obtained when passing 1-butene over iron oxide Fe<sub>2</sub>O<sub>3</sub>NH3P with a bed volume of 1 cm<sup>3</sup>.

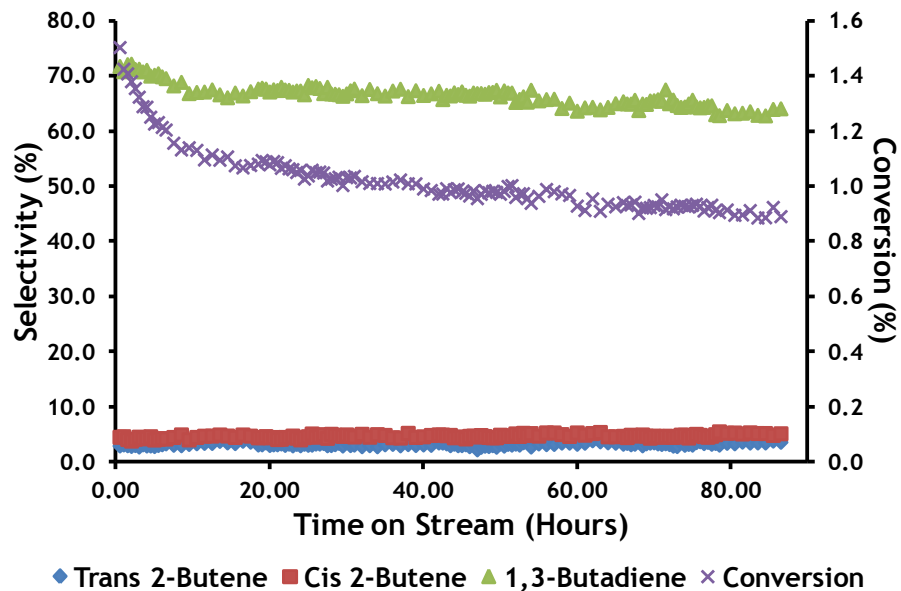


Figure 4.189 Selectivity/Conversion Major Components Iron Oxide Catalyst Fe<sub>2</sub>O<sub>3</sub>NH<sub>3</sub>P Bed Volume 1 cm<sup>3</sup>.

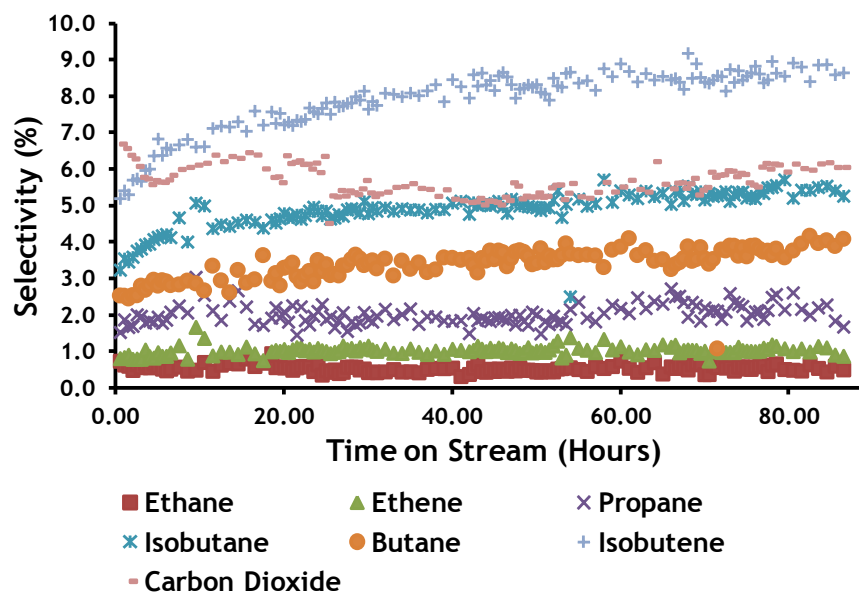


Figure 4.190 Selectivity Minor Components Iron Oxide Catalyst Fe<sub>2</sub>O<sub>3</sub>NH<sub>3</sub>P Bed Volume 1 cm<sup>3</sup>.

### 4.8.3 Post Reaction Characterisation of Iron Oxide Catalysts.

#### 4.8.3.1 Post Reaction X-Ray Diffraction Analysis of Iron Oxide Catalysts.

Ambient temperature X-Ray Diffraction was carried out as described in section 3.5.3.

Figure 4.191 below shows the post reaction ambient temperature XRD profile of iron oxide catalyst Fe<sub>2</sub>O<sub>3</sub>NaOHP.

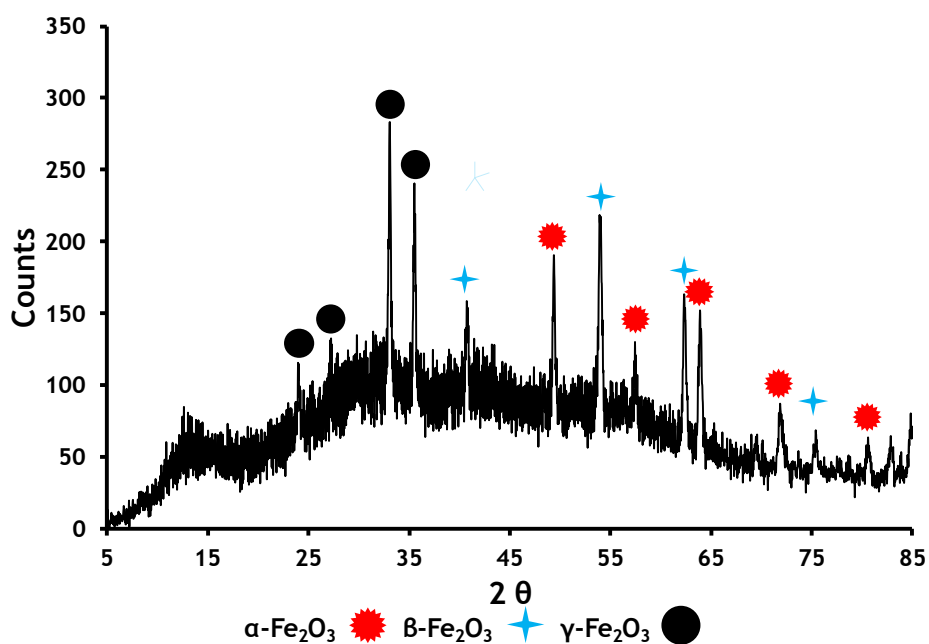


Figure 4.191 Post Reaction Ambient Temperature XRD Spectra of Iron Oxide Catalyst Fe<sub>2</sub>O<sub>3</sub>NaOHP.

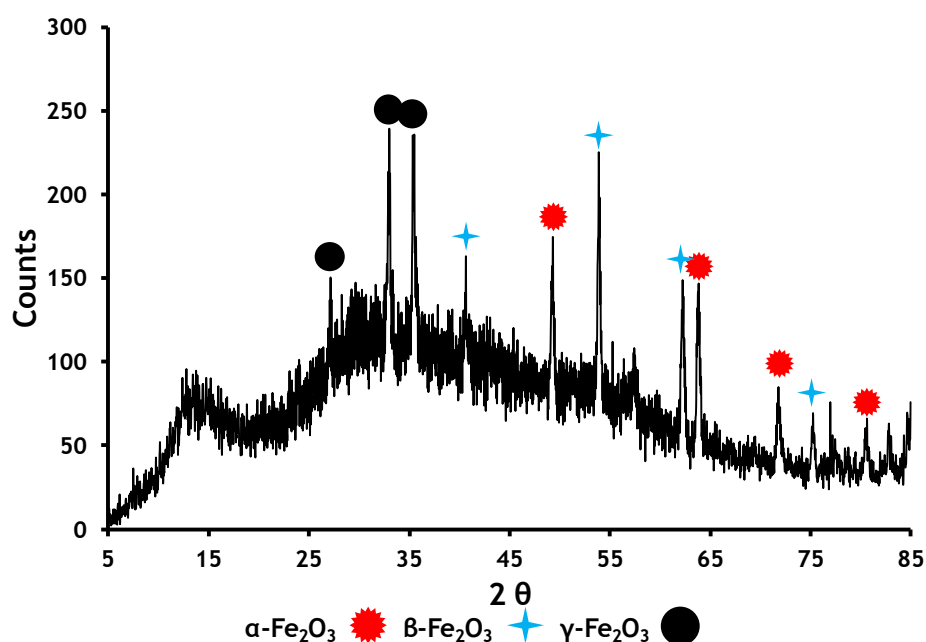
Table 4.57 below gives the particle size and the 2θ angle at which they were measured for α-Fe<sub>2</sub>O<sub>3</sub>, β-Fe<sub>2</sub>O<sub>3</sub> and γ- Fe<sub>2</sub>O<sub>3</sub>.

Table 4.57 Post Reaction Iron Oxide Catalyst Fe<sub>2</sub>O<sub>3</sub>NaOHP Particle Size Measurement.

	α-Fe <sub>2</sub> O <sub>3</sub>	β-Fe <sub>2</sub> O <sub>3</sub>	γ-Fe <sub>2</sub> O <sub>3</sub>
Degrees 2θ	49.4	54.0	33.1
Particle Size nm	38	30	35

Comparison of pre and post reaction iron oxide Fe<sub>2</sub>O<sub>3</sub>NaOHP shows an  $\alpha$ -Fe<sub>2</sub>O<sub>3</sub> particle size increase from 28 nm to 38 nm, a  $\beta$ -Fe<sub>2</sub>O<sub>3</sub> particle size increase from 27 nm to 30 nm and a  $\gamma$ -Fe<sub>2</sub>O<sub>3</sub> particle size increase from 28 nm to 35 nm.

Figure 4.192 below shows the post reaction ambient temperature XRD profile of iron oxide catalyst Fe<sub>2</sub>O<sub>3</sub>NH<sub>3</sub>P.



**Figure 4.192 Post Reaction Ambient Temperature XRD Spectra of Iron Oxide Catalyst Fe<sub>2</sub>O<sub>3</sub>NH<sub>3</sub>P.**

Table 4.58 below gives the particle size and the 2θ angle at which they were measured for  $\alpha$ -Fe<sub>2</sub>O<sub>3</sub>,  $\beta$ -Fe<sub>2</sub>O<sub>3</sub> and  $\gamma$ -Fe<sub>2</sub>O<sub>3</sub>.

**Table 4.58 Post Reaction Iron Oxide Catalyst Fe<sub>2</sub>O<sub>3</sub>NH<sub>3</sub>P Particle Size Measurement.**

	$\alpha$ -Fe <sub>2</sub> O <sub>3</sub>	$\beta$ -Fe <sub>2</sub> O <sub>3</sub>	$\gamma$ -Fe <sub>2</sub> O <sub>3</sub>
Degrees 2θ	49.3	53.9	33.0
Particle Size nm	37	30	28

Comparison of pre and post reaction iron oxide Fe<sub>2</sub>O<sub>3</sub>NH<sub>3</sub>P shows an  $\alpha$ -Fe<sub>2</sub>O<sub>3</sub> particle size decrease from 41 nm to 37 nm, a  $\beta$ -Fe<sub>2</sub>O<sub>3</sub> particle size decrease from 37 nm to 30 nm and a  $\gamma$ -Fe<sub>2</sub>O<sub>3</sub> particle size decrease from 41 nm to 28 nm.

#### 4.8.3.2 Post Reaction Raman Spectroscopy Analysis of Iron Oxide Catalysts.

Ambient temperature Raman spectroscopy was carried out as described in section 3.5.4.

Figures 4.193 to 4.194 below show the post reaction Raman bands for iron oxide catalysts Fe<sub>2</sub>O<sub>3</sub>NaOHP and Fe<sub>2</sub>O<sub>3</sub>NH<sub>3</sub>P. The Raman bands are tabulated in table 4.59 below to allow comparison.

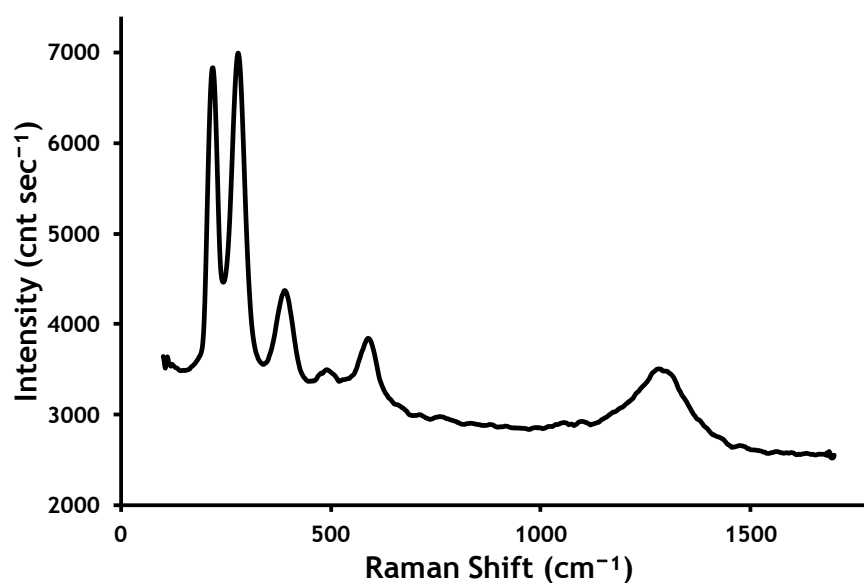


Figure 4.193 Post Reaction Ambient Temperature Raman Spectra of Iron Oxide Catalyst Fe<sub>2</sub>O<sub>3</sub>NaOHP.

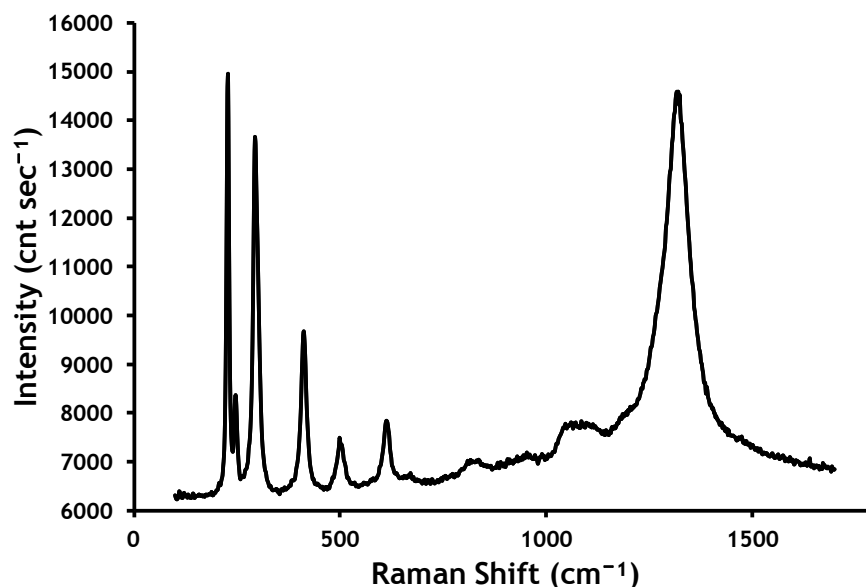


Figure 4.194 Post Reaction Ambient Temperature Raman Spectra of Iron Oxide Catalyst Fe<sub>2</sub>O<sub>3</sub>NH<sub>3</sub>P.

Table 4.59 Comparison of Post Reaction Raman Shift Bands Iron Oxide to Literature.

Raman Shift Bands (cm <sup>-1</sup> )							
	Ferric Oxide[43]						
Literature	225	245	291	410	495	611	1318
Iron Oxide Fe <sub>2</sub> O <sub>3</sub> NaOHP	219		279	389	491	589	1282
Iron Oxide Fe <sub>2</sub> O <sub>3</sub> NH <sub>3</sub> P	229	247	294	412	499	613	1317

#### 4.8.3.3 Post Reaction Surface Area Measurements of Iron Oxide Catalysts.

Surface area determination was carried out as described in section 3.5.1.

Table 4.60 below shows surface area, pore diameter and cumulative pore volume for iron oxide Fe<sub>2</sub>O<sub>3</sub>NaOHP and Fe<sub>2</sub>O<sub>3</sub>NH<sub>3</sub>P.

**Table 4.60 Post Reaction Surface Area Measurements of Iron Oxide Catalysts.**

Catalyst	Surface Area (m <sup>2</sup> g <sup>-1</sup> )	Pore Diameter (nm)	Cumulative Pore Volume (cm <sup>3</sup> g <sup>-1</sup> )
Fe <sub>2</sub> O <sub>3</sub> NaOHP	13	10	0.022
Fe <sub>2</sub> O <sub>3</sub> NH <sub>3</sub> P	3	3	0.002

Comparison of the pre and post reaction surface areas of the iron oxide catalysts shows a decrease from 26 m<sup>2</sup>g<sup>-1</sup> to 3 m<sup>2</sup>g<sup>-1</sup> for Fe<sub>2</sub>O<sub>3</sub>NH<sub>3</sub>P with no change for Fe<sub>2</sub>O<sub>3</sub>NaOHP.

#### **4.8.3.4 Post Reaction Thermo-gravimetric Analysis-Differential Scanning Calorimetry Analysis of Iron Oxide Catalysts.**

Thermo-gravimetric analysis/differential scanning calorimetry was carried out as described in section 3.5.2.

The post reaction TGA/DSC of both Fe<sub>2</sub>O<sub>3</sub>NaOHP and Fe<sub>2</sub>O<sub>3</sub>NH<sub>3</sub>P showed weight gains of less than 1%.

### **4.9 Zinc Ferrite Citrate Precursor.**

#### **4.9.1 Characterisation of Zinc Ferrite Citrate Precursor.**

##### **4.9.1.1 X-Ray Diffraction Analysis of Zinc Ferrite Citrate Precursor.**

Ambient temperature X-Ray Diffraction was carried out as described in section 3.5.3.

The XRD profile in figure 4.195 below shows the presence  $\alpha$ -Fe<sub>2</sub>O<sub>3</sub>,  $\beta$ -Fe<sub>2</sub>O<sub>3</sub>,  $\gamma$ -Fe<sub>2</sub>O<sub>3</sub> and zinc ferrite.

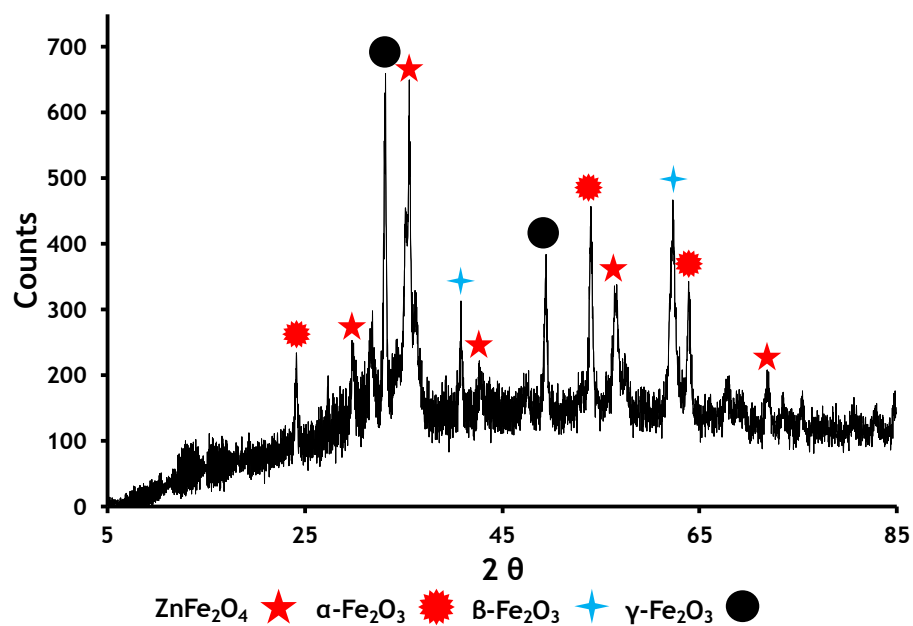


Figure 4.195 Ambient Temperature XRD Spectra of Zinc Ferrite Citrate Precursor.

#### 4.9.1.2 Raman Spectroscopy Analysis of Zinc Ferrite Citrate Precursor.

Ambient temperature Raman spectroscopy was carried out as described in section 3.5.4.

Figure 4.196 below shows the Raman profile for zinc ferrite citrate precursor. The Raman bands are tabulated in table 4.61 below.

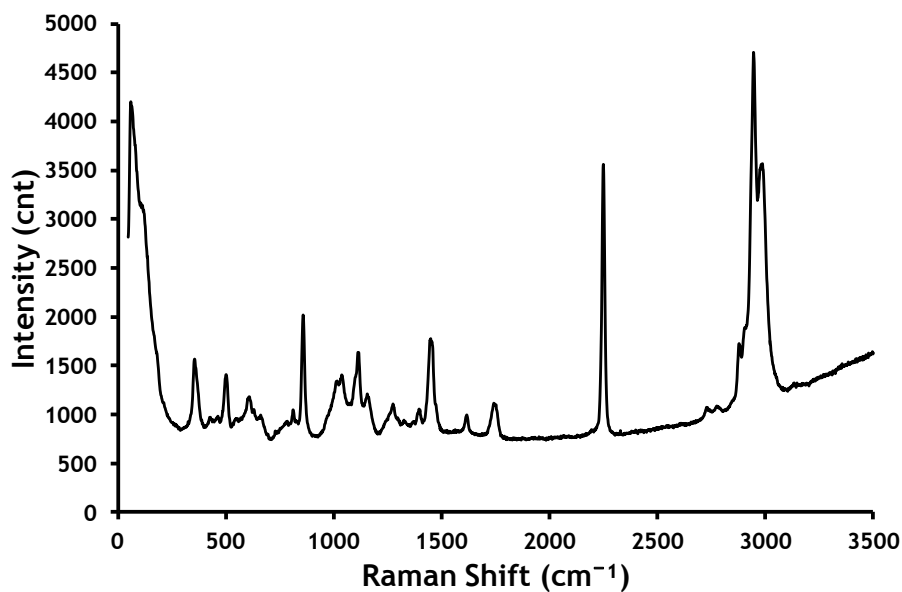


Figure 4.196 Ambient Temperature Raman Spectra of Zinc Ferrite Citrate Precursor.

Table 4.61 Comparison of Raman Shift Bands Zinc Ferrite Citrate Precursor to Literature.

Raman Shift Bands (cm <sup>-1</sup> )									
	Zinc Ferrite[36]							Fe <sub>2</sub> O <sub>3</sub> [43]	
Literature	221	246	330-355	451-498	647-659	1091-1106	1271-1298	611	
Zinc Ferrite Citrate Precursor			361	505		1114	1276	609	
	Unassigned Inorganic and Organic Bands								
Zinc Ferrite Citrate Precursor	812	863	1035	1162	1397	1456	1617	2250	2945

#### 4.9.1.3 Surface Area Measurements of Zinc Ferrite Citrate Precursor.

Surface area determination was carried out as described in section 3.5.1.

Table 4.62 below shows surface area, pore diameter and cumulative pore volume for zinc ferrite citrate precursor

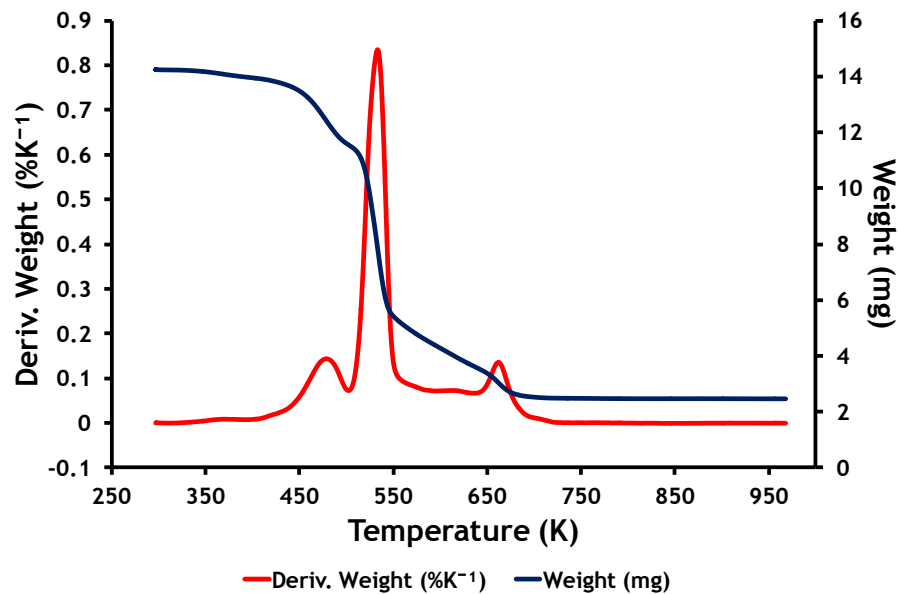
**Table 4.62 Surface Area Measurements of Zinc Ferrite Citrate Precursor.**

Catalyst	Surface Area (m <sup>2</sup> g <sup>-1</sup> )	Pore Diameter (nm)	Cumulative Pore Volume (cm <sup>3</sup> g <sup>-1</sup> )
Zinc Ferrite Citrate Precursor	24	27	0.1209

#### 4.9.1.4 Thermo-gravimetric Analysis-Differential Scanning Calorimetry Analysis of Zinc Ferrite Citrate Precursor.

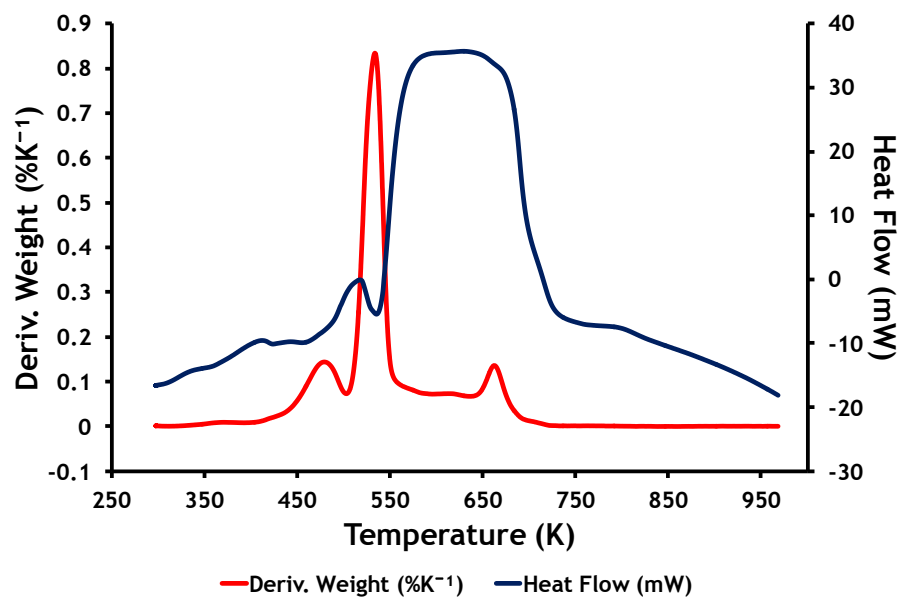
Thermo-gravimetric analysis/differential scanning calorimetry was carried out as described in section 3.5.2.

Figure 4.197 below shows a total weight loss of 83 % from zinc ferrite citrate precursor over the temperature range 290 K to 970 K.



**Figure 4.197 Pre-Reaction Zinc Ferrite Citrate Precursor TGA and Derivative Weight.**

The DSC profile in figure 4.198 below shows two exothermic events associated with the oxidation of the citrate precursor.



**Figure 4.198 Zinc Ferrite Citrate Precursor TGA/DSC DSC.**

Figure 199 below shows the evolution of water at 540 K, relative to the derivative weight.

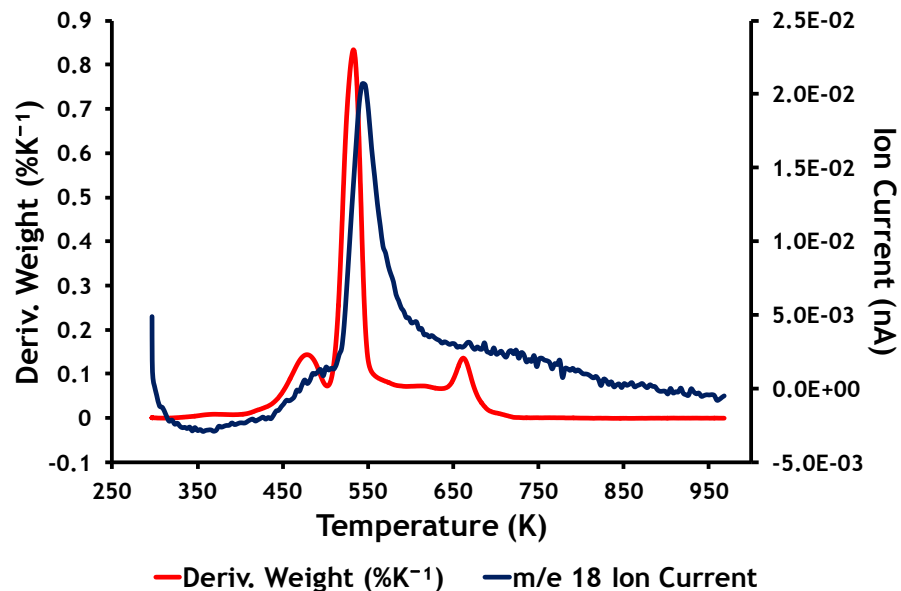


Figure 4.199 TGA/DSC Mass Spectrometer Profile Zinc Ferrite Citrate Precursor m/e 18.

Figure 200 below shows the evolution of carbon monoxide at 495 K, 540 K and 660 K, relative to the derivative weight.

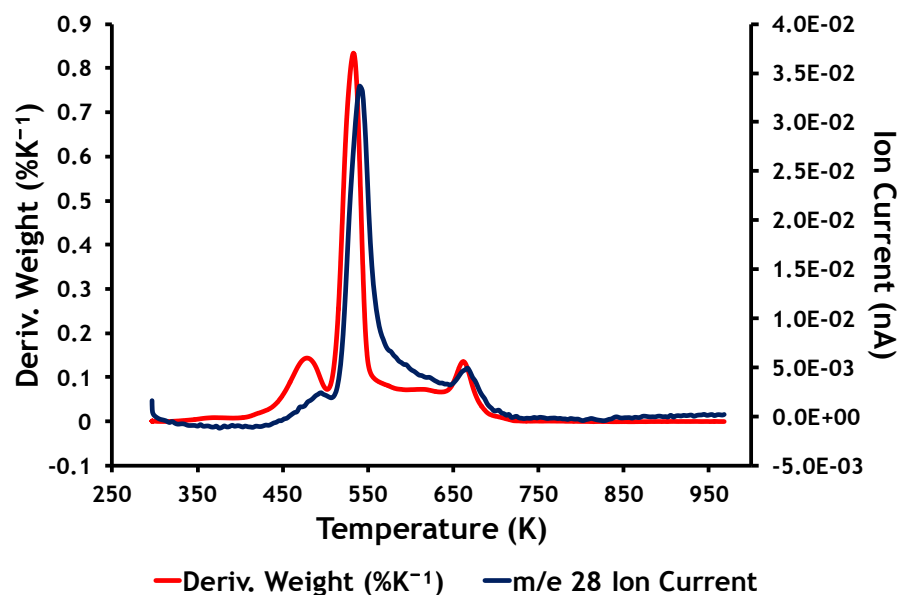


Figure 4.200 TGA/DSC Mass Spectrometer Profile Zinc Ferrite Citrate Precursor m/e 28.

Figure 201 below shows the evolution of nitrous oxide at 545 K and 685 K, relative to the derivative weight.

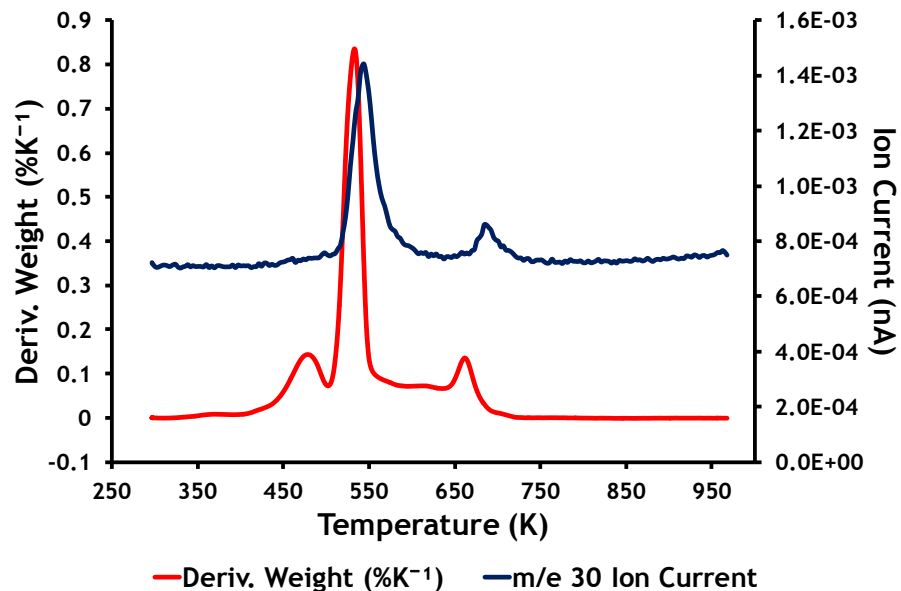


Figure 4.201 TGA/DSC Mass Spectrometer Profile Zinc Ferrite Citrate Precursor m/e 30.

Figure 202 below shows the evolution of carbon dioxide at 480 K , 535 K and 665 K, relative to the derivative weight.

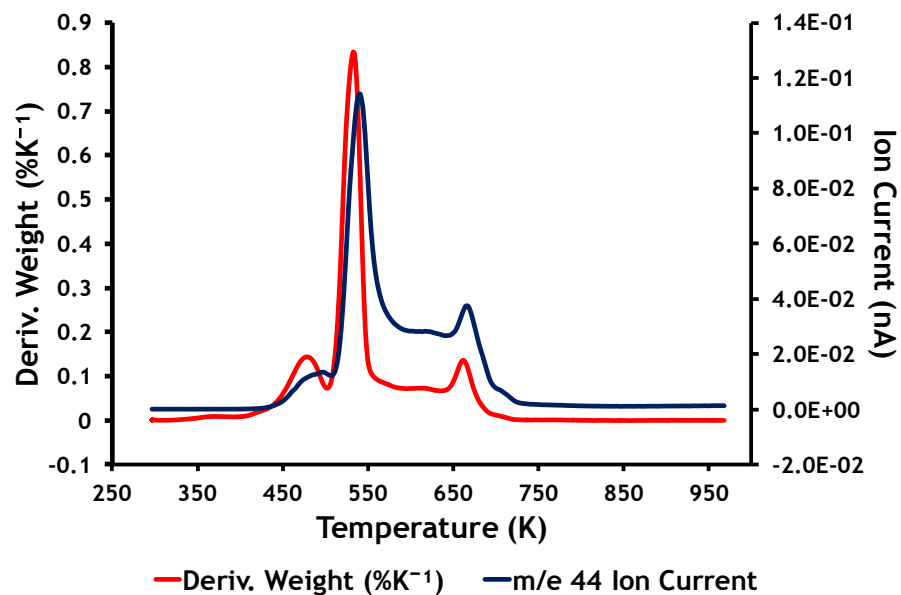


Figure 4.202 Zinc Ferrite TGA/DSC Mass Spectrometer Profile Citrate Precursor m/e 44.

Figure 203 below shows the evolution of nitric oxide at 475 K , 5635 K and 665 K, relative to the derivative weight.

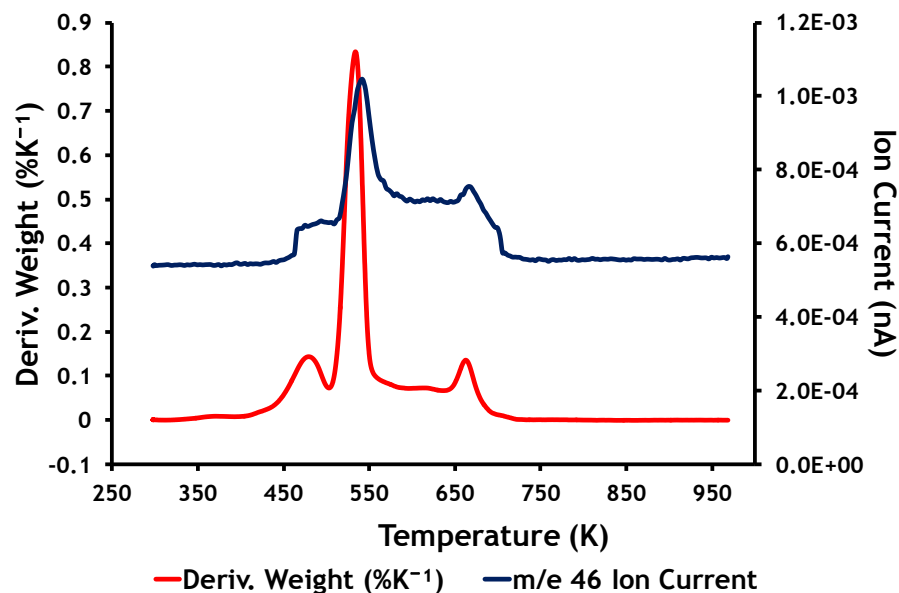


Figure 4.203 TGA/DSC Mass Spectrometer Profile Zinc Ferrite Citrate Precursor m/e 46.

Figure 204 below shows the uptake of oxygen at 550 K, relative to the derivative weight.

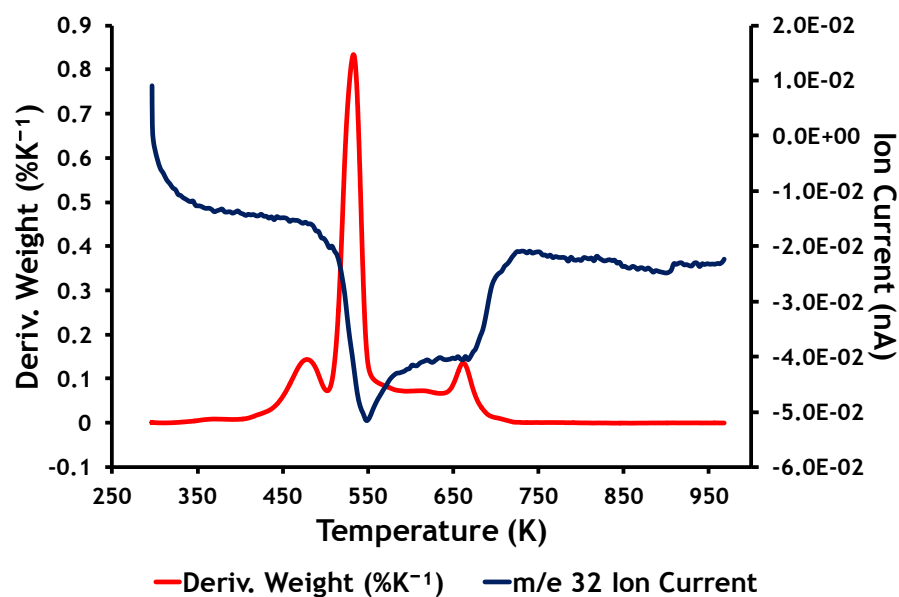


Figure 4.204 TGA/DSC Mass Spectrometer Profile Zinc Ferrite Citrate Precursor m/e 32.

No further work was carried out with this catalyst due to the large exotherm and associated gas evolution, which made large scale calcination impractical with the existing equipment.

## 5. Discussion.

In this section we will discuss the oxidative dehydrogenation of 1-butene to 1,3-butadiene over supported and bulk catalysts. Catalysts studied were  $\theta$ -alumina supported zinc ferrite and vanadia, bulk zinc ferrite, iron enriched zinc ferrite and iron oxide. Figure 5.1 shows the reaction schematic of 1-butene to 1,3-butadiene.

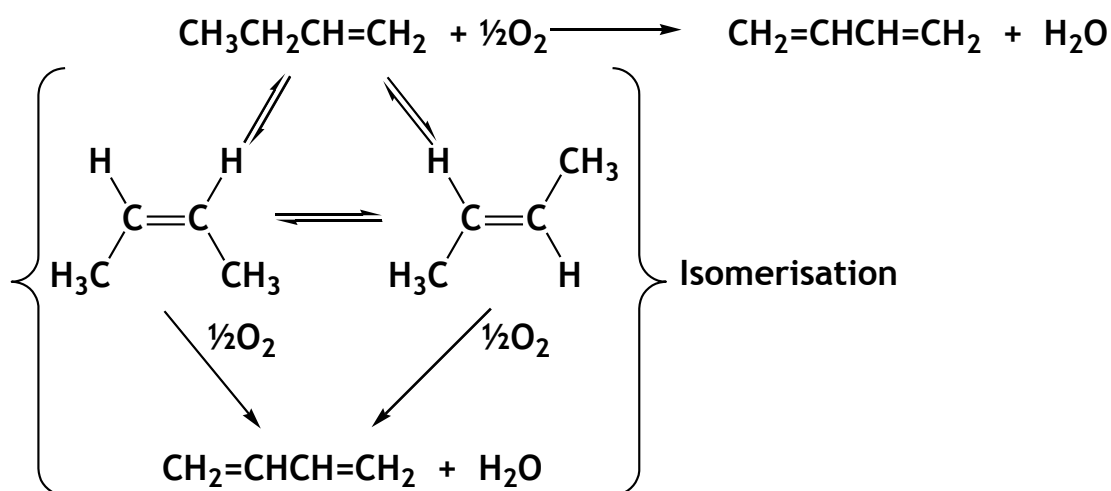


Figure 5.1 Reaction Schematic.

### 5.1 Alumina Support.

Most catalyst supports are assumed to be inert or non reactive in the catalytic process, however this is not always the case. For example, it has been established that  $\theta$ -alumina produces C1 to C3 'cracking' products in the butane dehydrogenation reaction due to the acid sites on the support.[45] Hence the reactivity of the  $\theta$ -alumina support for the oxidative dehydrogenation of 1-butene was investigated. Using a 3 cm<sup>3</sup> bed the selectivity to 1,3-butadiene was 3 %. The selectivities to cis-2-butene and trans-2-butene were 62 % and 34 % respectively with a 1-butene conversion of 39 %. These selectivities suggested that the initial product was cis-2-butene, which is not the thermodynamically favoured product. Analysis of the reaction products gave a cis-2-butene:trans-2-butene:1,3-butadiene mole ratio of 1.0:0.5:0.05 at 697 K. To see the reaction profile at an earlier stage a bed volume of 1 cm<sup>3</sup> was tested and gave selectivities of 68 %, 29 % and 2 % for cis-2-butene, trans-2-butene and 1,3-butadiene respectively with a 1-butene conversion of 11 %. Analysis of the

reaction products gave a cis-2-butene:trans-2-butene:1,3-butadiene mole ratio of 1.0:0.4:0.03 at 697 K. Therefore these results suggest that cis-2-butene is the primary product, which then isomerises to trans-2-butene.

Pre and post reaction XRD spectra gave similar profiles showing the presence of  $\alpha$ -alumina,  $\delta$ -alumina,  $\gamma$ -alumina and  $\kappa$ -alumina in addition to  $\theta$ -alumina. As there are no detectable phase changes between pre and post reaction, the XRD confirms that, as expected,  $\theta$ -alumina is stable under reaction conditions. The pre and post reaction TGA/DSC results only showed desorption of physisorbed water, while the absence of carbon dioxide evolution shows that there is no carbon laydown on the support. Surface area analysis of pre and post reaction samples shows no significant changes in surface area, cumulative pore volume or pore diameter.

## 5.2 $\theta$ -Alumina Supported Zinc Ferrite Catalysts.

Two impregnation methods were used to produce  $\theta$ -alumina supported zinc ferrite catalysts, spray and high pressure/high temperature. Only spray impregnation produced  $\theta$ -alumina supported zinc ferrite catalysts. The high pressure:high temperature impregnation produced a predominately  $\theta$ -alumina supported iron catalyst. This can be explained by the fact that this catalyst was washed prior to drying which may have stripped zinc and ferric nitrates from the alumina support.

Atomic adsorption analysis of the zinc ferrite supported catalysts 3.45 % zinc ferrite on alumina, 3.2 % Fe/0.39 % Zn on alumina and 8.81 % zinc ferrite/0.49 % Fe on alumina show a Fe:Zn mole ratio of 2.07:1, 9.57:1 and 2.56:1 respectively. Examination of the pre-reaction XRD profiles shows only alumina phases predominately  $\theta$ -alumina. The reason that no zinc ferrite, iron or zinc was seen in the profiles is most likely due to the amorphous nature of the supported phases on the support. Comparison of the pre and post XRD profiles shows no change in the crystal structure of these catalysts.

The pre-reaction temperature programmed Raman spectra of 3.45 % zinc ferrite on alumina and 3.2 % iron/0.39 % zinc on alumina show bands that can be

assigned to  $\theta$ -alumina and a single band that can be assigned to nitrate which is lost with increasing temperature. The ambient temperature Raman spectra of 8.81 %  $\text{ZnFe}_2\text{O}_4$ /0.49 % Fe on  $\text{Al}_2\text{O}_3$  also shows bands that can be assigned to  $\theta$ -alumina, and is the only supported catalyst to give a band that can be assigned to ferric oxide. Comparison of the pre and post reaction Raman spectra shows the loss of the  $356\text{ cm}^{-1}$  band and addition of bands at  $448\text{ cm}^{-1}$  and  $519\text{ cm}^{-1}$  for 3.45 % zinc ferrite on alumina; loss of the band at  $728\text{ cm}^{-1}$  and addition of bands at  $326\text{ cm}^{-1}$  and  $612\text{ cm}^{-1}$  for 8.81 % zinc ferrite/0.49 % iron on alumina; loss of the bands at  $356\text{ cm}^{-1}$  and  $431\text{ cm}^{-1}$  and addition of band at  $406\text{ cm}^{-1}$  for 3.2 % iron/0.39 % zinc on alumina. The change in the distribution of the Raman bands of the supported catalysts are likely due to structural changes as a result of the loss of nitrates with the supported catalysts which is seen in both the TGA/DSC analysis and the temperature programmed Raman results.

Comparison of the pre and post reaction surface area measurements shows no significant changes in the surface area, pore diameter or cumulative pore volume of the supported catalysts since the predominant species is  $\theta$ -alumina which masks any changes in the supported materials.

Pre-reaction TGA/DSC analysis of 3.45 % zinc ferrite and 3.2 % iron/0.39 % zinc on alumina shows a weight loss of 12 % and 10 % respectively with this loss being attributed to nitrous oxide, nitric oxide and di-nitrogen oxide; which correspond to the loss of nitrate seen in the corresponding temperature programmed Raman spectra. 8.81 % zinc ferrite/0.49 % iron on alumina shows a weight loss of 19 % which is attributed to nitrous oxide. Post reaction TGA/DSC of 3.45 % zinc ferrite on alumina gave a weight loss of 6 % which can be attributed to the evolution of carbon dioxide, which suggests there has been some carbon laydown on the catalyst. The 8.81 % zinc ferrite/0.49 % Fe on alumina shows a weight loss of 2 % which can be attributed to the desorption of physisorbed water, whereas 3.2 % iron/0.39 % zinc on alumina catalyst showed a weight loss of 11 % over a temperature range of 600 K to 650 K which can be attributed to the loss of nitrous oxide. This suggests that the 3.2 % iron/0.39 % zinc on alumina sample is continuing to lose nitrous oxide throughout the catalyst testing reaction due to incomplete calcination: increased calcination temperature and/or calcination duration would possibly remedy this issue.

The 3.45 % zinc ferrite on alumina and 3.2 % Fe/0.39 % Zn on alumina catalysts require 2 hours on stream to reach steady state, whereas 8.81 % zinc ferrite/0.49 % Fe on alumina sample requires 8 hours on stream to reach steady state which suggests that structure of 8.81 % zinc ferrite/0.49 % Fe on alumina is different from the other two supported catalysts and requires longer to form a stable structure.

Initially the oxidative dehydrogenation of 1-butene over 3.45 % zinc ferrite on alumina gives 1,3-butadiene, cis-2-butene and trans-2-butene selectivities of 79 %, 11 %, 7 % respectively, with a 1-butene conversion of 42 %. After 90 hours on stream the 1,3-butadiene selectivity decreased to 63 %, while the selectivities of cis-2-butene and trans-2-butene increased to 21 % and 15 % respectively. At the same time the 1-butene conversion decreased to 19 %. The decrease in 1,3-butadiene selectivity can be attributed to loss of zinc ferrite sites due to carbon lay down which is verified by the carbon dioxide evolution seen in the post reaction TGA/DSC.

Oxidative dehydrogenation of 1-butene over 3.2 % Fe/0.39 % Zn on alumina initially gave 1,3-butadiene, cis-2-butene and trans-2-butene selectivities of 75 %, 14 % and 9% respectively; the 1,3-butadiene selectivity decreased to 63 % and the cis-2-butene and trans-2-butene selectivities respectively increased to 21 % and 15 % after 90 hours on stream; 1-butene conversion decreased from 64 % to 44 %. The TGA/DSC analysis of post reaction 3.2 % Fe/0.39 % Zn on alumina catalyst did not show the evolution of carbon dioxide which means carbon laydown was not responsible for catalyst deactivation. The likely cause of deactivation is catalyst poisoning due to the continuing evolution of nitrous oxide over the reaction period.

8.81 % zinc ferrite/0.49 % Fe on alumina oxidative dehydrogenation of 1-butene initially gives 1,3-butadiene, cis-2-butene and trans-2-butene selectivities of 77 %, 13 % and 9 % respectively. After 90 hours on stream the 1,3-butadiene selectivity only decreased to 73 % while the cis-2-butene and trans-2-butene increased to 15 % and 11 % respectively. The 1-butene conversion only decreased from 45 % to 42 % which suggests that the higher zinc ferrite loading of the

8.81 % zinc ferrite/0.49 % Fe on alumina gives sufficient zinc ferrite sites to inhibit deactivation of the catalyst by carbon lay down.

### 5.3 $\theta$ -Alumina Supported Vanadia Catalysts.

Examination of the pre-reaction XRD profiles of the two vanadia on  $\theta$ -alumina catalysts that were prepared by spray impregnation, shows only alumina phases, predominately  $\theta$ -alumina. Comparison of the pre and post XRD profiles shows no change in the crystal structure of the 0.5 % vanadia on alumina suggesting that the reason that no vanadia was seen is due to the low vanadia loading on the support. However the post reaction 3.3 % vanadia on alumina shows the presence of  $V_3O_7$  and  $V_5O_9$ , suggesting that the vanadia was amorphous pre reaction.

The temperature programmed Raman spectra of 0.5 % vanadia on alumina shows a sharpening of the peaks during calcination, only one band attributed to  $V_2O_5$  is observed all other bands are attributed to alumina. Ambient temperature Raman spectra of 3.3 % vanadia on alumina only show bands associated with alumina as no vanadia bands could be assigned without any ambiguity. No post reaction Raman spectra was observed due to excessive fluorescence.

Comparison of the pre and post reaction surface areas shows no significant changes in the surface area, pore diameter or cumulative pore volume of the supported catalysts.

TGA/DSC of pre-reaction 0.5 % vanadia on alumina and 3.3 % vanadia on alumina shows weight losses of 5 % and 11 % respectively. The weight loss from the 0.5 % vanadia on alumina can be attributed to the evolution of nitrous oxide and carbon dioxide, the weight loss observed from 3.3 % vanadia on alumina is due to the evolution of carbon dioxide. Post reaction TGA/DSC of 0.5 % vanadia on alumina and 3.3 % vanadia on alumina catalysts show a weight loss of 3 % due to the desorption of physisorbed water at 360/435 K and 335 K respectively and carbon dioxide at 585 to 610 K and 760 K respectively.

Oxidative dehydrogenation of 1-butene over 0.5 % vanadia on alumina yielded 1,3-butadiene, cis-2-butene and trans-2-butene selectivities of 17 %, 51 % and 30 % respectively at a 1-butene conversion of ~35 % over 90 hours on stream with no detectable catalyst deactivation. Oxidative dehydrogenation of 1-butene over the 3.3 % vanadia on alumina catalyst gives 1,3-butadiene, cis-2-butene and trans-2-butene selectivities of 13 %, 39 % and 46 % respectively and a 1-butene conversion of ~67 % over 90 hours on stream with no detectable catalyst deactivation.

Comparison of the supported catalysts show that the vanadia catalysts give poor selectivity towards 1,3-butadiene and the highest 1-butene conversion in the case of the higher vanadia loading. The zinc ferrite and iron/zinc catalysts all gave similar initial selectivities towards 1,3-butadiene (75 % to 79 %) and 1-butene conversions (42 % to 51 %). However after 90 hours on stream only the 8.81 % zinc ferrite/0.49 % Fe on alumina catalyst showed no significant change in either selectivity or conversion.

#### **5.4 Bulk Zinc Ferrite ZF0.6MBP Catalysts.**

Bulk zinc ferrite catalyst ZF0.6MBP was prepared by co-precipitation of iron and zinc chlorides in 0.6M sodium hydroxide at 343K.

Analysis of the pre reaction XRD profile and the Raman spectra confirm the presence of zinc ferrite in agreement with the atomic absorption Fe:Zn mole ratio of 2.2:1. XRD analysis of the post reaction sample confirms the retention of the zinc ferrite structure. However when the pre and post reaction surface area measurements for the zinc ferrite catalyst (ZF0.6MBP) are compared a decrease from  $84 \text{ m}^2\text{g}^{-1}$  to  $37 \text{ m}^2\text{g}^{-1}$  is observed. On comparing pre and post reaction acid sites analysis, as shown in figures 4.70 and 4.83, it can be seen that there is a loss of two acid sites, one weak and one strong site. Figure 5.2 below shows a slight broadening of the post reaction EPR spectra over the pre reaction spectra indicating a small decrease in the Fe(III) occupancy in the tetrahedral sites within the defective zinc ferrite structure[46]. Examination of the pre and post reaction Raman spectra shows the loss of two bands which confirms structural changes on the catalyst. The observations above show that zinc ferrite (ZF0.6MBP) undergoes both bulk and structural changes.

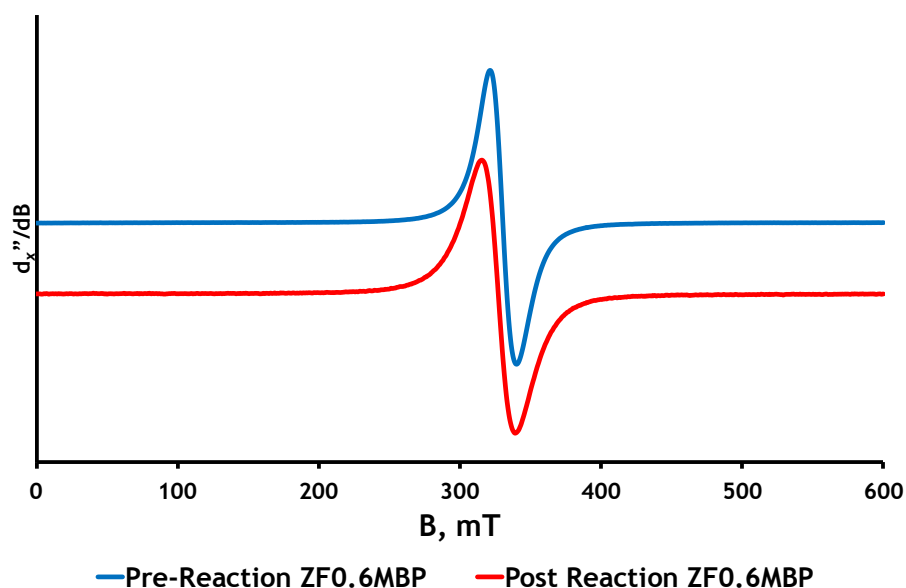


**Figure 5.2 Comparison of Pre and Post Reaction Zinc Ferrite ZFO.6MBP EPR Paramagnetic Measurement.**

As a consequence of the large reduction in surface area of post reaction zinc ferrite (ZFO.6MBP) it was decided to investigate whether these change were the result the reaction mixture or steam alone. Two samples of zinc ferrite catalyst (ZFO.6MBP) were subjected to steam/20 % oxygen in argon mixture at 693 K for 24 and 48 hours on stream respectively. On comparing fresh and steamed catalysts a 10 % reduction in the surface areas was observed.

Figure 4.74 shows the oxidative dehydrogenation of 1-butene over zinc ferrite catalyst (ZFO.6MBP) which shows the catalyst starting to deactivate after 20 hours on stream. Comparing cis-2-butene, trans-2-butene, 1,3-butadiene yields and 1-butene conversion at 20 hour and 90 hours on stream shows an 8 % and 11 % reduction in the cis-2-butene and trans-2-butene yields respectively which corresponds with the reduction of acid sites. Over the same period 1-butene conversion decreased by 35 % but 1,3-butadiene yield increased by 16 %. TGA/DSC analysis of post reaction zinc ferrite catalyst (ZFO.6MBP) shows desorption of physisorbed water at 350 K and carbon burn off at 550 K and 800 K suggesting that the deactivation was due to sintering and carbon laydown.

Comparison of our results with those of Lee *et al*[34] at 6 hours on stream shows an 8 % higher conversion of butene but a 29 % lower yield of 1,3-butadiene. The preparation method for our catalyst and that of Lee *et al* was identical, the surface area and XRD spectra results show no significant differences between the catalysts. Lee *et al* used 693 K as the reaction temperature, a GHSV of  $475 \text{ h}^{-1}$  and C4 raffinate-3 containing 57.9 % butene (7.5 % 1-butene, 33.9 % trans-2-butene and 16.5 % cis-2-butene) with an oxygen:butene ratio of 0.75:1. We also used 693 K as the reaction temperature and had an oxygen:1-butene ratio of 0.75:1; however our GHSV was only  $200 \text{ h}^{-1}$  and instead of raffinate we used pure 1-butene as the hydrocarbon feed. Another significant difference was the catalyst bed size, which was 10 times that used by Lee *et al* hence the linear velocity was much higher than that used by Lee and co-workers. Lee *et al* also only reported the first 6 hours of reaction and as a result they did not see any noticeable deactivation. The likely causes of the much lower 1,3-butadiene yield obtained, in the initial stages, is due to the difference in linear velocity of the gas and the hydrocarbon feed composition.

The pre and post reaction XRD profiles, pre reaction Raman spectra and pre and post reaction surface area measurement for zinc ferrite (ZF0.6MBP 24HSPT) gives the same bulk and structural information as zinc ferrite (ZF0.6MBP). For example figure 5.3 below shows a broadening of the post reaction EPR spectra over the pre reaction spectra indicating a decrease in the Fe(III) occupancy in the tetrahedral sites within the defective zinc ferrite structure[46].

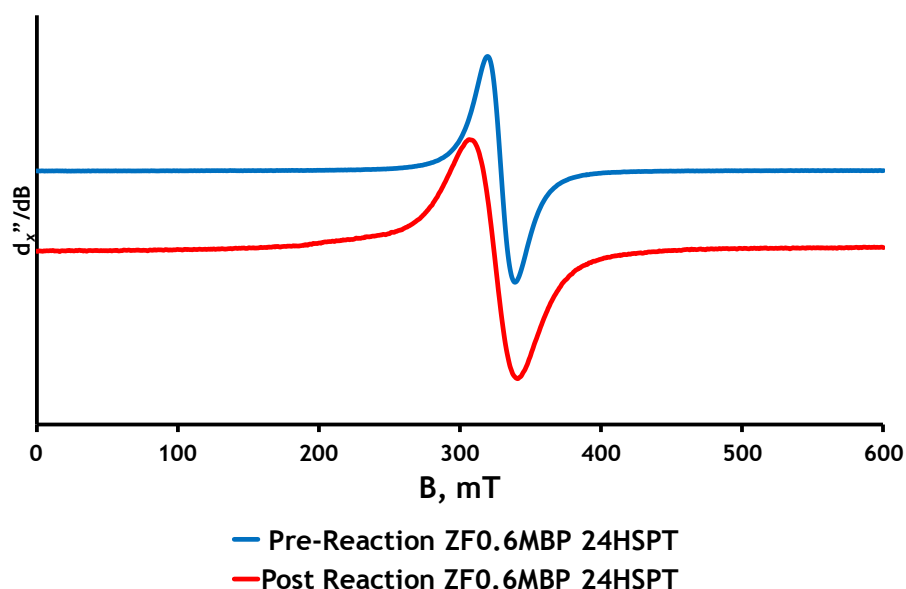


**Figure 5.3 Comparison of Pre and Post Reaction Pre-Steamed Zinc Ferrite ZF0.6MBP 24HSPT EPR Paramagnetic Measurement.**

Figure 4.76 shows the oxidative dehydrogenation of 1-butene over the zinc ferrite catalyst (ZF0.6MBP 24HSPT, pre-steamed for 24 h) which shows the catalyst continuing to activate over 90 hours on stream. Comparing cis-2-butene, trans-2-butene, 1,3-butadiene yields and 1-butene conversion at 2 hour and 90 hours on stream shows a reduction in the cis-2-butene and trans-2-butene yields of 18 % and 23 % respectively which corresponds with the reduction of acid sites, while 1-butene conversion increased by 16 % and 1,3-butadiene yield increased by 56 %. TGA/DSC analysis of port reaction zinc ferrite catalyst (ZF0.6MBP) shows desorption of physisorbed water at 375 K and carbon burn off at 550 K.

### 5.5 Bulk Zinc Ferrite ZF3MBPC Catalyst.

Bulk zinc ferrite catalyst ZF3MBPC was prepared by co-precipitation iron and zinc chlorides at ambient temperature in 3M sodium hydroxide.

The pre and post reaction XRD profiles, pre reaction Raman spectra and pre and post reaction surface area measurement for zinc ferrite (ZF3MBPC) gives the same bulk and structural information as zinc ferrite (ZF0.6MBP). On comparing pre and post reaction acid sites analysis as shown in figures 4.92 and 4.131 it can be seen that there is a loss of two acid sites, one medium and one strong site. Comparison of the pre and post quenched (100 K) SQUID measurements in figure

5.4 show a reduction in magnetism and figure 5.5 below shows a broadening of the post reaction EPR spectra over the pre reaction spectra. Both SQUID and EPR measurements indicate a decrease in the Fe(III) occupancy in the tetrahedral sites within the defective zinc ferrite structure[46, 47]. Examination of the pre and post reaction Raman spectra shows the loss of one band which confirms structural changes on the catalyst. The observations above show that zinc ferrite (ZF3MBPC) undergoes both bulk structural changes.

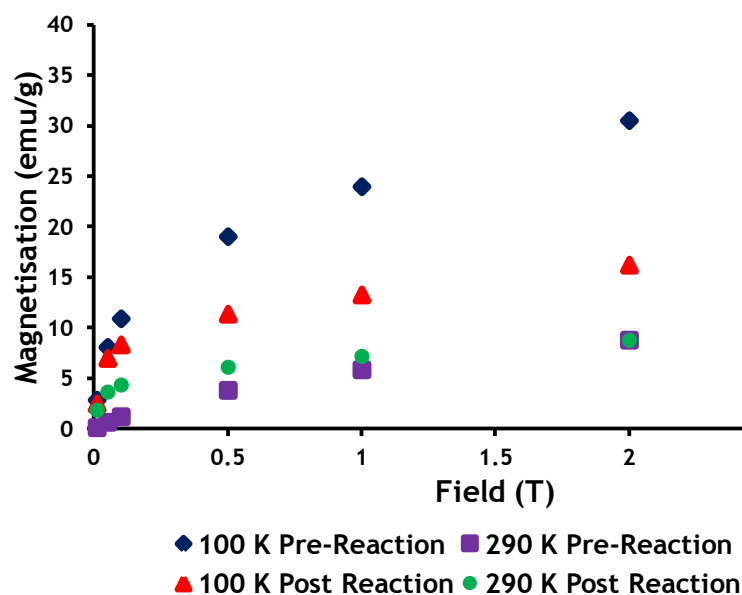
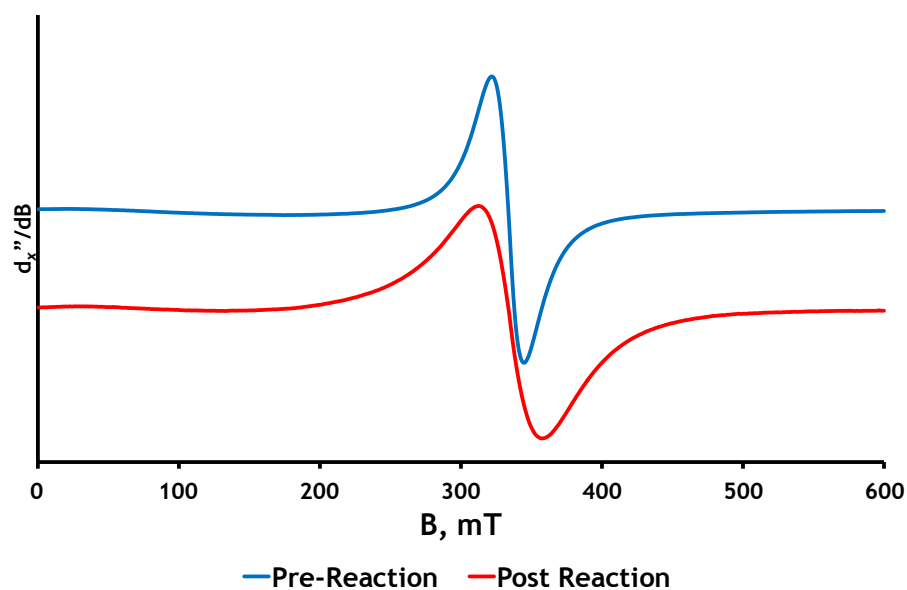


Figure 5.4 Comparison of Pre and Post Reaction Zinc Ferrite ZF03MBPC SQUID Magnetic Measurement.



**Figure 5.5 Comparison of Pre and Post Reaction Zinc Ferrite ZF3MBPC EPR Paramagnetic Measurement.**

Figure 4.95 shows a steady decline in 1-butene conversion until the catalyst reaches a stable state at 53 hours on stream. TGA/DSC analysis of post reaction zinc ferrite catalyst (ZF3MBPC) shows the evolution of carbon dioxide as a result of carbon lay down and oxidation of exposed reduced sites within the catalyst.

The following test profiles were carried out using zinc ferrite ZF3MBPC:-

Bed-profile

Temperature stability

Linear flow variations

Dual bed

Bed profile tests were carried out using zinc ferrite ZF3MBPC with the following catalyst volumes 3 cm<sup>3</sup>, 2 cm<sup>3</sup>, 1 cm<sup>3</sup> and 0.5 cm<sup>3</sup>.

Figure 5.6 below shows the comparison of the product selectivity and 1-butene conversion at 50 hours on stream. As expected the conversion increases down the bed, however it is interesting to note that most of the conversion is achieved in the first 20 % of the bed as is the highest selectivity. The isomerisation

reaction in contrast does not maximise until much later down the bed (~70 %) suggesting two independent reaction sequences.

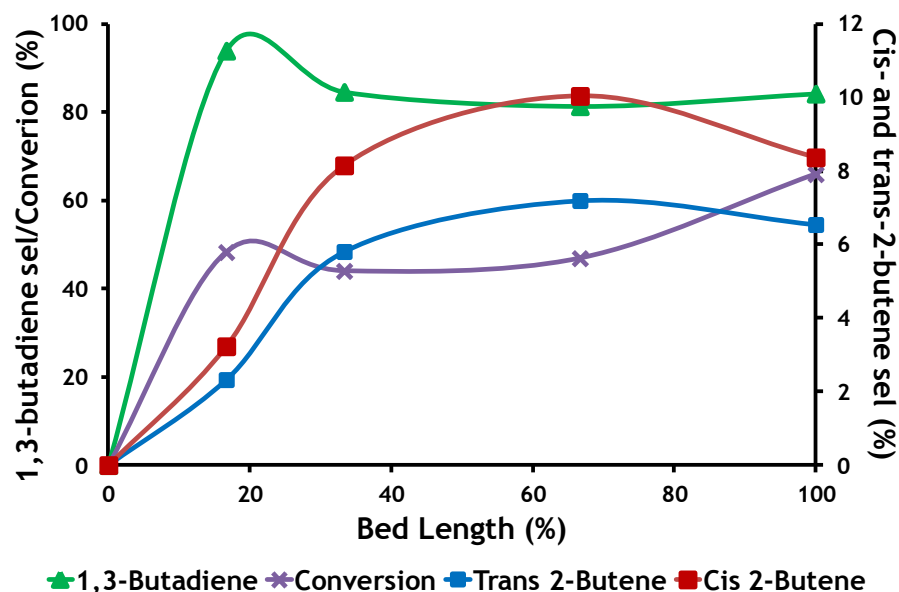


**Figure 5.6 Bed Length Comparison of Selectivities and Conversion at 50 Hours on Stream Zinc Ferrite ZF3MBPC.**

The temperature stability test regime was carried out with zinc ferrite ZF3MBPC as follows:- held at normal reaction temperature, temperature changed held for 48 hours returned to normal reaction temperature held for 24 hours and cycle repeated until study completed.

**Table 5.1 Zinc Ferrite ZF3MBPC Temperature Stability Test Regime.**

	Temperature Stability Test Regime							
Reaction Temperature (K)	693	653	693	713	693	633	693	613
Time on Stream (Hours)	48	48	24	48	24	48	24	48

The temperature stability test regime was conducted for a total of 315 hours on stream. Throughout the test period whenever the temperature was returned to 693K, the 1-butene conversion and product selectivities reverted to the original values. Changing the temperature by  $\pm 20$  K did not affect the 1-butene conversion or product selectivities. Lowering the temperature by 40K or more resulted in a decrease in the 1,3-butadiene selectivity and an increase in the

selectivities of cis-2-butene and trans-2-butene. No significant change in the 1-butene conversion was observed over the temperature test regime.

Linear flow variation tests were carried out using zinc ferrite catalyst (ZF3MBPC) with bed volumes of 3 cm<sup>3</sup> and 1 cm<sup>3</sup>. The 3 cm<sup>3</sup> bed volume was tested with linear flows of 11.85 Lh<sup>-1</sup> (NLV) and 23.70 Lh<sup>-1</sup> with no argon dilution (DLV); the 1 cm<sup>3</sup> bed volume was tested with linear flows of 11.85 Lh<sup>-1</sup> (NLV), 23.70 Lh<sup>-1</sup> without argon dilution (DLV) and 23.70 Lh<sup>-1</sup> with argon dilution (NLV + Ar).

Table 5.2 below shows the linear velocities quoted as gas hour space velocity (GHSV) and weight hour space velocity (WHSV).

**Table 5.2 Zinc Ferrite ZF3MBPC Gas and Weight Hour Space Velocities.**

	NLV (3 cm <sup>3</sup> )	DLV (3cm <sup>3</sup> )	NLV (1cm <sup>3</sup> )	DLV (1cm <sup>3</sup> )	NLV + Ar (1cm <sup>3</sup> )
LV (Lh <sup>-1</sup> )	11.85	23.7	11.85	23.7	23.7
GHSV (h <sup>-1</sup> )	200	400	600	1200	1200
WHSV (h <sup>-1</sup> )				2.6	1.3

Figure 4.118 shows the results at 50 hours on stream for the 200 h<sup>-1</sup> and 400 h<sup>-1</sup> GHSV tests, which show an increase in 1,3-butadiene yield and a decrease in cis-2-butene and trans-2-butene yields with increasing GHSV.

Figure 4.119 shows results at 50 hours on steam for the 600 h<sup>-1</sup> and 1200 h<sup>-1</sup> GHSV tests. These show an increase in 1,3-butadiene yield, 1-butene conversion and decreasing cis-2-butene and trans-2-butene yields with increasing GHSV. Therefore the oxidehydrogenation reaction is faster than the isomerisation reaction. The WHSV comparison shows only a slight increase in conversion with the lower WHSV.

Dual bed tests were carried out using different bed volume ratios of  $\theta$ -alumina and zinc ferrite ZF3MBPC to investigate the effect of isomerisation on the oxidehydrogenation reaction. The following  $\theta$ -alumina:zinc ferrite (Al:ZF) ratios were used 3:1, 1:1, 1:1 (mixed) and 0:1. From previous catalyst testing reactions on 3 cm<sup>3</sup> and 1 cm<sup>3</sup> alumina samples the feed composition exiting the alumina

bed of the dual bed reactors can be determined. With a 3 cm<sup>3</sup> bed of alumina a feed composition of 13 % trans-2-butene, 24 % cis-2-butene, 1 % 1,3-butadiene and 61 % 1-butene was obtained, whereas the 1 cm<sup>3</sup> alumina bed gives a feed composition of 3 % trans-2-butene, 7 % cis-2-butene, < 1 % 1,3-butadiene and 89 % 1-butene. Using the revised feed composition exiting the 3 cm<sup>3</sup> and 1 cm<sup>3</sup> alumina bed, the 1,3-butadiene yields at 50 h time on stream are 54 % and 49 % respectively.

Figure 4.126 shows the dual bed comparison which shows 1,3-butadiene selectivity order Al:ZF 3:1 < Al:ZF 1:1 < Al:ZF 0:1 < Al:ZF 1:1 (mixed). Cis-2-butene and trans-2-butene selectivity order Al:ZF 1:1 (mixed) > Al:ZF 0:1 = Al:ZF 1:1 > Al:ZF 3:1, 1-butene conversion order Al:ZF 0:1 < Al:ZF 1:1 < Al:ZF 1:1 (mixed) < Al:ZF 3:1. The addition of  $\theta$ -alumina as an isomerisation catalyst increases the conversion of 1-butene but due to higher yields in isomerisation products shows no significant change in 1,3-butadiene yield for Al:ZF 3:1 but shows a slight decrease in the case of Al:ZF 1:1. When the alumina and bulk zinc ferrite catalyst are mixed (Al:ZF 1:1 mixed) instead of in discrete catalyst beds the 1-butene conversion is lower than in the case of Al:ZF 3:1 but, due to the lower isomerisation products, gives the highest yield of 1,3-butadiene at 55 %. Figures 5.7 to 5.8 below show the average percentage gas composition post 3 cm<sup>3</sup> and 1 cm<sup>3</sup> alumina bed and gas composition post reaction alumina:zinc ferrite (ZF3MBPC) 3:1, 1:1 at 50 h TOS.

Tables 5.3 and 5.4 below show the average percentage gas composition post 3 cm<sup>3</sup> and 1 cm<sup>3</sup> alumina bed and gas composition post reaction alumina:zinc ferrite (ZF3MBPC) 3:1, 1:1 at 50 h TOS.

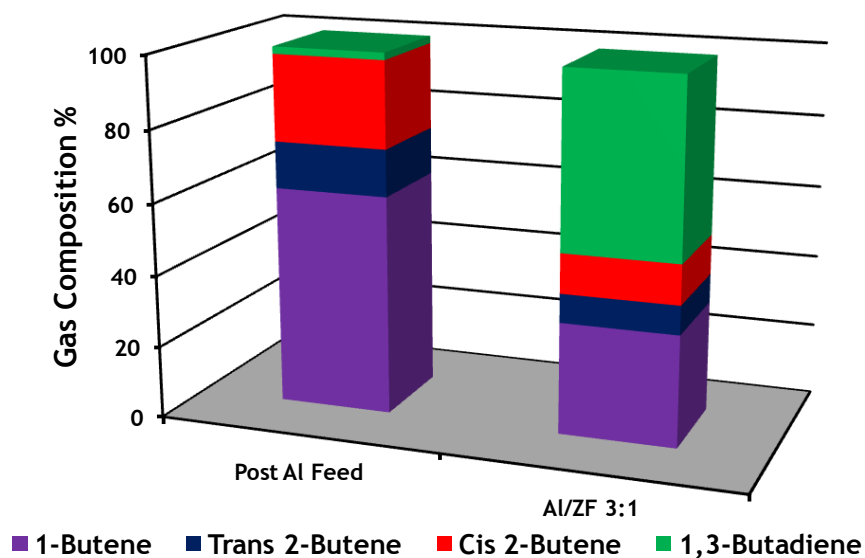


**Figure 5.7** Comparison of Average Gas Composition Post 3cm<sup>3</sup> Alumina Bed and Gas Composition Post Reaction Alumina:Zinc Ferrite (ZF3MBPC) 3:1 at 50 h TOS.

**Table 5.3** Comparison of Average Gas Composition Post 3cm<sup>3</sup> Alumina Bed and Gas Composition Post Reaction Alumina:Zinc Ferrite (ZF3MBPC) 3:1 at 50 h TOS.

	Post Al Feed (Gas Composition %)	Al/ZF 3:1 (Gas Composition%)
<b>Trans 2-Butene</b>	13	8
<b>Cis 2-Butene</b>	24	11
<b>1,3-Butadiene</b>	2	49
<b>1-Butene</b>	61	31

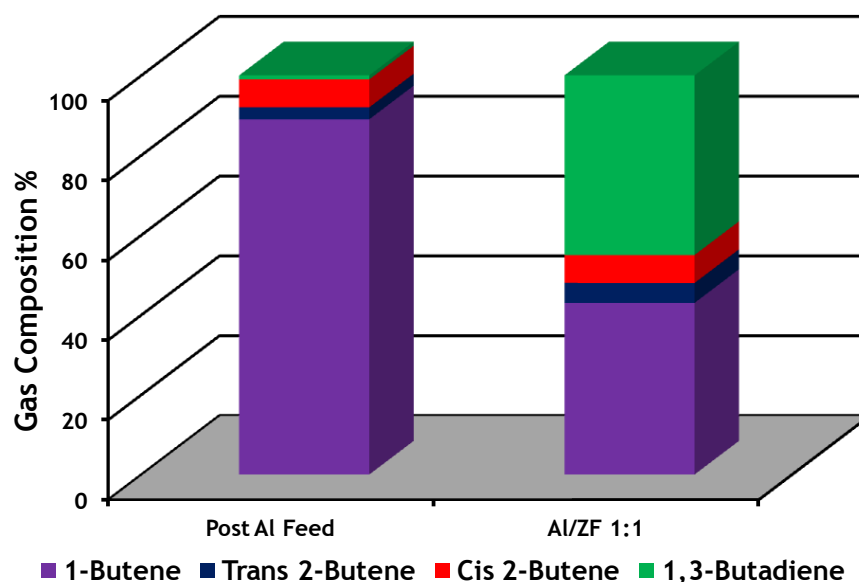


**Figure 5.8** Comparison of Average Gas Composition Post 1cm<sup>3</sup> Alumina Bed and Gas Composition Post Reaction Alumina:Zinc Ferrite (ZF3MBPC) 1:1 at 50 h TOS.

**Table 5.4** Comparison of Average Gas Composition Post 1cm<sup>3</sup> Alumina Bed and Gas Composition Post Reaction Alumina:Zinc Ferrite (ZF3MBPC) 1:1 at 50 h TOS.

	Post Al Feed (Gas Composition %)	Al/ZF 1:1 (Gas Composition %)
Trans 2-Butene	3	5
Cis 2-Butene	7	7
1,3-Butadiene	1	45
1-Butene	89	43

Figures 5.9 below shows the percentage gas composition post reaction alumina:zinc ferrite (ZF3MBPC) 3:1, 1:1 and 1:1 (mixed) at 50 h TOS.

Tables 5.5 below shows the percentage gas composition post reaction alumina:zinc ferrite (ZF3MBPC) 3:1, 1:1 and (mixed) at 50 h TOS.

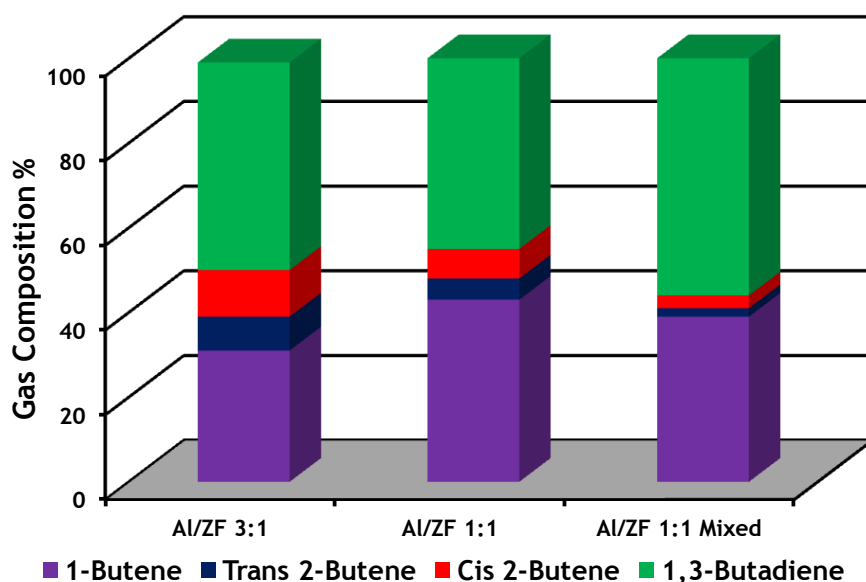


Figure 5.9 Comparison of Gas Composition Post Reaction Alumina:Zinc Ferrite (ZF3MBPC) 3:1, 1:1 and 1:1 Mixed at 50 h TOS.

Table 5.5 Comparison of Gas Composition Post Reaction Alumina:Zinc Ferrite (ZF3MBPC) 3:1, 1:1 and 1:1 Mixed at 50 h TOS.

	Al/ZF 3:1 (Gas Composition %)	Al/ZF 1:1 (Gas Composition %)	Al/ZF 1:1 Mixed (Gas Composition %)
Trans 2-Butene	8	5	2
Cis 2-Butene	11	7	3
1,3-Butadiene	49	45	56
1-Butene	31	43	39

## 5.6 Bulk Zinc Ferrite ZF3MBPD Catalyst.

Bulk zinc ferrite catalyst ZF3MBPD was prepared by co-precipitation iron and zinc chlorides at ambient temperature in 3 M sodium hydroxide.

The pre and post reaction XRD profiles, pre reaction Raman spectra and pre and post reaction surface area measurement for zinc ferrite (ZF3MBPD) gives the same bulk and structural information as zinc ferrite (ZF0.6MBP). On comparing pre and post reaction acid sites analysis, as shown in figures 4.137 and 4.151, it can be seen that there is a loss of three acid sites; two weak and one strong site. Examination of the pre and post reaction Raman spectra shows the loss of one

band which confirms structural changes on the catalyst and the addition of two bands which shows evidence of carbon laydown. The observations above show that zinc ferrite (ZF3MBPD) undergoes both bulk and structural changes.

Figure 4.138 shows a steady decline in 1-butene conversion until the catalyst reaches a stable state at 28 hours on stream. TGA/DSC analysis of post reaction zinc ferrite catalyst (ZF3MBPD) shows the evolution of carbon dioxide as a result of carbon lay down and oxidation of exposed reduced sites within the catalyst.

Zinc ferrite catalyst (ZF3MBPD) was used to study the alkene isomer effect on butene conversion and 1,3-butadiene selectivity.

Figure 4.146 shows the isomer comparison at 10 hours which shows the 1,3-butadiene selectivity and 1-butene conversion increases in the order of 1-butene < cis-2-butene. < trans-2-butene. The highest 1,3-butadiene yield of 76 % was obtained using trans-2-butene.

## **5.7 Iron Enriched Zinc Ferrite Catalysts.**

Iron enriched zinc ferrite catalysts ZFFeNH3P, ZFFeNH3PD and ZFFeNaOHP were prepared by co-precipitation of iron and zinc nitrates in either 14 M ammonium hydroxide or 14 M sodium hydroxide to give a Fe:Zn ration of 3:1.

Analysis of the pre reaction XRD profile and the Raman spectra of iron enriched zinc ferrite catalyst (ZFFeNH3P) confirm the presence of zinc ferrite, ferrous and ferric oxides and iron nitride; the Raman spectra also shows the presence of zinc oxide which is not inconsistent with the atomic absorption Fe:Zn mole ratio of 3.9:1. The iron enriched zinc ferrite catalyst (ZFFeNH3P) was prepared by dissolving iron and zinc nitrates in water with a metal ratio of 3:1 at ambient temperature, with the ammonia solution added in one aliquot with vigorous stirring. From the AA mole ratio results it would appear that this method of co-precipitation causes iron nitrate to convert to iron hydroxide at faster rate than zinc nitrate to zinc hydroxide which results in a portion of zinc nitrate remaining in solution. XRD analysis of the post reaction sample confirms the retention of the zinc ferrite and ferric oxide structures with the loss of ferrous

oxide and iron nitride. However when the pre and post reaction surface area measurements for the iron enriched zinc ferrite catalyst (ZFFeNH3P) are compared no change in surface area is observed. Examination of the pre and post reaction Raman spectra shows gain of three bands two associated with zinc ferrite and one associated with ferric oxide which confirms structural changes on the catalyst. The observations above show that iron enriched zinc ferrite catalyst (ZFFeNH3P) undergoes structural changes with the conversion of ferrous oxide and iron nitride to ferric oxide but does not undergo bulk changes.

Figure 4.166 shows that iron enriched zinc ferrite catalyst (ZFFeNH3P) deactivates over the first 20 hours. The initial 1,3 butadiene yield was 54 % which decreased before reaching steady state. On examining the 1,3-butadiene yield and 1-butene conversion in the steady state at 72 h on stream a 1,3-butadiene yield of 38 % and a 1-butene conversion of 42 % were obtained. TGA/DSC analysis of iron enriched zinc ferrite catalyst (ZFFeNH3P) confirms that there is no carbon laydown on the catalyst.

On comparing our results using iron enriched zinc ferrite catalyst (ZFFeNH3P) with those of Zhang *et al*[16] we find a lowering in butene conversion and 1,3-butadiene yield by 6 % and 7 % respectively (1 h TOS). However the conditions used by Zhang *et al* differed significantly from ours in terms of temperature, GHSV and oxygen:butene ratio, making a direct comparison difficult.

Analysis of the pre reaction XRD profile and the Raman spectra of iron enriched zinc ferrite catalyst (ZFFeNH3PD) confirm the presence of zinc ferrite, ferrous and ferric oxide; the Raman spectra also shows the presence of zinc oxide which is consistent with the atomic absorption Fe:Zn mole ratio of 3:1. Iron enriched zinc ferrite catalyst (ZFFeNH3PD) was prepared by dissolving in water iron and zinc nitrates with a metal ratio of 3:1 at ambient temperature. Ammonia solution was added drop-wise over 30 minutes with vigorous stirring. This preparation method allows co-precipitation to proceed in the molecular ratio of the solution. XRD analysis of the post reaction sample confirms the retention of the zinc ferrite, ferric oxide and iron nitride structures with the loss of ferrous oxide. However when the pre and post reaction surface area measurements for

the iron enriched zinc ferrite catalyst (ZFFeNH3PD) are compared no change in surface area is observed. Examination of the pre and post reaction Raman spectra shows the gain of two bands one associated with zinc ferrite and one associated with ferric oxide which confirms structural changes on the catalyst. The observations above show that iron enriched zinc ferrite catalyst (ZFFeNH3PD) undergoes structural changes with the conversion of ferrous oxide and to ferric oxide but does not undergo bulk changes.

Figure 4.168 shows the oxidative dehydrogenation of 1-butene over iron enriched zinc ferrite (ZFFeNH3PD). There is rapid deactivation over the initial 5 hours followed by a slow decline over the remaining time on stream to a conversion of 2 %. Comparison of the 1,3-butadiene yields at 10 hours and 70 hours on stream shows a decrease of 1 %, whereas the cis-2-butene and trans-2-butene yields over the same timescale exhibit no significant change. This reinforces the view that butadiene production and butene isomerisation occur on different sites. On comparing the carbon dioxide and isobutene yields of iron enriched zinc ferrite catalysts ZFFeNH3P and ZFFeNH3PD the yields ratios are 10:1 and 1:10 respectively TGA/DSC shows a weight change of less than 1 %.

Comparing the surface area, pore diameter and cumulative pore volume of iron enriched zinc ferrite catalysts ZFFeNH3P and ZFFeNH3PD shows that ZFFeNH3PD has significantly lower surface area, cumulative pore volume and higher pore diameter as well as being 28% denser than ZFFeNH3P. These changes possibly account for the different activities of these catalysts. Therefore it is clear that the preparation methodology is critical in preparing a good catalyst.

Analysis of the pre reaction XRD profile and the Raman spectra of iron enriched zinc ferrite catalyst (ZFFeNaOHP) confirm the presence of zinc ferrite and ferric oxide; the Raman spectra also shows the presence of zinc oxide in agreement with the atomic absorption Fe:Zn mole ratio of 31.7:1. The reason for the ZFFeNaOHP Fe:Zn mole ratio to be 10 times higher than ZFFeNH3PD is that zinc hydroxide is highly soluble in 14M sodium hydroxide and so much of the zinc has been kept in solution.[48] XRD analysis of the post reaction sample confirms the retention of the zinc ferrite and ferric oxide structures. Equally when the pre and post reaction surface area measurements for the iron enriched zinc ferrite

catalyst (ZFFeNaOHP) are compared no change in surface area is observed. Examination of the pre and post reaction Raman spectra shows no change in the Raman spectra. The observations above show that iron enriched zinc ferrite catalyst (ZFFeNaOHP) does not undergo structural bulk changes.

Figure 4.170 shows the oxidative dehydrogenation of 1-butene over iron enriched zinc ferrite catalyst (ZFFeNaOHP). The catalyst has very low activity (< 1 %) and shows continuous deactivation with time on stream. These results are consistent with a bulk iron oxide catalyst (see section 5.8 below)

## 5.8 Iron Oxide Catalysts.

Iron oxide catalysts Fe<sub>2</sub>O<sub>3</sub>NH<sub>3</sub>P and Fe<sub>2</sub>O<sub>3</sub>NaOHP were prepared by precipitation of iron nitrates in either 14 M ammonium hydroxide or 14M sodium hydroxide.

Analysis of the pre reaction XRD profile and the Raman spectra of iron oxide catalyst (Fe<sub>2</sub>O<sub>3</sub>NaOHP) confirm the presence of three phases of ferric oxide. XRD analysis of the post reaction sample confirms the retention of the three phases of ferric oxide. When the pre and post reaction surface area measurements for the iron oxide catalyst (Fe<sub>2</sub>O<sub>3</sub>NaOHP) are compared no change in surface area is observed. Examination of the pre and post reaction Raman spectra shows no change in the Raman spectra. The observations above show that iron oxide catalyst (Fe<sub>2</sub>O<sub>3</sub>NaOHP) does not undergo any bulk, structural changes.

Figure 4.187 shows the oxidative dehydrogenation of 1-butene over iron oxide catalyst (Fe<sub>2</sub>O<sub>3</sub>NaOHP). The catalyst has very low activity (< 1 %) and shows continuous deactivation with time on stream.

Analysis of the pre reaction XRD profile and the Raman spectra of iron oxide catalyst (ZFFeNH<sub>3</sub>P) confirm the presence of three phases of ferric oxide. XRD analysis of the post reaction sample confirms the retention of the three phases of ferric oxide. However when the pre and post reaction surface area measurements for the iron oxide catalyst (Fe<sub>2</sub>O<sub>3</sub>NH<sub>3</sub>P) are compared a decrease from 26 m<sup>2</sup>g<sup>-1</sup> to 3 m<sup>2</sup>g<sup>-1</sup> is observed. Examination of the pre and post reaction

Raman spectra shows no change in the Raman spectra. From the observations above it is clear that the iron oxide catalyst ( $\text{Fe}_2\text{O}_3\text{NH}_3\text{P}$ ) undergoes bulk changes, but does not undergo structural changes.

Figure 4.189 shows the oxidative dehydrogenation of 1-butene over iron oxide catalyst ( $\text{Fe}_2\text{O}_3\text{NaOHP}$ ). The catalyst has very low activity ( $< 1\%$ ) and shows continuous deactivation with time on stream.

From these results we can see that bulk iron oxides are poor catalysts for 1-butene oxidehydrogenation.

## 6. Conclusion.

The aim of this study was to investigate the activity and selectivity of a number of catalysts for the oxidative dehydrogenation of C4 alkenes to 1,3-butadiene. The catalysts prepared were supported zinc ferrite and vanadia on  $\theta$ -alumina, bulk iron oxide and zinc ferrites produced using a number of precipitation methods.

The  $\theta$ -alumina support was stable under reaction conditions but gave very poor 1,3-butadiene selectivity with only moderate 1-butene conversion. The support acted as an isomerisation catalyst with high cis-2-butene and trans-2-butene selectivities.

$\theta$ -alumina supported zinc ferrite and zinc doped iron catalysts gave high 1,3-butadiene selectivity and low cis-2-butene and trans-2-butene selectivities at moderate 1-butene conversion. The supported metal oxide catalysts all show, to some extent, decreasing 1,3-butadiene yield with time on stream which suggests deactivation of the zinc ferrite and zinc doped iron sites.

The  $\theta$ -alumina supported vanadia catalysts gave low selectivity towards 1,3-butadiene, while 1-butene conversion increased with vanadia loading. The catalysts showed higher selectivity to cis-2-butene and trans-2-butene with the lower vanadia loading catalyst giving a cis:trans ratio of 1:0.6 while the higher loading catalyst gave a cis:trans ratio of 1:1.25, suggesting that 1-butene is converted to cis-2-butene followed by cis/trans isomerisation.

Overall the supported catalysts proved to be unsuitable since they produced excessive quantities of cis and trans-2-butene especially the vanadia catalysts. The supported zinc ferrite catalysts also showed varying degrees of deactivation. Iron oxide catalysts gave moderate to high 1,3-butadiene selectivities but with low 1-butene conversions. Indeed the iron oxide catalysts gave such low 1-butene conversions that they were eliminated as possible ODH catalysts for 1-butene conversion to 1,3-butadiene.

Bulk zinc ferrites were found to be ideal catalysts for 1-butene ODH. They gave high 1,3-butadiene selectivity, moderate 1-butene conversion and low cis-2-butene and trans-2-butene selectivity. The surface area of the bulk zinc ferrite catalysts all decrease by at least 50 % during the ODH reaction and catalysts typically lose two acid sites during the reaction with no strong acid sites remaining. However after the initial sintering reaction, which causes the surface area to decrease and the loss of the acid sites, the catalysts proved to be thermally robust with no deactivation. The exception to this is the zinc ferrite (ZF0.6MBP) catalyst, which showed far higher isomerisation activity initially and noticeable deactivation due to carbon laydown. It is possible that using the lower base concentration resulted in more acid sites and hence higher isomerisation activity and associated carbon laydown. The magnetic and paramagnetic studies show that there is a loss of Fe(III) tetrahedral sites within the defective spinel structure of the catalysts. From the temperature studies it can be seen that the catalysts have good temperature stability and broad operating range (673 K to 713 K). Indeed from the bed profile and space velocity studies, it is clear that space velocity could be increased by a factor of 6 with no significant detriment to selectivity or conversion, which would represent a considerable improvement in process economics. The effect of the different isomers was studied using 1-butene, cis-2-butene, trans-2-butene and two different n-butene isomer compositions (13 % trans-2-butene, 24 % cis-2-butene, 1 % 1,3-butadiene, 61 % 1-butene and 3 % trans-2-butene, 7 % cis-2-butene, <1 % 1,3-butadiene, 89 % 1-butene) produced by introducing different  $\theta$ -alumina pre bed volumes. The reaction system that gave the highest 1,3-butadiene selectivity, butene conversion and lowest rate of isomerisation was the one with trans-2-butene as the hydrocarbon feed. In general, our results for C4 alkene conversion and 1,3-butadiene selectivity at low space velocity are slightly lower than those found in literature and this may be due to our use of single isomers instead of C4 raffinate-3.

In the literature it was suggested that additional iron in bulk zinc ferrite catalysts enhanced the activity of the catalyst. An iron enriched zinc ferrite catalyst could be prepared using ammonia as the base that gave high 1,3-butadiene selectivity with moderate 1-butene conversion. However the efficacy of the catalyst was dependent upon the method of base addition. Use of

sodium hydroxide as the base gave a catalyst that contains very little zinc and behaves in the same manner as an iron oxide catalyst. The iron enriched zinc ferrite catalysts to varying degrees show a decreasing 1,3-butadiene selectivity and an increasing cis-2-butene and trans-2-butene selectivity with time on stream. Therefore iron enriched zinc ferrite catalysts, although giving high 1,3-butadiene selectivity, had lower 1-butene conversion than the bulk catalysts and showed signs of deactivation.

## References

1. Totten, G.E., *A Timeline of highlights from the histories of ASTM committee D02 and the petroleum industry*. Viewed 20th December 2013.
2. <http://www.petroleum.co.uk/composition>.
3. <http://www.essentialchemicalindustry.org/processes/cracking-isomerisation-and-reforming.html>, Viewed 17th December 2013.
4. <http://www.chemeurope.com/en/encyclopedia/1%2C3-Butadiene.html>.
5. <http://www.bookrags.com/research/13-butadiene-chmc>, Viewed 31/12/2013.
6. [http://www.todayinsci.com/7/7\\_25.htm](http://www.todayinsci.com/7/7_25.htm), Viewed 31/12/2013.
7. <http://www.transparencymarketresearch.com/butadiene-market-downstream-applications.html>, Viewed 18th December 2013.
8. <http://www.ihs.com/products/chemical/planning/ceh/butadiene.aspx>, Viewed 6th January 2014.
9. <http://www.dow.com/productsafety/assess/finder.htm>, 20th June 2013.
10. <http://www.intermediates.basf.com/chemicals/butadiene-extraction/features>, Viewed 8th January 2014.
11. [http://cpmaindia.com/butadiene\\_about.php](http://cpmaindia.com/butadiene_about.php), Viewed 18th December 2013.
12. Harlin, M.E., et al., *Effect of Mg and Zr Modification on the Activity of VOx/Al2O3 Catalysts in the Dehydrogenation of Butanes*. *Journal of Catalysis*, 2001. **203**(1): p. 242-252.
13. Ajayi, B.P., et al., *n-Butane dehydrogenation over mono and bimetallic MCM-41 catalysts under oxygen free atmosphere*. *Catalysis Today*, 2013. **204**(0): p. 189-196.
14. Stobbe, D.E., et al., *Iron oxide dehydrogenation catalysts supported on magnesium oxide. Part 3.-But-1-ene dehydrogenation activity*. *Journal of the Chemical Society, Faraday Transactions*, 1991. **87**(10): p. 1639-1647.
15. Lee, H., et al., *Oxidative Dehydrogenation of n-Butene to 1,3-Butadiene Over ZnMelllFeO4 Catalysts: Effect of Trivalent Metal (Melll)*. *Catalysis Letters*, 2009. **131**(3-4): p. 344-349.
16. Zhang, M., et al., *Phase cooperation between the ZnFe2O4 and [small alpha]-Fe2O3 phases of ferrite catalysts in the oxidative dehydrogenation of n-butenes*. *Journal of the Chemical Society, Faraday Transactions*, 1992. **88**(4): p. 637-644.
17. Toledo, J.A., et al., *Oxidative dehydrogenation of 1-butene to butadiene on  $\alpha$ -Fe2O3/ZnAl2O4 and ZnFexAl2-xO4 catalysts*. *Catalysis Letters*, 1994. **30**(1-4): p. 279-288.
18. Jung, J., H. Lee, and I. Song, *Production of 1,3-Butadiene From C4 Raffinate-3 Through Oxidative Dehydrogenation of n-Butene Over Bismuth Molybdate Catalysts*. *Catalysis Surveys from Asia*, 2009. **13**(2): p. 78-93.
19. Jung, J.C., et al., *Reactivity of n-butene isomers over a multicomponent bismuth molybdate (Co9Fe3Bi1Mo12O51) catalyst in the oxidative dehydrogenation of n-butene*. *Catalysis Communications*, 2008. **9**(7): p. 1676-1680.
20. Jung, J., et al., *Effect of reaction conditions on the catalytic performance of Co9Fe3Bi1Mo12O51 in the oxidative dehydrogenation of n-butene to 1,3-butadiene*. *Korean Journal of Chemical Engineering*, 2008. **25**(6): p. 1316-1321.

21. Park, J.-H., et al., *Effects of iron content on bismuth molybdate for the oxidative dehydrogenation of n-butenes to 1,3-butadiene*. Applied Catalysis A: General, 2012. **431-432**(0): p. 137-143.
22. Park, J.-H., K. Row, and C.-H. Shin, *Oxidative dehydrogenation of 1-butene to 1,3-butadiene over BiFe<sub>0.65</sub>Ni<sub>x</sub>Mo oxide catalysts: Effect of nickel content*. Catalysis Communications, 2013. **31**(0): p. 76-80.
23. Park, J.-H., et al., *Oxidative dehydrogenation of n-butenes to 1,3-butadiene over BiMoFe<sub>0.65</sub>P<sub>x</sub> catalysts: effect of phosphorous contents*. Research on Chemical Intermediates, 2011. **37**(9): p. 1125-1134.
24. Vieira Soares, A.P., et al., *Synergy effects between  $\beta$  and  $\gamma$  phases of bismuth molybdates in the selective catalytic oxidation of 1-butene*. Applied Catalysis A: General, 2003. **253**(1): p. 191-200.
25. Liu, X., D.S. Su, and R. Schlögl, *Oxidative dehydrogenation of 1-butene to butadiene over carbon nanotube catalysts*. Carbon, 2008. **46**(3): p. 547-549.
26. Christmann, H.F., *Production of unsaturated compounds*, 1966, Petro-Tex Chemical Corporation: US 3270080.
27. Christmann, H.F., *Unsaturated Hydrocarbons By Oxidative Dehydrogenation Over Silica-Promoted Ferrite Catalysts*, 1967, Petro-Tex Chemical Corporation: US 3303238.
28. Croce, L.J., L. Bajars, and M. Gabliks, *Modified oxidative dehydrogenation catalysts*, 1972, Petro-Tex Chemical Corporation: US 3670042.
29. Woskow, M.Z. and H.F. Christmann, *Oxidative dehydrogenation catalyzed with promoted zinc ferrite*, 1974, Petro-Tex Chemical Corporation: US 3856880.
30. Shin, C.-H., et al., *Complex oxide catalyst of Bi/Bo/Fe for the oxidative dehydrogenation of 1-butene to 1,3-butadiene and process thereof*, 2010, Korea Kumho Petrochemical Company Limited: US 2013/0209351 A1.
31. Mamedova, A., et al., *Modified Zinc Ferrite Catalyst And Method Of Preparation And Use*, 2012, Saudi Basic Industries Corporation: WO 2012/030891 A1.
32. Jackson, S.D. and S. Rugmini, *Dehydrogenation of n-butane over vanadia catalysts supported on  $\theta$ -alumina*. Journal of Catalysis, 2007. **251**(1): p. 59-68.
33. Liu, Z.F., Tongxiang; Zhou, Han; Zhang, Di; Gong, Xiaolu; Guo, Qixin; Ogawa, Hiroshi *Synthesis of ZnFe<sub>2</sub>O<sub>4</sub>/SiO<sub>2</sub> composites derived from a diatomite template*. Bioinspiration & Biomimetics, 2007. **2**(1): p. 30-35.
34. Lee, H., et al., *Effect of Divalent Metal Component (Mell) on the Catalytic Performance of MellFe<sub>2</sub>O<sub>4</sub> Catalysts in the Oxidative Dehydrogenation of n-Butene to 1,3-Butadiene*. Catalysis Letters, 2008. **124**(3-4): p. 364-368.
35. Chung, Y.-M., et al., *Factors Affect on the Reaction Performance of the Oxidative Dehydrogenation of n-Butene to 1,3-Butadiene Over Zn-Ferrite Catalysts*. Catalysis Letters, 2009. **130**(3-4): p. 417-423.
36. Singh, J.P., et al., *Micro-Raman investigation of nanosized zinc ferrite: effect of crystallite size and fluence of irradiation*. Journal of Raman Spectroscopy, 2011. **42**(7): p. 1510-1517.
37. Luoqi, P., et al., *Method of producing butadiene by oxidatively dehydrogenating butene and used catalyst*, 2013, China Petroleum and Chemical Corporation: CN 103102238.

38. Richardson, J.T., R. Scates, and M.V. Twigg, *X-ray diffraction study of nickel oxide reduction by hydrogen*. Applied Catalysis A: General, 2003. **246**(1): p. 137-150.
39. <http://www.linkam.co.uk/ccr1000-features/>, Viewed 17th February 2014.
40. Kim, H.-S. and P.C. Stair, *Personal Communication*.
41. Ikushima, Y. and M. Arai, *Raman spectroscopy study on the dynamic behavior of nitrate anion in zinc nitrate solution at high temperatures and pressure*. Chemical Physics, 1998. **238**(3): p. 455-464.
42. Sharma, S.K., *Raman study of ferric nitrate crystalline hydrate and variably hydrated liquids*. The Journal of Chemical Physics, 1974. **61**(5): p. 1748-1754.
43. Wei, Q., et al., *Facile Synthesis of  $\alpha$ -Fe<sub>2</sub>O<sub>3</sub> Nanostructured Films with Controlled Morphology*. MATERIALS TRANSACTIONS, 2009. **50**(6): p. 1351-1354.
44. Ibáñez, M., et al., *Identification of the coke deposited on an HZSM-5 zeolite catalyst during the sequenced pyrolysis-cracking of HDPE*. Applied Catalysis B: Environmental, 2014. **148-149**(0): p. 436-445.
45. Rugmini, S. and S.D. Jackson, *Personal Communication*.
46. Sproules, S., *Personal Communication*.
47. Toledo-Antonio, J.A., et al., *Correlation between the magnetism of non-stoichiometric zinc ferrites and their catalytic activity for oxidative dehydrogenation of 1-butene*. Applied Catalysis A: General, 2002. **234**(1-2): p. 137-144.
48. Pourbaix, M., *Atlas of Electrochemical Equilibria in Aqueous Solutions*.